2D Photonic Crystals to Enhance Up-Conversion Emission for Silicon Photovoltaics

Jonathan Andrew Scott Morton

Submitted for the degree of Doctor of Philosophy

Heriot-Watt University

The School of Engineering and Physical Sciences

15th December 2015

ABSTRACT

This thesis investigates the application of 2D photonic crystals to enhance the emission of up-conversion layers to improve the efficiency of silicon photovoltaics. Two up-conversion material compositions are of particular interest in this work: erbium doped titanium dioxide (TiO_2:Er) and erbium doped yttrium fluoride (YF_3:Er). The 2D photonic crystals under investigation are composed of TiO_2:Er and air; and YF_3:Er and silicon. These nano-structures are investigated using both simulation and experimental methods. Further work in this thesis analyses the properties of the highly conductive polymer poly(3,4-ethylenedioxythiophene):poly(styrenesulfonate) (PEDOT:PSS) for use as a transparent electrode and thin film electrically conductive adhesive for the application of silicon photovoltaics. The design and geometrical parameters for the 2D photonic crystals were optimised through simulations (plane wave expansion and finite-difference time-domain), before the structures were experimentally fabricated and optically characterised. The novel analysis of the refractive index of the prepared up-conversion materials using ellipsometry was a key step in the design of the photonic crystal structures. A maximum photoluminescence enhancement of 3.79 times was observed for the 980 nm emission profile, however this could not be successfully attributed to a photonic crystal effect. The optical, mechanical and electronic properties of PEDOT:PSS were characterised for thin film samples, using novel ellipsometry analysis.

Dedication

The work carried out for this thesis would not have been possible without the love and support of my wife, Lucy, who has kept my spirits high during the difficult times. Thank you for believing in me.

Acknowledgements

The friendship, support and advice of colleagues and friends at Heriot-Watt University have been invaluable to me throughout my PhD studies.

Professor Bryce S. Richards, thank you for the opportunity to carry out my PhD at Heriot-Watt University.

To everyone working in solar energy research at Heriot-Watt, we have all been on a unique journey; thank you for keeping me afloat when times were tough and for your expert up-conversion and solar advice. Ale, Dalila, Dan, Dave, Dorothy, Efthymios, Eliyas, Gudrun, Junjie, Mandy, Morgan, Paolo, Sean and Yiorgos.

Dr Bill MacPherson and Dr Jose Marques-Hueso, thank you for all of your help and support, which allowed me to complete my experimental work and write up my thesis. I am hugely grateful for all of the time you have given me and for your encouragement and belief. I am very grateful.

I have made so many good friends during my time at Heriot-Watt, who have contributed both technical and academic advice, bust most importantly friendship. Alan, Alasdair, Antonio, Dirk, Frauke, Helen, Loraine, Mark, Mäiwenn, Melanie, Neill, Peter, Richard, Rosario, Ross, Thomas, Witold and Wojciech.

Thank you to all of the technical staff in both Electrical and Mechanical Engineering, in addition to the stores managers for their patience and advice for all of my questions.

Finally, thank you to Rosemary and Kevin for all of the conversations and always putting a smile on my face when I arrive at work each morning.

ACADEMIC REGISTRY

Research Thesis Submission

Name*:*	Jonathan Andrew Scott Morton		
School/PGI:	Engineering and Physical Sciences		
Version: *(i.e. First, Resubmission, Final)*	Final	Degree Sought (Award **and** Subject area)	PhD Physics

Declaration

In accordance with the appropriate regulations I hereby submit my thesis and I declare that:

1) the thesis embodies the results of my own work and has been composed by myself

2) where appropriate, I have made acknowledgement of the work of others and have made reference to work carried out in collaboration with other persons

3) the thesis is the correct version of the thesis for submission and is the same version as any electronic versions submitted*.

4) my thesis for the award referred to, deposited in the Heriot-Watt University Library, should be made available for loan or photocopying and be available via the Institutional Repository, subject to such conditions as the Librarian may require

5) I understand that as a student of the University I am required to abide by the Regulations of the University and to conform to its discipline.

* *Please note that it is the responsibility of the candidate to ensure that the correct version of the thesis is submitted.*

Signature of Candidate*:*		Date:	

Submission

Submitted By *(name in capitals):*	
Signature of Individual Submitting:	
Date Submitted:	

For Completion in the Student Service Centre (SSC)

Received in the SSC by *(name in capitals):*			
1.1 Method of Submission *(Handed in to SSC; posted through internal/external mail):*			
1.2 E-thesis Submitted (mandatory for final theses)			
Signature:		Date:	

TABLE OF CONTENTS

GLOSSARY

a	Lattice constant
$\boldsymbol{a}$	Real space unit vector
A	Oscillator magnitude
Ab	Absorbance
ACA	Anisotropic conductive adhesive
AM	Air mass
A/A_n	Amplitude
$at\%$	Atomic percent
$\boldsymbol{b}$	Reciprocal space unit vector
B	Fitting parameter
Br_n	Broadening – Full Width at Half Maximum
BS	Beam splitter
c	Speed of light
CHF_3	Fluoroform, trifluoromethane
$[CF_2]_n$	perfluoroethylene
C/C_n	Fitting parameter
d	Thickness
DBR	Distributed Bragg reflector
e	electron
E	Energy
$e\text{-}beam$	electron beam
ECA	Electrically conductive adhesive
E_{0n}	Peak transition energy
E_{gn}	Band gap energy
E/E_n	Energy
Er^{3+}	Trivalent erbium
$Er(NO_3)_3$	Erbium nitrate
ESA	Excited state absorption
ETU	Energy transfer up-conversion
$FDTD$	Finite-difference time-domain
FIB	Focused Ion Beam
$\boldsymbol{G}$	Lattice vector
$Genosc$	Generalised oscillator
GSA	Ground state absorption
h	hole
$\hbar$	Plank's constant/2π
ICA	Isotropic conductive adhesive
I_{mpp}	Maximum power point current
InGaAs	Indium Gallium Arsenide
$ICP\text{-}RIE$	Inductively coupled plasma reactive ion etching
ITO	Indium Tin Oxide
J	Area normalized current density
J_0	Dark saturation current density
J_L	Light generated current density
J_{sc}	Short circuit current density
k	Boltzmann's constant
m^*	Carrier effective mass
$MEEP$	MIT Electromagnetic Equation Propagation
MPB	MIT Photonic Bands
MPE	Mean percentage error
MSE	Mean squared error
n	Refractive index
n	Ideality factor
N	Carrier concentration
$NdYAG$	Neodymium-doped yttrium aluminium garnet
O_2	Dioxygen
OPO	Optical parametric oscillator

PEDOT:PSS	poly(3,4-ethylenedioxythiophene):poly(styrenesulfonate)	TE	Transverse Electric
PET	poly(ethylene terephthalate)	TiO_2	Titanium dioxide
PFCB	perfluorocyclobutane	TiO_2:Er	Erbium doped TiO_2
P_{in}	Incident power	TM	Transverse Magnetic
PMMA	polymethyl methacrylate	Tr	Transmission
Pr^{3+}	Trivalent praseodymium	TTIP	Titanium tetra-isopropoxide
PWE	Plane wave expansion	V	Operating voltage
q	Electronic charge	V_{mpp}	Maximum power point voltage
r	Radius	V_{oc}	Open circuit voltage
RCA	Radio Corporation of America	*VASE*	Variable Angle Surface Ellipsometry
R_d	Diffuse reflectance	w	Rotational speed
$\tilde{R}_p$	Fresnel coefficient for p polarised light	*XRD*	X-ray Diffraction
$\tilde{R}_s$	Fresnel coefficient for s polarised light	YF_3	Yttrium fluoride
R_s	Series resistance	YF_3:*Er*	Erbium doped yttrium fluoride
R_{sh}	Shunt resistance	Γ	Gamma-direction
R_{sp}	Spectral reflectance	Δ	Delta
SEM	Scanning Electron Microscopy	ε_n	Oscillator form
SF_6	Sulfur hexafluoride	k	k-space unit vector
sccm	Standard cubic centimeters per minute	λ	Wavelength
Si	Silicon	μ	Carrier mobility
$SiCl_4$	Silicon tetrachloride	υ	normalised frequency
SiO_2	Silicon dioxide	ρ	Resistivity
SOI	Silicon on Insulator	σ	Conductivity
t	Time	τ_n	Scattering time
T	Operating temperature	Ψ	Psi
TCO	Transparent conductive oxide	ω	Frequency

LIST OF PUBLICATIONS

Conference Papers

J. Marques-Hueso, Sean K. MacDougall, Alessandro Boccolini, **Jonathan Morton**, Georgios E. Arnaoutakis, and Bryce S. Richards. "Up-conversion Photovoltaics: Challenges and Possible Solutions from Nano-Photonics." 2nd International Symposium on Energy Challenges and Mechanics, 2014.

Bryce S. Richards, J. Marques-Hueso, Sean K. MacDougall, Alessandro Boccolini, **Jonathan Morton**, E. D. Mammo, Georgios E. Arnaoutakis, and Aruna Ivaturi. "Progress Towards Enhancing the Performance of c-Si Photovoltaic Devices via Up-and Down-Conversion." In *Optical Nanostructures and Advanced Materials for Photovoltaics*, pp. PT3C-1. Optical Society of America, 2013.

J. Morton, J. Marques-Hueso, and B. Richards, "Enhanced Up-conversion for Photovoltaics using 2D Photonic Crystals," In *Renewable Energy and the Environment, OSA Technical Digest (online)* (Optical Society of America, 2013), paper JM3A.19.

Jonathan A. S. Morton, J. Marques-Hueso, and B. Richards, "Erbium Doped Two Dimensional Photonic Crystals for Band Edge Lasing," In *Photonic Crystal Materials and Devices X, SPIE Proceedings Vol. 8425 (online)* (SPIE, 2012), paper 84251W. doi: 10.1117/12.922416

Chapter 1 - Introduction

In this chapter, the motivation behind the work in this study will be detailed. Solar power is becoming increasingly important and ways to improve the efficiency are of great interest. A closer look at the solar spectrum provides an understanding of the benefits of up-conversion for photovoltaics, which is the main topic of study in this thesis. Finally, an overview of the structure of this thesis is presented.

1.1 Motivation for the Work

Increasing resources of energy are required by human society to meet the needs of a rapidly growing population. The past 100 years has seen a rapid population growth due to an increase in agricultural productivity and medical advances [1]. Conventional sources of energy are finite and damaging to the environment (fossil fuels), or are costly and dangerous to dispose of (nuclear). Furthermore, current global trends in energy consumption and supply are economically, environmentally and socially unsustainable [1]. Therefore there is a demand for clean and safe energy that will last for many generations and that will fill the pending void in energy supply. Renewable sources of energy, including the energy from the sun, provide an invaluable resource for power generation [2, 3].

Solar energy is a vast and plentiful resource: by far the largest renewable energy potential. It has been reported that the annual primary energy consumption in 2001 (4.25×10^{20} J) could be achieved from the amount of energy that falls on the earth in less than one hour [4]. Solar power generation also provides significant flexibility of installation and zero pollution during operation. The main disadvantages of all renewable energy generation compared to conventional sources is the low conversion efficiency and associated high cost per watt.

The utilisation of solar energy can be achieved through both passive and active systems. A passive solar heating system absorbs and stores the heat from the sun directly, within a very well insulated body. An example of such a system is a carefully orientated, well insulated house, with windows to collect the suns energy directly and appropriate insulation in the walls, flooring and ceiling to contain the heat [5]. Active solar energy systems collect energy from the sun using a heat absorbing fluid that is pumped through a collector. The collected heat can be used directly, or stored in a well-insulated body for

future use. This process is used by solar thermal collectors to heat water for domestic and industrial use throughout the world.

The conversion of the Sun's energy to electricity (photovoltaics) provides an alternative method for energy generation. There has been a rapid uptake of the use of photovoltaic solar panels over the last two decades as the price of manufacture has come down, while efficiency of the solar panels has increased. Cheap, modular solar panels provide an excellent source of electricity in locations where the cost of installing conventional electrical generation systems is too high [6]. This is of particular importance in developing nations, where the self-sufficient electricity generation, with little maintenance required, can have profound benefits for education and healthcare.

1.2 Up-conversion: Making the Most of the Solar Spectrum

The sun can be considered at first approximation to be a black body emitter of radiation. The solar energy radiation that reaches the vicinity of the Earth is traditionally split into two distinct spectra due to the effect of the Earth's atmosphere. The spectrum of the sun outside the earth's atmosphere is called *air mass zero (AM0),* with a corresponding power density of approximately 1.353 kW/m^2 [7]. While entering the Earth's atmosphere, the solar radiation is attenuated due to gas absorption, water absorption and dust particle scattering. The attenuation depends on the path length travelled through the atmosphere. When the sun is directly overhead, the solar spectrum that reaches earth is termed *AM1* [8]. When the sun is at 60° overhead, the spectrum is termed AM2, and so on. To allow comparison between solar panel efficiencies, the universally accepted standard terrestrial solar spectrum is given as AM1.5, corresponding to a power density of 1kW/m^2.

For most single band gap solar cells, the main loss of efficiency is due to the incomplete use of the solar spectrum. For silicon solar cells, around 35% of the energy from the sun is lost due to inefficient absorption of photons of energy greater than the semiconductor band gap. This excess energy is lost as heat in the semiconductor lattice. A further 20% of the sun's energy is lost due to transmission of photons of energy less than the band gap of silicon.

The photons that are lost due to transmission can be utilized through the application of an up-converter layer placed at the rear side of bifacial silicon photovoltaic cell (Figure 1-1). This up-converting layer absorbs two or more photons of low energy and emits a single

photon of energy greater than that of the silicon band gap. A detailed description of the up-conversion mechanism is presented in section 2.4.

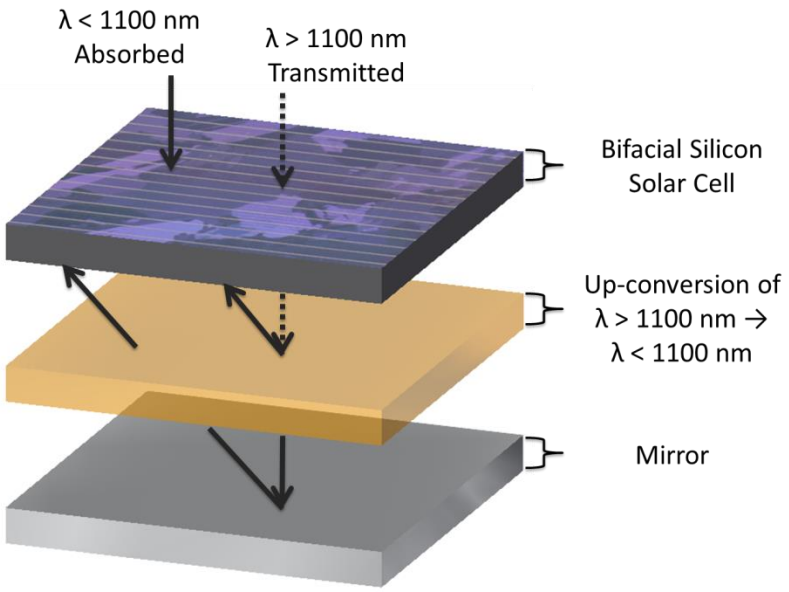

Figure 1-1: Photons of energy less than the band gap of the bifacial silicon cell (λ > 1100 nm) are transmitted through the photovoltaic layer and are absorbed by the up-conversion material below.

The potential for up-conversion to enhance the efficiency of silicon photovoltaics is significant. Figure 1-2 shows the *AM1.5* spectrum of the sun (blue), with the area corresponding to the absorption by a crystalline silicon solar cell shown in green. The spectral distribution that is available for two photon up-conversion for use with a crystalline silicon solar cell is shown in yellow. The extra available power density provided by up-conversion to a crystalline silicon solar cell for *AM1.5* is 35% (164 W/m^2 for up-conversion over the range 1.15 – 2.21 μm) [9]. Further details of the theoretical potential for the use of up-conversion with silicon photovoltaics are given in section 2.3.2.

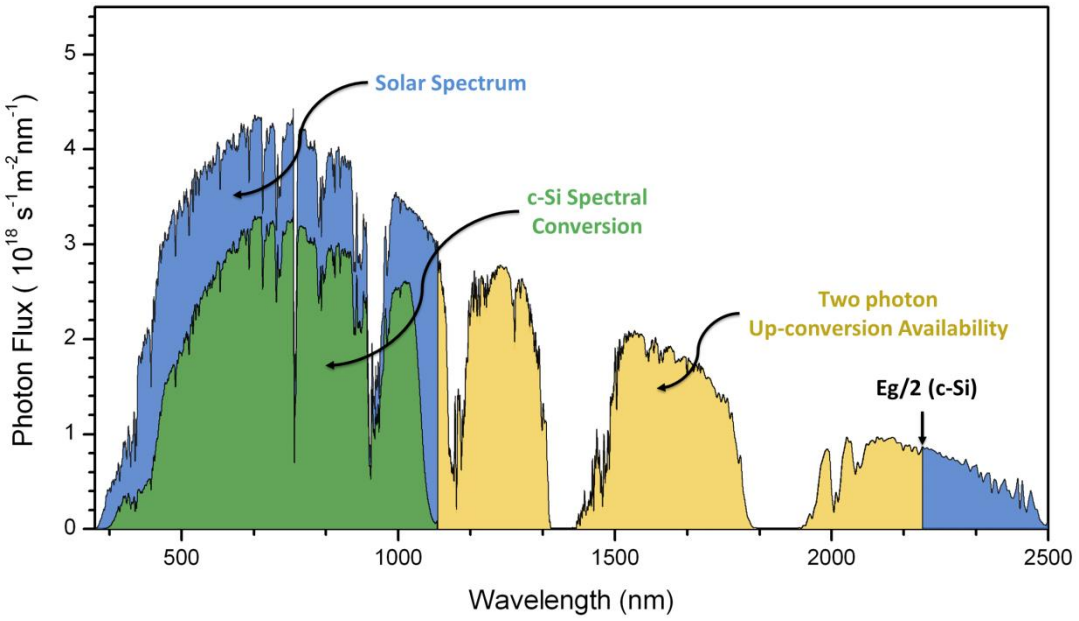

Figure 1-2: The *AM1.5* solar spectrum is shown (blue) with the corresponding areas that can be absorbed by a crystalline silicon solar cell (green) and can be used for up-conversion with a crystalline silicon solar cell (yellow). The upper wavelength limit for 2 photon up-conversion is equal to half the value of the band gap energy of crystalline silicon. Graph adapted from [10].

Experimental demonstrations of the use of up-conversion for photovoltaics have yet to reach anywhere close to the theoretical potential offered by this application. The main barriers to improved efficiency are the weak absorption of the Lanthanide ions that are commonly used in up-conversion materials; and competing loss mechanisms from non-radiative recombination [11]. Therefore there is much work to do in this area of research, with huge gains to be made; not only within the academic field of study, but in the rapidly expanding commercial market as well. The huge potential gains in efficiency and the significant implications for the world energy market are the motivation for the work of this thesis.

1.3 Thesis Overview

The work presented in this thesis investigates the potential for 2D photonic crystals to be used to enhance the efficiency of thin films of up-conversion material, suitable for use with bifacial crystalline silicon solar panels.

Chapter 2 provides a critical review of the relevant work that has already been carried out related to this field of study. The areas of work reviewed cover up-conversion for Enhancing Solar Energy Efficiency; 2D photonic crystals for enhancing luminescent emission; and the use of poly(3,4-ethylenedioxythiophene):poly(styrenesulfonate)

(PEDOT:PSS) as a transparent conductive contact. The use of a transparent conductive contact on the rear surface of a bifacial solar cell is required to make the most of any increase performance provided by the up-conversion layer by avoiding the detrimental partial shielding of the active photovoltaic layer by traditional metal fingers and bus bar electrical contacts.

Chapter 3 presents work carried out on simulating the interaction of light with 2D photonic crystals, to provide further understanding of the use of photonic crystals to enhance the up-conversion process, in addition to optimisation of the geometrical parameters of the photonic crystals required for the experimental fabrication.

Chapter 4 details the equipment and methods used for the fabrication and characterisation of the 1D and 2D nanostructured layers created during this study.

Chapter 5 discusses and evaluates the fabrication of 2D photonic crystals composed of erbium doped titanium dioxide and air. Two methods of fabricating up-converting erbium doped titanium dioxide thin films are investigated, along with the techniques used to pattern the 2D photonic crystal structures into these layers and the optical characterisation.

Chapter 6 presents the work carried out on the fabrication and characterisation of up-converting 2D photonic crystals of silicon and erbium doped yttrium fluoride. The analysis of the refractive index of the thin films of up-converting material was key to allow the geometrical structures of the photonic crystals to be tuned correctly.

Chapter 7 provides a wide ranging analysis of the optical, mechanical and electrical properties of thin films of the conductive polymer PEDOT:PSS for use as a transparent conductive electrode on the rear of a bifacial silicon solar cell. The mild fabrication conditions, flexible nature and good electrical characteristics of this transparent polymer make it a particularly versatile transparent conductive electrode.

Chapter 8 summarises the conclusions of the work carried out in this thesis. Furthermore, the future work required to build upon this study is suggested along with some experimental validation of how this could be achieved is discussed.

1.4 References

1. V. Balzani, and N. Armaroli, *Energy for a Sustainable World: From the Oil Age to a Sun-Powered Future* (Wiley, 2010).
2. R. E. H. Sims, "Renewable energy: a response to climate change," Solar Energy **76**, 9-17 (2004).
3. M. I. Hoffert, K. Caldeira, G. Benford, D. R. Criswell, C. Green, H. Herzog, A. K. Jain, H. S. Kheshgi, K. S. Lackner, J. S. Lewis, H. D. Lightfoot, W. Manheimer, J. C. Mankins, M. E. Mauel, L. J. Perkins, M. E. Schlesinger, T. Volk, and T. M. L. Wigley, "Advanced Technology Paths to Global Climate Stability: Energy for a Greenhouse Planet," Science **298**, 981-987 (2002).
4. N. S. Lewis, and D. G. Nocera, "Powering the planet: Chemical challenges in solar energy utilization," Proceedings of the National Academy of Sciences **103**, 15729-15735 (2006).
5. G. Miller, and S. Spoolman, *Living in the Environment: Principles, Connections, and Solutions* (Cengage Learning, 2008).
6. M. Boxwell, *Solar Electricity Handbook: A Simple, Practical Guide to Solar Energy : how to Design and Install Photovoltaic Solar Electric Systems* (Greenstream Publishing, 2012).
7. M. A. El-Sharkawi, *Electric Energy: An Introduction, Third Edition* (Taylor & Francis, 2012).
8. S. Magee, *Solar Photovoltaic Operation and Maintenance for Residential, Commercial and Utility Systems* (Createspace Independent Pub, 2010).
9. B. S. Richards, "Enhancing the performance of silicon solar cells via the application of passive luminescence conversion layers," Solar Energy Materials and Solar Cells **90**, 2329-2337 (2006).
10. W. G. J. H. M. van Sark, A. Meijerink, and R. E. I. Schropp, "Nanoparticles for Solar Spectrum Conversion," Nanotechnology for Photovoltaics, 351-390 (2010).
11. B. S. Richards, I. Aruna, S. K. W. MacDougall, and J. Marques-Hueso, "Up- and Down-Conversion Materials for Photovoltaic Devices," in *Photonics for Solar Energy Systems Iv*, R. Wehrspohn, and A. Gombert, eds. (2012).

Chapter 2 - A Critical Review of Up-conversion for Enhanced Solar Energy Efficiency, 2D Photonic Crystals for Enhanced Luminescent Emission and PEDOT:PSS as a Transparent Conductive Contact

2.1 Overview of the Chapter

This chapter presents a critical review of the relevant work that has been carried out in the subject areas relating to this thesis. The basic theory of silicon solar cells is presented, along with a summary of the fabrication process of bifacial silicon solar cells. An analysis of the efficiency limitations due to sub band-gap losses is covered and present techniques for improving silicon solar cell efficiency are reviewed, with a focus on spectral conversion. The concept of up-conversion is presented along with a review of recent up-conversion materials. The theory of photonic crystals is then introduced. This is followed by a summary of the work on using 2D photonic crystals to enhance luminescent emission, photovoltaic efficiency and up-conversion efficiency. Transparent conductive contacts for photovoltaics are reviewed, with an additional focus on the further uses of the highly conductive polymer and transparent contact PEDOT:PSS. Transparent conductive contacts on the rear of a bifacial solar cell can be used to avoid the detrimental shielding of traditional metal contacts and allow for a uniform intermediate layer between the up-conversion layer and the rear of the bifacial cell. Finally, the aims and objectives of this thesis are summarised.

2.2 Solar Energy Conversion in Silicon Photovoltaics

The dominance and relatively low fabrication cost of silicon photovoltaics in the commercial market is a significant motivation for improving the module efficiency of silicon panels. The maximum efficiency of a crystalline silicon solar cell to date is 25.6% at one-sun [1]. This is approaching the maximum efficiency determined by Shockley and Queisser of around 31% (section 2.2.3) [2]. Mono-crystalline silicon solar cells are more efficient, however more expensive to produce than their poly-crystalline counterparts. Therefore for a proof of concept study, mono-crystalline silicon solar cells are the most appropriate to use.

This section will introduce the theory behind the conversion of sunlight to electricity in a crystalline silicon solar cell and introduce the concept of a bifacial solar cell. A bifacial

cell allows for efficient absorption of light at both the front and rear of the cell (section 2.2.1). A summary of the fabrication process for a bifacial silicon solar cell is presented. Bifacial solar cells are required to maximise the potential of an up-conversion layer, which is applied at the rear of a solar cell. Finally, the efficiency losses in a silicon solar cell due to sub-band gap transmission is presented. It is this loss mechanism that the work of this thesis aims to address.

2.2.1 Theory of Crystalline Silicon Solar Cells

A typical silicon solar cell has one p-n junction just below the front surface of the cell. The p-n junction spatially separates electrons and holes by the intrinsic electric field of the junction. When light of energy greater than that of the electronic band gap of the silicon semiconductor is absorbed, an electron-hole pair is generated. The intrinsic electric field of the junction separates the electron and hole before they can recombine, resulting in a potential difference across the junction. When an external circuit with a load is connected to the front and rear surface of the p-n junction, the charge carriers generated and separated by the p-n junction can flow through the external circuit as an electrical current.

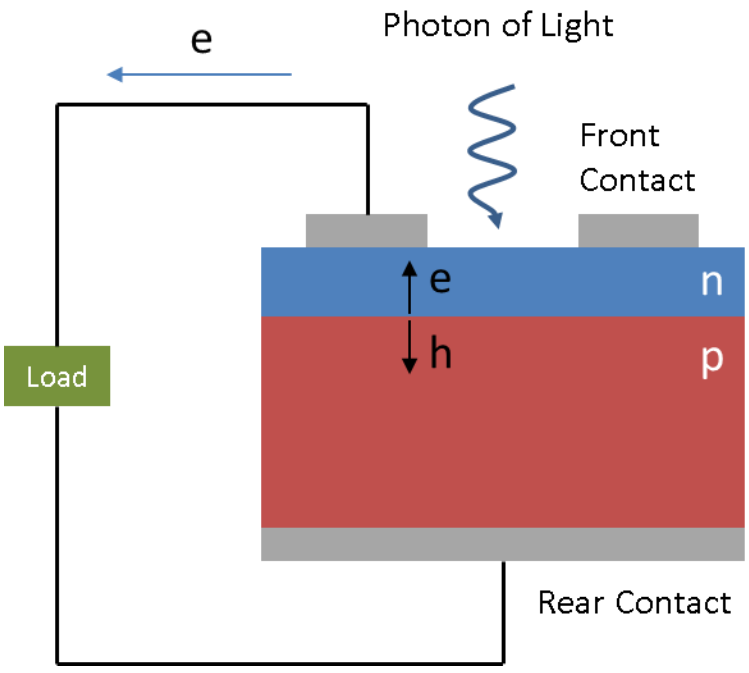

Figure 2-1: A photon incident on the p-n junction creates and electron hole pair. The electrons (e) and holes (h) are quickly separated by the intrinsic electric field of the junction. If an external circuit is connected through contacts, the electrons will flow around the external circuit and through a load.

The current density of the solar cell is key to assessing its performance. The area-normalised current density J is given by

$$J = J_L - J_0\left(exp^{\left(\frac{q(V+JR_s)}{nkT}\right)} - 1\right) - \frac{V + JR_s}{R_{sh}} \qquad 2.1$$

where J_L is the light generated current density (mA/cm^2), J_0 is the dark saturation current density, V is the operating voltage. k is Boltzmann's constant (1.380×10^{-23} J/K), R_s is the series resistance, R_{sh} is the shunt resistance, n is the diode ideality factor, T is the operating temperature and q is the electronic charge (1.602×10^{-19} C).

The final part of the current density equation (2.1) deals with the shunt resistance of the solar cell. A low shut resistance causes power losses in solar cells by allowing an alternative path for the light generated current to flow. The presence of the shunt resistance is typically due to manufacturing defects in the cell. The current produced by the solar cell (J) is therefore equal to the current produced by the source J_L, minus the current that flows through the diode $\left(J_0\left(exp^{\left(\frac{q(V+JR_s)}{nkT}\right)} - 1\right)\right)$, minus the current flowing through the shunt resistor $\left(\frac{V+JR_s}{R_{sh}}\right)$.

For the special case when the voltage is zero and $J = J_L$, this current is defined as the short circuit current density J_{sc}. The voltage at which $J = 0$ is defined as the open circuit voltage V_{oc}. The most efficient operating scenario for the cell is called the maximum power point voltage V_{mpp} and the maximum power point current I_{mpp}. At this point the efficiency of conversion of sun's energy into electrical energy is given as

$$\eta = \frac{V_{mpp}I_{mpp}}{P_{in}} \qquad 2.2$$

where P_{in} is the incident power on the solar cell [3].

Bifacial silicon solar cells allow for the absorption of light at both the front and rear of the solar cell. They typically consist of a double junction, commonly of the doping order n^+-p-n^+. One of the most recent high performing bifacial cells was developed by Ohtsuka *et al*, who fabricated a cell with a 21.3% front efficiency and 19.8% rear efficiency [4]. These experimental efficiencies refer to the electrical junctions formed at both the front and rear of the cell due to doping of the silicon. A bifacial silicon solar cell is required for the application of an up-converting layer at the rear of the cell. Placing the up-converting

layer at the rear of the cell ensures that the normal high efficiency operation of the cell at the front surface is not impeded. A p-n junction on the rear of the cell will ensure that the maximum increase in efficiency from the up-converting layer directly below can be obtained.

2.2.2 Bifacial Silicon Solar Cell Fabrication Techniques

A summary of the fabrication steps for a bifacial silicon solar cell is presented in Figure 2-2. The steps shown are for an initial p-type silicon wafer, adapted from Duran [5].

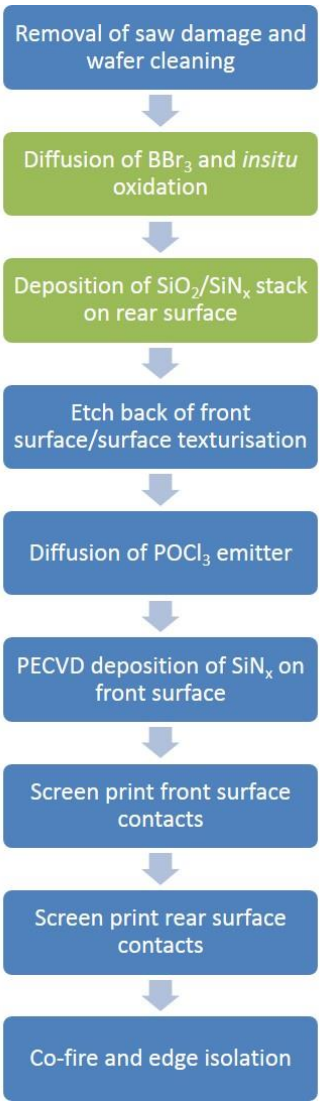

Figure 2-2: Fabrication steps for a bifacial cell. The additional steps for a bifacial cell, compared to a monofacial cell, are shown in green.

The additional fabrication steps required for a bifacial cell, compared to a monofacial cell are shown in green. Both of these steps use methods closely related to those already in

use for the mass fabrication of monofacial cells. The disadvantage of bifacial cells is the cost of the additional fabrication steps, which must be mitigated by gains in efficiency.

2.2.3 Sub-Band Gap Transmission Limitations

The conversion efficiency of any single junction solar cell has an upper limit that is determined by the band gap energy (E_g) of the constituent semiconductor material. A photon of energy less than E_g passes through the semiconductor (Figure 2-3). This process is known as transmission. A photon of energy greater than E_g can be absorbed by the semiconductor, creating an electron-hole pair. However the excited pair quickly loses the energy in excess of the band gap energy to heat within the semiconductor material (Figure 2-3). This process is known as lattice thermalisation [6].

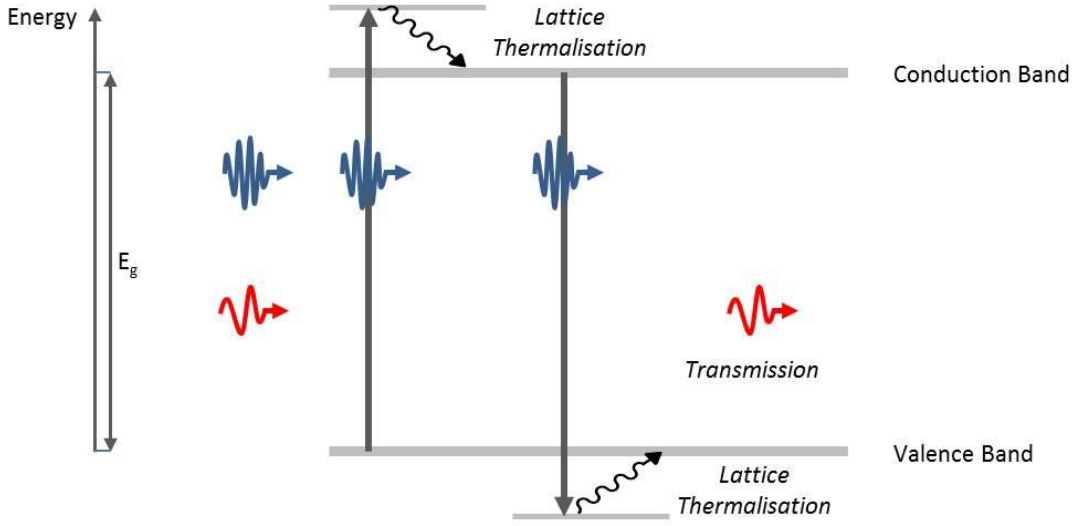

Figure 2-3: A photon of energy less than Eg is transmitted through the semiconductor. A photon of energy greater than Eg can lose energy to the lattice (Lattice Thermalisation).

The maximum efficiency that can be achieved by a single band gap material at one-Sun was found to be around 31%, with an optimal band gap of 1.3 eV, by Shockley and Queisser [2]. This assumes that the only unavoidable losses are due to the emission of photons by radiative recombination of electron-hole pairs [6]. One-sun corresponds to the standard illumination of a solar cell at AM 1.5 (terrestrial air mass coefficient), equivalent to 1 kW/m^2. The band gap of silicon (Eg = 1.12 eV) is very close to the optimal band gap, therefore the theoretical maximum efficiency of silicon is around 30% [6]. Novel ways to improve the efficiency of silicon solar cells beyond their single band gap limit are therefore essential to continue the development of this well established technology.

2.3 Techniques for Enhancing Solar Cell Efficiency

The current photovoltaic technologies that dominate the commercial market have allowed for solar panel technology to become a significant contributor to energy generation worldwide. These technologies include amorphous silicon; mono- and poly-crystalline silicon; CIGS (Copper Indium Gallium Selenide); and Cadmium Telluride. Much of the recent research in solar cell efficiency has been focused on "third generation photovoltaics" including tandem solar cells, intermediate band solar cells and spectral conversion.

This section will introduce reported methods for enhancing solar cell efficiency and their limitations. The concept of spectral conversion for enhanced solar energy efficiency will then be presented.

2.3.1 Reported Methods for Enhancing Solar Cell Efficiency and their Limitations

Solar cell technology is commonly divided into three generations. First generation solar cells consist of p-n junctions in crystalline silicon. A drive towards thinner, cheaper photovoltaic panels resulted in the second generation, or "thin film" solar cells. These include CdTe, CIGS and amorphous silicon. Third generation solar cells encompass a range of emerging technologies, that look at ways to increase the conversion efficiency of sunlight to electricity beyond the single junction band gap limit (Shockley-Queisser limit). Up-conversion falls within the class of third generation solar cells, therefore the focus of the review of the current methods for enhancing solar cell efficiency will be on third generation technologies.

A vast amount of research has been carried out to maximise the efficiency of crystalline silicon solar cells towards their theoretical single junction limit. Significant increases in efficiency have resulted through the addition of surface texturing [7], antireflection coatings [8], reducing recombination at the electrical contacts [9] and buried electrical contacts [10]. However these systems are all still limited by the theoretical single junction limit of around 30% at one sun concentration.

Concentrating photovoltaics offer an alternative way to increase the efficiency of a cell, while recuing the cost of the photovoltaic material required. This allows for more complex and costly photovoltaic materials to be used with cheap optical elements, resulting in a cost effective overall system. Highly concentrating photovoltaics often utilize both primary and secondary concentrating elements, where the primary element is

typically a Fresnel lens or compound parabolic reflector [11]. The improved efficiency of cells under concentrated sunlight is due to an increased open circuit voltage (which increases logarithmically with luminous power) and a high operational voltage (which reduces non-radiative recombination) [11]. The highest gains in efficiency through concentrated photovoltaics have been achieved using multijunction solar cells consisting of InGaP/GaAs; GaInAsP/GaInAs, achieving 44±2.6% efficiency [1]. The significant disadvantages of concentrated photovoltaics are the complex cell design (see below) and the requirement for the module to track the sun throughout the day.

Another way in which the efficiency of a solar cell can be improved is to use a stack of heterojunctions made from semiconducting materials of decreasing band gap energy. These structures are known as tandem or multi-junction solar cells. Maximum efficiencies of 42% for a two layer stack (1.9 and 1.0 eV) and 49% for a three layer stack (2.3, 1.4 and 0.8 eV) under one-sun have been calculated by Ameri *et al* [12]. For an infinite number of solar cells, the theoretical maximum efficiency under one-Sun was found to be 68% [12]. Experimental efficiencies of tandem solar cells have reached as high as 34.1 % (GaInP/GaInP/Ge), under one-sun [13].

A major disadvantage of tandem solar cells is the high cost of the complex fabrication process. The different layers can either be connected in-series, with two terminals for the cell stack, or each layer in the stack can be treated as an individual cell with the I-V curves optimised separately externally. For ease of fabrication, the in-series structure has become the design of choice. However this design is more sensitive to spectral variations, even more so for an increased number of band gaps in the structure. Furthermore, it requires the same current to flow through each layer and is therefore limited by the worst electrically performing layer [14].

Intermediate band solar cells and impurity PV solar cells offer an alternative way to broaden the spectral range of absorption by introducing one or more energy levels within the bandgap to absorb photons of lower energy in parallel with the normal operation of a single bandgap cell. These devices have the same theoretical limiting efficiency as a three level tandem cell: 63% at maximum concentration and 48% at one sun concentration [14]. For a practical device, spectral selectivity and photon selection limits the overall efficiency that can be obtained, however the current from the low energy levels can be independent from the main energy level gap. These intermediate states are introduced by

doping the main semiconductor with defects. However the complex fabrication requirements have meant that no advantage in efficiency has yet been obtained [14].

A further method for increasing solar cell efficiency are hot carrier cells. The concept is to use a material with a small band gap energy to absorb a very wide range of photon energies. The photogenerated charge carriers must then be collected while they are at elevated energies ('hot') before they can recombine [14]. This requires contacts that only accept carriers over a very narrow range of energies. The issue of slowing carrier cooling is a very difficult one to solve practically, with only a very small amount of experimental evidence for slowed cooling [15]. Therefore hot carrier solar cells remain a very difficult concept to demonstrate.

The complex fabrication requirements associated with all of the above mentioned current methods mean that significant improvements to solar cell efficiency using these techniques may still be some way off. Therefore alternative third generation photovoltaic devices are required to continue their development. One such method that offers a much simplified fabrication procedure is through the application of an optically coupled, electrically isolated spectral conversion layer.

2.3.2 Spectral Conversion for Enhancing Solar Cell Efficiency

Spectral conversion offers the potential to improve the efficiency of a single junction photovoltaic device beyond its fundamental band gap limit by modifying the intensity distribution of the solar spectrum. This can be done by applying luminescence down-conversion and up-conversion layers to the front and rear of a silicon solar cell respectively.

Down-conversion is the process by which multiple electron-hole pairs are formed from one incident photon of energy larger than twice the band gap of the semiconducting material (Figure 2-4). The luminescence converter is ideally located on the front surface of a conventional silicon single junction solar cell, with a reflector on the rear surface. The maximum efficiency for this system was calculated to be 38.6% by Trupke *et al* [16]. The disadvantage of down conversion is that as it sits in the front surface of the solar cell, it is very difficult to minimise detrimental scattering, absorption and reflection of the spectrum of the sun that is normally absorbed by the photovoltaic material below.

Up-conversion is the process by which two or more photons of energy less than the band gap of the semiconducting material are converted to one photon of energy greater than

the band gap (Figure 2-3). This is achieved by sequential excitation of electrons into an excited state via a real metastable state [17]. The luminescence converter can be located on the rear surface of a conventional silicon solar cell. The maximum efficiency for this system, for non-concentrated sunlight, was calculated to be 47.6% by Trupke *et al* [17]. The disadvantage of up-conversion is that it is a non-linear process and requires a bifacial cell if placed at the rear.

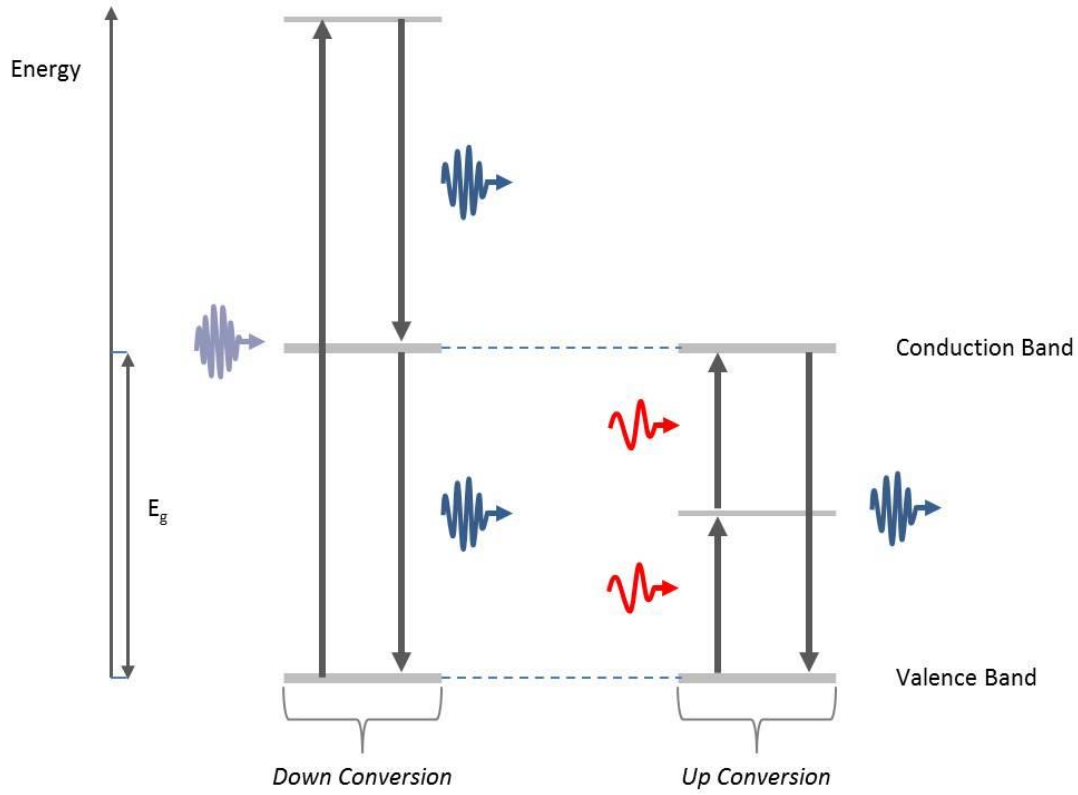

Figure 2-4: Spectral Conversion Processes: In down-conversion, one high energy photon is converted into two or more lower energy photons. In up-conversion, two or more low energy photons are converted into one higher energy photon.

There are two distinct advantages of down-conversion and up-conversion layers over tandem solar cells for enhanced efficiency. Firstly, both down-conversion and up-conversion layers are passive optical components, therefore carrier collection still occurs at the single junction. In comparison, the photocurrents generated within each layer of the tandem solar cell must match, continuously, to avoid significant mismatch losses. Secondly, the application of down-conversion and up-conversion layers to photovoltaics does not require modification of the existing solar cell [6].

Limiting mechanisms within up-conversion include multi-phonon transitions to lower energy levels, radiative emission to lower energy levels, and energy transfer between ions

[6]. Furthermore, only photons emitted within the escape cone of the up-conversion layer-solar cell interface will enter the solar cell. The development of down-conversion material for photvoltaics is still at a very early stage, therefore the limiting mechanisms are still unknown. Significant losses in a down-conversion layer mounted on the front surface of a solar cell will result from the reflection of light at the top surface of the down-conversion layer, in addition to luminescence emission escaping out of the front surface [6].

Previous research into up-conversion for alternative applications [18-21] has meant there is a larger amount of literature and experimental development of this technique, compared with down-conversion. Furthermore the ability to place the up-conversion layer at the rear of the cell, thereby not interfering with the normal front collection by the semiconductor material, makes this technique one of particular interest.

2.4 Up-Conversion for Silicon Photovoltaics

The use of up-conversion for enhancing silicon solar cell efficiency offers an elegant solution with great potential [17]. This area of study is still at the very early stages and so recent materials can only provide a fraction of the enhancement that could be achieved. Therefore it is necessary to explore a range of techniques to improve the up-conversion efficiency of these layers.

This section will introduce the theory of up-conversion materials and detail common up-conversion materials. The limitation of low conversion efficiency will be analysed and the use of photonic crystals for enhancing up-conversion efficiency will be introduced.

2.4.1 Theory of Up-Conversion and Common Up-Conversion Materials

The upper limit of the conversion efficiency that can be achieved for a two-step (three level) up-conversion process was theoretically investigated by Trupke *et al* in 2002, using detailed-balance calculations [17]. The authors considered an ideal up-conversion layer on the rear side of a single-junction bifacial solar cell, with a reflector on the rear side of the up-conversion layer. The upper limit on the energy conversion efficiency of the system was found to be 47.6% at one-sun.

Rare earth ions, in particular lanthanide ions, are ideal candidates for up-conversion. They have luminescent properties that cover the ultraviolet, visible and near infrared wavelengths. Furthermore, these properties do not significantly deviate when doped into different materials, due to outer electron shielding [22]. Therefore it is the host material

that determines the non-radiative rate of the luminescent ion. Up-conversion has been observed in many rare earth ions including trivalent praseodymium (Pr^{3+}) and trivalent erbium (Er^{3+}) [23].

Erbium is an ideal candidate for up-conversion for silicon based photovoltaics. The specific advantages have been outlined by Shalav *et al* [22]. The authors highlight that the energy level separations between subsequent levels required for up-conversion are nearly equal (1480-1580 nm) as shown in Figure 2-5. Furthermore, the spectral power from the normalised AM 1.5 spectrum yields 25 W/m^2 in this wavelength range. The emission of erbium at 980 nm is of particular use for silicon photovoltaics as it lies just above the band gap of silicon. Therefore erbium is an ideal candidate as the absorber (1480-1580 nm) and emitter (980 nm) for up-conversion with silicon photovoltaics. The additional wavelengths emitted by the Sun, out with the range of 1480-1580 nm, but above 1100 nm are suitable for up-conversion as well (Figure 1-2), however require these different absorber and emitter species and are beyond the scope of this work.

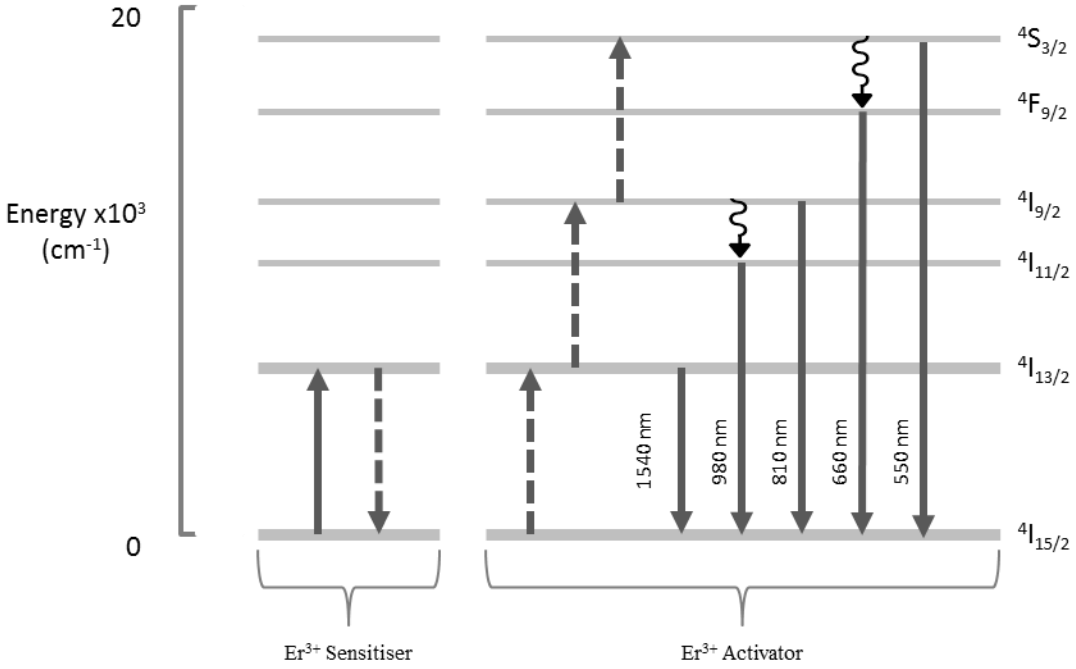

Figure 2-5: Three step energy transfer process between two erbium ions. Energy relaxation in the sensitizer ion can result in energy transfer to a neighbouring activator ion. The three step process results in photons (980 nm) of energy greater than the band gap of silicon. Solid arrows represent absorption and emission (up and down respectively). Dotted arrows represent energy transfer and wavy arrows represent phonon emission.

Erbium has a preferred bonding state that is trivalent (Er^{3+}), with an electronic structure [Xe]4f115s25p6. The partially filled 4f electronic shell is shielded by both the full 5s and 5p shells, resulting in very distinct intra-4f transitions. An additional effect of the shielding is that erbium absorption and emission are relatively invariant to the type of host material used, which eases the engineering of the host materials [24].

Many mechanisms have been identified for up-conversion using trivalent rare earth metals. These include ground state absorption/excited state absorption (GSA/ESA), energy transfer up-conversion (ETU), cooperative processes and avalanche up-conversion [22]. Other energy conversion mechanisms that will limit the up-conversion process are: multi-phonon transitions to lower energy levels; radiative emission to lower undesirable energy levels; and energy transfer between ions [22].

The emission intensity of erbium is dependent upon the host material. Lattice phonons can contribute significantly to the up-conversion mechanism. Investigations into the effect of the host material have been carried out by Ohwaki and Wang in 1994 [25]. They showed that the up-conversion efficiency increased for the host materials YF_3, YI_3, YBr_3 and $BaCl_2$ respectively, which is in agreement with the electronic and phononic properties expected. Furthermore, the direct compounds $ErCl_3$, $ErBr_3$, ErI_3 and ErF_3 were all found to have lower efficiencies than the doped host materials, due to concentration quenching at higher concentrations [25].

The host material for the rare earth ions should have low phonon energies to reduce loss by non-radiative decay. A major problem of rare earth based up converters, like Erbium doped $NaYF_3$, is the weak narrow absorption range of the of the rare earth ion [26]. Goldschmidt *et al*. report that the absorption range of erbium in a $NaYF_3$ matrix is around 100 nm wide [26]. The authors proposed to overcome this problem by combining the up-converter with a fluorescent material. The fluorescent material should have a broad absorption of wavelengths below the band gap of the solar cell, and emit in the absorption range of erbium. The work presented in this thesis is for a proof of principal concept, therefore the host materials were chosen for properties other than their absolute up-conversion efficiency, including their refractive index. Therefore alternative host materials could further increase any increase in up-conversion efficiency presented here.

Other rare earth ions exhibit emission at wavelengths that are suitable for silicon solar cells, however they have low absorption. The low absorption can be overcome by using sensitizer ions. The sensitizer ion exhibits good absorption and transfers the energy to an

activator ion, which emits at the desired wavelength [23]. Ytterbium-erbium doped $NaYF_4$ has been shown to be one of the most efficient up converters to date [23]. This is helped by the low phonon energies and relatively broad absorption and excitation spectrum of the $NaYF_4$ crystal [22]. However the maximum external quantum efficiency was measured to be only 3.4% at 6 mW 1523 nm excitation. For ease of fabrication and interpretation of the results, the work for this thesis will focus on doping using a single type of rare earth ion.

Up-conversion has been observed in various organic materials. However the efficiencies tend to be low and require high pump powers. A recent study by Monguzzi *et al.* demonstrated that up-conversion can be observed under lower pump intensities in organic materials [27]. The authors develop a multi-component polymeric film containing an organic sensitizer (PdPh4TPB) and activator (BPEA), both of which are commercially available. The polymer up-conversion layer was prepared on a glass substrate. Significant absorption was observed at 1.2 mW/cm^2 for 633 nm light, with emission occurring at 515 nm [27]. Although high up-conversion efficiencies have been achieved for organic converting layers, the strong absorption of the organic material in the near IR range severely limits their use with silicon PV.

Up-converting material can be doped into the bulk photovoltaic semiconductor, referred to as the impurity photovoltaic effect [28]. The dopant introduces intermediate energy levels within the semiconductor band gap, from which up-conversion can occur. This process requires specialized fabrication equipment that was not available for the study in this thesis.

For the purpose of this proof of concept work carried out for this thesis, the single rare earth ion source of Er^{3+} will be doped in a host of YF_3. The erbium ion has shown to exhibit strong up-conversion absorption and emission at the wavelengths required for a silicon solar cell. Furthermore, the fluoride host can be prepared and doped using fairly straightforward wet chemistry techniques and will provide a low phonon energy host that will help to observe the up-conversion signal. The doped fluoride will also be suitable for deposition in thin films by evaporation.

2.4.2 Application of Up-conversion Layers to Photovoltaic Cells

The first photovoltaic efficiency enhancement by up-conversion was reported by Gibart *et al*. in 1996 [29]. A 100 μm vitroceramic layer, doped with Er^{3+} and Yb^{3+} was applied to the rear of a substrate free gallium arsenide solar cell. The efficiency of the cell was found to be 2.5% under 25.6 W/cm^2 illumination at 1.39 eV (below the band gap of GaAs) [29, 30]. The authors did not provide an external quantum efficiency value for direct comparison.

The first enhancement by up-conversion for silicon photovoltaics was reported in 2007 by Shalav *et al* [22]. They applied a layer of $NaY_{0.8}F_4:Er_{0.2}^{3+}$ to the back surface of a bifacial crystalline silicon solar cell, with double sided buried contacts and a rear reflector below the up-conversion layer. A quartz-tungsten-halogen lamp was used to measure the external quantum efficiency response of the cell. A maximum external quantum efficiency of 5.5×10^{-6} absolute was measured for the device under the lamp at 1523 nm excitation. The external quantum efficiency is the number of electron hole pairs collected by the solar cell to the number of photons incident on the front surface of the cell.

The initial work carried out by Shalav *et al* was further developed by Richards and Shalav to improve upon their initial results [30]. The external quantum efficiency of the up-conversion-photovoltaic device measured at 6 mW for 1523 nm excitation was found to be 3.4%. This was achieved using the same material composition as before: $NaY_{0.8}F_4:Er_{0.2}^{3+}$. However the external quantum efficiency measured could only be achieved using 1000× concentration of the sun's spectrum [30].

Since the work by Richards and Shalav the optical properties of additional materials have been investigated for their up-conversion potential [23], however they were not measured in conjunction with a photovoltaic layer. It was not until 2014 when Fischer *et al* measured an improved up-conversion-photovoltaic external quantum efficiency by measuring the photovoltaic charactersitics of a bifacial silicon solar cell with a rear mounted up-conversion layer of microcrystalline β-$NaYF_4$:25% Er^{3+} in PFCB (perfluorocyclobutane) [31]. They measured an increase in current density of 4.03 mA/cm^2 for concentrated solar radiation of 77 suns.

To achieve this improved performance, Fischer *et al* tuned not only the up-conversion layer, but also the properties of the bifacial cell relating to the transmission of sub-band gap photons. Their investigation of front and rear surface texturing on the transmission

properties of a bifacial cell revealed that a planar front and rear sided cell offered the highest transmittance (and rear external quantum efficiency), resulting in it being the best suited for the application of rear mounted up-conversion layers [32]. These results perform a key bench mark for the testing of all future up-conversion materials on their performance on a silicon photovoltaic cell.

2.4.3 Current Methods for Enhancing Up-conversion Efficiency

Current up-conversion materials for use with silicon solar cells have low conversion efficiencies, due to non-radiative decay paths and narrow absorption bands. Developments to the host material to minimise the associated phonon energy will continue to help improve the efficiency of conversion. However further improvements can be made by controlling and enhancing the electric field density, which can have significant effects on the conversion due to the non-linear nature of the process. Such alterations to the electric field density can be achieved using nanostructured hosts. The problem of a narrow absorption range is fundamental to the rare earths and host material used. However additional spectral conversion within the up-conversion layer using quantum dots can further increase the efficiency of the up-converting layer.

Nanostructured host materials offer a range of properties that can enhance up-conversion. These properties have been summarised by Struempel *et al*. and include: a change in the electron-phonon interaction (changes the lifetime); a discrete phonon density of states and low frequency phonon cut off (may reduce energy transfer); enlarged surface, therefore more surface active ions and additional surface states due to impurities [23]. Nanostructured 2D photonic crystals provide the focus of this work due to their tenability and potential to greatly alter the electric field density.

By combining an yttrium and erbium doped phosphor with PbS quantum dots, Pan *et al*. demonstrated that an increase in photocurrent of 60% could be achieved when illuminated with LED's emitting at 1450 and 1550 nm [33]. The quantum dots and phosphors were dissolved together in an oxide, or separately in silicone before being applied to the rear of a bifacial silicon solar cell. The PbS quantum dots absorb in the range where both the bifacial solar cell and up-conversion phosphor do not (1200-1500 nm) and emit in the range where the up-conversion material is active [33]. Although not the focus of this work, quantum dots could provide a complimentary addition to a photonic crystal enhanced up-converter. A key limitation of quantum dots that limits their efficiency is fluorescence intermittence; more commonly referred to as "blinking" [34]. This process

constitutes the random switching on and off of the luminescent properties under continuous excitation, significantly limiting the efficiency [34]. Stability and performance degradation of quantum dots also presents a significant issue that needs to be overcome for long term use [35].

2.5 Optical Properties of Photonic Crystals

Photonic crystal structures provide an efficient way of controlling light within a dielectric material. In particular, highly directional emission perpendicular to the plane of a 2D photonic crystal slab can be achieved. This could significantly enhance the proportion of luminescent emission that is within the escape cone of an up-conversion layer. Furthermore, control of the local electromagnetic field distribution within the up-converter material can allow an enhancement of the non-linear conversion. Increasing the efficiency of the spectral conversion layer could allow a commercially significant improvements with the addition of an up-conversion layer to a photovoltaic cell.

This section will introduce the theory of photonic crystals and detail the application of 2D photonic crystals for enhanced luminescent emission. The use of photonic crystals for enhancing photovoltaic efficiency and up-conversion efficiency will then be presented.

2.5.1 Theory of Photonic Crystals

A photonic crystal is a structure with a periodic variation in dielectric constant. If the materials exhibit minimal absorption of light, then the refraction and reflection of light from all of the sequential interfaces can lead to defined modes of propagation [36]. Photonic crystals can be designed to exhibit photonic band gaps, where light of certain frequencies is prevented from propagating in certain directions. The size and shape of the band gap, which strongly influences the properties of the photonic crystals is determined by the periodicity and effective dielectric contrast.

Photonic crystal structures can be grouped within three categories: 1D, 2D and 3D. Simple examples of each type are shown in Figure 2-6.

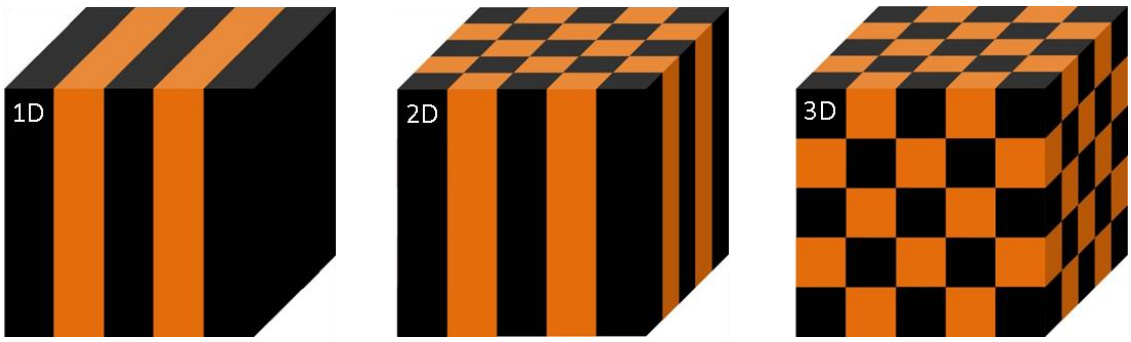

Figure 2-6: The different colours represent different dielectric constants. The dimension of the photonic crystals is determined by the number of axes in which periodicity of the dielectric constant is apparent. A 1D photonic crystal is also known as a dielectric stack.

There are distinct advantages of working with 2D photonic crystals. Although they are periodic along two axes, the interface between the photonic crystal structure (the top and bottom surfaces of the photonic crystal slab) and the external medium (most often air) along the third axis results in effective 3D control. This is a significant advantage because the structure of a 2D photonic crystal is a lot easier to fabricate than that of a 3D photonic crystal, however electromagnetic control in 3D is retained.

The most widely used and important tool for describing the properties of a photonic crystal is its band structure. The band structure represents a diagram of allowed states ("modes") of the photonic crystal. It uses the same terminology that was originally developed for describing electronic bands in solid state physics. The band structure describes the properties of the photonic crystal in k-space ("Fourier Space"), which simplifies the classification of the structure's properties. Performing a spatial Fourier transform of the electromagnetic field distribution results in a series of separated orthogonal modes that can be plotted as frequency (ω) as a function of wavevector (k). This ω-k diagram is known as a dispersion diagram, or band structure in the case of periodic structures.

In the simplest case, the equation for an electromagnetic wave propagating in a uniform medium is given by

$$\nabla^2 E(r,t) = \frac{k^2}{\omega^2}\frac{\partial^2 E(r,t)}{\partial t^2} \qquad 2.3$$

where the speed of light, $c = \omega/k$.

When periodicity in the refractive index is added in one direction, this is known as a "Bragg mirror" or 1D Photonic Crystal. The concept of a reciprocal lattice (from solid state physics) provides a very useful way of describing this structure. Here the relationship between a unit vector in real space (***a***) and reciprocal space (***b***) is given as

$$\mathbf{a}.\mathbf{b} = 2\pi \qquad 2.4$$

The lattice vector ***G*** can then be described in terms of a linear combination of the reciprocal space unit vectors ***b*** **(**Figure 2-7**)** [37]. From this information, the band structure can be deduced [36].

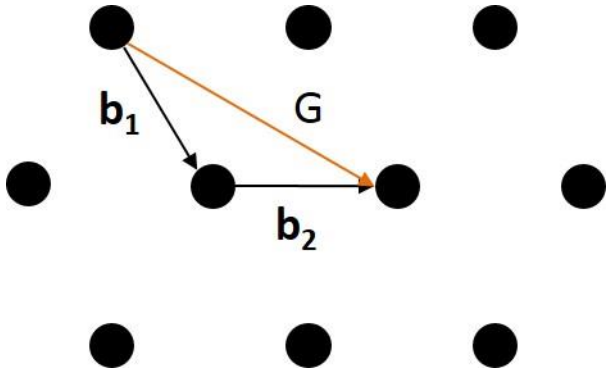

Figure 2-7: The lattice vector *G* can be described in terms of a linear combination of the space unit vectors b_x.

The same concept is used for a 2D photonic crystal. For the purpose of explanation, we can examine the common case of a triangular lattice of holes in a planar dielectric slab. In this case, the lattice constant of the triangular array ***a*** is defined as two vectors:

$$\mathbf{a_1} = \begin{pmatrix} \boldsymbol{a} \\ \mathbf{0} \end{pmatrix}, \qquad \mathbf{a_2} = \begin{pmatrix} \frac{\boldsymbol{a}}{\mathbf{2}} \\ \frac{\sqrt{\mathbf{3}}}{\mathbf{2}}\boldsymbol{a} \end{pmatrix} \qquad 2.5$$

Using the fact that the dot product of vectors with identical index is 2π and that vectors with non-equal index are orthogonal allows the following conditions to be made: from which the components of the vectors can be obtained.

$$\mathbf{a_1}.\mathbf{b_1} = \boldsymbol{2\pi}, \qquad \mathbf{a_1}.\mathbf{b_2} = \mathbf{0}$$

$$\mathbf{a_2}.\mathbf{b_1} = \mathbf{0}, \qquad \mathbf{a_2}.\mathbf{b_2} = \boldsymbol{2\pi} \qquad 2.6$$

The graphical relationship between ***a*** and ***b*** is represented in Figure 2-8. One possible unit cell for this structure in real space is called the Wigner-Seitz unit cell and it is constructed by connecting perpendicular mid-point intersections of the linear connections between the nearest lattice points. The space enclosed represents the smallest repeatable area from which the lattice can be drawn.

The Brillouin zone in reciprocal space is constructed in the same way as the Wigner-Seitz unit cell, expect that it is from the lattice composed of the reciprocal vectors. The Brillouin zone has three highly symmetric points: *K* and *M* on the edges and Γ in the center.

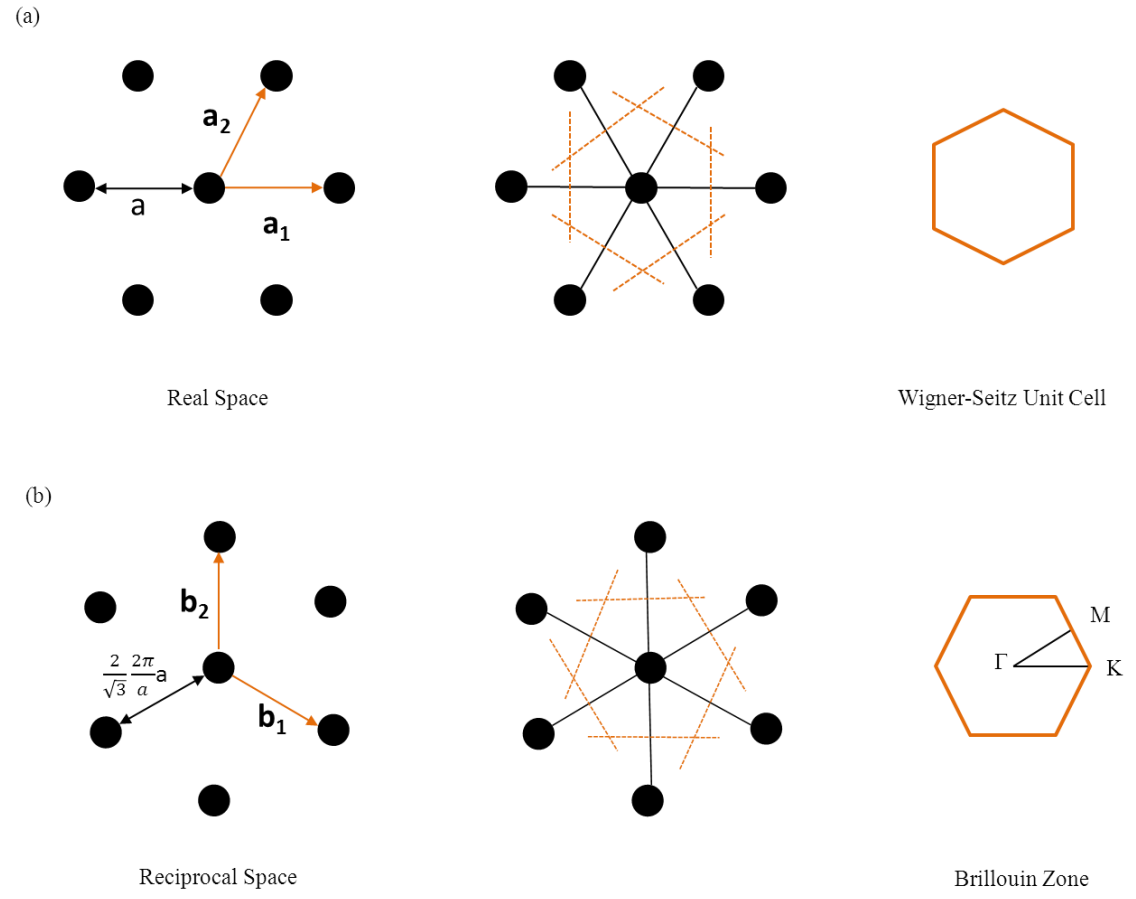

Figure 2-8: (a) Triangular lattice of cylindrical holes in a dielectric slab. The Wigner-Seitz unit cell and its construction is shown in orange. (b) The same lattice, but in reciprocal space. The Brillouin zone and its construction is shown in orange.

In this 2D case, the lattice vector ***G*** has different lengths in different lattice directions. In the *M* direction its length is given by $\frac{1}{\sqrt{3}}\frac{2\pi}{a}$ and in the *K* direction by $\frac{2}{3}\frac{2\pi}{a}$. The periodic nature of the photonic crystal means that the band structure can be greatly simplified, representing the different symmetry directions Γ-*K* and Γ-*M* on the different axes. By including the direction *K*-*M* into diagram completes the description of the photonic

crystal. The band structure in the range of $0 \ldots k \ldots + \frac{\pi}{a}$ is known as the irreducible Brillouin zone, analogous to solid state physics [36]. An example of a band structure for a 2D photonic crystal is shown in Figure 2-9.

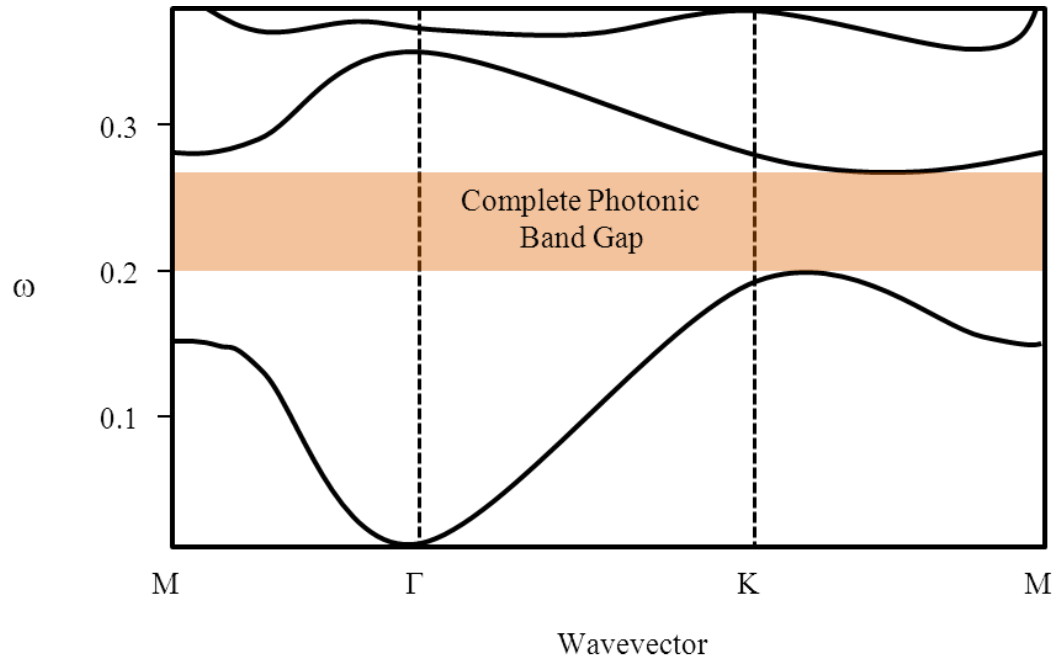

Figure 2-9: A complete photonic band exists in a band structure when no modes of propagation (Bloch modes) occur for any wavevector over a particular frequency range.

The band structure provides a wealth of information for understanding the properties of the photonic crystal. The band structure describes all possible modes of propagation within the system. The vertical axis represents the normalized temporal frequency, in multiples of c/a, where c is the speed of light and a is the lattice constant as before. The units of the normalised spatial frequency are a/λ, which are dimensionless. This means that the information deduced from the band structure can be scaled accordingly to the desired wavelength or lattice constant: the information is scale invariant.

If there is a range of frequencies over which no propagation modes are present for any wavevector, there exists a complete photonic band gap. This is the case for the band structure in Figure 2-9, where the complete photonic band gap is marked and labelled accordingly. The polarization of electromagnetic waves means that there exists separate band structures for both the transverse electric (TE) and transverse magnetic TM polarizations. The field distribution for the respective polarisations means that 2D photonic crystals composed of air holes in a dielectric typically have large band gaps for

TE polarized modes, while photonic crystals of unconnected dielectric pillars typically have large band gaps for TM polarized modes [36].

The distribution of light, given by a solution of the wave equation for a periodic modulation in refractive index, is known as a Bloch mode. Therefore the Bloch modes represent the modal distributions of light that are allowed to propagate through a photonic crystal. The Bloch modes are also mutually orthogonal. The orthogonality means that they occupy a different space. The first two bands of increasing normalised frequency are often referred to as the dielectric band and air band respectively, due to the space in which the mode predominantly resides. The localization of the bands becomes a key feature of the design of a photonic crystal to ensure that there is a high overlap of the electromagnetic field and the optical gain medium (see Chapter 3).

2.5.2 2D Photonic Crystals for Enhanced Luminescent Emission

In recent years, extensive study has been carried out in the development of 2D photonic crystals to achieve emission perpendicular to the plane of the PC. The most common way in which this has been achieved is by using a microcavity, formed from a localized photonic band gap defect state. By optimising the geometry of the cavity, high Q-factor microlasers with low thresholds have been demonstrated [38-40]. However, the emission associated with these devices does not exhibit high directionality and the emission surface is small.

A second way of obtaining emission perpendicular to the crystal plane is to make use of a flat dispersion curve at the edge of a photonic band gap [41-43]. The density of photonic modes is very high at a flat band edge, therefore the group velocity tends towards zero. As a result, a near stationary mode is formed that is suitable for the enhancement of spontaneous or stimulated emission. The spectral range and directionality of the emission from the photonic crystal is dependent upon the curvature of the photonic band [44]. By designing a 2D photonic crystal to operate at the Γ point, emission perpendicular to the plane of the photonic crystal can be achieved, with the benefit that the whole area of the device is emitting.

An early demonstration of band edge lasing in a photonic crystal was carried out by Meier *et al* in 1999 [43]. The authors etched a triangular lattice of air holes into SiO_2 by reactive ion etching. The lattice constant and radius of the holes were 400 and 100 nm respectively [43]. An organic film 150 nm thick, doped with commercially available laser dyes

(coumarin 490 and DCM), was deposited on the surface of the etched silica. Two emission peaks were observed at 580 nm (TM polarization) and 596 nm (TE polarization) by pumping the structure at 337 nm at a power of 50 kW/cm^2. The organic layer provided the lasing gain medium, while the 2D photonic crystal provided the distributed feedback required for lasing. The high threshold pump power was attributed by the authors to the lack of a complete band gap, allowing for coupling to leaky modes [43].

Following the first report of band edge lasing in a photonic crystal, research in the area increased steadily. Effects of the geometry on the band structure and laser emission were reported. Noda *et al* demonstrated selection of the laser polarization mode by modifying the hole shape in a square lattice geometry [45]. A 2D photonic crystal structure of elliptical holes (400 nm lattice constant) was formed on an n-InP substrate. A layer of InGaAs/InP multiple quantum wells was stacked on top of the substrate, providing the gain medium. Lasing of a single wavelength and linear polarization was achieved, in accordance with their theoretical results [45]. The previous work by Meier *et al* and Noda *et al* demonstrates that 2D photonic crystals can be to achieve such high optical feedback and that lasing is observed. Although the power from sunlight would never reach the pump power required for lasing, this study aims to make use of the key properties underpinning the enhanced optical emission.

Additional studies have looked into characterising the band edge modes. A square lattice of holes etched into InGaAs quantum wells was prepared by Kwon *et al* to investigate the band edge modes of an in plane band edge laser, exhibiting 1.55 μm emission [46]. Through a combination of theoretical and experimental analysis, the authors characterised the lasing modes, and demonstrated low threshold pump powers of around 0.62 mW and 0.67 mW for different band edge modes emitting in the plane of the photonic crystal [46].

A further reduction in threshold power was achieved in 2005 by Bakir *et al*, who developed a 2D photonic crystal layer on top of a distributed Bragg reflector (DBR) [41]. A graphite photonic crystal structure of holes was etched into a 250 nm thick InP-based membrane. The membrane included four 50 Å thick $InAs_{0.65}P_{0.35}$ quantum wells, separated by 200 Å InP barriers. The DBR, composed of three quarter wavelength pairs of Si/SiO_2, was attached to the 2D photonic crystal using an SiO_2 bonding layer. The device was pumped at 780 nm and lasing emission was observed at 1552 and 1554 nm (for variations in the bonding layer thickness) [41]. The high quality factor achieved for emission at 1552 nm resulted in an extremely low threshold power of 15 μW.

Previous reports have demonstrated the great potential of 2D photonic crystals to enhance luminescent emission, to the point where lasing can be observed. The intensity from the sun's light non-concentration is not expected to achieve lasing in a photonic crystal up-conversion material. However this study aims to make use of the principles leading to the enhanced emission to improve the up-conversion efficiency.

2.5.3 Photonic Crystals for Enhanced Photovoltaic Efficiency

There have been few reports of the use of photonic crystal structures to enhance spectral conversion in PV. However the application of photonic crystals to PV is not new. Previous research has predominantly focused on enhancing light trapping in thin film crystalline silicon solar cells. Crystalline silicon has an indirect band gap, resulting in weak absorption of light in the near infrared range [47]. Therefore solar cells made from crystalline silicon fail to absorb a significant portion of the solar spectrum that is absorbed by standard silicon cells. Traditional approaches of light trapping in a solar cell are based on geometric optics [48]. Texturing the front surface of the solar cell introduces scattering of incident rays away from the normal, therefore increasing the path length of the photon within the semiconductor [49, 50]. Furthermore, an increased path length can be achieved by placing an aluminium reflector at the back of the panel. In reality, the textured front surface will not reach the ideal case of Lambertian scattering, and the reflectance of the aluminium back reflector will not be greater than 80% for the wavelength range of light incident from the crystalline silicon bulk region [47]. Therefore alternative methods are required to further improve light trapping.

The application of wave optics to light trapping can increase efficiencies beyond those obtained by geometric optics. Such optical systems include gratings, DBRs (anti-reflection coatings) and photonic crystals. A theoretical analysis of the efficiency gain obtained by applying a DBR, a 2D photonic crystal and 3D photonic crystal to 2 μm thick crystalline silicon solar cells was performed by Bermel *et al* in 2007 [47]. They found through simulations that the overall efficiency of the cell could be increased to 24.0% by applying a DBR plus a 1D grating, made of crystalline silicon and silicon dioxide, to the rear of the cell; 26.3% by adding a 2D photonic crystal made of air holes in silicon; and 26.5% by adding a 3D inverse opal photonic crystal made of air holes arranged in an fcc lattice in crystalline silicon [47].

Experimental verification of the theoretical enhancement has been carried out by Zeng *et al*. They reported a 19% increase in short circuit current in a 5 μm thick monocrystalline

silicon solar cell with Si/SiO_2 DBR and 1D grating on a silicon substrate [50]. Furthermore, the use of inverse opal ZnO 3D PCs for selective transmission and reflection in a tandem solar cell has been demonstrated by Bielawny *et al* [51]. The authors reported a 52% drop in transmission for wavelengths around 600 nm and 95.7% average transmittance for wavelengths between 700-1100 nm for an amorphous silicon/microcrystalline silicon tandem cell [51]. As the DBR is applied to the front of the solar cell, the application of a 2D photonic crystal up-conversion layer to the rear of the cell would not affect integration with a front DBR layer to further improve any efficiency improvements observed. However thorough investigation of the effect of the front DBR on the wavelengths of absorption of the up-conversion layer would be required to avoid increased reflection of these wavelengths from the top surface.

2.5.4 Photonic Crystals for Enhanced Up-conversion Efficiency

The enhancement of up-conversion using photonic crystal structures has recently been reported by Markowicz *et al* [52]. The authors developed a 3D photonic crystal of polystyrene spheres, infiltrated with Coumarin 503 dye. They reported an enhancement of the up-conversion emission spectra at the edge of the photonic band gap. The threshold for laser emission was not met, however a significant increase in emission was observed. Although it was mentioned that the feedback was due to coupling between the incident field and the counter propagating wave created by Bragg reflection from the (111) crystal plane, the effect was not investigated further [52]. This work by Markowicz *et al* has demonstrated the principle of enhancing up-conversion using the band edge of a 3D photonic crystal, paving the way for the work carried out in this study to increase the up-conversiup-conversion efficiency using a 2D photonic crystal.

The use of photonic crystal structures as spectrally selective filters for up-conversion was proposed by Peters *et al* [53]. They describe a system where light is guided from a fluorescent concentrator (broadband absorption, emitting in the spectral range of the up converter) to the up converter material by geometric or photonic crystal constraints. A photonic crystal acting as a selective filter is positioned between the fluorescent converter and up converting material [53]. Therefore no radiation from the up converting layer is lost to the fluorescent converter. In addition, the authors suggest that a second spectrally selective PC filter could be placed between the up converter and the silicon solar cell, reflecting unconverted light from the up-conversion layer [53]. Selective filtering could prove to be an important addition as an intermediate layer between the photovoltaic and

up-conversion layer. However it has very little effect on the electric field density, which is key to making significant enhancements to the non-linear up-conversion process.

A system for enhancing up-conversion using flat band edge states in DBRs has been proposed by Johnson *et al* [54]. The authors propose the use of a DBR to enhance the electromagnetic field in the vicinity of Er^{3+} ions. This field enhancement can be achieved by populating the low group velocity modes that result from the 1D photonic crystal dispersion characteristics. The non-linear dependence of the emission intensity on the absorption intensity of the up-conversion process is expected to result in an efficiency enhancement [54]. This concept is similar to that under investigation in this study. The 1D structure described by Johnson *et al* has the disadvantage of acting over a limited range of acceptance angles, due to the 1D control of light [54]. The 2D photonic crystal under analysis in this study will act over a much wider range of angles [36].

A report in 2011 detailed the enhancement of up-conversion from erbium doped $YbPO_4$ with the inverse opal structure [55]. The authors of this report prepared an inverse opal structure by using a binary disorder template of polystyrene microspheres. They observed that the emission at 523 and 548 nm was strongly enhanced, corresponding to an overlap with the long wavelength photonic band edge. The enhancement was attributed to the standing wave effect [55].

It has been shown that 1D and 3D photonic crystal structures have been used to effectively enhance the efficiency of up-conversion. However there was found to be no evidence of work carried out on 2D photonic crystals to enhance the efficiency of up-conversion. This study will therefore provide the first experimental results to investigate the effect of 2D photonic crystals on up-conversion efficiency.

2.6 Transparent Conductive Contacts

Transparent conductive contacts have become a significant component of photovoltaic devices. Different solar cell technologies require the use of different transparent contacts, therefore thorough investigation of their parameters relevant to solar cell fabrication is vital to choosing the correct contact to use.

This section will introduce a summary of transparent conductive contacts for photovoltaics. The current uses of the highly conductive polymer PEDOT:PSS, which can be used as a transparent conductive contact, will then be presented. The use of a transparent conductive contact on the rear surface of a bifacial solar cell is required to

make the most of any increase performance provided by the up-conversion layer by avoiding the detrimental partial shielding of the active photovoltaic layer by traditional metal fingers and bus bar electrical contacts.

2.6.1 A Summary of Transparent Conductive Contacts for Photovoltaics

New and established photovoltaic technologies require different characteristics of the transparent conductive layer. These requirements include good conductivity and favourable deposition conditions among many others. The transparent contacts are typically composed of either very thin pure metals, wide band-gap oxide semiconductors, or highly doped conjugated organic polymers [56].

Thin metallic layers offer a simple and relatively cheap solution to a transparent conductive contact. However the transparency of these materials generally decreases exponentially with increasing thickness, in practice very thin films of 10-20 nm are required for adequate transparency in the visible. At these thin dimensions, metals easily aggregate into droplets during deposition, therefore it is very difficult to achieve uniform consistent films [57]. Recent work has examined ways of improving the film uniformity. O'Conner *et al* demonstrated that the co-evaporation of silver with magnesium allowed for the aggregation issues to be mitigated, resulting in a low sheet resistance of 15 Ω/□, which is comparable to the standard device grade Indium Tin Oxide (ITO) films [58].

Transparent conductive oxides (TCOs) have been leading the way in the performance of transparent conductive contacts. A detailed examination of the requirements for TCOs has been carried out by Fortunator *et al* [56]. They highlight the performance and versatility of indium tin oxide, which has become the mainstay of modern contacts. This material is commonly deposited by rf or dc sputter coating onto a substrate heated to 250-350°C, which offers low resistivity of 1×10^{-4} to 3×10^{-4} Ω/cm [56]. However the relatively harsh processing conditions, brittle composition and increasing cost of component materials required to achieve the desired electrical performance for many TCOs have resulted in renewed efforts to find alternative materials.

Organic polymers offer a highly flexible alternative to metal and inorganic transparent conductive contacts and can be processed at lower temperature conditions. Although the transparency of the polymers used previously has been comparable to that of ITO, the resistivity is commonly a lot higher. One of the most widely used highly conductive polymers is poly(3,4-ethylenedioxythiophene):poly(styrenesulfonate), more commonly

known as PEDOT:PSS. A recent study has reported significant reductions in the resistivity of this polymer by optimising the process conditions and through the addition of solvents [59]. Gasiorowski *et al* introduced dimethyl sulfoxide to the PEDOT:PSS polymer, which resulted in a decrease in resistivity from 1.821 Ω/cm for the pure PEDOT:PSS to 1.035×10^{-3} Ω/cm for the sample containing 10% dimethyl sulfoxide [59]. The continuing reduction in resistivity and low temperature, ambient processing temperature deposition conditions will ensure that highly conductive polymers will become increasingly used in novel photovoltaic devices. However it should be noted that issues with stability of highly conductive polymers such as PEDOT:PSS in air must be overcome for long term use [60].

Therefore, a complete analysis of the fundamental properties (optical, electrical, mechanical, etc.) of available transparent conductive contact materials is essential for choosing the correct material to optimise the solar cell. The work in this thesis presents an analysis of the fundamental properties of PEDOT:PSS for both the application of the conductive polymer for use with a 2D photonic crystal up-converting layer on the rear of a bifacial crystalline silicon solar cell, as well as acting as a reference for future work using this material.

2.6.2 Current Uses of PEDOT:PSS

The low temperature processing conditions, electrical conductivity and flexibility of the polymer make PEDOT:PSS a highly desirable conductive material for many applications.

PEDOT:PSS has become an important constituent of photovoltaic technology. Furthermore, by combining it with various additives, the desired properties of the polymer can be tuned. Recent work includes: the demonstration that a graphene/PEDOT:PSS composite used as the counter electrode in dye sensitized solar cell can result in cell efficiencies comparable with a platinum counter electrode [61]; the addition of a fluorosurfactant to achieve highly conductive, flexible and stretchable PEDOT:PSS films [62]; and developments in its use as a hole transport layer in organic photovoltaics [63].

A further advantage of PEDOT:PSS is that it has been shown to provide very good coverage to structured silicon surfaces. Chen *et al* investigated the coverage of PEDOT:PSS, deposited using spin coating, on a chemically etched structured silicon surface, with features on the scale of 1-3 μm. Optimising the speed of the spin coater allowed for excellent coverage to be obtained with an average layer thickness of 40 nm

[64]. These results highlight the potential for PEDOT:PSS to be used to provide excellent surface coverage on highly texturised surfaces such as 2D photonic crystal arrays of pillars.

The use of PEDOT:PSS as a conductive adhesive has previously been investigated. Tung *et al* demonstrated the application of bonding of poly(ethylene terephthalate) (PET) strips using a PEDOT:PSS film of unspecified thickness [65]. This film was found to have a shear strength of 0.2 MPa. The authors also demonstrated that the addition of graphene oxide to the PEDOT:PSS solution resulted in an order of magnitude increase in conductivity of the resulting thin film [65].

PEDOT:PSS has been shown to be a versatile and desirable material for a variety of applications. However there has been no simultaneous analysis of this material's optical, electrical and mechanical properties on the samples prepared under the same fabrication conditions has yet been carried out. This information is highly desirable in choosing whether to use PEDOT:PSS as the transparent contact for the solar cell device under consideration. The results of the experimental analysis of these key fundamental properties will be presented in Chapter 7 of this thesis. [60]

2.7 Overview and Goals of the Thesis

The objective of this thesis is to fabricate, understand and critically evaluate a 2D photonic crystal up-conversion layer for use with silicon photovoltaics. There has been increasing development of up-conversion materials, however their efficiency remains low. 2D photonic crystals have been demonstrated to provide fundamental control of the electromagnetic density within the photonic crystal layer. The work in this thesis represents the first to be carried out to investigate the use of 2D photonic crystals to enhance the efficiency of up-conversion.

The work presented here also provides the first complete analysis of the electronic, optical and mechanical properties of the highly conductive polymer PEDOT:PSS. These properties are essential for correct choice of a transparent conductive contact for use with a solar cell. Therefore it is intended that this work can act as a source of reference for future design considerations to best optimise the solar cell.

The work of this thesis in the proceeding chapters is arranged as follows: Chapter 3 presents the results of the 2D photonic crystal simulations that were developed to provide the geometrical properties for the novel devices constructed. Chapter 4 contains a detailed

review of the fabrication and characterisation techniques used in this study. In Chapter 5 the fabrication and analysis of Er doped TiO_2 thin films and 2D photonic crystals is presented. Chapter 6 details the work carried out on the fabrication of Er doped YF_3:Er thin films and the combining of these films with silicon 2D photonic crystals to form Si-YF_3:Er 2D photonic crystals. The effect of these structures on the optical properties of the up-conversion layer is extensively analysed. In Chapter 7 the complete analysis of the optical, electrical and structural properties of thin films of PEDOT:PSS is detailed and examined. A summary of the future work leading on from this study is presented in Chapter 8 and the concluding remarks for the thesis are detailed in Chapter 9.

2.8 References

1. M. A. Green, K. Emery, Y. Hishikawa, W. Warta, and E. D. Dunlop, "Solar cell efficiency tables (version 44)," Progress in Photovoltaics: Research and Applications **22**, 701-710 (2014).
2. W. Shockley, and H. J. Queisser, "Detailed balance limit of efficiency of p-n junction solar cells," Journal of Applied Physics **32**, 510 (1961).
3. B. S. Richards, *Novel Uses of Titanium Dioxide for Silicon Solar Cells* (Centre for Photovoltaic Engineering, The Unversity of New South Wales, Sydney, 2002).
4. H. Ohtsuka, M. Sakamoto, K. Tsutsui, and Y. Yazawa, "Bifacial silicon solar cells with 21·3% front efficiency and 19·8% rear efficiency," Progress in Photovoltaics: Research and Applications **8**, 385-390 (2000).
5. C. Duran, "Bifacial Solar Cells: High Efficiency Design, Characterization, Modules and Applications," (Universitat Konstanz, 2012), p. 130.
6. B. S. Richards, "Enhancing the performance of silicon solar cells via the application of passive luminescence conversion layers," Solar Energy Materials and Solar Cells **90**, 2329-2337 (2006).
7. J. H. Zhao, A. H. Wang, M. A. Green, and F. Ferrazza, "19.8% efficient "honeycomb" textured multicrystalline and 24.4% monocrystalline silicon solar cells," Applied Physics Letters **73**, 1991-1993 (1998).
8. S. Chattopadhyay, Y. F. Huang, Y. J. Jen, A. Ganguly, K. H. Chen, and L. C. Chen, "Anti-reflecting and photonic nanostructures," Materials Science & Engineering R-Reports **69**, 1-35 (2010).
9. L. C. Olsen, and F. W. Addis, "INVESTIGATION OF HIGH-EFFICIENCY SILICON MINP SOLAR-CELLS," Solar Cells **17**, 151-166 (1986).

10. B. S. Richards, "Comparison of TiO2 and other dielectric coatings for buried-contact solar cells: a review," Progress in Photovoltaics **12**, 253-281 (2004).
11. A. Luque, "Will we exceed 50% efficiency in photovoltaics?," Journal of Applied Physics **110** (2011).
12. T. Ameri, G. Dennler, C. Lungenschmied, and C. J. Brabec, "Organic tandem solar cells: A review," Energy & Environmental Science **2**, 347-363 (2009).
13. M. A. Green, K. Emery, Y. Hishikawa, W. Warta, and E. D. Dunlop, "Solar cell efficiency tables (version 39)," Progress in Photovoltaics **20**, 12-20 (2012).
14. G. Conibeer, "Third-generation photovoltaics," Materials Today **10**, 42-50 (2007).
15. F. Chen, A. N. Cartwright, H. Lu, and W. J. Schaff, "Time-resolved spectroscopy of recombination and relaxation dynamics in InN," Applied Physics Letters **83**, 4984-4986 (2003).
16. T. Trupke, M. A. Green, and P. Wurfel, "Improving solar cell efficiencies by down-conversion of high-energy photons," Journal of Applied Physics **92**, 1668-1674 (2002).
17. T. Trupke, M. A. Green, and P. Würfel, "Improving solar cell efficiencies by up-conversion of sub-band-gap light," Journal of Applied Physics **92**, 4117-4122 (2002).
18. P. Ceroni, "Energy Up-Conversion by Low-Power Excitation: New Applications of an Old Concept," Chemistry-a European Journal **17**, 9560-9564 (2011).
19. Z. Hou, C. Li, P. a. Ma, Z. Cheng, X. Li, X. Zhang, Y. Dai, D. Yang, H. Lian, and J. Lin, "Up-Conversion Luminescent and Porous NaYF4:Yb3+, Er3+@SiO2 Nanocomposite Fibers for Anti-Cancer Drug Delivery and Cell Imaging," Advanced Functional Materials **22**, 2713-2722 (2012).
20. F. Auzel, "Upconversion and anti-stokes processes with f and d ions in solids," Chemical Reviews **104**, 139-173 (2004).
21. F. Wang, D. Banerjee, Y. Liu, X. Chen, and X. Liu, "Upconversion nanoparticles in biological labeling, imaging, and therapy," Analyst **135**, 1839-1854 (2010).
22. A. Shalav, B. S. Richards, and M. A. Green, "Luminescent layers for enhanced silicon solar cell performance: Up-conversion," Solar Energy Materials and Solar Cells **91**, 829-842 (2007).
23. C. Strümpel, M. McCann, G. Beaucarne, V. Arkhipov, A. Slaoui, V. Švrček, C. del Cañizo, and I. Tobias, "Modifying the solar spectrum to enhance silicon solar cell efficiency—An overview of available materials," Solar Energy Materials and Solar Cells **91**, 238-249 (2007).

24. A. Bellemare, "Continuous-wave silica-based erbium-doped fibre lasers," Progress in Quantum Electronics **27**, 211-266 (2003).
25. O. Junichi, and W. Yuhu, "Efficient 1.5 μ m to Visible Upconversion in Er 3+ - Doped Halide Phosphors," Japanese Journal of Applied Physics **33**, L334 (1994).
26. J. C. Goldschmidt, P. Loper, S. Fischer, S. Janz, M. Peters, S. W. Glunz, G. Willeke, E. Lifshitz, K. Kramer, and D. Biner, "Advanced upconverter systems with spectral and geometric concentration for high upconversion efficiencies," in *Optoelectronic and Microelectronic Materials and Devices, 2008. COMMAD 2008*(2008), pp. 307-311.
27. A. Monguzzi, R. Tubino, and F. Meinardi, "Multicomponent Polymeric Film for Red to Green Low Power Sensitized Up-Conversion," The Journal of Physical Chemistry A **113**, 1171-1174 (2009).
28. M. J. Keevers, and M. A. Green, "Extended infrared response of silicon solar cells and the impurity photovoltaic effect," in *Photovoltaic Energy Conversion, 1994., Conference Record of the Twenty Fourth. IEEE Photovoltaic Specialists Conference - 1994, 1994 IEEE First World Conference on*(1994), pp. 1433-1436 vol.1432.
29. G. Pierre, A. François, G. Jean-Claude, and Z. Khaled, "Below Band-Gap IR Response of Substrate-Free GaAs Solar Cells Using Two-Photon Up-Conversion," Japanese Journal of Applied Physics **35**, 4401 (1996).
30. B. S. Richards, and A. Shalav, "Enhancing the Near-Infrared Spectral Response of Silicon Optoelectronic Devices via Up-Conversion," Electron Devices, IEEE Transactions on **54**, 2679-2684 (2007).
31. S. Fischer, B. Fröhlich, H. Steinkemper, K. W. Krämer, and J. C. Goldschmidt, "Absolute upconversion quantum yield of β-NaYF4 doped with Er3+ and external quantum efficiency of upconverter solar cell devices under broad-band excitation considering spectral mismatch corrections," Solar Energy Materials and Solar Cells **122**, 197-207 (2014).
32. S. Fischer, A. Ivaturi, B. Frohlich, M. Rudiger, A. Richter, K. W. Kramer, B. S. Richards, and J. C. Goldschmidt, "Upconverter Silicon Solar Cell Devices for Efficient Utilization of Sub-Band-Gap Photons Under Concentrated Solar Radiation," Photovoltaics, IEEE Journal of **4**, 183-189 (2014).
33. A. C. Pan, C. del Cañizo, E. Cánovas, N. M. Santos, J. P. Leitão, and A. Luque, "Enhancement of up-conversion efficiency by combining rare earth-doped

phosphors with PbS quantum dots," Solar Energy Materials and Solar Cells **94**, 1923-1926 (2010).

34. F. Zhang, *Photon Upconversion Nanomaterials* (Springer Berlin Heidelberg, 2015).
35. C.-H. M. Chuang, P. R. Brown, V. Bulović, and M. G. Bawendi, "Improved performance and stability in quantum dot solar cells through band alignment engineering," Nat Mater **13**, 796-801 (2014).
36. J. D. J. Joannopoulos, S. G. Winn, J. N. Meade, R. D. , *Photonic Crystals Molding the Flow of Light* (Princeton University Press, 2008).
37. T. Krauss, "The Bandstructure - Hand Out for the Masters Course on Photonic Crystals and Plasmonics," (Univeristy of St Andrews, 2012).
38. Y. Akahane, T. Asano, B. S. Song, and S. Noda, "High-Q photonic nanocavity in a two-dimensional photonic crystal," Nature **425**, 944-947 (2003).
39. O. Painter, R. K. Lee, A. Scherer, A. Yariv, J. D. O'Brien, P. D. Dapkus, and I. Kim, "Two-dimensional photonic band-gap defect mode laser," Science **284**, 1819-1821 (1999).
40. H. Y. Ryu, M. Notomi, and Y. H. Lee, "High-quality-factor and small-mode-volume hexapole modes in photonic-crystal-slab nanocavities," Applied Physics Letters **83**, 4294-4296 (2003).
41. B. Bakir, C. Seassal, X. Letartre, P. Viktorovitch, M. Zussy, L. Di Cioccio, and J. M. Fedeli, "Surface-emitting microlaser combining two-dimensional photonic crystal membrane and vertical Bragg mirror," Applied Physics Letters **88** (2006).
42. C. Monat, C. Seassal, X. Letartre, R. Regreny, P. Rojo-Romeo, P. Viktorovitch, M. L. d'Yerville, D. Cassagne, J. P. Albert, E. Jalaguier, S. Pocas, and B. Aspar, "InP-based two-dimensional photonic crystal on silicon: In-plane Bloch mode laser," Applied Physics Letters **81**, 5102-5104 (2002).
43. M. Meier, A. Mekis, A. Dodabalapur, A. Timko, R. E. Slusher, J. D. Joannopoulos, and O. Nalamasu, "Laser action from two-dimensional distributed feedback in photonic crystals," Applied Physics Letters **74**, 7-9 (1999).
44. J. Mouette, C. Seassal, X. Letartre, P. Rojo-Romeo, J. L. Leclercq, P. Regreny, R. Viktorovitch, E. Jalaguier, P. Perreau, and H. Moriceau, "Very low threshold vertical emitting laser operation in InP graphite photonic crystal slab on silicon," Electronics Letters **39**, 526-528 (2003).

45. S. Noda, M. Yokoyama, M. Imada, A. Chutinan, and M. Mochizuki, "Polarization mode control of two-dimensional photonic crystal laser by unit cell structure design," Science **293**, 1123-1125 (2001).
46. S. H. Kwon, H. Y. Ryu, G. H. Kim, Y. H. Lee, and S. B. Kim, "Photonic bandedge lasers in two-dimensional square-lattice photonic crystal slabs," Applied Physics Letters **83**, 3870-3872 (2003).
47. P. Bermel, C. Luo, L. Zeng, L. C. Kimerling, and J. D. Joannopoulos, "Improving thin-film crystalline silicon solar cell efficiencies with photonic crystals," Optics Express **15**, 16986-17000 (2007).
48. R. Dewan, I. Vasilev, V. Jovanov, and D. Knipp, "Optical enhancement and losses of pyramid textured thin-film silicon solar cells," Journal of Applied Physics **110** (2011).
49. L. Zeng, Y. Yi, C. Hong, J. Liu, N. Feng, X. Duan, L. C. Kimerling, and B. A. Alamariu, "Efficiency enhancement in Si solar cells by textured photonic crystal back reflector," Applied Physics Letters **89**, 111111 (2006).
50. L. Zeng, P. Bermel, Y. Yi, B. A. Alamariu, K. A. Broderick, J. Liu, C. Hong, X. Duan, J. Joannopoulos, and L. C. Kimerling, "Demonstration of enhanced absorption in thin film Si solar cells with textured photonic crystal back reflector," Applied Physics Letters **93** (2008).
51. A. Bielawny, J. Uepping, P. T. Miclea, R. B. Wehrspohn, C. Rockstuhl, F. Lederer, M. Peters, L. Steidl, R. Zentel, S.-M. Lee, M. Knez, A. Lambertz, and R. Carius, "3D photonic crystal intermediate reflector for micromorph thin-film tandem solar cell," Physica Status Solidi a-Applications and Materials Science **205**, 2796-2810 (2008).
52. P. Markowicz, C. Friend, Y. Z. Shen, J. Swiatkiewicz, P. N. Prasad, O. Toader, S. John, and R. W. Boyd, "Enhancement of two-photon emission in photonic crystals," Opt. Lett. **27**, 351-353 (2002).
53. M. Peters, J. C. Goldschmidt, P. Loeper, B. Gross, J. Uepping, F. Dimroth, R. B. Wehrspohn, and B. Blaesi, "Spectrally-Selective Photonic Structures for PV Applications," Energies **3**, 171-193 (2010).
54. C. M. Johnson, P. J. Reece, and G. J. Conibeer, "Up-conversion luminescence enhancement in erbium-doped porous silicon photonic crystals for photovoltaics," Physics and Simulation of Optoelectronic Devices Xix **7933** (2011).

55. Z. Yang, K. Zhu, Z. Song, D. Zhou, Z. Yin, and J. Qiu, "Effect of photonic bandgap on upconversion emission in YbPO4:Er inverse opal photonic crystals," Applied Optics **50**, 287-290 (2011).
56. E. Fortunato, D. Ginley, H. Hosono, and D. C. Paine, "Transparent Conducting Oxides for Photovoltaics," MRS Bulletin (Materials Research Society) **32**, 242-247 (2007).
57. M. Shtein, "Thin Metal Flms as Simple Transparent Conductors," SPIE Newsrom: Solar & Alternative Energy (2009).
58. B. O'Connor, C. Haughn, K.-H. An, K. P. Pipe, and M. Shtein, "Transparent and conductive electrodes based on unpatterned, thin metal films," Applied Physics Letters **93** (2008).
59. J. Gasiorowski, R. Menon, K. Hingerl, M. Dachev, and N. S. Sariciftci, "Surface morphology, optical properties and conductivity changes of poly(3,4-ethylenedioxythiophene): poly(styrenesulfonate) by using additives," Thin Solid Films **536**, 211-215 (2013).
60. M. P. de Jong, L. J. van IJzendoorn, and M. J. A. de Voigt, "Stability of the interface between indium-tin-oxide and poly(3,4-ethylenedioxythiophene)/poly(styrenesulfonate) in polymer light-emitting diodes," Applied Physics Letters **77**, 2255-2257 (2000).
61. W. Hong, Y. Xu, G. Lu, C. Li, and G. Shi, "Transparent graphene/PEDOT-PSS composite films as counter electrodes of dye-sensitized solar cells," Electrochemistry Communications **10**, 1555-1558 (2008).
62. M. Vosgueritchian, D. J. Lipomi, and Z. Bao, "Highly Conductive and Transparent PEDOT:PSS Films with a Fluorosurfactant for Stretchable and Flexible Transparent Electrodes," Advanced Functional Materials **22**, 421-428 (2012).
63. Y. Kim, A. M. Ballantyne, J. Nelson, and D. D. C. Bradley, "Effects of thickness and thermal annealing of the PEDOT:PSS layer on the performance of polymer solar cells," Organic Electronics **10**, 205-209 (2009).
64. T.-G. Chen, B.-Y. Huang, E.-C. Chen, P. Yu, and H.-F. Meng, "Micro-textured conductive polymer/silicon heterojunction photovoltaic devices with high efficiency," Applied Physics Letters **101** (2012).
65. V. C. Tung, J. Kim, L. J. Cote, and J. Huang, "Sticky Interconnect for Solution-Processed Tandem Solar Cells," Journal of the American Chemical Society **133**, 9262-9265 (2011).

Chapter 3 - Simulation of 2D Photonic Crystals

3.1 Overview of Simulation of 2D Photonic Crystals

In this chapter, the simulation of the photonic band structures and electric field densities for 2D photonic crystals of TiO_2:Er/air and Si/YF_3:Er is presented to find the optimum geometrical parameters for energy conversion. The simulations were achieved using a plane wave expansion (PWE) software MPB (MIT Photonic Bands) [1] and a Finite-Difference Time-Domain (FDTD) software MEEP (MIT Electromagnetic Equation Propagation) [2]. Three optimization parameters were considered. First, to find a flat band edge adjacent to a complete photonic band-gap and to maximize the width of the band gap. Second, to localize the density of states for the chosen band to the Gamma (Γ) direction. Third, to ensure that a high electric field density occurred in the up-conversion material. Three common highly symmetric 2D photonic crystal designs and their associated inverse structures were investigated to find the optimum band structure. These were square, triangular and hexagonal arrays of cylindrical features.

Triangular lattices of pillars were found to be the optimum structure for both the TiO_2:Er/air photonic crystal (pillars of TiO_2:Er) and the Si/YF_3:Er photonic crystal (pillars of Si). The resulting pillar radii and lattice constant for the size and spacing of the pillars were determined for the wavelengths of 980 nm and 1523 nm, corresponding to the centers of excitation and emission of tri-valent erbium. These geometries were used in the fabrication of the 2D photonic crystals described in Chapter 5 and Chapter 6.

3.2 Plane Wave Expansion Simulations

For a periodic dielectric structure, the allowable frequencies (eigenfrequencies) for the propagation of light in all crystal directions, and field distributions for any frequency of light are required to be known to correctly predict the propagation of light through the structure. The electromagnetic modes of a photonic crystal can be expressed in terms of Bloch states. Bloch waves can be thought of as plane waves that have been modulated in space by a periodic pattern. The modes of a photonic crystal form a set of continuous functions that are arranged in order of increasing frequency and band number, where the bands are numbered in order of increasing normalised frequency starting at 1. This set of continuous functions is known as the band structure [3].

The geometry of a 2D photonic crystal can be designed so that a flat dispersion band edge occurs in the direction perpendicular to the plane of the photonic crystal slab (Γ-direction). The high density of states at a flat band edge results in near stationary modes (slow light modes) that can enhance the up-conversion process. The scale invariance of Maxwell's equations implies that the dispersion characteristics are common to all photonic crystals with the same geometric relationships. Therefore once the desired dispersion diagram has been found, the wavelength at which the flat band edge lies can be tuned by scaling all distances uniformly [3].

One of the most reliable methods for calculating the eigenfrequencies and field distributions is the PWE method. PWE is a frequency domain approach that directly computes the eigenstates and eigenvalues of Maxwell's equations. Therefore each field computed has a definite frequency. The PWE calculations for this work were carried out using the MPB software, which iteratively improves approximate eigenstates.

An advantage of frequency domain methods is that very closely spaced modes appear as two separate eigenvalues in the results. Furthermore, the frequencies and eigenstates are calculated at the same time, allowing for the results to be immediately analysed. A traditional disadvantage of this method is that all of the lower eigenstates up to the one of interest must be calculated, often resulting in the calculation of large numbers of bands. MPB offers a targeted solver approach to overcome this problem, however convergence can be poor [4].

3.2.1 Design Considerations for Plane Wave Expansion Simulations

The simulations were designed and performed by programming script using MIT's in-house scripting language Scheme [5]. Scheme, a statistically focused dialect of the Lisp programming language, was the scripting language which all commands for both MPB and MEEP were written. Neither MPB nor MEEP do not involve a graphical user interface, therefore script files containing the desired commands to define the geometry, boundary conditions and all other parameters were written in order to carry out the simulations. The script files were executed through a Bash Unix shell, using a Linux based operating system. An example of one of the Scheme simulation files written and used in this study can be found in Appendix A.

Due to the symmetry of a 2D Photonic Crystal, all modes can be classified into one of two polarizations: transverse electric (TE) and transverse magnetic (TM). The transverse

plane corresponds to the x-y plane in which the refractive index of the photonic crystal varies. Therefore the transverse electric/magnetic polarization corresponds to the electric/magnetic field being confined within the x-y plane, respectively. The solutions for the TE and TM modes are simulated separately using the PWE method.

3.2.2 Setting up of Plane Wave Expansion Code for Simulations

The PWE simulation code developed was tested against results available in open literature to confirm that the code had been set up correctly for use in this study. The original paper by Johnson and Joannopoulos detailing the mathematical description of the MPB software has been cited over 2,500 times (Google Scholar – as of April 2015), providing confidence in the use of this code for the work in this study. The 2D PWE code set up for this thesis was used to obtain the band diagrams for the 2D photonic crystals analysed by Johnson *et al.*, who used the same software approach [6]. A comparison of the band structures is shown in Figure 3-1.

The shaded regions in Figure 3-1 (c) and (d) represent the light cone regions. Leaky modes occur in the light cone region, whereas guided modes are found in the unshaded region below. The boundary between the regions exhibiting leaky and guided modes is known as the light line [3, 7].

Published (a,c) Calculated (b,d)

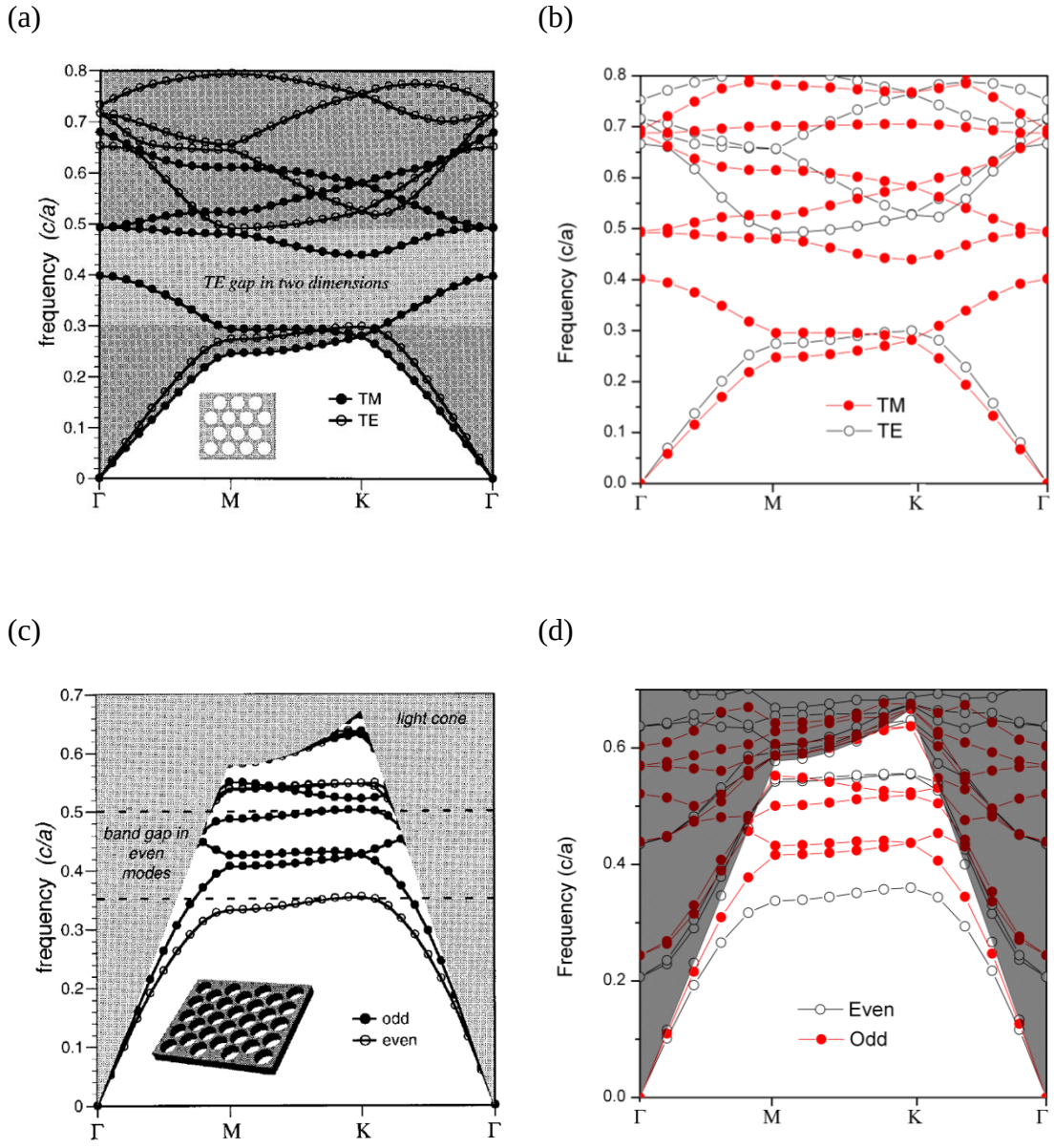

Figure 3-1: The code developed for this work was tested against structures published in literature, showing concurring results. The 2D (b) and 3D (d) PWE band diagram for a triangular array of air holes in a slab of refractive index n=12 are identical to those published by Johnson *et al.* [6] for their 2D (a) and 3D (c) simulations by PWE.

A very good comparison between the band structures obtained by Johnson *et al.* and the code developed for this piece of work was is observed, provides confidence in the setup of the code used for the work of this thesis. The same research team used this PWE method to predict the band structure of experimentally fabricated 2D photonic crystal slabs of air holes in GaAs, on a $Al_{0.9}Ga_{0.1}As$ base [7].

3.3 Finite-Difference Time-Domain Simulations

The advantage of a time-domain method, like FDTD, is that all of the frequencies (peaks in the fourier transform) can be acquired from the propagation of a single field. Furthermore, bands can be calculated individually, unlike the frequency domain calculations described previously. A disadvantage of time-domain methods is that the frequency resolution is inversely related to the simulation time. Therefore to achieve 10 times increase in resolution requires a 10 times longer simulation time. Furthermore, it is difficult to be confident that all states have been found, especially those that are very close together. The FDTD calculations for this work were carried out using the MIT Electromagnetic Equation Propagation (MEEP) software.

The difficulties in finding and resolving all of the states within a specific frequency region means that FDTD can be a slow and incomplete method for the prediction of band diagrams. However the ability to simulate bands individually allows for additional analysis of specific eigenmodes to be carried out. Therefore FDTD simulations were used in this study to further explore the electric field distributions of the eigenmodes of interest.

3.3.1 Design Considerations for Finite-Difference Time-Domain Simulations

As with the PWE considerations mentioned in Section 3.2.1, the FDTD simulations were designed and performed by programming script using MIT's in house scripting language Scheme and executed through a Bash Unix shell. The desired polarization (TE or TM) was achieved by selecting the orientation of the dipole current source. In order to observe the propagation of the electromagnetic modes, a simulation area consisting of 16 rows and columns of air holes was used.

3.4 Simulation of TiO_2:Er/Air 2D Photonic Crystals

The propagation of light through a 2D photonic crystal of TiO_2:Er and air was investigated by simulation to determine the optimum geometrical properties for enhancing up-conversion emission at 980 nm, following excitation at exactly 1523 nm. These absorption and emission wavelengths correspond to the characteristic peaks of the up-conversion of trivalent Erbium, which forms the optically active component of the experimentally fabricated materials in this thesis. Therefore these peak wavelengths, and the corresponding refractive indices of materials at these wavelengths, were used in the simulated models throughout this study. The 2D PWE method was used to model the photonic crystal band structure and the electric field distribution. The 2D FDTD method

was used to validate and further investigate the electric field distribution by analysing the time evolution of the field following excitation of a point dipole source. Finally, transmission measurements using the 2D FDTD method were carried out to check the correspondence between the 2D PWE photonic crystal band structure and the 2D FDTD results.

3.4.1 2D Plane Wave Expansion

Simulations were carried out using the 2D PWE method to model the propagation of light through a 2D photonic crystal of TiO_2:Er and air. It has previously been shown that square [8] and triangular [9] arrays of holes in high index media exhibit a third orthogonal photonic band with a flat band edge (low group velocity) in the Γ-direction. Simulations were carried out using the literature accepted value of 2.488 for the refractive index of the rutile phase of TiO_2 at 980 nm [10]. This value corresponded to the refractive index in the direction of the ordinary ray of the birefringent material, which is lower than that of the extraordinary ray ($n_{(980)}$ = 2.752) [10]. The lower refractive index was chosen as it provided the lower refractive index contrast with air and so would provide the "worst case scenario" for the simulations. For the purpose of analysing the simulation results, the TiO_2 will be considered to be the "up-conversion material".

Finding and maximising the width of the band gap was achieved by analysing the separation of the 3rd and 4th photonic bands. Maximising the band gap reduces the chance of losses due to population of states of similar normalised frequencies. The 3rd and 4th bands have been shown in literature to achieve photonic band gaps between them for a range of refractive index contrasts, with flat bad edges [8, 11]. The photonic band diagrams were calculated for a range of radius (r) to lattice constant (a) ratios and the size of the complete photonic band gap (minimum separation between bands 3 and 4) was calculated.

The minimum separation between the 3rd and 4th photonic bands of a 2D photonic crystal of square and triangular arrays of air holes in TiO_2 was analysed. The minimum separation was found by subtracting the maximum normalized frequency of the 3rd band from the minimum normalized frequency of the 4th band. A positive separation corresponded to a complete photonic band gap, which was found to occur for both geometries, as shown in Figure 3-2: however it was achieved for the TM polarization only. The maximum complete photonic band gap for the square and triangular lattices were achieved at r/a=0.46 and 0.51 respectively.

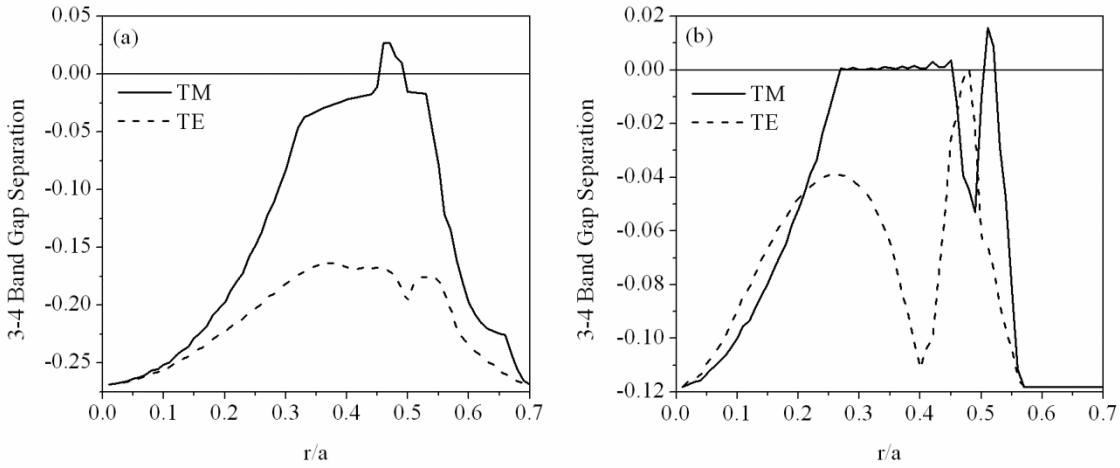

Figure 3-2: For both square (a) and triangular (b) geometries, a complete photonic band gap is observed between the 3rd and 4th photonic bands for the TM polarization only.

Next, the electric field distributions of the 3rd photonic bands in the Γ-direction were investigated to provide information on the mode overlap with the up-converting material. A higher overlap of the electric field with the up-converting material is expected to achieve a higher efficiency of emission [12]. The electric field distribution for the square lattice, shown in Figure 3-3, reveals that there is a significant overlap of the dipole modes with the air holes. Because this is the only square array structure to show a complete photonic band gap, this geometry was chosen to be investigated further.

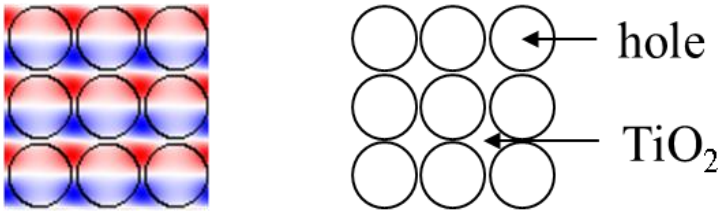

Figure 3-3: The electric field distribution (left) for a square array of air (n_{air} = 1) holes in TiO_2 (n_{TiO2} = 2.488), calculated using plane wave expansion. The black lines represent the contours between the different refractive indices. The blue-white-red colour scheme represents a scale where white corresponds to zero and blue and red are arbitrary positive and negative values. A greater intensity in colour indicates a greater positive or negative value for the electric field at that point. The electric field for this structure was found to show significant overlap with the up-conversion material; i.e. the area between the air holes.

For the triangular array of air holes in TiO_2, the electric field distributions for the range of *r/a* values that corresponded to a complete photonic band gap were analysed, with the results shown in Figure 3-4. The overlap of the field with the up-conversion material was found to decrease with increasing *r/a* from 0.27 to 0.45, which were all shown to have a similar band gap separation. There is a poor overlap of the field with the up-conversion

layer for the large band gap separation associated with r/a = 0.51. Furthermore, the air holes are so large that there is very little up-conversion material left, making this structure very difficult to fabricate on the nanoscale dimensions required. The strong overlap of the field occurring for r/a = 0.27 makes this structure the most suitable to use.

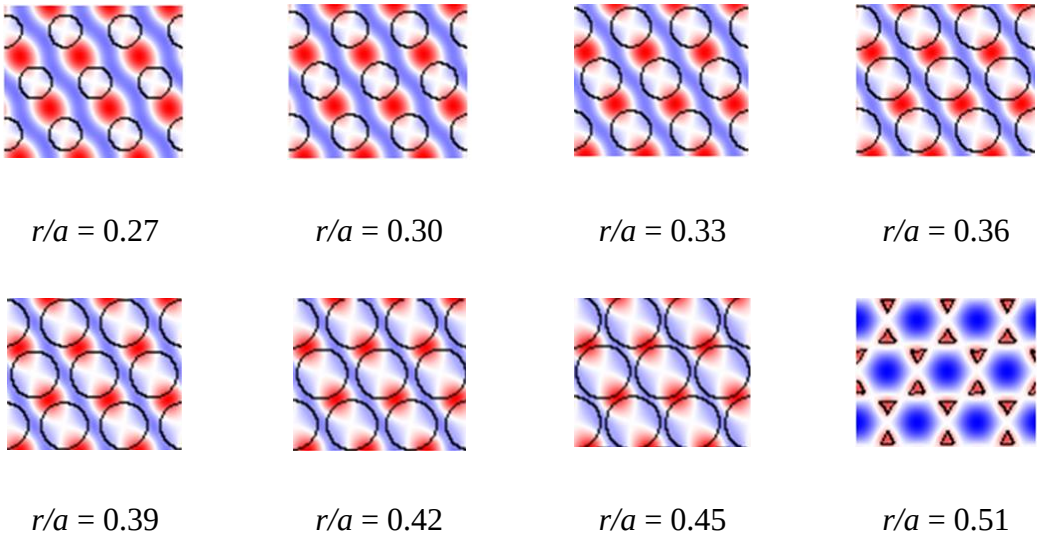

Figure 3-4: The large holes and therefore small amount of up-conversion material remaining for r/a = 0.51 geometry makes it unsuitable for fabrication. The strong overlap of the field shown for r/a = 0.27 makes this structure the most suitable to use.

3.4.2 2D Finite-Difference Time-Domain for Electric Field Distribution

Validation of the electric field distribution was carried out using the finite difference time domain software MEEP. The use of a second method of simulation allowed for a comparison to be made between the results to provide confidence in the simulation methods. A single dipole current source was used to stimulate the mode resonance. The dipole source was placed in a non-symmetric position to allow for all modes to be excited. The distribution of the band edge mode was recorded over the duration of a full period (1/normalised frequency). Snapshots of the electric field, perpendicular to the plane of the crystal were taken for each $t_{period}/20$ time step.

The mode evolution of a square lattice of r/a = 0.46 is shown in Figure 3-5. As the mode propagates in space and time, the overlap of the mode with the gain medium varies. The dipole mode distribution predicted by the frequency-domain analysis (Figure 3-3) is clearly observed.

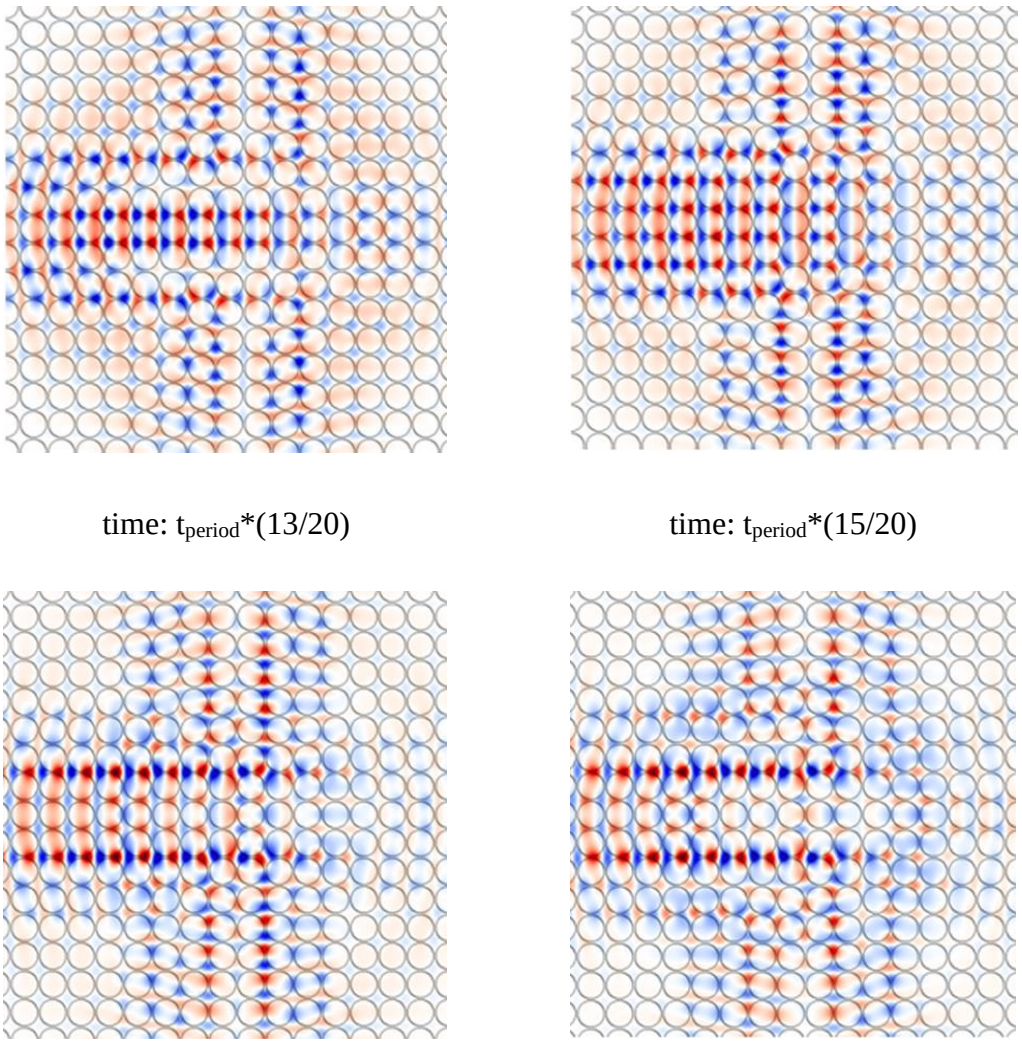

Figure 3-5: A dipole mode distribution is observed to propagate through the square lattice (*r/a* = 0.46, n_{TiO2} = 2.488) using time-domain calculations. These results are in agreement with those obtained using the frequency-domain calculations shown in Figure 3-3.

A comparison of a spatial section of the FDTD simulation after a time of t_{period}*(15/20) with the electromagnetic distribution using the PWE method for the square array of holes in TiO_2 is shown in Figure 3-6. The red and blue colours represent arbitrary positive and negative values for the electromagnetic field and therefore interest lies in the overall spatial distribution of the field, rather than the particular colour. It can be seen that the electric field distribution predicted by the FDTD method (a) follows the same spatial distribution as that predicted by the PWE method (b). Therefore these results provide confidence that the overlap of the electromagnetic field with the up-conversion material will be high.

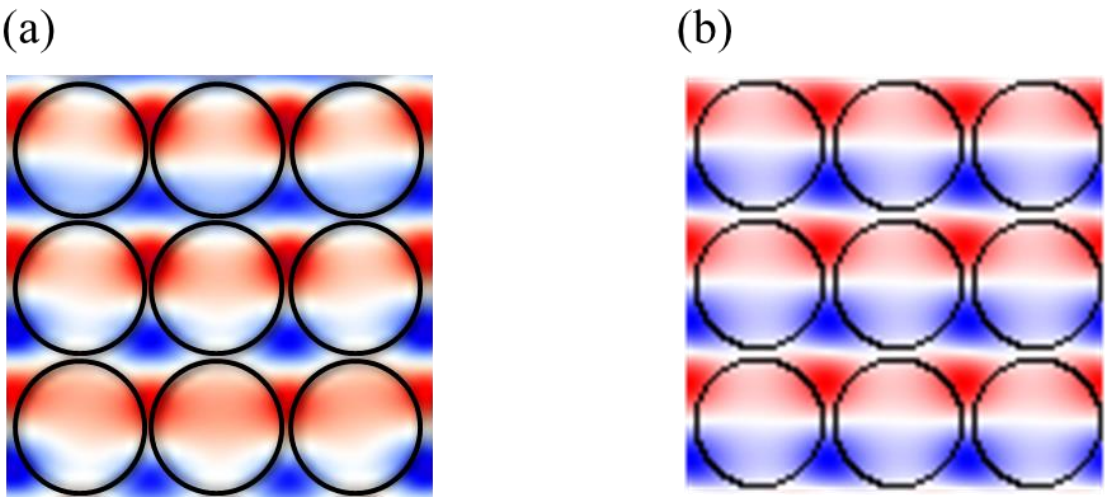

Figure 3-6: Comparison of the spatial distribution of the electromagnetic field predicted by the FDTD method (a) and the PWE method (b) show a convergence towards a similar distribution for a square array of air holes in TiO_2. This provides confidence that that the field will lie predominantly in the up-conversion material, rather than the air gaps.

The mode evolution for the triangular array of holes in TiO_2 for the previously identified r/a = 0.27 structure was investigated. The dipole mode identified using the PWE expansion method (Figure 3-4), is clearly shown in the FDTD time propagation of the mode in Figure 3-7.

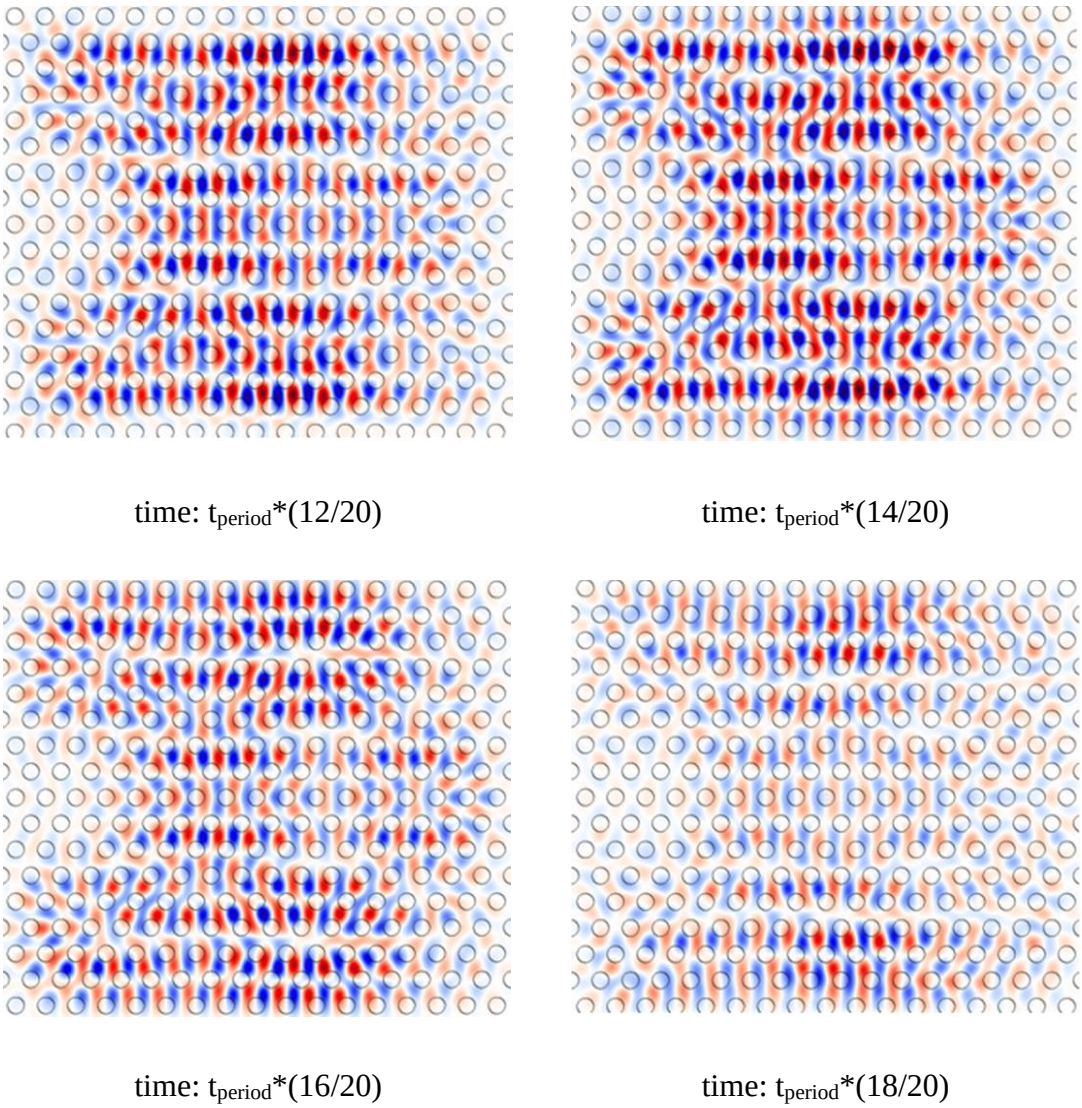

Figure 3-7: A dipole mode distribution is observed to propagate through the triangular lattice (*r/a* = 0.27, n = 2.488) using time-domain calculations. These results are in agreement with those obtained using the frequency-domain calculations shown in Figure 3-4.

A comparison of a spatial section of the FDTD simulation after a time of t_{period}*(14/20) with the electromagnetic distribution using the PWE method for a triangular array of holes of *r/a* = 0.27 is shown in Figure 3-8. As was concluded previously for the square array of holes, the results provide confidence that the overlap of the electromagnetic field with the up-conversion material will be high.

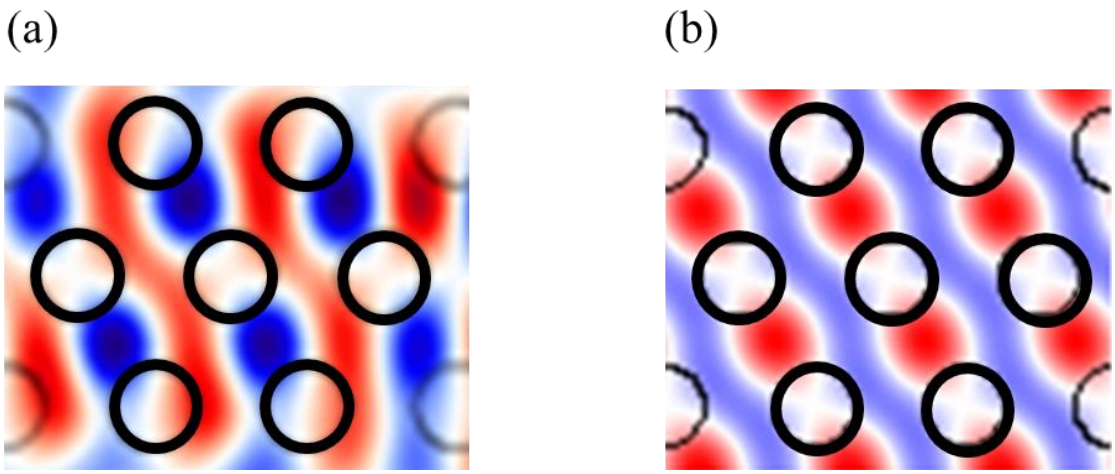

Figure 3-8: Comparison of the spatial distribution of the electromagnetic field predicted by the FDTD method (a) and the PWE method (b) show a convergence towards a similar distribution for a triangular array of air holes in TiO_2. This provides confidence that that the field will lie predominantly in the up-conversion material, rather than the air gaps.

Comparison of the electromagnetic field distributions results using a 2D plane wave expansion method and a 2D finite-difference time-domain method provided confidence in the simulation methods chosen. This allowed for the photonic band structures calculated using plane wave expansion to be compared, as discussed in the following section.

3.4.3 Photonic Band Structure Analysis for Optimised Geometry

The photonic band diagrams modelled using PWE for the optimised square and triangular arrays of holes in TiO_2 were investigated. The band diagrams for the square array (r/a = 0.46) reveals a flat band edge for the 3rd photonic band that extends fully in the Γ-X-directions, as shown in Figure 3-9(a). This corresponds to a wide cone angle of acceptance/emission that would include the in-plane X-direction. Therefore tuning the emission wavelength to this flat band edge would result in propagation of the emission within the plane of the 2D photonic crystal, which would be detrimental to the application of the layer. This is because the emitted 980 nm light would have to travel through a much greater path length to reach the photovoltaic layer as desired, risking parasitic reabsorption. The band diagram for the triangular array (r/a = 0.27) reveals a very narrow band gap separation in the Γ-direction, as shown in Figure 3-9(b). This may therefore result in losses due to the population of states exhibiting very similar wavelengths of acceptance.

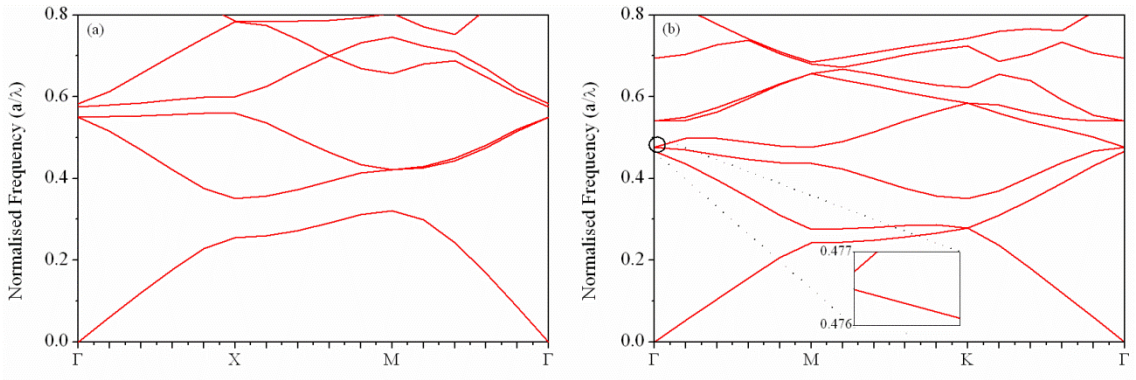

Figure 3-9: (a) The square lattice of air holes in TiO_2 reveals a distinct complete photonic band gap, with flat 3rd and 4th bands extending in the Γ-X-direction. (b) The triangular lattice of air holes in TiO_2 shows a very narrow band gap localised in the Γ-direction.

The further analysis of the separation of the 3rd and 4th bands of the triangular array in the Γ-direction was carried out to quantify the separation for structures tuned to 980 nm and 1523 nm emission. It was found that for a 2D photonic crystal tuned to enhance 980 nm (or 1523 nm) by aligning with the 3rd band in the Γ-direction, the 4th band in the Γ-direction would occur at 979.5 nm (or 1522 nm). These very small separations would result in significant leaking of the electric field into undesired states.

3.4.4 Finite-Difference Time-Domain Transmission Measurements

The photonic band structure in a particular crystallographic direction can be further analysed by simulating the transmission of electromagnetic waves through the structure.

Difficulties arise when computing the transmission perpendicular to the PC to demonstrate band edge lasing. Initial investigations using 3D simulations to analyse the emission perpendicular to the PC structure for a range of source geometries, polarizations, orientations and combinations, were unable to reproduce the expected band edge enhancement. An inherent nature of time-domain 3D simulations is that they are considerably more computationally expensive than those in 2D. Therefore compromises in the resolution, run-time, or structure size must be made in order to set feasible simulations.

A 2D time-domain simulation was set up to investigate the transmission of a TE polarized wave in the M-direction of the PC. The M-direction in k-space corresponds to the direction of the arrow as shown in Figure 3-10.

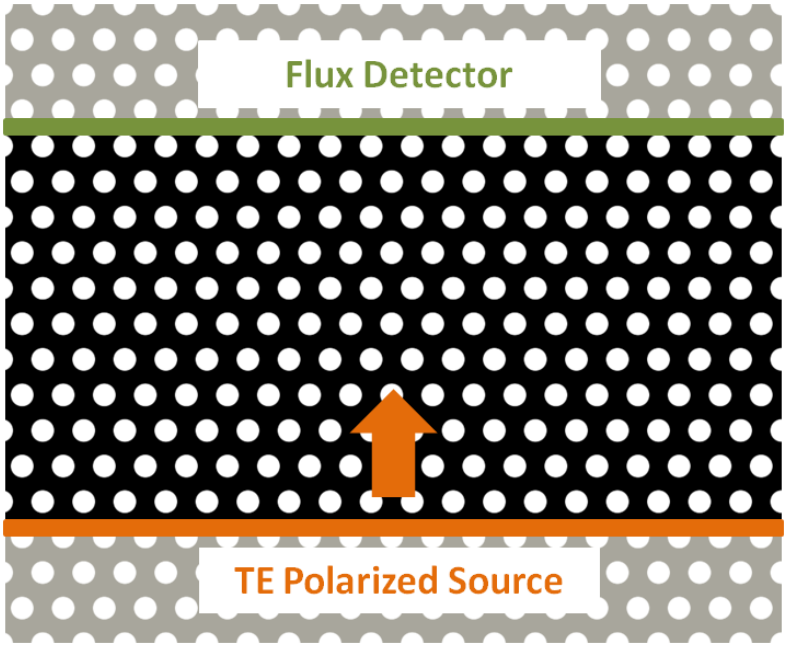

Figure 3-10: The 2D FDTD simulation of the transmission in the M-direction of k-space was carried out using the setup shown in the schematic diagram. The source and detector were separated by 13 times the lattice constant of the photonic crystal structure. The arrow corresponds to the M-direction in k-space.

The results of the FDTD transmission spectrum are compared with the PWE band diagram for validation. A clear correspondence between the band gaps in the M-direction of the band structure, and the minimum transmission in the transmission spectra are observed in Figure 3-11. Even though the separation between the source and detector was relatively small (13 times the lattice constant), the transmission within the band gaps is shown to reduce to zero.

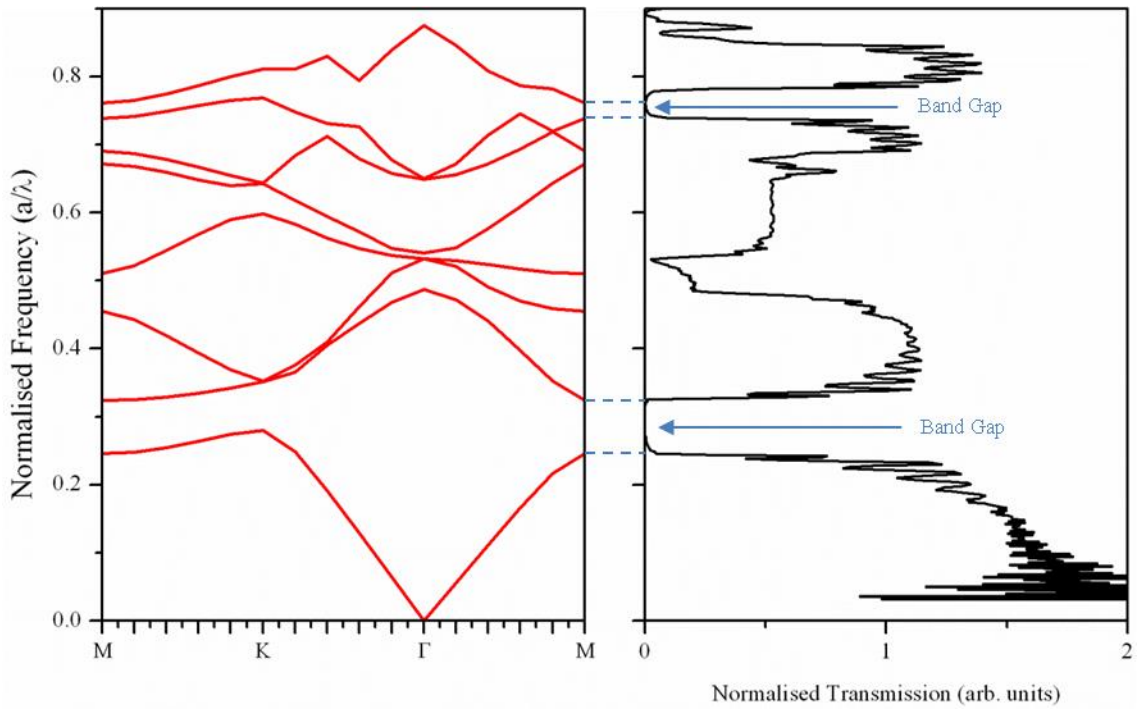

Figure 3-11: The normalised transmission in the M-direction in k-space (right), modelled using the FDTD method was shown to correspond very well with the PWE band structure (left) from only 13 repeating units of the lattice constant between source and detector.

The result of the FDTD transmission simulation provides useful validation of the PWE band structure diagrams, providing confidence in the geometries determined for the fabrication of the devices.

3.4.5 Simulation Analysis for Experimentally Determined TiO_2:Er Refractive Index

The initial simulation analysis was carried out before the experimental results of for the refractive index of erbium doped TiO_2 had been obtained. In this section, the experimentally determined values for TiO_2:Er are used to determine the optimum geometry for the fabrication of the 2D photonic crystals using the experimentally produced film.

Optimisation of the geometry of the TiO_2:Er/Air 2D photonic crystals was carried out using the experimentally determined value of n = 2.07, for the sputter deposited homogeneous amorphous TiO_2:Er phase calcinated at 500°C, to maximise the complete photonic band gap between the 3rd and 4th bands. This value of the refractive index was subsequently refined as the model was developed, therefore differs a little from the refractive index values presented in section 5.3.1. However the value of n = 2.07 for which the simulations are performed in this section provide a much better approximation of the

geometries required for the TiO_2:Er prepared films, than using the literature value of TiO_2 alone. The experimental value of n = 2.07 and the literature value of n = 2.488 differ due to the difference in the crystallinity, as the literature accepted value corresponds to the rutile phase of TiO_2, whereas the experimental value corresponds to the amorphous phase. The reasons for choosing the amorphous phase over rutile for the experimental work are discussed in Chapter 5.

Simulations were carried out for the three most common 2D photonic crystal geometries: Triangular, Hexagonal and Square arrays of holes and pillars. The geometrical representation of these structures is shown in Figure 3-12. Black represents the dielectric medium, whereas white represents air.

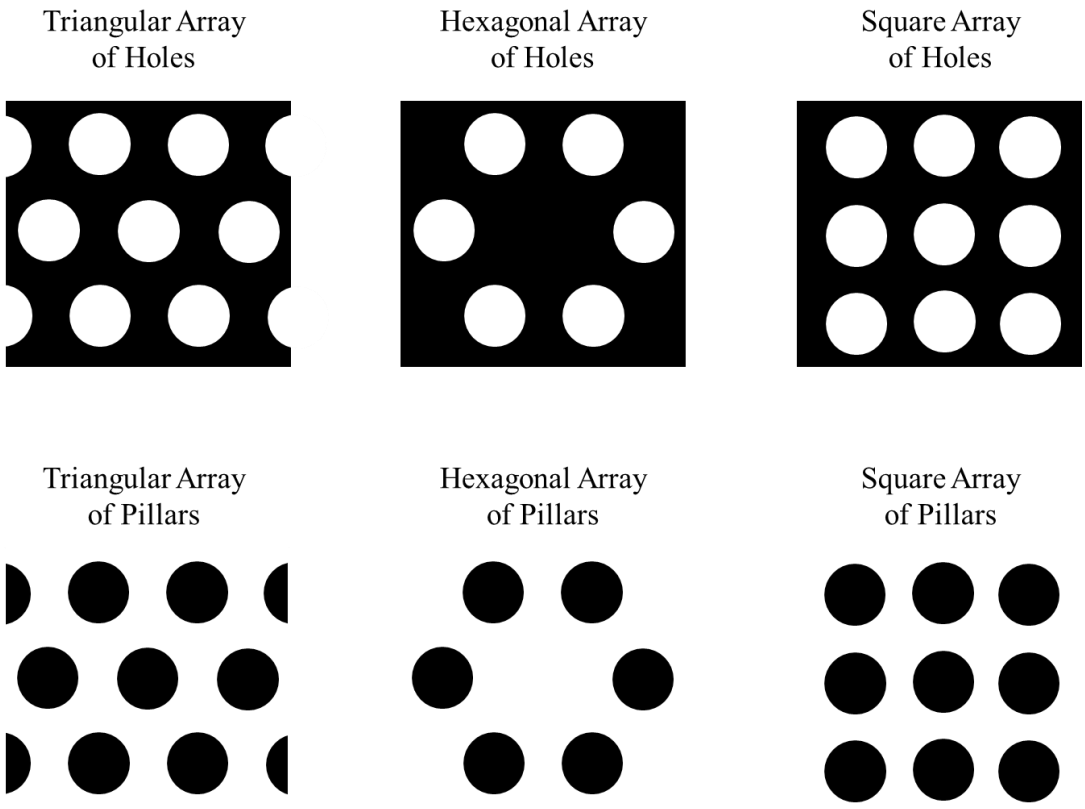

Figure 3-12: Triangular, hexagonal and square arrays of holes and pillars were used in the simulations. The black represents a dielectric medium, whereas the white represents air.

The results for both transverse electric (TE) and transverse magnetic (TM) polarizations are detailed in Figure 3-13. It is shown that large photonic band gaps occur for the TM polarization of a hexagonal array of holes at r/a = 0.29 and for the TM polarization of a triangular array of pillars at r/a = 0.33.

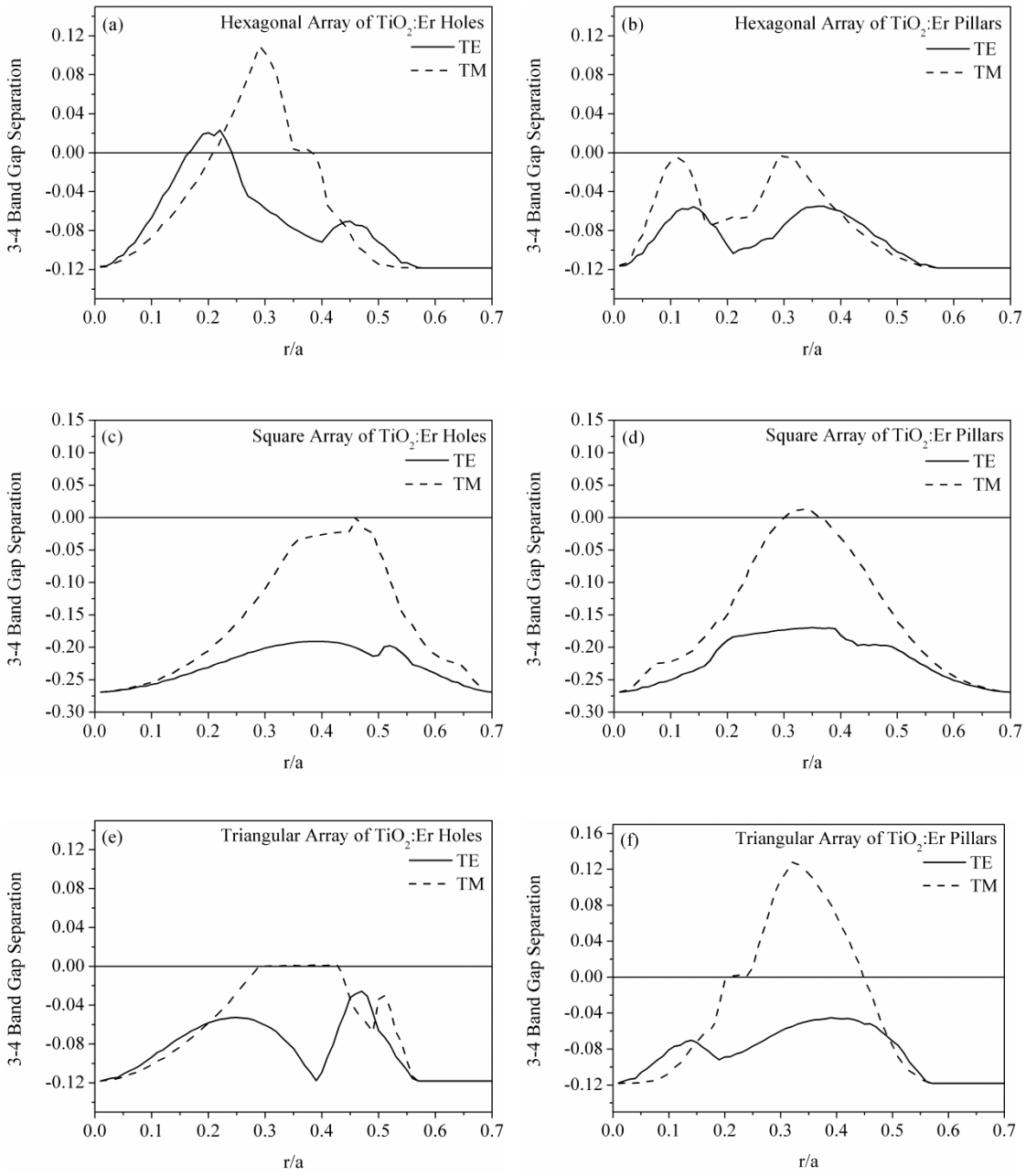

Figure 3-13: Large separations between the 3rd and 4th bands were observed for the TM polarization of a hexagonal array of holes at r/a = 0.29 and for the TM polarization of a triangular array of pillars at r/a = 0.33.

The photonic band diagrams and electromagnetic modes were compared for the geometries of the Hexagonal, Square and Triangular arrays exhibiting the largest band gaps. The photonic band diagram for the square array structure with the largest 3-4 band gap separation, a square array of TiO_2:Er pillars with $r/a = 0.33$, is shown in Figure 3-14. The dip in the 4th photonic band in the M-direction results in a very small separation between the lowest normalised frequency of the 4th band and the highest normalised frequency of the 3rd band. This means that a photonic crystal tuned to the flat band edge of the 3rd photonic band in the Γ-direction would have a high probability of leaking into

states of the 4th photonic band. Furthermore, the 2nd photonic band in the Γ-direction reaches a very similar normalised frequency as the 3rd photonic band in the same direction. Therefore there would be a high probability of the electromagnetic field leaking into states in the 2nd photonic band as well. The leaking of the electromagnetic field into multiple states would occur due to a) the excitation or emission spectrum having a finite wavelength range and b) imperfections in the fabrication process resulting in variation in the geometrical parameters. A photonic crystal tuned to the band edge of the 4th photonic band in the Γ-direction would result in leaking into the degenerate states of the 4th photonic band in the two other directions with same normalised frequency.

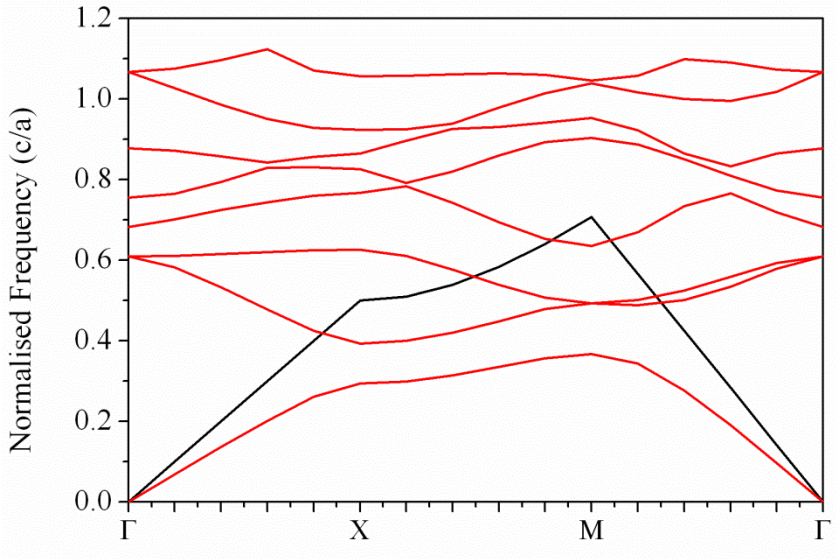

Figure 3-14: The photonic band structure of a square array of TiO_2:Er pillars of *r/a* = 0.33. The very small separation between the 3rd and 4th photonic bands, in addition to the convergence of the 2nd and 3rd bands in the Γ-direction, means that there is a very high probability of the electromagnetic field leaking into modes out with the desired states.

The photonic band diagrams for the hexagonal array of holes and triangular array of pillars are shown in Figure 3-15 (a) and Figure 3-15 (b) respectively. The maximum 3-4 band gap separation for the hexagonal array of holes occurred at *r/a* = 0.29, while the maximum separation for the triangular array of pillars occurred at *r/a* = 0.32. The electromagnetic mode distributions for the 3rd and 4th bands in the Γ-direction are shown on the right of the band diagrams. It can be seen from the two band structures that both the hexagonal array of holes and triangular array of pillars have converged upon a common structure. For ease of fabrication, the triangular pattern was chosen to investigate further for the remainder of this work.

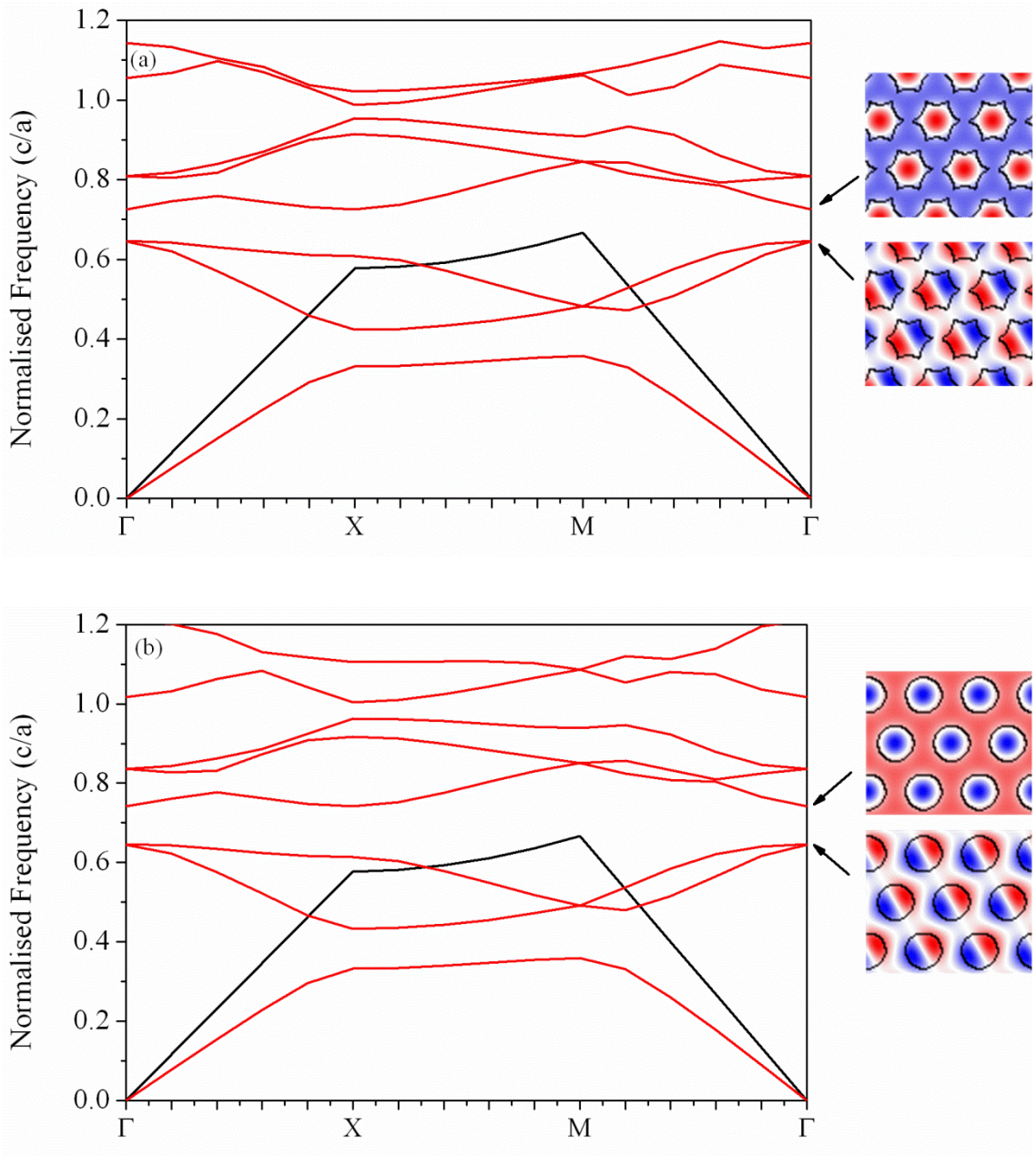

Figure 3-15: The optimisation of the hexagonal (a) and triangular (b) lattices for maximum 3-4 band gap separation have resulted in both hole/pillar distributions converging upon a common geometrical form. These geometrical forms, with the associated electromagnetic mode distributions, are shown for the 3rd and 4th band edges in the Γ-direction on the right hand sides of the graphs.

The flat band edge of the 3rd photonic band in the Γ-direction was chosen to be the most appropriate to use. The electromagnetic field distribution shows that the field is confined as a dipole within the pillars of TiO_2:Er and therefore a very good overlap of the electromagnetic field with the up-conversion material would be achieved. The disadvantage of using this band edge is that the second band edge in the Γ-direction lies very close in normalised frequency, therefore there is likely to be a loss of the electromagnetic field to these modes. The 4th photonic band edge in the Γ-direction in

comparison shows degenerate states in the X-direction and the electromagnetic field is widely distributed between the up-converting TiO_2:Er and air. The overlap of the electric field with the air will reduce the intensity of the electric field in the up-converting material, therefore reducing the emission from the non-linear process. The occupation of additional states by the electromagnetic field will result in further spreading of the electromagnetic filed into air overlapping distributions, in addition to reducing the component of the field that exhibits a low group velocity at the band edge.

From the normalised frequency values, we can calculate the geometrical properties of the photonic crystal that would be required to enhance up-conversion using the flat band edge effect. The 3rd photonic band in the Γ-direction has a normalised frequency (υ) of $\upsilon = 0.646\ c/a$, and as $\lambda = c/\upsilon$, we can conclude that $c/\lambda = 0.646\ c/a$ and hence $a = 0.646 \cdot \lambda$. Therefore the corresponding pillar radius and lattice constant of the triangular array of pillars required to locate the wavelength of interest at the flat band edge and is shown in

Table 3-1. Previous work in the literature has shown examples of enhancing emission by locating the band edge at the wavelength of emission (section 2.5.2). However there has been no previous work found on enhancing emission by locating the excitation wavelength at the band edge. For the work of this thesis, geometries were optimised for band edge located at both the excitation and emission wavelengths to explore both possibilities.

Wavelength to Locate at Flat Band Edge (nm)	r (nm)	a (nm)
980	203	633
1523	315	984

Table 3-1: The hole radius (*r*) and lattice constant (*a*) for the optimised triangular array of TiO_2:Er pillars in air for locating the flat band edge of the 3rd photonic band in the Γ-direction at 980 nm or 1523 nm respectively.

These optimised geometrical parameters were used in the experimental fabrication of the TiO_2:Er/air 2D photonic crystals as described in Chapter 5. Difficulties in etching the TiO_2:Er limited the opportunity to analyse the optical properties of this type of up-converting photonic crystal. Therefore a second set of 2D photonic crystals consisting of Si and YF_3:Er were also fabricated in the work of this thesis (Chapter 6). The next section of this chapter will present the simulation work carried out to optimise the geometrical parameters for this second type of photonic crystal.

3.5 Simulation of Si/YF_3:Er 2D Photonic Crystals

The propagation of light through a 2D photonic crystal of silicon and YF_3:Er was investigated by simulation to determine the optimum geometrical properties for enhancing up-conversion emission at 980 nm, following excitation at 1523 nm. The 2D PWE method was used to model the photonic crystal band structure and the electric field distribution to find the optimum geometrical parameters for the 2D photonic crystal.

3.5.1 2D Plane Wave Expansion

Photonic band diagrams were used to optimise the geometrical features of the 2D photonic crystal composed of silicon and YF_3:Er. As mentioned at the beginning of this chapter, the optimisation conditions were to: first find a flat band edge adjacent to a complete photonic band-gap and to maximize the width of the band gap; and second, to localize the density of states for the chosen band to the Γ-direction.

It was found that the absolute refractive index of the material had a large impact on the size of the band gap, however little impact on the ratio of *r/a*. The variation in band gap separation with *r/a* for refractive indices of n = 1.15, 1.35 and 1.60 for the area surrounding a triangular array of Si pillars shows that the peak separation stays constant at around *r/a* = 0.32 as shown in Figure 3-16.

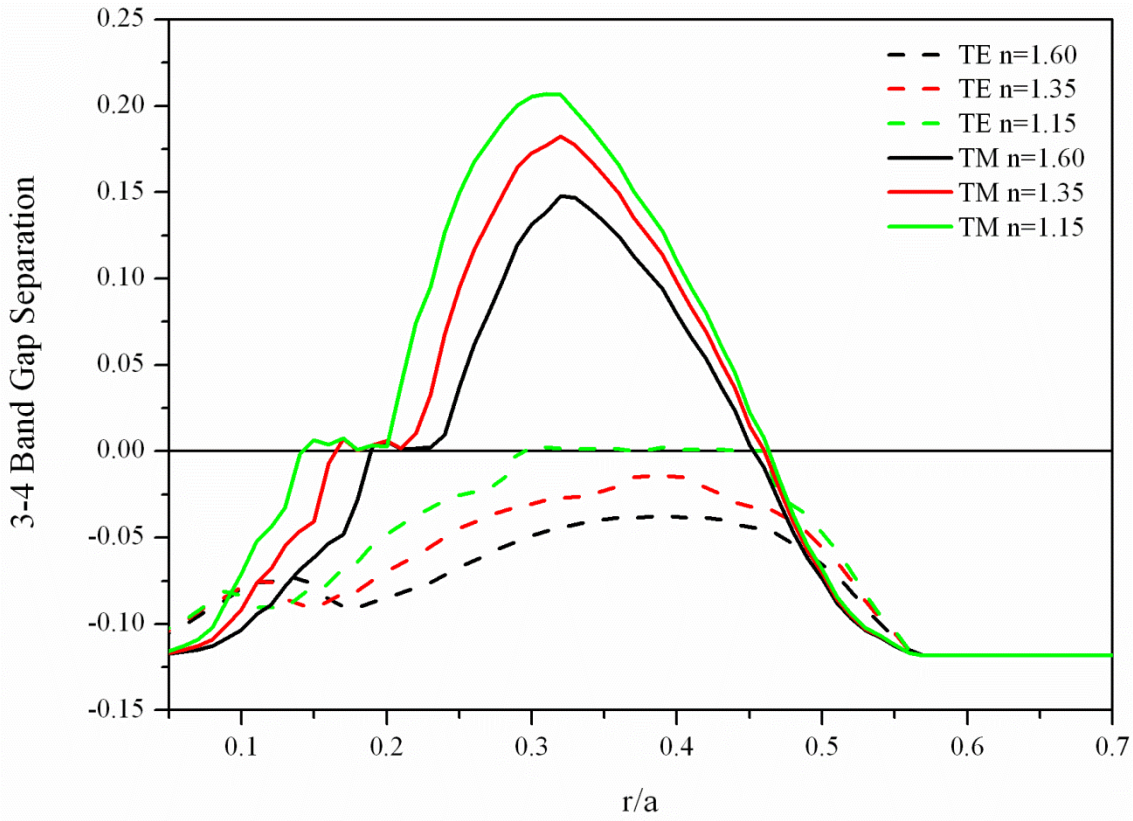

Figure 3-16: The variation in band gap separation was found to increase with increasing refractive index contrast between the two photonic crystal materials, however the *r/a* ratio at peak separation remained constant. This was consistent for both the TE and TM polarisations.

As the refractive index of both the TiO_2:Er and YF_3:Er were found to have slight variations in repeatability (sections 5.3.1 and 6.4.5), simulations were carried out with refractive indices for the materials that resulted in a minimum refractive index contrast for the photonic crystals. Therefore devices would be optimised for the "worst case scenario". The fabrication of these devices would cover a range of geometrical parameters centered around the optimised values. This would mean that if the refractive index of the material varied slightly from that expected, the position of the photonic band edge would only change by a small amount and so one of the photonic crystals exhibiting a variation in a geometrical parameter would be resonant at the desired wavelength.

The second set of simulations was carried out for 2D photonic crystals of Si and YF_3:Er. The refractive indices of Si at 980 nm and 1523 nm were found in literature to be $n_{(980)} = 3.58$ and $n_{(1523)} = 3.48$ respectively [13]. The refractive index of the YF_3:Er layer was measured by ellipsometry in section 6.4.5 to be around $n_{(980)} = 1.53$ and $n_{(1523)} = 1.52$ respectively. However variations in the measurements of the refractive index of the YF_3:Er between samples meant that the simulations were carried out with a refractive index at the higher end of the range of values measured, to minimise the contrast in

refractive index between the silicon and YF_3:Er. Therefore the simulations were carried out using a refractive index of n = 1.60 for the up-converting layer.

Optimisation of the geometry of the Si/YF_3:Er 2D photonic crystals was carried out to maximise the complete photonic band gap between the 3rd and 4th bands. The results for both TE and TM polarizations are detailed in Figure 3-17 for hexagonal, square and triangular arrays of holes and pillars of Si. The terminology used was kept the same as that for TiO_2:Er discussed previously, however with YF_3:Er in the place of air. Therefore a pillar of Si refers to pillars of Si surrounded by a medium of YF_3:Er, whereas an array of Si holes refers to an array of holes in Si where the holes have been filled in with a YF_3:Er medium. It is shown in Figure 3-17 that large photonic band gaps occur for the TM polarization of a hexagonal array of (YF_3:Er filled) holes at r/a = 0.29 and for the TM polarization of a triangular array of Si pillars at r/a = 0.33.

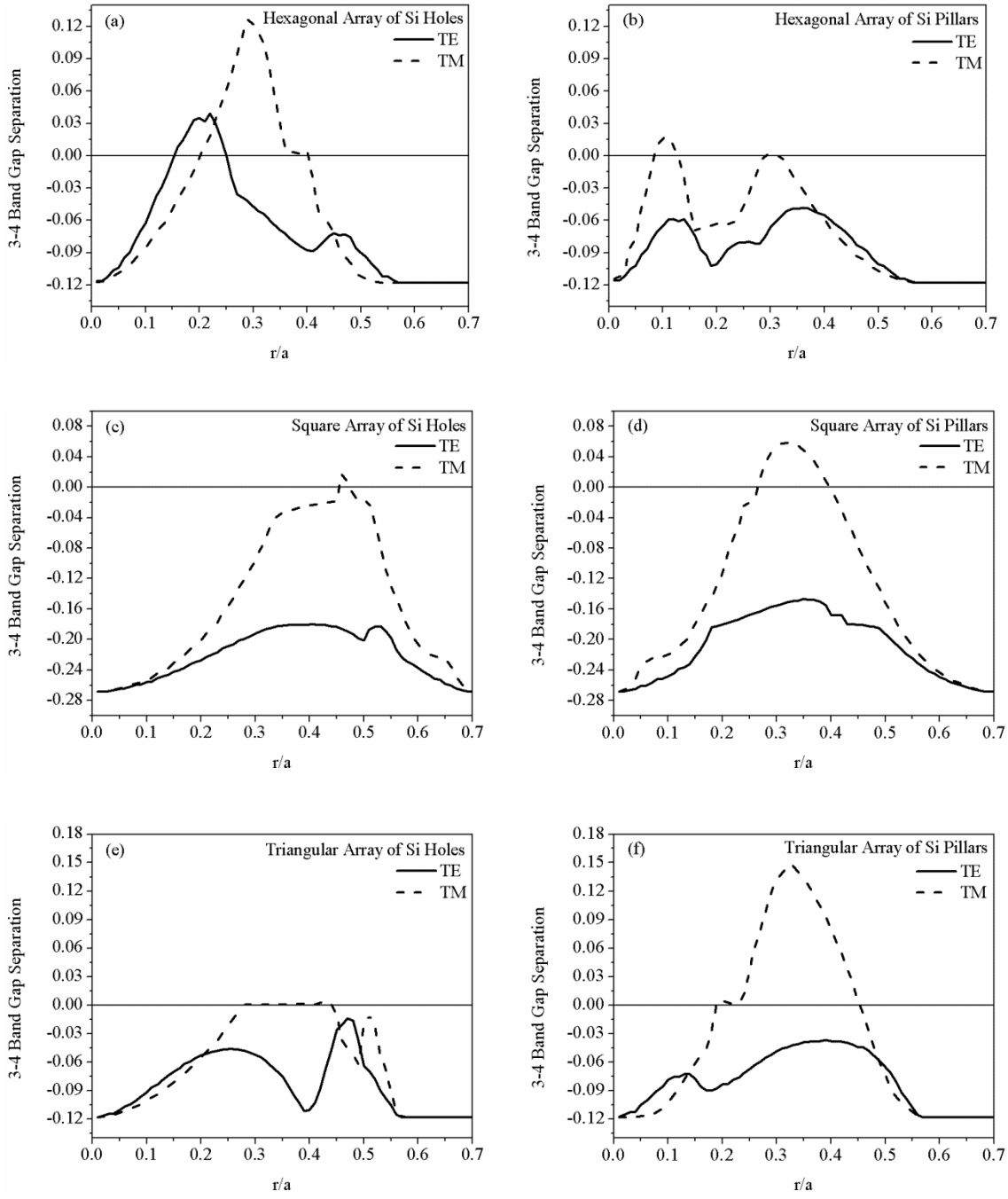

Figure 3-17: Analysis of the separation between the 3rd and 4th photonic bands shows that the largest complete band gaps exist for the TM polarisation of the hexagonal array of holes and the triangular array of pillars.

The photonic band diagrams and electromagnetic modes were compared for the geometries exhibiting the largest band gaps. The comparison shown in Figure 3-18 reveals that both the hexagonal array of holes and triangular array of pillars have converged upon a common structure, as was observed for the TiO_2:Er/air photonic crystals in section 3.4.5. The distribution of electromagnetic modes for the 3rd (lower) and 4th (upper) bands are shown on the right of each graph. As mentioned previously, the triangular array of pillars is easier to fabricate than a hexagonal array of holes using a

positive photoresist and the lift off technique, therefore the triangular pattern was chosen to investigate further for the remainder of this work.

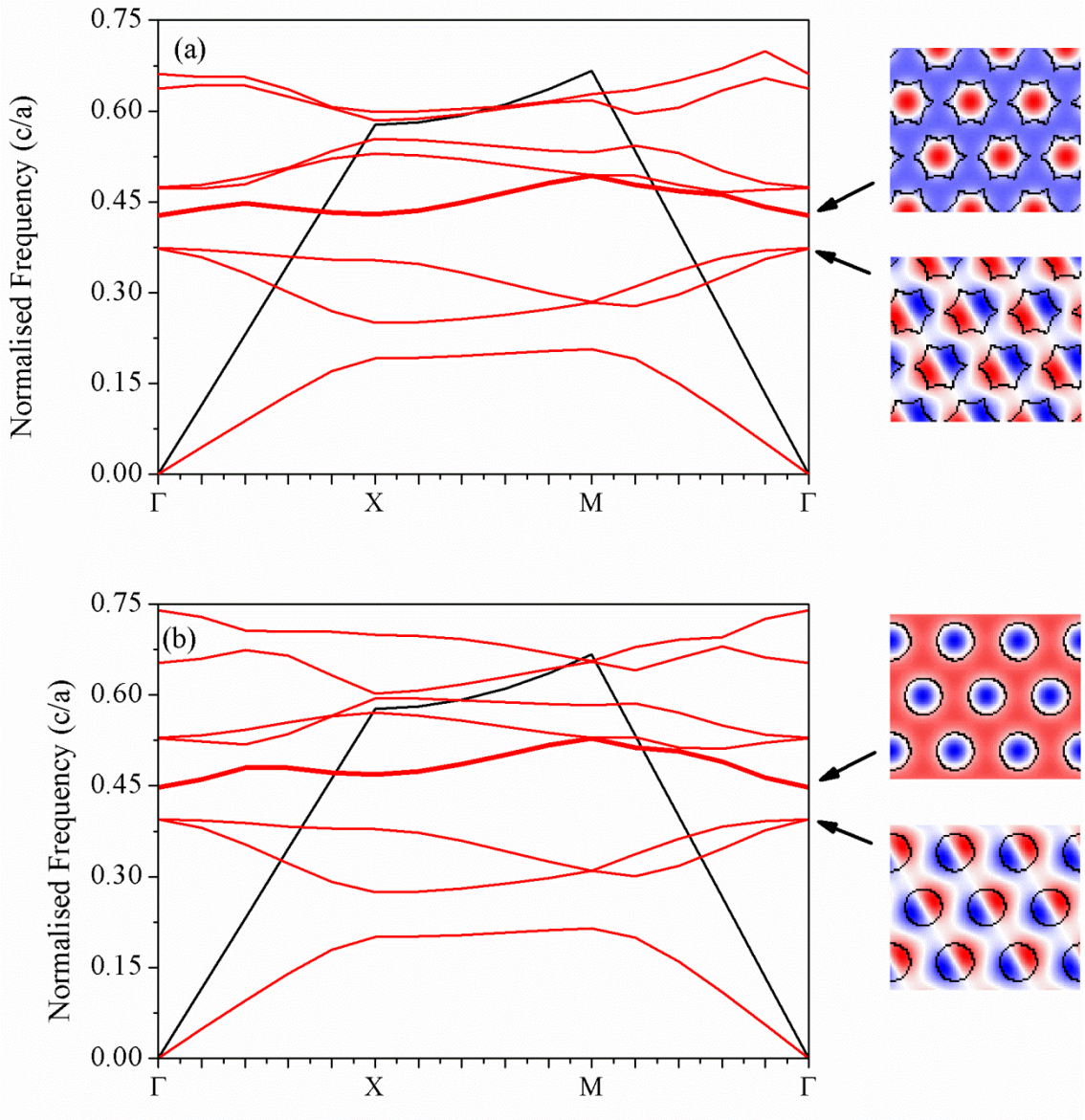

Figure 3-18: The photonic band diagrams and electromagnetic field distributions in the Γ-direction for the 3rd and 4th photonic bands are shown for (a) *r/a* = 0.29 hexagonal array of YF_3:Er filled holes surrounding Si pillars and (b) *r/a* = 0.33 triangular array of Si pillars surrounded by YF_3:Er.

A flat band edge in the Γ-direction was found to exist for both the 3rd and 4th bands. The choice of which band to use was determined by analyzing the electromagnetic field diagram for each band in the Γ-direction. As discussed for the TiO_2:Er/air photonic crystals, a high overlap of the electromagnetic field with the gain medium is required to maximize the effect of the band edge. As the gain medium of YF_3:Er resides in the spaces between the Si pillars, a higher overlap with the gain medium is achieved in the Γ-direction of the 4th band. The (blue) component of the electromagnetic field residing in

the Si pillars for the 4th band in the Γ-direction will result in a decrease in efficiency of the effect, compared to the field existing predominantly in the space between the pillars. However an additional advantage of using the 4th band edge is that 2nd and 3rd band edges converge to a similar normalised frequency in the Γ-direction and so would result in losses due to delocalization of the field into multiple states.

The final stage of optimisation process was to localize the density of states in the Γ-direction. This was achieved by investigating a narrow range of *r/a* values centered on the maximum photonic band gap geometry to check the localization of states in the desired 4th band in the Γ-direction. It was shown in Figure 3-17 that the maximum band gap separation for the triangular lattice was observed for *r/a* = 0.31. Therefore the 3rd and 4th bands for *r/a* = 0.25, 0.27, 0.29, 0.31 and 0.33 were investigated and are shown in Figure 3-19. At the largest *r/a* value of 0.33, it can be seen that the density of states for the 4th band are not localised to the Γ-direction: a dip in the band in the X direction intersects the frequency at which the 4th band intersects the Γ-direction. At the minimum *r/a* value of 0.25, the band gap separation becomes very small. Therefore there was found to be an optimum *r/a* value of 0.29, which was used for the remainder of the work in this study.

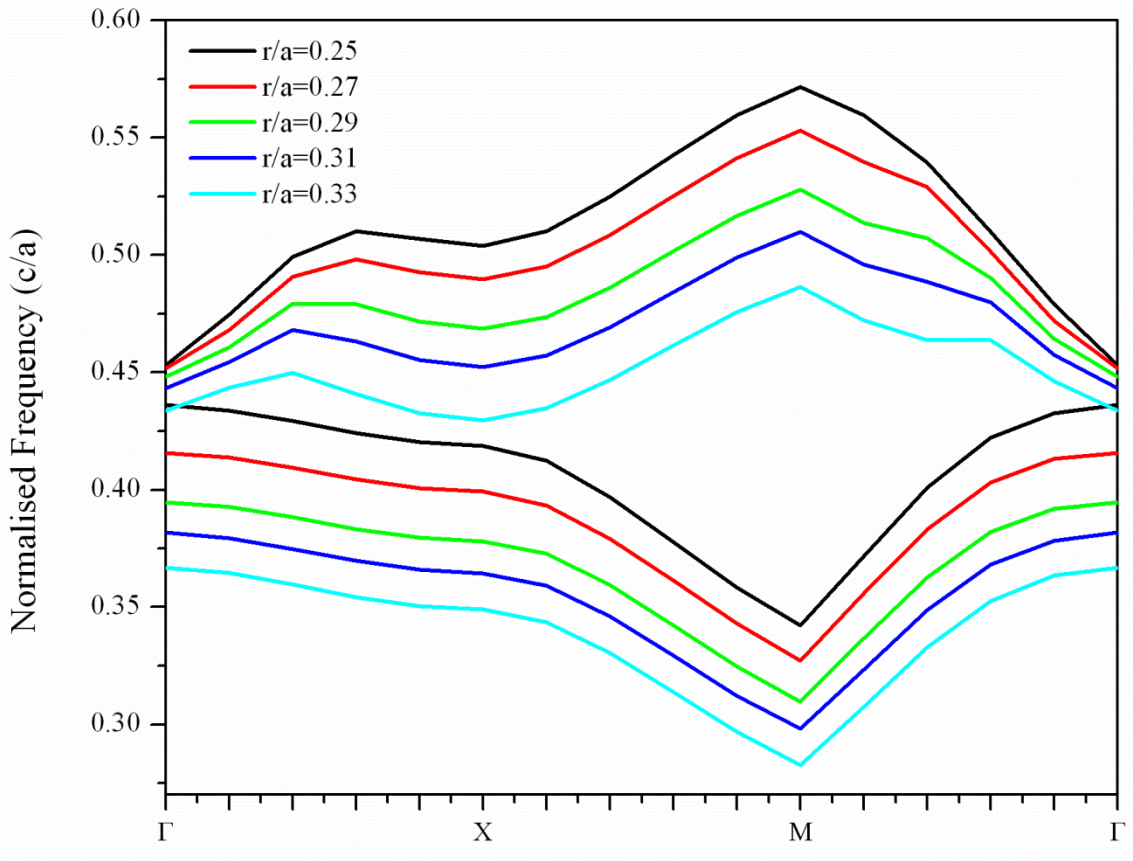

Figure 3-19: The 3rd (lower) and 4th (upper) bands are shown as a function of variation in *r/a*. At the largest *r/a* value of 0.33 the density of states for the 4th band are not localised to the Γ-direction as a dip in the band in the X direction intersects the frequency at which the 4th band intersects the Γ-direction. At the minimum *r/a* value of 0.25, the band gap separation becomes very small. The optimum *r/a* value was found to be 0.29.

The resulting optimised band structure derived using a 2D PWE method for a Si/YF_3:Er 2D photonic crystal is shown in Figure 3-20. The 3rd and 4th bands of the TM polarisation exhibit a large complete photonic band gap, with a good localization of states in the 4th band in the Γ-direction. The electric field distribution of the 4th band (bold line) in the Γ-direction reveals a high overlap of the electromagnetic field with the up-converting layer in the (red) space between the (black edged) Si pillars.

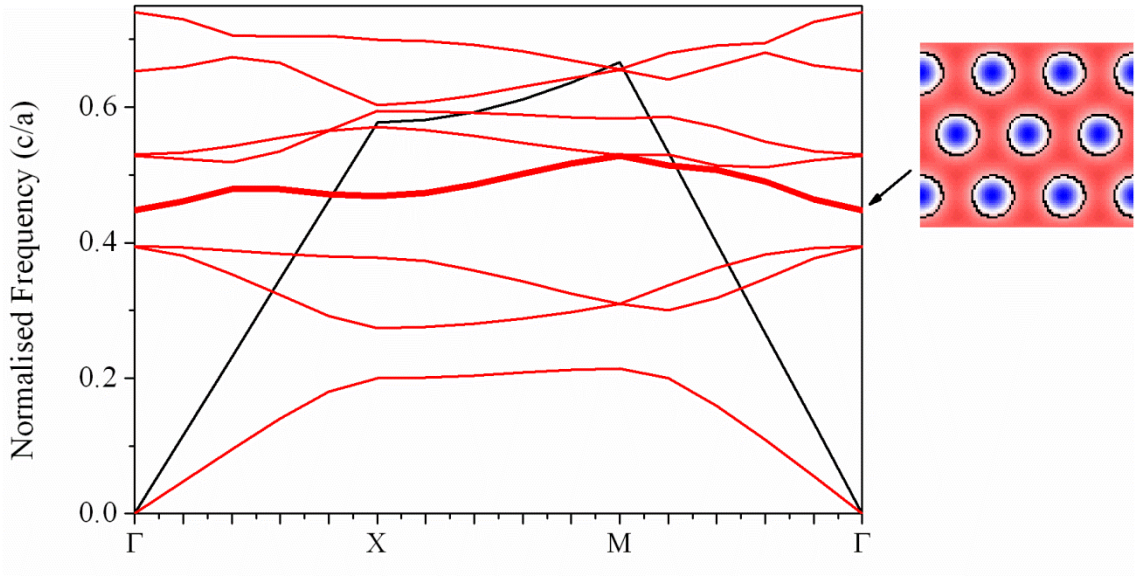

Figure 3-20: The optimised band structure for a 2D photonic crystal of Si/YF_3:Er. The electromagnetic field distribution of the 4th band (bold line) in the Γ-direction reveals a good overlap of the field with the up-converting YF_3:Er medium shown in red.

The normalised frequency at which the 4th band overlaps the Γ-direction is 0.448 c/a. Therefore the lattice constant *a* and pillar radius *r* can be found to align the wavelengths of interest (1523 nm and 980 nm) with the 4th band edge in the Γ-direction, using the method outlined in section 3.4.5. The resulting parameters, shown in Table 3-2, were used as the starting point for the fabrication of the 2D photonic crystal structures in Chapter 6.

Wavelength to Enhance (nm)	Pillar Radius (nm)	Lattice Constant (nm)
980	127	439
1523	198	682

Table 3-2: The hole radius (*r*) and lattice constant (*a*) for the optimised triangular array of Si pillars surrounded by YF_3:Er for locating the flat band edge of the 4th photonic band in the Γ-direction to 980 nm and 1523 nm respectively.

3.6 Conclusion of Simulations

Plane wave expansion and finite difference time domain simulations were carried out to explore the properties of 2D photonic crystals and to optimise the geometrical parameters for the fabrication of photonic crystals of TiO_2:Er/air and Si/YF_3:Er. PWE provided a fast and convenient way of simulating photonic band diagrams, from which the geometrical parameters could be tuned to locate a particular feature of the band gap geometry at a specified wavelength. The PWE simulations also allowed for the prediction of the

electromagnetic field distribution at a particular normalised frequency and direction in k-space to be determined. Time consuming FDTD simulations were carried out to validate the PWE results and to provide further information on the propagation of the electromagnetic mode in time.

The 2D photonic crystal band diagrams were optimised for locating a discrete flat band edge in the Γ-direction, showing good overlap of the electromagnetic field with the up-conversion medium, with the wavelengths of interest. Triangular lattices of pillars were found to be the optimum structure for both the TiO_2:Er/air photonic crystal (pillars of TiO2:Er) and the Si/YF_3:Er photonic crystal (pillars of Si). These results were based on measured refractive indices of TiO_2 and YF_3:Er carried out in later chapters of this study. The resulting pillar radii and lattice constant for the size and spacing of the pillars were determined for the wavelengths of 980 nm and 1523 nm, corresponding to the centers of excitation and emission of tri-valent erbium. These geometries would be used in the fabrication of the 2D photonic crystals described in Chapter 5 and Chapter 6.

3.7 References

1. S. Johnson, and J. Joannopoulos, "Block-iterative frequency-domain methods for Maxwell's equations in a planewave basis," Optics Express **8**, 173-190 (2001).
2. A. F. Oskooi, D. Roundy, M. Ibanescu, P. Bermel, J. D. Joannopoulos, and S. G. Johnson, "Meep: A flexible free-software package for electromagnetic simulations by the FDTD method," Computer Physics Communications **181**, 687-702 (2010).
3. J. D. J. Joannopoulos, S. G. Winn, J. N. Meade, R. D. , *Photonic Crystals Molding the Flow of Light* (Princeton University Press, 2008).
4. "MPB Introduction," (2008), http://ab-initio.mit.edu/wiki/index.php/MPB_Introduction, Accessed 22.02.15.
5. C. Hanson, "MIT Scheme Release 7.5," (1969), https://groups.csail.mit.edu/mac/ftpdir/scheme-7.5/22.02.15.
6. S. G. Johnson, S. Fan, P. R. Villeneuve, J. D. Joannopoulos, and L. A. Kolodziejski, "Guided modes in photonic crystal slabs," Physical Review B **60**, 5751-5758 (1999).
7. E. Chow, S. Y. Lin, S. G. Johnson, P. R. Villeneuve, J. D. Joannopoulos, J. R. Wendt, G. A. Vawter, W. Zubrzycki, H. Hou, and A. Alleman, "Three-dimensional control of light in a two-dimensional photonic crystal slab," Nature **407**, 983-986 (2000).
8. S. Kim, S. Ahn, J. Lee, H. Jeon, P. Regreny, C. Seassal, E. Augendre, and L. Di Cioccio, "Milliwatt-level fiber-coupled laser power from photonic crystal band-edge laser," Optics Express **19**, 2105-2110 (2011).
9. H.-Y. Ryu, S.-H. Kwon, Y.-J. Lee, Y.-H. Lee, and J.-S. Kim, "Very-low-threshold photonic band-edge lasers from free-standing triangular photonic crystal slabs," Applied Physics Letters **80**, 3476-3478 (2002).
10. J. R. Devore, "Refractive indices of rutile and sphalerite," Journal of the Optical Society of America **41**, 416-419 (1951).
11. B. Bakir, C. Seassal, X. Letartre, P. Viktorovitch, M. Zussy, L. Di Cioccio, and J. M. Fedeli, "Surface-emitting microlaser combining two-dimensional photonic crystal membrane and vertical Bragg mirror," Applied Physics Letters **88** (2006).
12. K. Sunghwan, L. Jeongkug, J. Heonsu, and K. Hyo Jin, "Fiber-coupled surface-emitting photonic crystal band edge laser for biochemical sensor applications," Applied Physics Letters **94**, 133503-133503-133503 (2009).

13. M. A. Green, "Self-consistent optical parameters of intrinsic silicon at 300K including temperature coefficients," Solar Energy Materials and Solar Cells **92**, 1305-1310 (2008).

Chapter 4 - Materials and Methods

4.1 Overview of Materials and Methods

In this chapter, the fabrication techniques and characterisation methods used in this work are presented. A wide range of equipment was required for the fabrication of the nanoscale structures, most of which were shared resources within the department. Characterisation of the materials produced was essential at every stage to understand where improvements could be made and to feed back into the simulation models to predict more accurate results. Where a deeper understanding of the techniques were required were required to carry out the work in this study (e.g. Reactive Ion Etching and Ellipsometry), a more detailed description of the technique is presented for reference in later sections. The novel aspects of adaptations to equipment and methodologies are presented in the experimental results chapters: Chapters 5-7.

4.2 Fabrication Techniques

A range of advanced fabrication techniques were required to prepare 1D and 2D nanoscale features for a range of organic and inorganic materials. Details of the techniques used and brief introductions to the physical and chemical concepts underpinning the techniques are provided where required. A schematic representation of the general fabrication procedure to prepare thin films of 2D photonic crystals is shown in Figure 4-1, along with the associated fabrication techniques that are discussed in this Chapter. The one fabrication technique that is not represented in the general fabrication procedure diagram is Focused Ion Beam Etching, which does not require the addition of a mask before the etching of the thin film can be carried out.

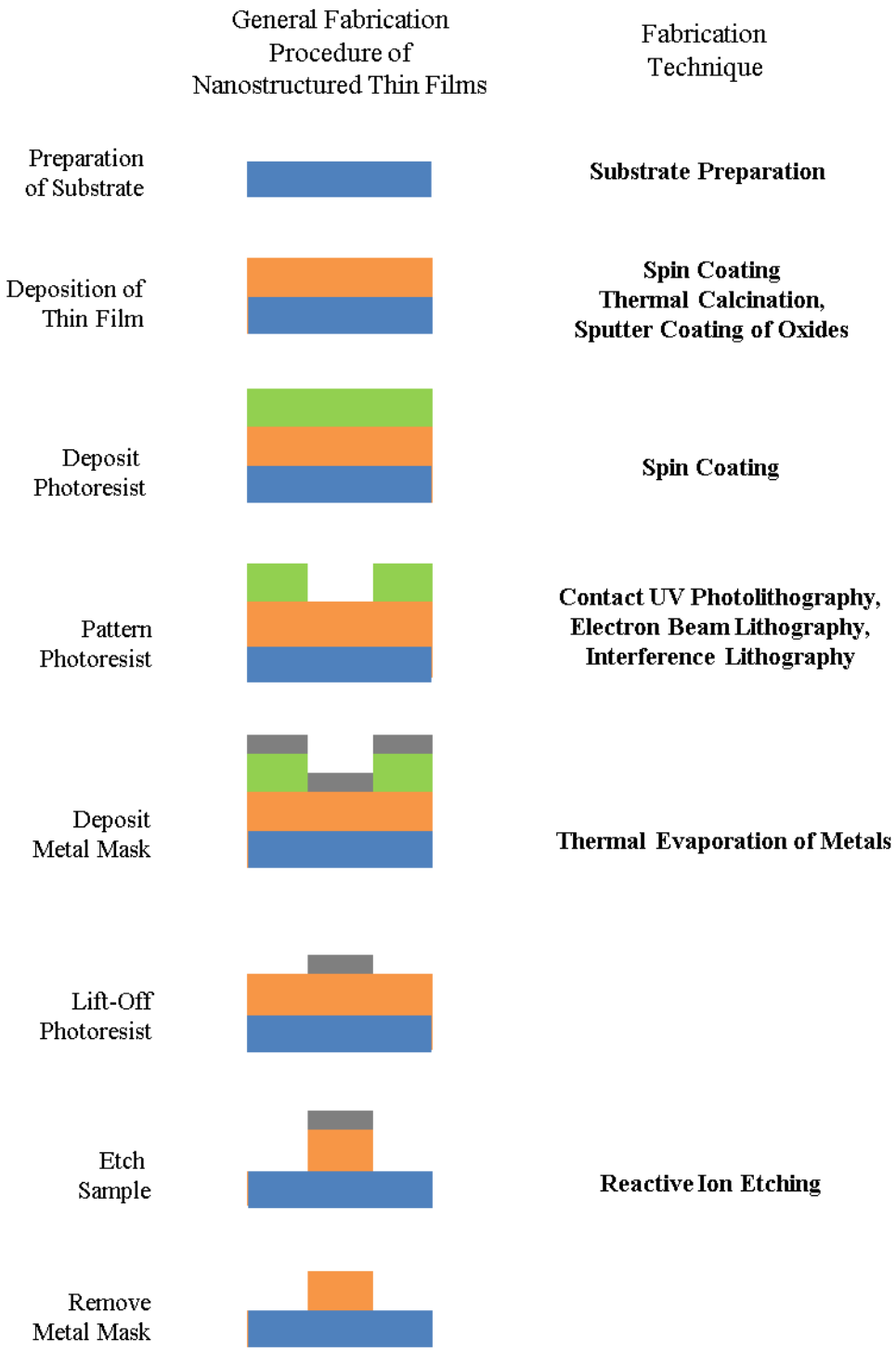

Figure 4-1: The general fabrication procedure used for fabricating the nanostructured 2D photonic crystal thin film layers is shown, with a pictorial representation of the steps and the associated fabrication techniques.

4.2.1 Si Substrate Preparation

Si substrates were prepared using the standard RCA-1 (Radio Corporation of America) cleaning method [1]. This method is used to remove organic residue and films from Si wafers. New Si wafers were cut up into either 13 × 13 mm, or 10 × 10 mm squares for use in this work, therefore only contamination from organic residue or water marks from the diamond cutting saw were expected. RCA-1 cleaning leaves a very thin SiO_2 oxide layer (1-2 nm) on the surface of the Si wafer, which was not required to be removed for the work in this thesis as both TiO_2 and YF_3 have been reported elsewhere to be successfully deposited onto SiO_2 [2, 3].

4.2.2 SiO_2 and Microscope Slide Substrate Preparation

SiO_2 (pure fused silica) and microscope slide (70% SiO_2) substrates were prepared using a Hellmanex (Helma GmbH) cleaning method. The substrates were scrubbed using a soft brush with a 2% solution of Hellmanex in deionized water. The substrates were then rinsed for 10 minutes in sequential ultrasonic baths of deionized water, acetone and isopropanol. The substrates were blown dry with N_2 between each rinse.

4.2.3 Spin Coating

Spin coating was carried out using a SCS P6700 spin coater [4]. Samples were held in place using either a vacuum seal or custom build mounts. Uniform films were achieved by using a fast ramp rate and maintaining the desired rpm for 20-30 seconds. Accurate control of the thickness of the film, to around 10 nm, was achieved using this method (Figure 4-2). Film thickness uniformity deteriorated towards the edges of the sample. However due to the small sample areas used in this thesis (typically 30 μm × 30 μm) any macro-scale uniformity observed through spin coating did not affect the local thickness uniformity within the sample area.

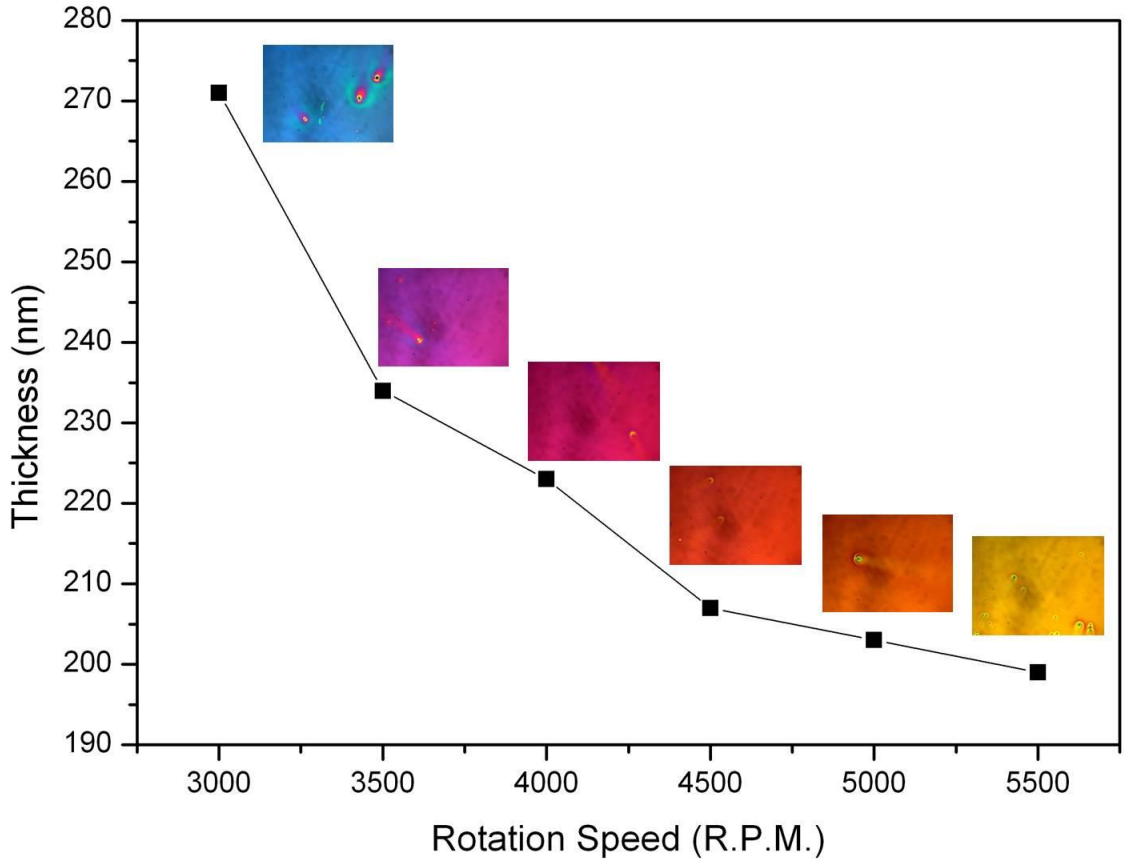

Figure 4-2: Control of the thickness of a thin film during spin coating is achieved by varying the rotational speed. The change in colour of the resulting films (of UV photoresist shown here) with thickness is clearly observed.

4.2.4 Thermal Calcination

Calcination is the process by which materials are heated in air (or a specially controlled atmosphere) to bring about a change in the material's phase, or to remove a volatile component. This is as a result of oxidation, reduction, or another thermally processed treatment [5].

Calcination was carried out using the Carbolite MTF tube furnace [6] . This system was fitted with a Eurotherm controller to allow control of the ramp rate, dwell temperature and dwell time for 8 separate stages from room temperature to 1100°C. Samples were placed in porcelain combustion boats in the center of the tube. The furnace was kept in a fume cupboard for safe removal of any gases emitted during heating.

Calcination allowed for the phase of TiO_2 thin film layers to be accurately controlled. In Figure 4-3 the change in phase from amorphous to a mixture of anatase and rutile is clearly observed as a result of a change in calcination temperature of 500°C and 1000°C

respectively. Further details of the preparation and calcination of TiO_2 thin films is provided in section 5.2.4. Calcination provided a simple and effective solution for the variation of phase and resulting refractive index of TiO_2 for the work in this thesis.

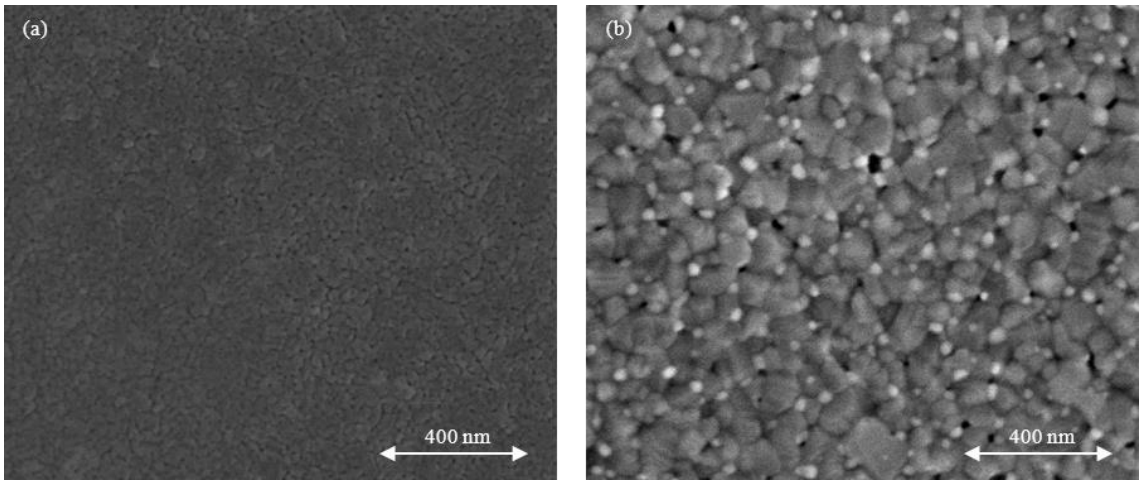

Figure 4-3: The SEM micrograph shows that the phase of TiO_2 could be varied by the process of calcination. (a) shows the dense homogeneous form of the amorphous phase (calcinated at 500°C), while (b) depicts a granular form associated with the anatase/rutile phase (calcinated at 1000°C).

4.2.5 Contact UV Photolithography

UV photolithography is the process in which ultraviolet light is used to expose an unmasked area of a photosensitive material (photoresist). The solubility of the photoresist is changed in the exposed regions, allowing for selective developing in a solvent solution.

Contact UV photolithography was carried out using a glass plate with a Cr mask of rectangular features of around 100 μm in width. A positive tone photoresist ma-P 1215 (Microresist Technology) was spin coated at 3000 rpm to provide a layer of around 1500 μm in thickness. Prior to exposure, the samples were pre-baked on a hotplate at 100°C for 90 s to remove any remaining solvent. The samples were exposed to ultraviolet light using a UVP CL-1000 cross-linker. Development of the resist was carried out using a ma-D 331 (Microresist Technology) developer. Samples were immersed in the developer for 30 s before being rinsed in deionized water and blown dry with N_2 gas.

4.2.6 Electron Beam Lithography

Electron beam lithography allows for features of around 10 nm or greater to be created in a photoresist [7]. A focused beam of electrons is scanned across the photoresist to change its solubility. This allows for selective developing in a solvent solution.

Electron beam lithography was performed by Dr Jose Marques-Hueso using a Raith Pioneer system to pattern features into a PMMA (MICROCHEM) positive tone photoresist. This photoresist is capable of achieving 0.1 nm resolution for high source voltages [8]. The lithography was carried out using a 30 kV source of around 0.2 nA at a 10.3 mm working distance. The PMMA samples were pre-baked before exposure on a hot plate at 180°C for 90 s to remove any excess solvent. The development of the photoresist was achieved by immersing the samples in a solution of 1:3 methyl isobutyl ketone to isopropanol for 30 s. The samples were then immersed in a stopper solution of isopropanol for a further 30 s before blow drying with air.

A triangular array of holes in a PMMA photoresist layer following development is shown in Figure 4-4. The dielectric nature of both the PMMA layer and the TiO_2 substrate below means that the image of the scanning electron microscope is a little blurry due to charging effects. However the granular TiO_2 layer is clearly visible below the regular array of well-defined electron beam exposed holes in the PMMA. The electron beam lithography system and PMMA photoresist therefore provided the required resolution and repeatability for the work in this thesis.

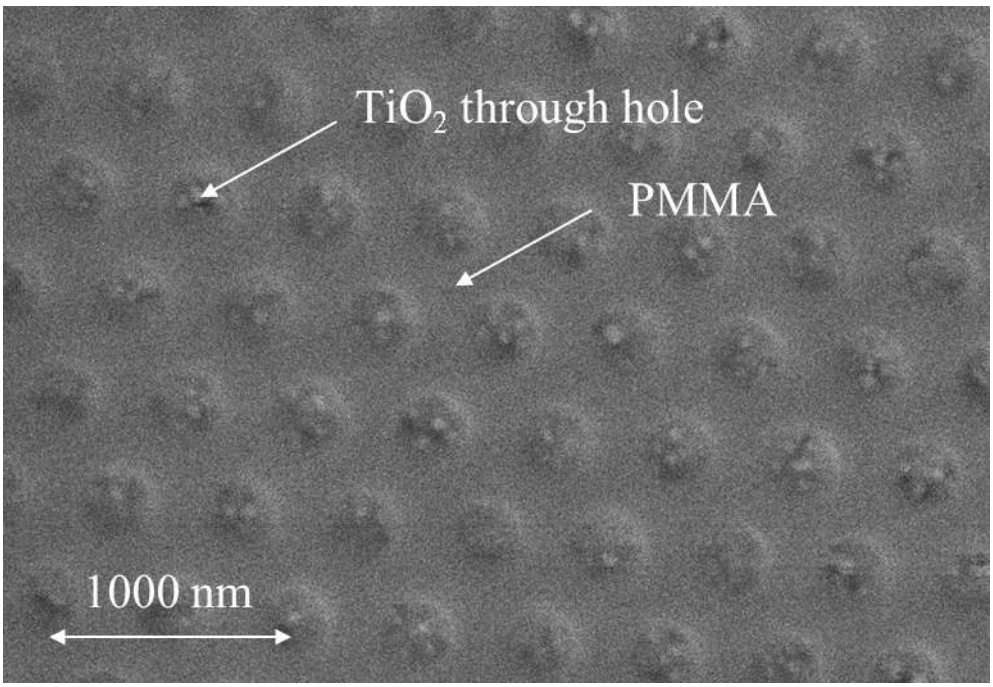

Figure 4-4: SEM micrograph. A regular array of holes in the PMMA top layer is observed, with the granular TiO_2 layer visible below.

4.2.7 Inductively Coupled Plasma Reactive Ion Etching (ICP-RIE)

Reactive ion etching is the process by which high energy ions and radical species are produced in a plasma to provide a selective etch. A glow discharge is formed by applying an RF voltage across the plasma. The RF voltage is required due to the often insulating nature of the sample surface (photoresist, SiO_2, TiO_2), which would not sustain a DC bias [9]. The boundary region between the plasma and the substrate surface of the sample is known as the sheath. Substantial electric fields develop across the sheath due to the higher loss of negative electrons than positive ions to the reactor wall, which results in the directed acceleration of positive ions towards the sample surface. Due to the directional acceleration of positive ions and isotropic nature of the electron flux, charging is a common effect leading to feature profile distortions. Neutral radicals are also formed in the plasma, which lead to isotropic etching [9].

Inductively coupled plasma reactive ion etchers include a coil of current that induces a time varying magnetic flux in the gas. Electrons absorb energy from this field, however the field does not propagate into the plasma as it is absorbed quickly by plasma electrons. The increased electron energy in the gas results in a higher ion flux in the plasma, therefore high ion densities at low pressures can be achieved [9].

The etching characteristics of reactive ion etching result from the combination of spontaneous etching from radical ions and the kinetic sputtering from ion bombardment. A reactive layer is formed at the surface of the sample, due to the adsorption of the radical species. Ion bombardment acts to improve the penetration of the radical species below the layer surface, while the radical species weaken the bonding at the sample surface resulting in higher sputter rates. Therefore a much higher rate of etching is achieved due to the synergy of the two etching processes [9, 10]. Reactive ion etching requires that all of the elements in the compound being etched can form volatile species with the reactive gas plasma.

Inductively coupled plasma reactive ion etching was carried out using the Oxford Instruments PlasmalabSystem 100. Samples were placed on a 4 inch carrier wafer (carbon or silicon) before being transferred to the reaction chamber through the evacuated loading bay. A mass flow controller was used to control the rate of flow of gas (Ar, CHF_3, O_2, SF_6, $SiCl_4$) to the chamber.

The results of a controlled etch to achieve tapered silicon pillars, fabricated using ICP-RIE, is shown in Figure 4-5. These structures were achieved as part of a set of etches carried out in this thesis to characterise the anisotropy of the silicon etch process (section 6.3). The chromium hard masks used for this etch were prepared using thermal evaporation (section 4.2.8).

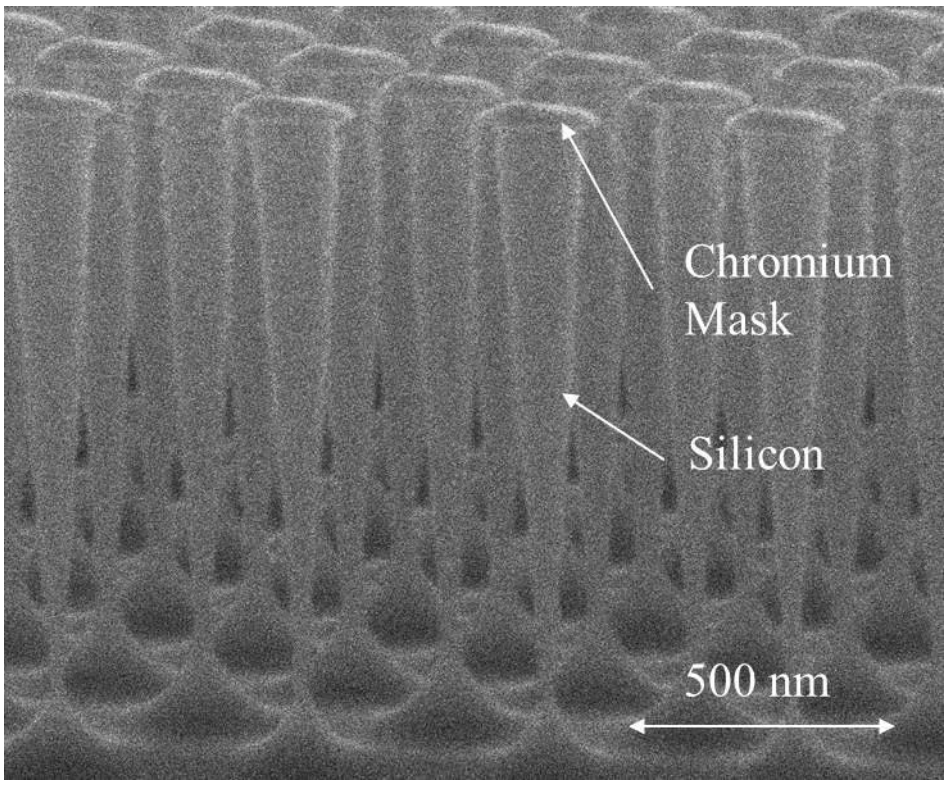

Figure 4-5: SEM micrograph. ICP-RIE allowed for controlled fabrication of nanostructures. Tapered pillars of silicon are shown along with the chromium hard masks still intact.

4.2.8 Thermal Evaporation of Metals

Thermal evaporation is the process by which a source material is heated to evaporation, through resistive heating of a filament, and condenses on a substrate in a thin layer [11]. The evaporation is carried out in a vacuum to allow the evaporated material to travel directly to the substrate without colliding with a background gas, and to minimise the effect of undesired reactions of the source material (e.g. oxidation).

The thermal evaporation of metals was carried out using an Edwards Coating System E306A. For the evaporation of aluminium a tungsten coil filament was used, whereas for the evaporation of chromium (sublimation) a coiled basket filament was used. The thickness of the deposited film was measured during the evaporation using an Edwards FTM4 film thickness monitor to measure the oscillation period of a water cooled quartz crystal.

4.2.9 Sputter Coating of Oxides

Sputter coating is the process by which high energy ions are directionally accelerated onto a source target, resulting in the ejection of source material that condenses on the surface of a substrate [11]. The acceleration of ions is controlled by an RF field. Halogen gases such as Ar are commonly used due to their inert chemical nature and large atomic size. Sputtering is carried out in a vacuum to allow directional travel and avoid undesired chemical reactions.

The sputter coating of SiO_2 and TiO_2 thin films was carried out in an Edwards Auto 306 Vacuum Coater. The source targets were held in place on top of the magnetron using stainless steel clamps, where each target material had its own set of clamps to avoid cross-contamination. Ar was used as the sputtering gas at pressures of around 1×10^{-4} mBar.

4.2.10 Focused Ion Beam Etching

Focused ion beam etching is the process in which a focused beam of ions is used for the ablation of material by the process of sputtering [12]. Liquid-metal ion sources are typically used in conjunction with a tungstan needle to cause ionization and field emission of the source atoms. As it is a purely physical process, redeposition of the sputtered material can occur.

The focused ion beam etching was carried out using a Quanta 3D FEG SEM/FIB system. A Ga liquid metal ion source was used for the etching, resulting in a resolution of 7 nm at 30 kV.. A platinum deposition needle was used to produce localised thin films of platinum to reduce the effects of charging.

A scanning electron micrograph of a trench fabricated using focused ion beam etching is shown in Figure 4-6. The trench allowed for cross-sectional images of the holes to be observed. Focused ion beam etching was employed in the work of this thesis to both directly fabricate photonic crystal structures, in addition to fabricating trenches for cross-sectional analysis (Chapters 5 and 6).

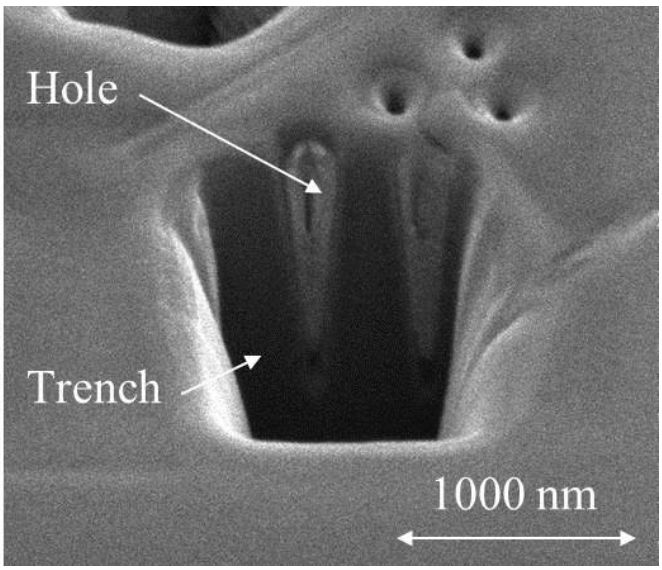

Figure 4-6: SEM micrograph. A trench was fabricated in the top surface of a layer of TiO_2 using FIB to allow the observation of the cross sectional features of the holes.

4.2.11 Interference Lithography

Interference lithography is a technique to allow the large scale patterning of regular arrays of features. This is achieved using the variation in intensity due to the interference between multiple beams of coherent light, without the need of complex optical systems or masks [13].

An interference lithography system was designed and built to allow the demonstration of fabrication of nanoscale arrays of pillars or holes to be achieved over large areas for industrial use. The details of this system are described in Appendix D.

4.3 Characterisation

A range of advanced characterisation techniques were required to analyse the materials and nanoscale features fabricated. Details of the systems used and brief introductions to the concepts underpinning the techniques used are provided where required. Specific adaptations required for this work are presented.

4.3.1 Variable Angle Surface Ellipsometry

Ellipsometry is a sensitive measurement technique that uses the change in polarization of light to characterise thin films. The sensitivity is derived from the measurement of the relative phase change of a beam of reflected light, which is very much greater than the sensitivity of reflected intensity measurements. Ellipsometry is also more accurate than

reflected intensity measurements as the absolute intensity is not measured, therefore no special reference material is required [14].

The values measured are expressed as Ψ and Δ and are related to the ratio of the Fresnel coefficients $\tilde{R}_p$ and $\tilde{R}_s$ for p- and s-polarised light respectively as [15]:

$$\frac{R_p}{R_s} = \tan(\psi)e^{i\Delta} \tag{4.1}$$

The addition of variable angles of incidence and measurements at more than one wavelength allows for both the angles of incidence and spectral acquisition range to be optimised for particular samples and sample parameters. Ellipsometry is most effective when the wavelength of light used is just smaller or larger than the film thickness. It also works best when the roughness of the sample surface is less than around 10% of the probe beam wavelength. Furthermore, the thickness uniformity should not vary by more than around 10% in the sample area illuminated [15].

Ellipsometry provides very high precision measurements, however the accuracy cannot be quantified without measurements from a system of comparable precision. If the model developed to fit the experimental data is unique, and therefore does not contain strongly correlated parameters, the results of the model will be very precise as well. Ellipsometry results are constantly checked against results from other techniques in the literature and are found to be accurate, which provides confidence in the accuracy of the work carried out in this study. Although there is no general method for calculating the accuracy of ellipsometry, a recent study proposing to quantify the accuracy concluded that a dual rotating compensator ellipsometer (analogous to the one used in this thesis) was greater than 0.1% [16].

The ellipsometry measurements for this work were carried out using a V-VASE (J.A. Woollam) variable angle spectroscopic ellipsometer. Measurements were acquired over the full spectral range of 300-2500 nm and at angles of 65, 70 and 75°. The measurements were taken using zone averaging, which meant that the data was averaged from that acquired with the input polarizer positioned in each of the four quadrants, which helped to eliminate any systematic errors from polarizer calibration offset.

The modelling of the ellipsometric data was performed using WVASE®, the software package designed by the J.A. Woollam company. Transparent (non-absorbing) regions of the refractive index were modelled as a function of wavelength using a Cauchy dispersion

model. The complete modelling of both transparent and absorbing regions of the refractive index required a more complex generalised oscillator model. Both models are briefly described below.

The Cauchy equation is an empirical relationship between the refractive index of a material and the wavelength of light incident on the material. The equation is commonly truncated to the first three terms for use with ellipsometry modelling, as shown below:

$$n(\lambda) = A + \frac{B}{\lambda^2} + \frac{C}{\lambda^4} \tag{4.2}$$

where *n* is the real component of the refractive index, λ is the wavelength and *A*, *B* and *C* are constants determined experimentally [15]. *A* sets the dispersion range, while *B* and *C* give the dispersion shape. The imaginary component of the refractive index, *k*, is equal to zero for transparent films.

The generalised oscillator (Genosc) models the dielectric function as a linear sum of the real and complex oscillator terms. Every Genosc layer consists of two Pole oscillators and an offset ($e1$). Additional oscillators (Gaussian, Drude and Tauc-Lorentz) are added to account for absorption where required [15]. The forms of the Pole oscillators and additional oscillators used in this work are detailed below.

Pole 1:

$$\varepsilon_{n\_pole} = \frac{A_n . E_n}{E_n^2 - E^2} \tag{4.3}$$

Pole 2:

$$\varepsilon_{n\_pole} = \frac{A_n . E_n^2}{E_n^2 - E^2} \tag{4.4}$$

Where ε_n is the dielectric constant, E_n is the oscillator peak position, A_n is oscillator magnitude and *E* is the energy in eV.

Gaussian:

$$\varepsilon_{n\_gaussian} = \varepsilon_{n1} + i\varepsilon_{n2} \tag{4.5}$$

$$\varepsilon_{n2} = A_n e^{-\left(\frac{E-E_n}{\sigma}\right)^2} - A_n e^{-\left(\frac{E+E_n}{\sigma}\right)^2}$$

$$\sigma = \frac{Br_n}{2\sqrt{ln2}}$$

Where Br_n is the oscillator broadening (FWHM). Further information on the structure of ε_{n1} is described by Woollam [15].

Drude:

$$\varepsilon_{n\_rtDrd} = \frac{-\hbar^2}{\varepsilon_0 \rho_n (\tau_n . E^2 + i\hbar E)} \tag{4.6}$$

$$\rho_n = \frac{m^*}{N_n q^2 \tau_n} = \frac{1}{q\mu N}$$

Where the carrier effective mass m^*=1, the carrier concentration N=1.35×10^{20} cm^{-3}, the carrier mobility μ=405.59 cm^{2}V^{-1}s^{-1} and the single electron charge q=1.6×10^{-19}. τ_n is the scattering time in seconds. $\hbar$ = Plank's Constant/π, ε_0 is the vacuum dielectric constant and E is the oscillator peak position.

Tauc-Lorentz:

$$\varepsilon_{n\_T-L} = \varepsilon_{n1} + i\varepsilon_{n2} \tag{4.7}$$

$$\varepsilon_{n2} = \left[\frac{A_n Eo_n C_n (E-Eg_n)^2}{\left(E^2-Eo_n^2\right)^2 + C_n^2 E^2} . \frac{1}{E}\right] \quad \text{when } E > Eg_n$$

$$\varepsilon_{n2} = 0 \qquad \text{when } E \leq Eg_n$$

Where E_{0n} is the peak transition energy, E_{gn} is the band gap energy, C_n is a fitting parameter and A_n is the amplitude. Further information on the structure of ε_{n1} is described by Woollam [15].

During the modelling process, the key parameters of the oscillators used were allowed to vary to fit the model to the experimental data. The way in which these oscillators were added to the model, the order in which the parameters were varied and the inclusion of additional features (e.g. gradients, surface roughness, intermediate layers) were carried out in accordance with the procedure suggested by Pribil and Wagner [18].

4.3.2 Fluorescence Spectrometer with Confocal Microscope

Fluorospectroscopy is the process by which photons emitted by fluorescence are measured. Fluorescence is the emission of light from an electron in an excited singlet state following the absorption of energy from electromagnetic radiation. Emission happens very rapidly, with typical lifetimes in the order of 10 ns [19]. For this work, the absorption of light at 1523 nm and fluorescence up-converted emission at 980 nm were of particular interest.

Fluorescence measurements were carried out using an Edinburgh Instruments FLSP920 fluorescence spectrometer, in conjunction with a custom built confocal microscope. The microscope was required to excite and measure the fluorescence emitted from the 2D photonic crystal samples, which exhibited a patterned area of around 30 μm × 30 μm. The sample area was limited in size by the patterning time required by electron beam lithography. Imaging of the sample area was also required to accurately locate the excitation spot. The confocal microscope, built together with PhD colleague Mr Eliyas Mammo, is described below.

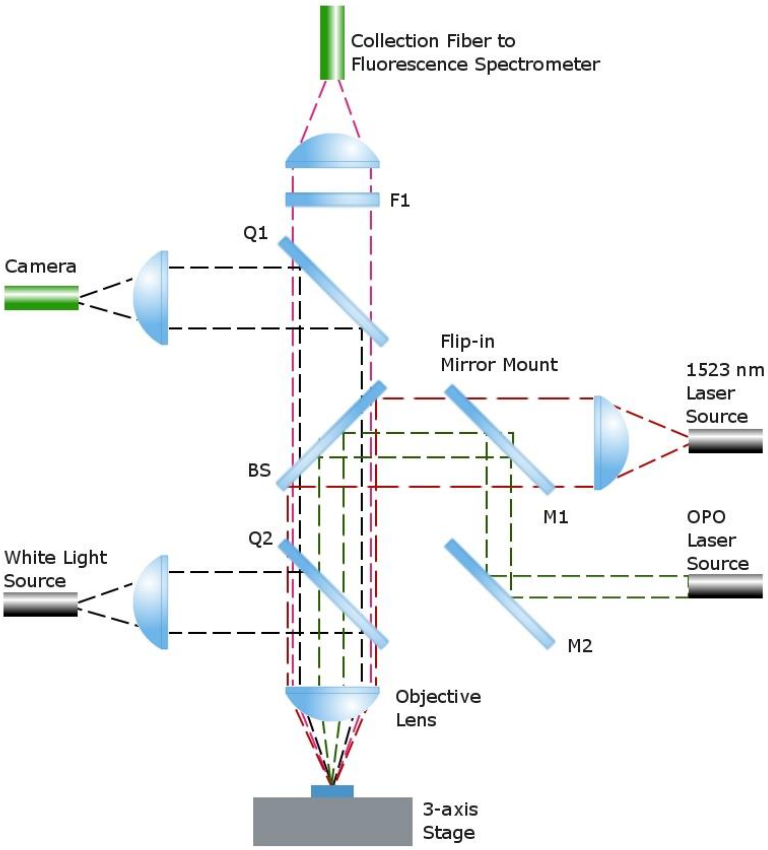

Figure 4-7: A confocal microscope was built as an addition to the Edinburgh Instruments FLSP920 fluorescence spectrometer to allow excitation at 1523 nm and collection at 980 nm from a 30 µm × 30 µm sample area.

A schematic diagram of the vertical confocal microscope setup is shown in Figure 4-7. A 1523 nm continuous laser source (HP Agilent 8168F) provided light for excitation. The light from the fiber was collimated, reflected off a hot mirror beam splitter (BS) and focused onto the sample using a 100× microscope objective lens. The theoretical spot size from the objective for 1523 nm light was calculated to be 2.83 µm. Pulsed laser excitation was supplied from an optical parametric oscillator (OPO) (GWU – VisIR 2) that was pumped using a pulsed NdYAG (Quanta-Ray INDI) laser of pulse duration 6-7 ns. A flip-in mirror mount was used to select the excitation source.

Positioning of the sample was carried out using a white light source, camera and 3-axis stage. The white light source was collimated, reflected off a quartz window (Q2) and focused onto the sample through the objective lens. The light reflected from the sample was focused onto a camera after reflecting off a second quartz window (Q1). The spot

position was found using a sample of 25% doped $NaYF_3$ that emitted a strong up-conversion signal at 550 nm when excited at 1523 nm. The green emission was large enough to be observed on the camera and the position was re-calibrated each time the system was turned on.

The emitted light was focused into a 1 mm core diameter multimode fiber and coupled into the entrance slit of the monochromator of the detection arm of the fluorescence spectrometer. The wavelength of interest was selected by a grating and detected using a photomultiplier tube and liquid nitrogen cooled infrared detector. The lamp synchronised TTL output from the NdYAG driver was used to provide the reference timing signal for sampling the detector counts for lifetime measurements using the pulsed excitation source (Appendix C).

A 1300 nm short pass filter was used to remove any reflected or fluorescent 1523 nm light that passed through the beam splitter. Non-integer harmonics of the monochromator gratings were found to result in a component of 1523 nm light scattering into the detector when the grating was positioned for 1014 nm, resulting in a signal count rate comparable to that being measured from the up-conversion emission. Therefore the short pass filter was required to remove the anomalous effect.

4.3.3 Absorption and Reflectance Spectrometry

Absorbance is a measure of the transition of electrons from an occupied ground state orbital to unoccupied orbitals of a higher energy state. Therefore the energy measured during absorbance spectrometry is the difference in energy between the ground and excited states [20].

Absorbance measurements were carried out using a Perkin Elmer Lambda 950 spectrometer. The spectral range of this system was from 200-2500 nm and data was acquired in steps of 1 nm, with a 0.5 nm excitation monochromator slit width. Measurements were taken with the samples placed in the center of a spectralon coated integrating sphere (150 mm diameter). Therefore the transmission (*Tr*), spectral reflectance (R_{sp}) and diffuse reflectance (R_d) were all detected simultaneously allowing for the absorbance (*Ab*) to be indirectly measured. The absorbance was calculated by the spectrometer as $Ab = -\log(Tr + R_{sp} + R_d)$.

4.3.4 X-Ray Diffraction Spectrometry

X-ray diffraction (XRD) is the process in which a crystalline array of atoms diffract a beam of x-rays in specific directions, which can be analysed to determine the size and shape of the atomic unit cell. The diffraction of x-rays results from both the scattering of individual atoms, as well as the interference between the waves scattered by the individual atoms [21]. The directions of diffraction and relative intensities are used to determine the electron density within the crystal.

XRD analysis was carried out using a powder diffractometer (Bruker D8 Advance), operating with Ge-monochromated Cu $K_{\alpha 1}$ radiation of wavelength 1.5406 Å. Data was collected over an angular range of 5-85 degrees in units of 2θ two theta for 30 minutes using a LynxEye linear detector. Theta is the angle of the incident x-ray beam as well as the angle of the diffracted x-ray beam, therefore the total angle between the incident and diffracted beam is two theta. This system was used to measure both powder and thin film samples: the latter were prepared on amorphous silica substrates.

4.3.5 Profilometry

Contact profilometry (Mechanical Stylus Profilometry) is the process in which the surface roughness, or small feature step heights of a sample is measured by scanning a diamond stylus across a sample's surface [22]. The contact force between the stylus and surface is set and the profilometer measures the small variations in vertical displacement as a function of position. The resolution is controlled by the scan speed and data sampling rate and is sub-nanometer in the vertical direction.

Contact profilometry was carried out using a Dektak profilometer. No sample preparation was required and the measurements were carried out along a single specified line. Samples with very soft polymer layers were sometimes found to be scratched by the stylus and so were not suitable for measurement.

4.3.6 Scanning Electron Microscopy

Scanning electron microscopy is the process in which a focused beam of electrons is scanned across a sample to provide information on the sample topology and composition. The electrons interact with atoms at or near the sample surface and the inelastic scattered electrons are detected using a secondary electron detector, which is the most common method of detection. The wide depth of field and manipulation of the sample position and

rotation allows for 3D analysis of the sample to be carried out. The difference in the electron density of different atoms and compounds provides a contrast in the scattered electron density that can be used to distinguish between adjacent materials [23].

SEM analysis was carried out using a Quanta 3D FEG SEM/FIB system with a secondary electron detector. The resulting resolution of the system operating in high vacuum with the secondary electron detector ranges from 1.2 nm at 30 kV to 2.9 nm at 1 kV. The samples for this work did not require any additional conductive coatings for analysis. Analysis was carried out using a 5 kV beam under high vacuum conditions.

The scanning electron microscope provided the required resolution to accurately image the nanostructures fabricated for this thesis. A scanning electron micrograph of the cross-section of a 2D photonic crystal of pillars of silicon and erbium doped yttrium fluoride (YF_3:Er) is shown in Figure 4-8. The effects of charging are limited and the underlying crystalline structure of the YF_3:Er is visible. Therefore this system provided the necessary resolution required to accurately analyse the nanostructures of interest. The analysis of the Si/YF_3:Er 2D photonic crystals is carried out in Chapter 6.

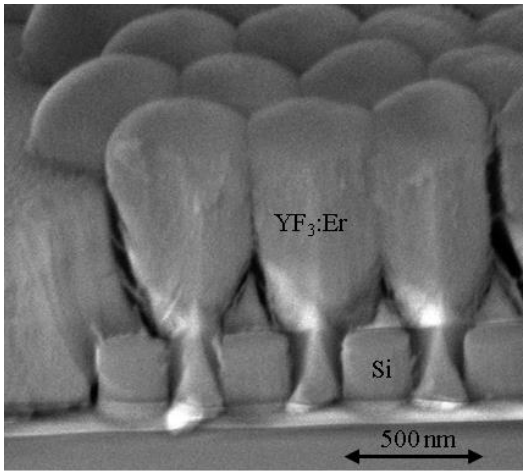

Figure 4-8: The scanning electron micrograph depicts the cross section of a 2D photonic crystal of silicon pillars and YF_3:Er. The resolution of the scanning electron microscope is high enough to accurately analyse the features of interest for the work in this thesis.

4.3.7 4-Point Probe

A 4-point probe is used to measure conductivity. Four equally spaced tungsten probes are positioned in contact with the surface of a sample. A current is applied between the two outer probes and the resulting voltage is measured across the two inner probes; ideally without drawing any current [24]. The resistivity ρ is defined as:

$$\rho = \frac{1}{\sigma} = 2\pi a s \frac{V}{I} \tag{4.8}$$

where σ is the conductivity, a is the sample thickness correction factor, s is the probe pacing, V is the voltage and I is the current.

For sample thicknesses that are less than half of the probe spacing, the sample thickness correction factor becomes:

$$a = 0.72 \frac{t}{s} \tag{4.9}$$

where t is the sample thickness. Therefore the resistivity and conductivity can be calculated as [24]:

$$\rho = \frac{1}{\sigma} = 4.53 t \frac{V}{I} \tag{4.10}$$

Conductivity measurements were carried out using a K&S 30074-point probe, with a Kiethly 224 programmable current source and 160B digital multimeter. Five measurements were taken over a series of currents and the conductivity was obtained from the gradient of the linear fit of the plot of V vs I, as shown in Figure 4-9.

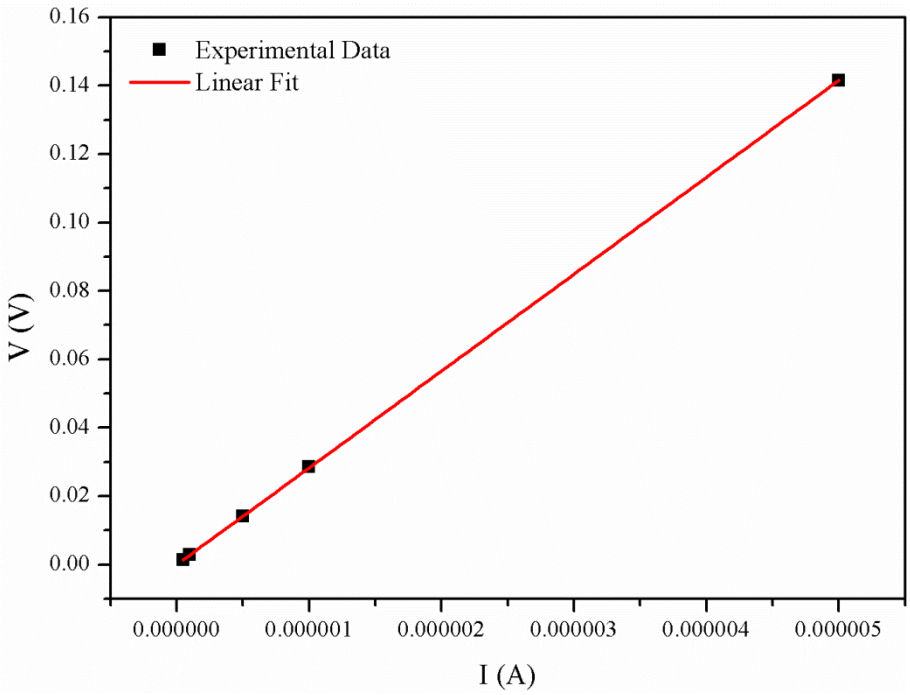

Figure 4-9: The voltage measured across the two inner probes was measured as a function of the current applied to the two outer probes. Measuring the gradient of the linear fit allowed for the

conductivity of the sample to be calculated. The experimental data shown here was used in the conductivity measurements discussed in section 7.3.

4.4 Conclusions of Materials and Methods

A wide range of fabrication and characterisation techniques were used to carry out the work in this study. Some of these systems were in good working order and could be used as found (e.g. profilometer and ICP-RIE), where the majority of time was spent on optimising fabrication conditions, or analysing data. Other systems were set up from scratch (e.g. interference lithography and confocal microscope), or required significant adaptations (thermal evaporation and ellipsometry analysis). Novel aspects of the equipment and techniques used are presented in Chapters 7-9.

4.5 References

1. Bachman, "RCA-1 Silicon Wafer Cleaning," (UCI Integrated Nanosystems Research Facility, The Unversity of California, Irvine, 1999).
2. E. L. Payrer, R. M. Almeida, C. Jimenez, P. D. Szkutnik, and J. L. Deschanvres, "Growth of lanthanide-doped YF3 thin films by pulsed liquid injection MOCVD: Influence of deposition parameters on film microstructure," Surface & Coatings Technology **230**, 22-27 (2013).
3. O. Setyawati, M. Engenhorst, S. Wittzack, F. Köhler, C. Woidt, T. Woit, V. Daneker, M. Bartels, and H. Hillmer, "Dry etching of TiO2/SiO2 DBR mirrors for tunable optical sensor arrays," (2010), pp. 75910R-75910R-75918.
4. "Speciality Coating Systems," (2014), http://scscoatings.com/equipment/spin_coating/index.aspx, Accessed 01.04.15.
5. J. J. McKetta, *Encyclopedia of Chemical Processing and Design: Volume 6 - Calcination Equipment to Catalysis* (Taylor & Francis, 1978).
6. Carbolite, "MTF - Wire Wound Single Zone Tube Furnaces," http://www.carbolite.com/products/furnaces/laboratory-tube-furnaces/mtf-wire-wound-tube-furnaces/function-features/, Accessed 01.04.15.
7. C. Vieu, F. Carcenac, A. Pepin, Y. Chen, M. Mejias, A. Lebib, L. Manin-Ferlazzo, L. Couraud, and H. Launois, "Electron beam lithography: resolution limits and applications," Applied Surface Science **164**, 111-117 (2000).
8. MICROCHEM, "NanoTM PMMA and Copolymer," (1254 Chestnut Street, Newton, MA, 02464, U.S.A).
9. G. Cunge, *Plasma etching and reactive ion etching: the fundamentals and applications* (CEI-Europe AB, 2013).
10. D. L. Flamm, "Mechanisms of silicon etching in fluorine-containing and chlorine-containing plasmas," Pure and Applied Chemistry **62**, 1709-1720 (1990).
11. K. K. Schuegraf, *Handbook of thin-film deposition processes and techniques: principles, methods, equipment, and applications* (Noyes Data Corporation/Noyes Publications, 1988).
12. L. A. Giannuzzi, and N. C. S. University, *Introduction to Focused Ion Beams: Instrumentation, Theory, Techniques and Practice* (Springer US, 2006).
13. M. Maldovan, and E. L. Thomas, *Periodic Materials and Interference Lithography: For Photonics, Phononics and Mechanics* (Wiley, 2009).

14. H. Fujiwara, *Spectroscopic Ellipsometry: Principles and Applications* (Wiley, 2007).
15. I. J. A. Woollam Co., *Guide to Using WVASE32 Spectroscopic Ellipsometry Data Acquisition and Analysis Software* (Lincoln, NE, 1994).
16. B. Johs, and C. M. Herzinger, "Quantifying the accuracy of ellipsometer systems," physica status solidi (c) **5**, 1031-1035 (2008).
17. A. S. Ferlauto, G. M. Ferreira, J. M. Pearce, C. R. Wronski, R. W. Collins, X. Deng, and G. Ganguly, "Analytical model for the optical functions of amorphous semiconductors from the near-infrared to ultraviolet: Applications in thin film photovoltaics," Journal of Applied Physics **92**, 2424-2436 (2002).
18. G. Pribil, and T. Wagner, *Woollam WVASE Training Course* (LOT-QuantumDesign, Darmstadt, 2013).
19. J. R. Lakowicz, *Principles of Fluorescence Spectroscopy* (Springer, 2007).
20. D. N. Sathyanarayana, *Electronic Absorption Spectroscopy and Related Techniques* (Universities Press, 2001).
21. A. Guinier, *X-ray Diffraction in Crystals, Imperfect Crystals, and Amorphous Bodies* (Dover, 1994).
22. A. F. von Recum, *Handbook Of Biomaterials Evaluation: Scientific, Technical And Clinical Testing Of Implant Materials, Second Edition* (Taylor & Francis, 1998).
23. A. Khursheed, *Scanning Electron Microscope Optics and Spectrometers* (World Scientific, 2011).
24. F. M. Smits, "Measurement of sheet resistivities with the four-point probe," Bell System Technical Journal, The **37**, 711-718 (1958).

Chapter 5 - Fabrication of TiO_2:Er 2D Photonic Crystals

5.1 Chapter Overview

In this chapter the fabrication and analysis of thin films and 2D photonic crystals of erbium doped titanium dioxide (TiO_2:Er) is presented. Both sol-gel and sputter deposition methods were investigated for the fabrication of TiO_2:Er thin films with the required optical and structural properties. Two etching methods, reactive ion etching and focused ion beam etching were investigated as suitable methods for fabricating 2D photonic crystals in the TiO_2:Er films. Measurements of the refractive index, performed using ellipsometry, were essential to determining the correct geometry of the 2D photonic crystal.

Thin films of TiO_2:Er were successfully prepared using both the sol-gel and sputter deposition methods. The refractive index was found to increase with annealing temperature, from 500°C to 1000°C. The refractive index at the top of the film annealed at 1000°C was found to be consistent with a mixed anatase/rutile phase, expected at this temperature. However, unexpectedly, the refractive index was found to vary significantly from the bottom to the top of the thin films for both annealing temperatures. For the film annealed at 1000°C, the refractive index was found to vary from 1.38 at the bottom to 2.32 at the top.

Measurement of the up-conversion emission at 980 nm, upon excitation at 1523 nm, was observed for films prepared by both deposition methods. However the sol-gel prepared film exhibiting emission was mechanically compromised, showing cracking and not suitable for patterning into a 2D photonic crystal. Thicker un-cracked films of TiO_2:Er were prepared using sputter deposition, however a thickness of 4500 nm was required to observe only a very small up-conversion emission of around 50% greater than the background count rate.

Reactive ion etching and focused ion beam etching were both investigated for use of fabricating the 2D photonic crystal patterns. However limitations in both techniques left them unsuitable for carrying out the deep anisotropic etch of 4500 nm required. It was concluded that available fabrication methods were not suitable for creating anisotropic 2D photonic crystals in TiO_2:Er to the required depths.

Therefore a different composition of materials to form the 2D photonic crystal were investigated: pillars of silicon surrounded by up-converting YF_3:Er. Anisotropic reactive ion etching of silicon has been studied extensively in literature due to its use in the microelectronics industry [1], while YF_3 has previously reported to be a good host for up-converting rare earth ions [2]. The results of this approach are reported in Chapter 6.

5.2 TiO_2:Er Thin Films by the Sol-Gel Method

There are several important properties of TiO_2 that make it a highly suitable material from which to create photonic crystal structures. Firstly, TiO_2 has a fairly large refractive index ($n>2.5$ for the anatase phase and $n>2.7$ for the rutile phase) [3], which is high enough to be able to form complete photonic band gaps [4]. Secondly, it has a very low thermal expansion coefficient of $7\text{-}9\times10^{-6}K^{-1}$ from room temperature up to 1000°C. This ensures that the critical geometrical properties of the photonic crystal do not change with environmental temperature fluctuations [4]. Finally, TiO_2 shows low absorption over a wide wavelength range including the near infrared [5]. Importantly for this work, TiO_2 can easily be doped with Er via the sol-gel method.

5.2.1 Chemical Synthesis and Deposition of TiO_2:Er Thin Films

The sol-gel method provides a straight forward method of controlled doping of TiO_2 with Er and deposition of thin films of the material by spin coating. The sol-gel method used was based on the conventional sol-gel process detailed by Nishide *et al*. [6]. An Er solution was prepared by dissolving 0.4 g of $Er(NO_3)_3$ into 2 ml of ethanol. An acid catalyst solution was prepared by adding 2.40 ml of 70% HNO_3 to 5.13 ml of H_2O, from which 0.06 ml were added to 1.20 ml of ethanol in a glass vial. The sol-gel was prepared by adding 0.60 ml of titanium tetra-isopropoxide (TTIP) dropwise to the acidified ethanol. This solution was stirred using a magnetic stirrer for 12 hours, before 0.50 ml of the Er solution were added to achieve 10% Er doping. After 2 hours of further stirring, the sol-gel (Figure 5-1) was ready to be used.

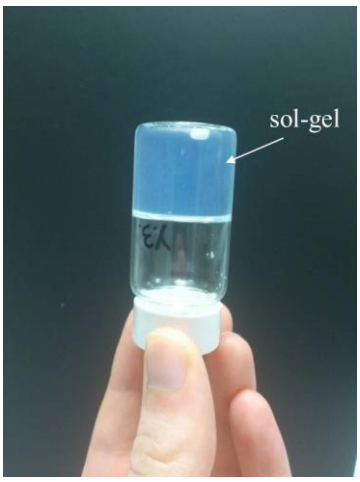

Figure 5-1: The sol-gel prepared was a semi-transparent gel, which held its shape upon inversion of the vial.

Deposition of thin films of the TiO_2:Er was achieved using spin coating. Samples were deposited by pipette onto 1.3 mm × 1.3 mm square Si wafers, which were cleaned using the procedure detailed in section 4.2.1. Any remaining sol-gel solution on the surface of the pipette tip was found to crystallise into particulates very rapidly, therefore the pipette tips could only be used once to avoid detrimental effects of particulates in the thin films.

On deposition of the thin films, the samples were calcified in ambient conditions to achieve the desired phase of TiO_2. The samples were calcified inside a tube furnace as described in section 4.2.4 for 2 hours at the desired temperature, with a ramp rate of 1°C/min. Three phases of TiO_2 can be achieved, depending on the final calcination temperature: amorphous (300°C), anatase (400-900°C) and rutile (>1100°C) [3]. At intermediate temperature, the film is likely to contain a multiphase structure.

5.2.2 Effects of Rotational Deposition Speed and Viscosity on Film Structural Properties

Thick films of TiO_2:Er were required to achieve a good representation of the simulated structures and to maximise the up-conversion signal emitted at 980 nm for detection. The simulations were performed in two dimensions, therefore the structure in direction perpendicular to the plane of the photonic crystal slab was assumed to extend unchanged to infinity. Therefore increasing the thickness of the layer improves the correlation between the simulated and experimental structures. It was expected that the thickness should be at least as thick as the repeating unit of the structures in the plane of the photonic crystal: therefore greater than around 1000 nm. The two main ways in which the film thickness can be varied using spin coating are by varying the rotational speed, or the

viscosity of the sol-gel. The viscosity can be varied by diluting the concentration of the sol-gel through the addition of ethanol to the stock solution. The depositions were carried out with both the sol-gel and substrate at room temperature to avoid temperature related changes to viscosity.

The film thickness was found to increase by a factor of 1.8 for a reduction in Ethanol volume per 0.1 ml of TTIP from 0.50 to 0.25, as shown in Figure 5-2. However it was found that films of greater than around 130 nm cracked during calcination. Films of less than 120 nm were found to retain their form during the calcination process. The formation of cracks above the 130 nm film thickness was found to occur for spin speeds for both 1600 and 2000 rpm.

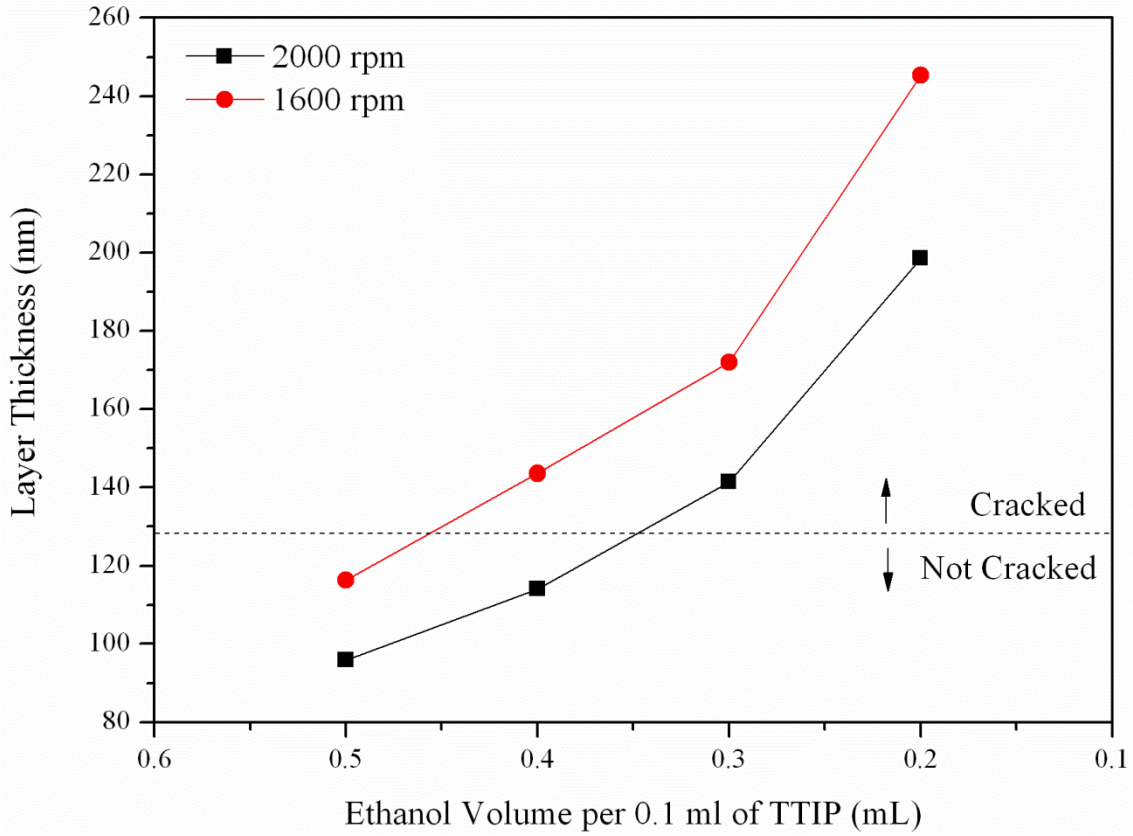

Figure 5-2: The cracking of the TiO_2 thin films was found to occur above a threshold thickness of around 130 nm, which was independent to the spin speed of deposition.

Cracking of the TiO_2:Er thin films was severely detrimental to the fabrication of the 2D photonic crystals. A photonic crystal of high quality factor requires homogeneous regions of constant refractive index, with clearly defined boundaries. Cracking would lead to internal variations within the refractive index of the TiO_2:Er film. The cracking in a thin film of TiO_2:Er is clearly observed in a microscope image of the thin film layer Figure 5-3.

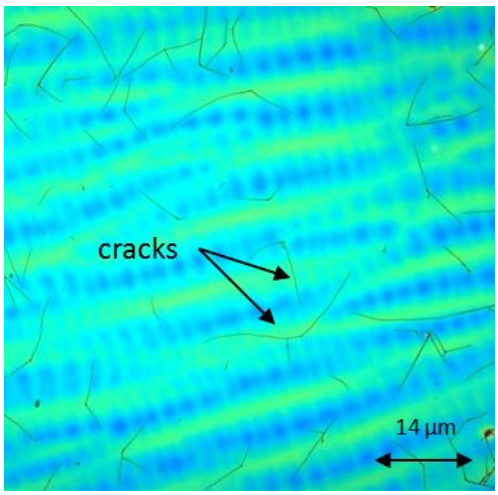

Figure 5-3: Cracking of the TiO_2:Er sol-gel spin coated films can be clearly seen in the optical microscope image.

The cracking was believed to be as a result of the evaporation of water, ethanol and the breakdown of other organic compounds during the initial heating of the films. Kao *et al.* demonstrated the loss of these compounds to be resulting in a 50% weight loss of sol-gel prepared TiO_2 films pyrolysed between 100-300°C [7]. Very thin films of TiO_2 allow for the rapid escape of water and organic gases from the film, while the TiO_2 is annealing. However the additional volume of gas required to escape from thicker films breaks through the newly formed TiO_2 crystal structure in order to escape, resulting in fissures and cracks in the thin film. Their maximum film thickness of 100 nm was found to be very similar to the maximum thickness of 130 nm observed in this work. It was not possible to observe any up-conversion at 980 nm from the 120 nm TiO_2:Er thin films, when excited at 1523 nm. Therefore thicker films were required in order to observe and enhance the up-conversion signal.

5.2.3 TiO_2:Er Film Stacking

Thicker films of homogenous TiO_2:Er using the sol-gel method can be prepared by multi-layer deposition, resulting in a series of stacked films. This is achieved by heat treating each film following deposition to remove any remaining organic compounds, before annealing the final multilayer stack to achieve the desired phase [7]. The heat treatment to degrade and remove the organic compounds was carried out at 325°C . The general fabrication technique for multilayer films of TiO_2:Er is as follows:

1. Spin coat TiO_2:Er sol-gel (0.4 ml Ethanol) at 1800 rpm for 30 s to give ~120 nm thick film

2. Heat treatment of the sample on hot plate at 325°C for 10 minutes
3. Cool the sample to room temperature
4. Spin coat the sample next layer of TiO_2:Er sol-gel at 1800 rpm for 30 s to give ~120 nm thick film
5. Repeat until desired layer thickness is achieved
6. Anneal film stack in tube furnace at desired temperature for 2 hours

Stacking of films using this method allowed for thicker films to be obtained. However, there was found to be a limit to the number of films that could be stacked together before cracking of any further layers was observed. The limit for the aforementioned fabrication conditions was found to be 5 layers, resulting in a total thickness of ~600 nm. Repeatability of un-cracked films was very poor: only around 1 in 6 film stacks were suitable for further analysis.

5.2.4 Structural Properties of Calcified TiO_2:Er Films

The change in phase associated with the final calcination temperature was also found to be accompanied by a change in the structural properties of the TiO_2:Er films. The calcification of the films at 500°C to achieve the anatase phase resulted in a smooth dense film with very small grains, as shown in Figure 5-4(a). The grains were measured to be 27±3 nm in diameter. However calcification of films at 1000°C to achieve the rutile phase was found to produce a film with much larger grains, as shown in Figure 5-4(b). These grains appeared to be separated into two distinct sets: large (darker) and small (lighter). The large grains were measured to be 94±16 nm, with the smaller grains 33±4 nm in diameter.

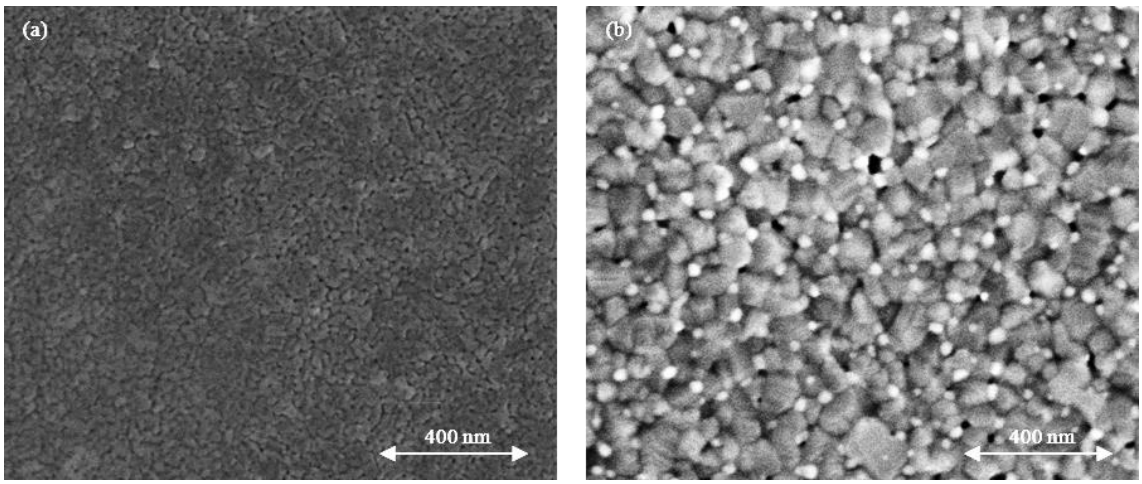

Figure 5-4: Scanning electron micrographs. (a) The TiO_2:Er film calcinated at 500°C to achieve the anatase phase reveals a dense structure with small interconnected grains. (b) The film annealed at 1000°C to achieve the rutile phase reveals much larger grains.

The granular structure observed for these films of TiO_2:Er is very similar to that observed previously by Kim *et al* [3]. The SEM results of their amorphous film, after annealing at 500°C, showed a homogeneous film that was analogous to the 500°C annealed film prepared in this study. Furthermore, their rutile structure that was prepared by annealing at 1000°C showed the same distinctive grain structure. Kim *et al* attribute these grains to an agglomerated state of secondary particles, where the density of the film increases with a further increase in calcination temperature due to the reduction in pores between adjacent grains [3]. These secondary particles all contain the primary crystalline structure of the rutile phase.

The sizes of the secondary particles measured for this thesis were found to differ from those reported by Kim *et al*. The secondary particles measured by Kim *et al* were found to be in the range of 150-300 nm in diameter, compared to the 94±16 nm measured for the films in this study, which is considerably smaller. Kim *et al* attribute the increasing grain size with annealing temperature to be due to accelerated sintering of the TiO_2 nanoparticles. The difference in the grain sizes between the two studies may be a result in the different catalysts used in the sol-gel preparation. Kim *et al* used an HCl catalyst, whereas HNO_3 was used in this study. The catalyst used in the preparation has been shown elsewhere to be influential in the temperature at which the phase change occurs upon calcination, however no direct comparison between HCl and HNO_3 was made [8]. Furthermore, the concentration of the catalyst has been shown by Ahn *et al* to play an important role in the grain size and temperature of phase transition of a sol-gel prepared TiO_2 layer [9].

The structural properties of the anatase film made it the preferred choice for use as a 2D photonic crystal. Although the anatase film was found to be granular, the grain sizes were very small compared to the wavelength of light of interest (980 nm, 1523 nm), therefore this film could be considered homogeneous with respect to the light. The rutile film, however, was found to consist of grains that were large compared to the wavelengths of light of interest. This would mean that the film would appear porous and the boundaries between the high and low refractive index regions would be ragged and uneven.

5.2.1 Ellipsometry Modelling of TiO_2:Er Thin Films

Characterisation of the refractive index of the spin coated TiO_2:Er thin films was essential to correctly model the band structure of the 2D photonic crystals. This characterisation was carried out using ellipsometry [10], using the system described in section 4.3.1. Measurements were taken using the auto-retarder, which meant that the input polarisiation was induced with a phase change that resulted in the reflected light having near circular polarization. Circularly polarized light provides the most accurate measurements for a rotating analyser ellipsometer, however it greatly increases the measurement acquisition time. The modelling of the experimental data was carried out using the software WVASE (J. A. Woollam Co., Inc.). The thin films of TO_2:Er were required to be free from cracks in order to obtain a uniform film on which reliable analysis could be carried out.

The thin films of TiO_2:Er investigated using ellipsometry were prepared on bare Si wafers. This provided a high contrast in refractive index between the TiO_2:Er layer (expected to be around n=2.0-2.7) and the substrate (around n=3.5), ensuring a strong signal from the oxide-silicon interface, therefore maximising the signal to noise ratio.

The general ellipsometry modelling procedure, as detailed in section 4.3.1, was used to model the experimental data. The analysis of the data was carried out over the full spectral range available, from 300-2500 nm, to maximise the accuracy of the model.

A Genosc layer (see section 4.3.1) was used to accurately model the real and imaginary components of the refractive index of the TiO_2:Er thin film. This Genosc layer models the dielectric function as a linear sum of the real and complex oscillator terms. As detailed in section 4.3.1, every Genosc layer consists of two Pole oscillators and an offset ($e1$). Additional oscillators (e.g. Lorentz, Gaussian) are added to account for absorption where

required [11]. A schematic of the layered model used for the analysis is shown in Figure 5-5.

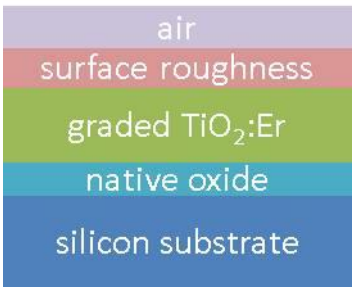

Figure 5-5: A schematic diagram represents the 5 layers used to model the refractive index of the TiO_2:Er sol-gel prepared layer.

Characterisation of the refractive index of the films calcinated at 500°C and 1000°C was carried out. The models developed for both films fitted very well with the experimental data. A model was developed in collaboration with James Hilfiker at J.A.Woollam (J. A. Woollam Co., Inc.). The parameters of the oscillators in this model were optimised with respect to the experimental data acquired for each film. The oscillators and their parameters used for both the 500°C and 1000°C models are detailed in Table 5-1 and Table 5-2 respectively. The MSE values of the final optimised models for each of the films were 5.2 (500°C) and 41.1 (1000°C).

Oscillator	En (eV)	An (eV)	Brn (eV)
Pole 1	4.75±0.02	20.8±0.6	0
Pole 2	0.001	0.04±0.02	0
Gaussian	4.23±0.01	1.90±0.06	0.59±0.01

Table 5-1: Oscillator parameters for the optimised model developed for the refractive index of 10% Er doped TiO_2, calcinated for 1 hour at 500C. The associated e1 offset used in this model was 2.92±0.03 eV.

The value of the MSE is determined during the modelling process using the following expression:

$$MSE = \sqrt{\frac{1}{2N-M}\sum_{i=1}^{N}\left[\left(\frac{\psi_i^{mod}-\psi_i^{exp}}{\sigma_{\psi,i}^{exp}}\right)^2+\left(\frac{\Delta_i^{mod}-\Delta_i^{exp}}{\sigma_{\Delta,i}^{exp}}\right)^2\right]} \quad (5.1)$$

Where N is the number of measured ψ and Δ pairs, M is the total number of real valued fit parameters, σ is the standard deviation and ψ and Δ are related to the Fresnel coefficients as described previously in equation 4.1.

Oscillator	En (eV)	An (eV)	Brn (eV)	e1 offset (eV)
Pole 1	7.25±0.09	202±11	0	-
Pole 2	0.001	0.02±0.01	0	-
Gaussian	4.05±0.03	14.9±4.7	3.19±0.10	-
e1 offset	-	-	-	-0.73±0.15

Table 5-2: Oscillator parameters for the optimised model developed for the refractive index of 10% Er doped TiO_2, calcinated for 1 hour at 1000C

A gradient in refractive index from the bottom to the top of the thin film was found to be a key feature for the films annealed at 1000°C, as shown in the top graph of Figure 5-6. The real component of the refractive index, *n*, of the film annealed at 500°C was found to be 2.02±0.04 at the bottom of the film and 2.03±0.04 at the top of the film at 980 nm. Therefore any gradient in refractive index observed for the films annealed at 500°C was in the bounds of the measurement uncertainty. The refractive index measured at 550 nm (2.08±0.04 bottom, 2.09±0.04 top) is slightly higher than results published elsewhere for un-doped TiO_2 for the same temperature ($n_{undoped}$ = 2.02), however is within the range expected for the anatase phase [3]. The real component of the refractive index of the film annealed at 1000°C was found to be 1.38±0.03 at the bottom of the film and 2.32±0.05 at the top of the film. The high refractive index at the top of the film is consistent with that expected for an intermediate anatase-rutile phase [3].

The imaginary component of the refractive index, *k*, was found to be consistent for both the top and bottom of films calcinated at 500°C (Figure 5-6). However for the 1000°C films a separation between the refractive index dispersion is observed for the strong absorption below 350 nm. The high component of *k* below around 350 nm corresponds to the semiconductor band gap absorption. Furthermore, the non-zero *k* value observed slightly above the band gap of TiO_2 (higher wavelength) can be attributed to a scattering effect of the nanocrystalline TiO_2 grains [12].

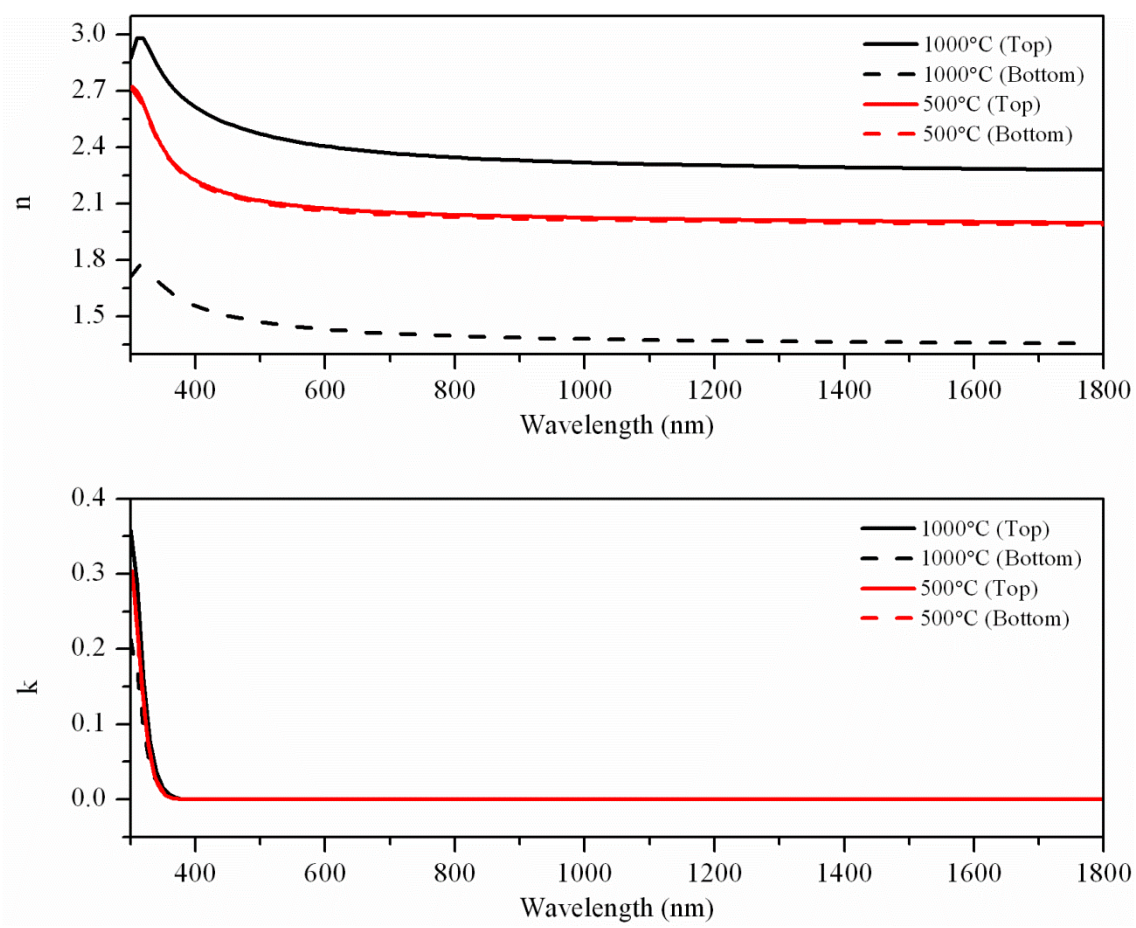

Figure 5-6: The real component of the refractive index (*n*) was found to vary between the top and bottom of the TiO_2:Er films, in particular for the film calcinated at 1000°C. The imaginary component of the refractive index (*k*), in comparison, was found to show little variation for the film calcinated at 500°C, with a slight variation for the film calcinated at 1000°C.

Further understanding of the change in refractive index between the top and bottom of the film annealed at 1000°C is achieved by examining the depth profile of the optimised model. It can be seen from Figure 5-7 that the increase in refractive index occurs at around half way through the film thickness. The granular nature of the TiO_2:Er film resulting in a porous structure is likely to be the cause of this change in refractive index.

Only one other report investigating the change in refractive index with film thickness of a TiO_2 layer has been found [12]. This work was carried out by Mosaddeq-ur-Rahman *et al* for an un-doped TiO_2 sol-gel layer deposited on both SiO_2 and Si. They found that the direction of the refractive index gradient, from the interface with the substrate to the top of the TiO_2 layer, depended critically on the substrate. The higher refractive index was observed at the substrate/TiO_2 layer interface for a silicon substrate, whereas the lower refractive index was observed at the substrate/TiO_2 interface for the silica substrate. The authors attributed the change to the substrate topography: the amorphous silica substrate

inhibiting crystalisation, compared to the crystalline silicon substrate promoting crystallization from its surface [12]. The silicon substrates used by the authors had had their native oxide layer removed, whereas the silicon substrates used in the work for this thesis retained their native oxide. Therefore the very thin (1-3 nm) native oxide surface would form a comparable topography to the amorphous SiO_2 substrate used by Mosaddeq-ur-Rahman *et al*. This would result in the agreement of the direction of the refractive index gradient observed between the silicon substrate with native oxide used in this thesis and the SiO_2 substrate used by Mosaddeq-ur-Rahman *et al*.

The work in this study investigates a higher maximum temperature (1000°C) than that analysed previously (800°C) [12]. Mosaddeq-ur-Rahman *et al* have previously shown that films annealed at 800°C result in a lower refractive index at the silicon/TiO_2 interface than those annealed at 600°C, even though the refractive index at the surface is much higher for the film annealed at 800°C as expected due to normal crystallization of the material. The authors attribute the decrease in refractive index at the substrate interface to diffusion of Si ions into the TiO_2 layer by diffusion at the high temperature. The same effect of a reduction in the refractive index in the TiO_2 at the interface has been observed in this thesis, for the films annealed at 1000°C. Therefore it is proposed that this reduction in refractive index is due to the same diffusion of Si atoms, however further work is required to prove this hypothesis.

A further contributing factor to the change in refractive index with thickness could be due to a preferential uptake of oxygen at the surface of the film during calcination. However this would only be the case if the film was initially non-stoichiometric. This concept is discussed further in section 5.3.1. For reasons discussed in section 5.5, further analysis of these films was not required for this study.

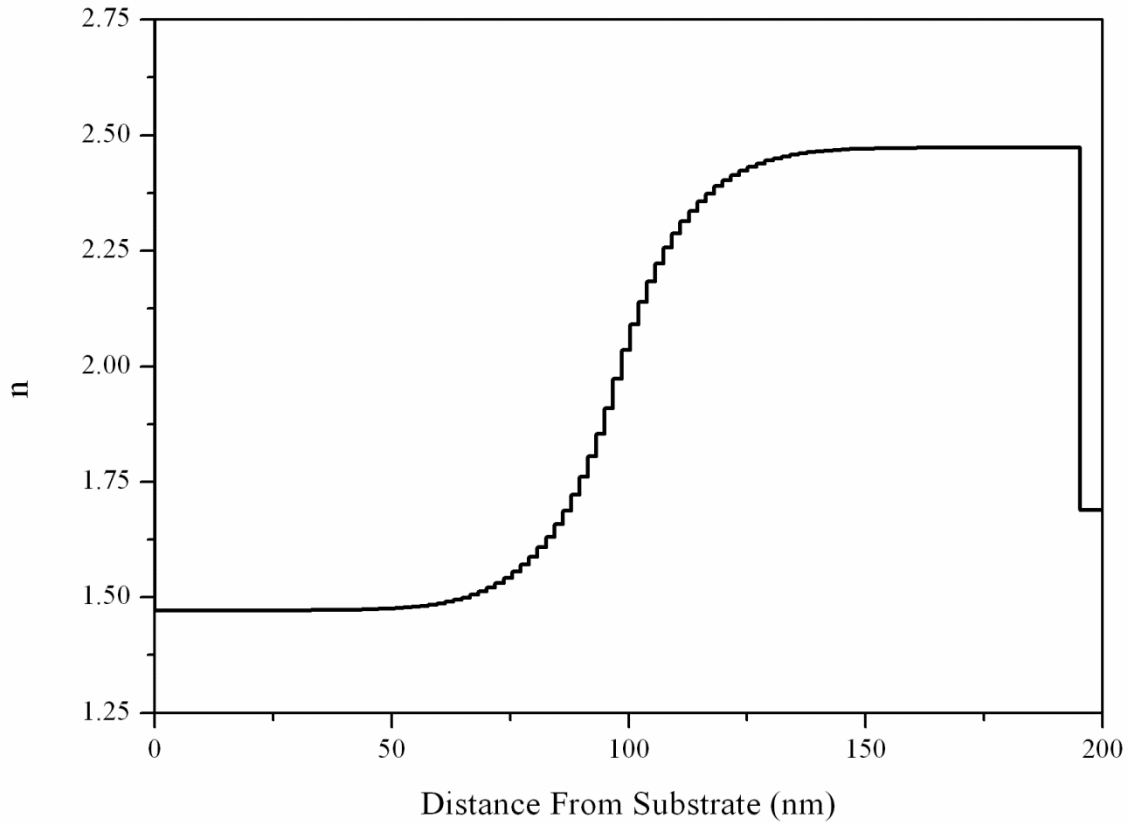

Figure 5-7: The calculated depth profile of the TiO_2:Er film calcinated at 1000°C reveals a sharp increase in *n* at around half way through the film. The surface roughness layer used in the modelling of the film contributes a sharp reduction in *n* at the very top of the film.

A surface roughness layer was found to improve the fit of the model to the experimental data. This layer is shown in Figure 5-7 as a dip in the refractive index, furthest from the substrate. The SEM images of the top surface of the film, shown in Figure 5-8, show that the surface is rough and grainy. The surface roughness layer is represented by a mixture of the TiO_2:Er layer below and air.

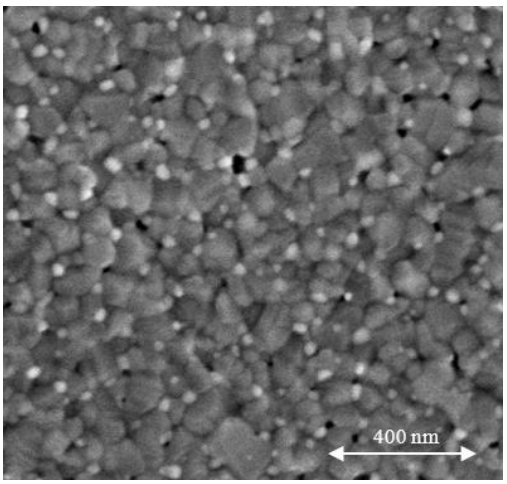

Figure 5-8: SEM micropgraph of the surface of the TiO_2:Er films. The films annealed at 1000°C were rough due to the granular nature of the film.

This study is the first to provide a detailed ellipsometry analysis of a doped TiO_2 thin film. It has confirmed the effect of a graded refractive index profile with film thickness, and highlighted the importance of retaining or removing the native oxide layer on the surface of a crystalline silicon substrate to the direction of the resulting refractive index gradient. The work carried out previously by Mosaddeq-ur-Rahman *et al* [12] modelled the TiO_2 using two separate layers: one for the inhomogeneous (grainy) TiO_2 that has a constant refractive index profile, and another for the interfacial component of the layer is adjacent to the substrate and has a linear gradient.

The model developed for the work carried out in this thesis uses a single layer to model the continuous change in refractive index throughout the layer. Furthermore, this model does not assume a linear refractive index gradient and allows the order of the gradient polynomial to fit as required to the experimental data. Finally, the model used in this thesis uses experimental data taken over three collection angles (60°, 65° and 70°) and a wider spectroscopic range (300-2500 nm), compared to the model developed by Mosaddeq-ur-Rahman *et al* (70° collection over the range 300-850 nm). It is proposed that the model developed for this work is the most complete one to date for analysing the refractive index gradient in TiO_2 based thin films. However no direct comparison of the experimental fit between the two models can be made as Mosaddeq-ur-Rahman *et al* did not provide an error in the fit of their model to the experimental data.

5.2.2 Reflectance Measurements of TiO_2:Er

Reflectance measurements were carried out to confirm the position of the absorption bands of the TiO_2:Er material. Diffuse reflectance measurements were carried out using the Perkin Elmer system detailed in section 4.3.3., for both powder and thin film samples. Due to the very small volume of material within the thin film layer that would be illuminated, any absorptions bands were expected to be very weak. Therefore the powder sample was included to provide the most relevant confirmation of the absorption band positions.

The thin film samples were prepared on substrates of SiO_2 (2 μm thickness) on Si, where the SiO_2 layer had been deposited previously by electron beam evaporation to act as a rear reflector. The thin film samples consisted of 5 multi-stacked layers, resulting in a thickness of around 600 nm. The samples were calcinated at 500°C to achieve the anatase phase. The thin film samples were normalised to an uncoated SiO_2-Si bare substrate.

The characteristic absorption bands of tri-valent Er are shown in Figure 5-9 for the powder sample. Of particular importance for this work is the strong absorption band at around 1523 nm. However no specific absorption peaks are observed for the thin film samples. The oscillations observed a result of Fabry-Perot resonances of the thin film sample. The condition for maximum reflectivity occurs when the wavelength of light is equal to an integer multiple of the thickness of the cavity (film thickness) for the situation where the incident light is incident an angle normal to the surface of the film. From Figure 5-9 it can be seen that a peaks in reflectance are observed at 592 nm and 1184 nm, corresponding to 1× the layer thickness and 2× the layer thickness respectively. The additional oscillations at high wavelengths are believed to be due to fractional orders of resonance.

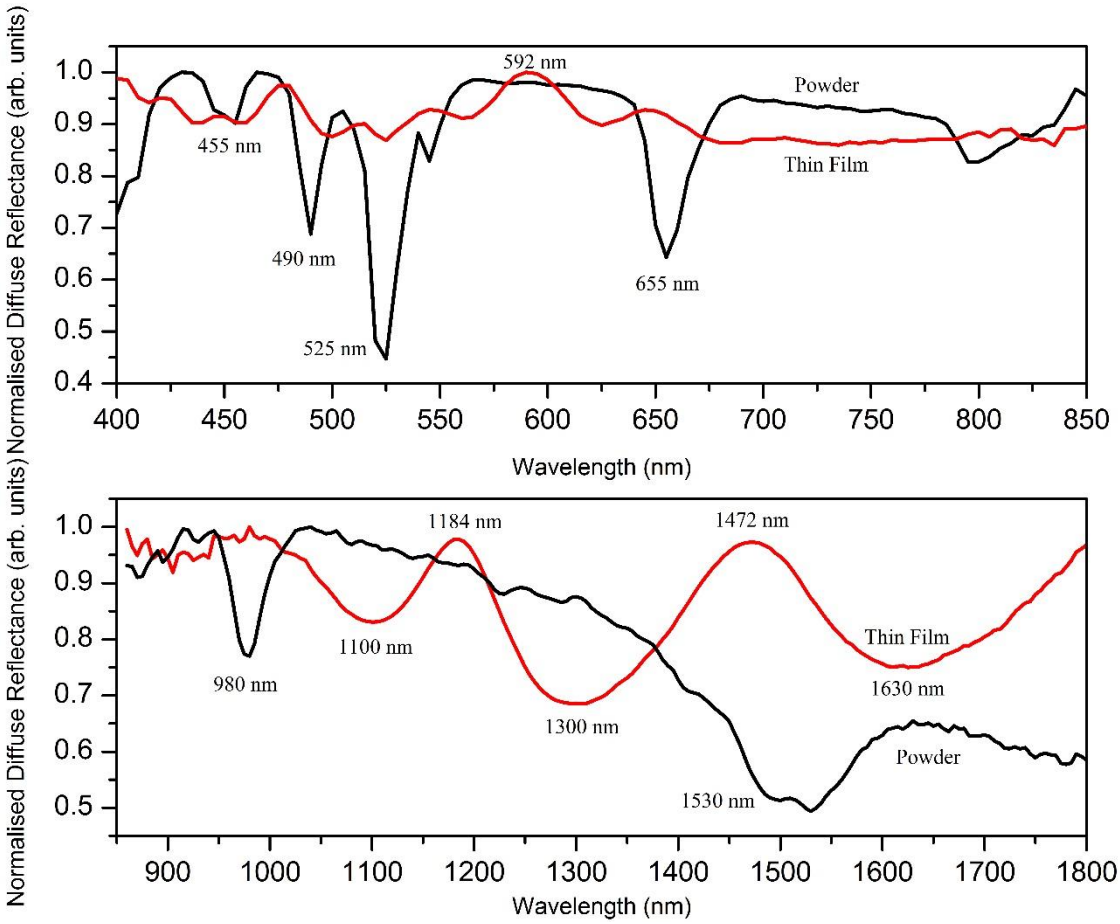

Figure 5-9: Reflectance measurements for TiO_2:Er powder and thin films. Absorption bands, represented by a dip in reflectance, were observed for the powder samples, but not for the thin films. The position of the absorption bands in the powder sample corresponded with those expected for trivalent Er. The peaks in reflectance at 592 nm and 1184 nm were fund to correspond to Fabry-Perot resonances for the film.

The diffuse reflection measurements confirmed that the desired position of the absorption bands of trivalent Er were maintained within a TiO_2 host.

5.2.3 Up-Conversion Measurements of Sol-Gel Prepared TiO_2:Er

Detection of the up-conversion emission at 980 nm from the reference unpatterned TiO_2:Er thin films was required in order to quantify any enhancement in the signal due to the photonic crystal patterns. Measurements were carried out using the confocal setup detailed in Section 4.3.2.

Emission measurements were carried out for thin film samples of increasing thickness, from 192 nm to 600 nm, of 10% Er doping concentration. The 980 nm emission was only observed for the thickest sample of 600 nm, which is shown in Figure 5-10 with the emission from an undoped TiO_2 thin film of the same thickness for comparison. The

emission was measured using a 5 nm emission slit size and 1.70±0.05 mW excitation at 1523 nm. The small peak observed for both undoped and doped emission at around 1017 nm was due to non-integer harmonics of 1523 nm excitation signal scattering into the detector.

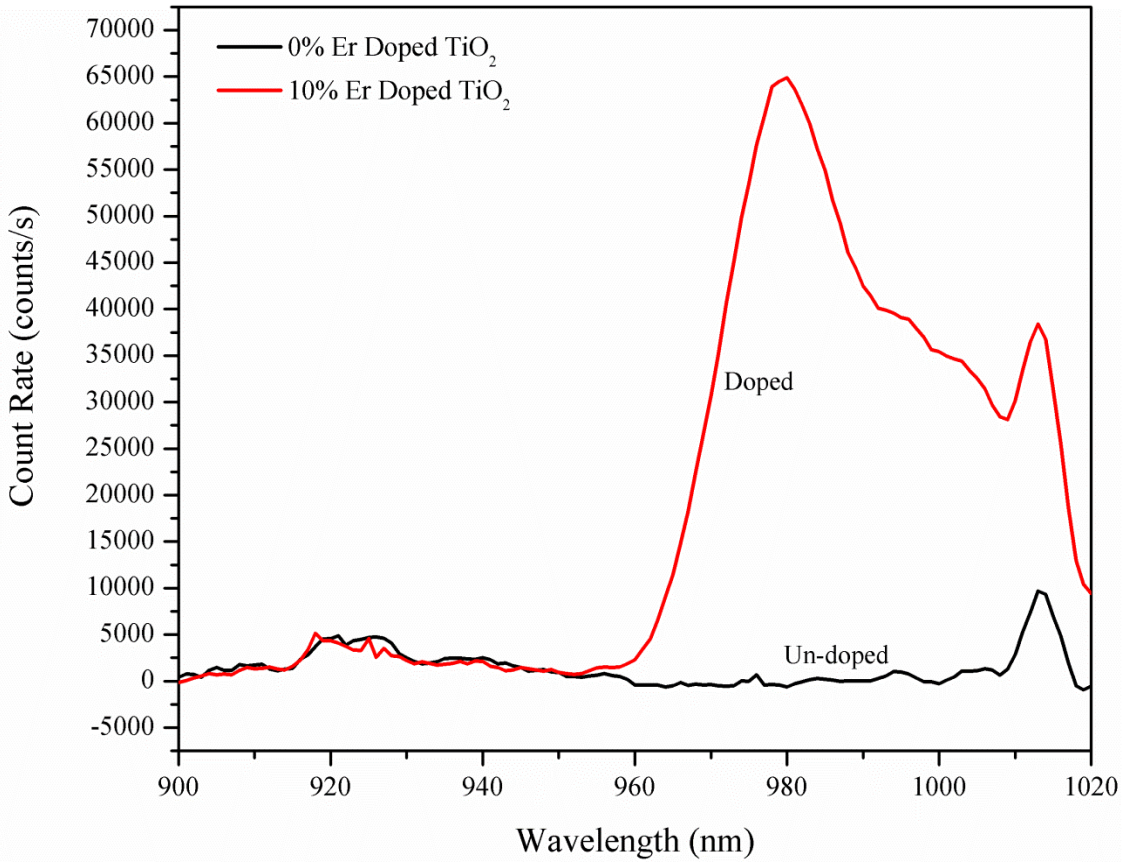

Figure 5-10: RED: Photoluminescent emission at 980 nm was only observed for the thickest Er doped thin film of TiO_2 (600 nm thickness). BLACK: The emission of an un-doped thin film of TiO_2 of the same thickness for comparison.

Closer inspection of the 600 nm film from which the 980 nm peak was detected reveals that significant cracking of the film has taken place during fabrication. A comparison of the cracking of multi-stacked TiO_2:Er films with increasing film thickness is shown in Figure 5-11. The deposition of a 2 layer stack of 120 nm films, shown in Figure 5-11(a), reveals slight cracking of the film. In comparison, the deposition of a 5 layer stack of 120 nm films, shown in Figure 5-11(b), reveals extensive cracking across the entire surface.

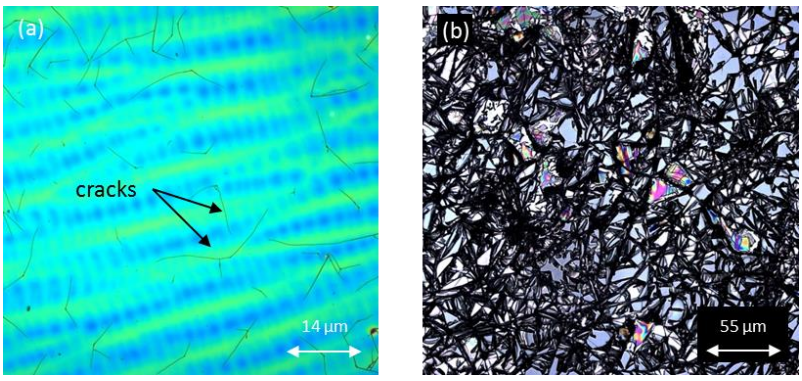

Figure 5-11: (a) A 2 layer stack of 120 nm thick TiO_2:Er films resulted in a small amount of cracking observed on the surface of the stacked films. (b) The cracking increased with the addition of each layer, until significant cracking of the surface was observed for a total thickness of 600 nm.

Although emission at 980 nm was observed for the 5 layer stack, the extensive cracking of the film makes the sample unsuitable for patterning into a 2D photonic crystal. The cracking introduces localised variations in the refractive index of the TiO_2:Er, as well as internal scattering of light within the layer. This increased scattering results in an increase in path length of the excitation light, leading to an effective increase in the concentration of light within the layer. Due to the nonlinear nature of the up-conversion process, this could have greatly increased the up-conversion emission at 980 nm. Therefore it is not known whether an uncracked multilayer stack of films of the same thickness would have also resulted in 980 nm light being detected.

The limitations of achieving smooth, uncracked layers of a thickness large enough to observe the up-conversion emission from Er doped TiO_2 indicate that the preparation of thin films by sol-gel deposition will not allow for the desired films to be achieved for photonic crystal patterning. Therefore an alternative deposition method of sputter coating was investigated.

5.3 TiO_2:Er Thin Films by Sputter Deposition Method

The deposition of Er doped TiO_2 films by sputter deposition allowed for thicker films with no cracking to be obtained. The deposition was carried out in the system described in section 4.2.9. The advantage of sputter deposition over sol-gel spin coating is that the desired material is directly deposited onto the substrate using chemically inert Ar ions. Therefore there is no contamination from additional precursors or organic molecules. Furthermore films of several micrometers in thickness could be achieved during a single run. The disadvantage is that it must be carried out in a vacuum chamber.

Doping of the TiO_2 layer with Er was achieved by placing Er wire on the surface of a 2" TiO_2 sputter target. The wires were placed radially on the circular surface in order to provide as a symmetric a distribution as possible, with respect to the target and the resulting toroidal plasma distribution above the target. This technique has previously been used to successfully to dope In_2O_3 with Er [13]. The surface area covered by the Er wire was calculated to be 10%, in order to attempt to achieve a similar doping concentration. This was a very rudimentary method of doping the TiO_2 layer and was likely to result in significant variations in the doping concentration across the deposited thin film. To attempt to minimise the doping variations, the substrate was positioned as far away from the source target as possible, while still maintaining a sensible deposition rate. The etch rate of the Er metal with respect to the TiO_2 target would also play a significant role in the final doping concentration. However for the purposes of this work, the method chosen was suitable as a first approximation to test the viability of the technique. A more consistent Er doping concentration could be achieved in future work by preparing a pre-doped TiO_2 sputter target.

Initial tests revealed that the sputter deposition rate was very slow, therefore a long deposition time was required to achieve the desired thickness of 1-2 μm. Samples thicker than 2 μm were expected to be very difficult to fully etch the photonic crystal features, while thicknesses of <600 nm (from sol-gel deposition) had previously shown to be too thin to measure an up-conversion signal. The deposition conditions used for the sputtering are detailed in Table 5-3. The thin films were sputtered onto silicon substrates.

RF Power (W)	Ar Pressure (mBar)	Distance of Substrate from Target (cm)	Deposition Rate (nm/hour)
120	1×10^{-3}	15	150

Table 5-3: The RF sputter conditions used for the deposition of Er doped TiO_2 required several hours of deposition to achieve the desired thickness of 1-2 μm.

The RF Power was limited to a maximum value of 120 W and the coatings were carried out in 1 hour segments. This was done to avoid excessive heating of the sputter target, which could result in the target cracking. Samples were prepared using this method up to 4500 nm in thickness, without any sign of the cracking.

5.3.1 Effects of Annealing and Ellipsometry Analysis of Sputter Prepared TiO_2:Er Thin Films

The samples prepared by RF sputter coating were annealed in a tube furnace to analyse the refractive index of the films. A gradient in the refractive index between the top and bottom of the layer was observed, as found previously for the sol-gel films. By comparing the refractive index of the sol-gel and sputter coated films annealed at 500°C (Figure 5-12), it can be seen that there is a greater gradient change for the sputter coated film than the sol-gel prepared film. The refractive index of the top of the layer for the sputter coated film is also much higher than that of the sol-gel film.

The gradient in refractive index may be due to a change in stoichiometry of the film with thickness (deposition time). The change in stoichiometry during the sputtering process has been reported elsewhere as a common effect for oxide targets [14]. Furthermore sputtering a TiO_2 target with Ar alone (no O_2 available in the system used), as was carried out in this study, can result in non-stoichiometric TiO_2 films [15]. Annealing in air will result in an uptake of oxygen by the film towards stoichiometry, however this process may not be uniform throughout the thickness of the film. The increase in refractive index observed from the bottom to the top of the film is consistent with a change from non-stoichiometric to stoichiometric TiO_2 [15]. This is consistent with a reduction in oxygen uptake the further from the surface of the film, as would be expected from the annealing procedure.

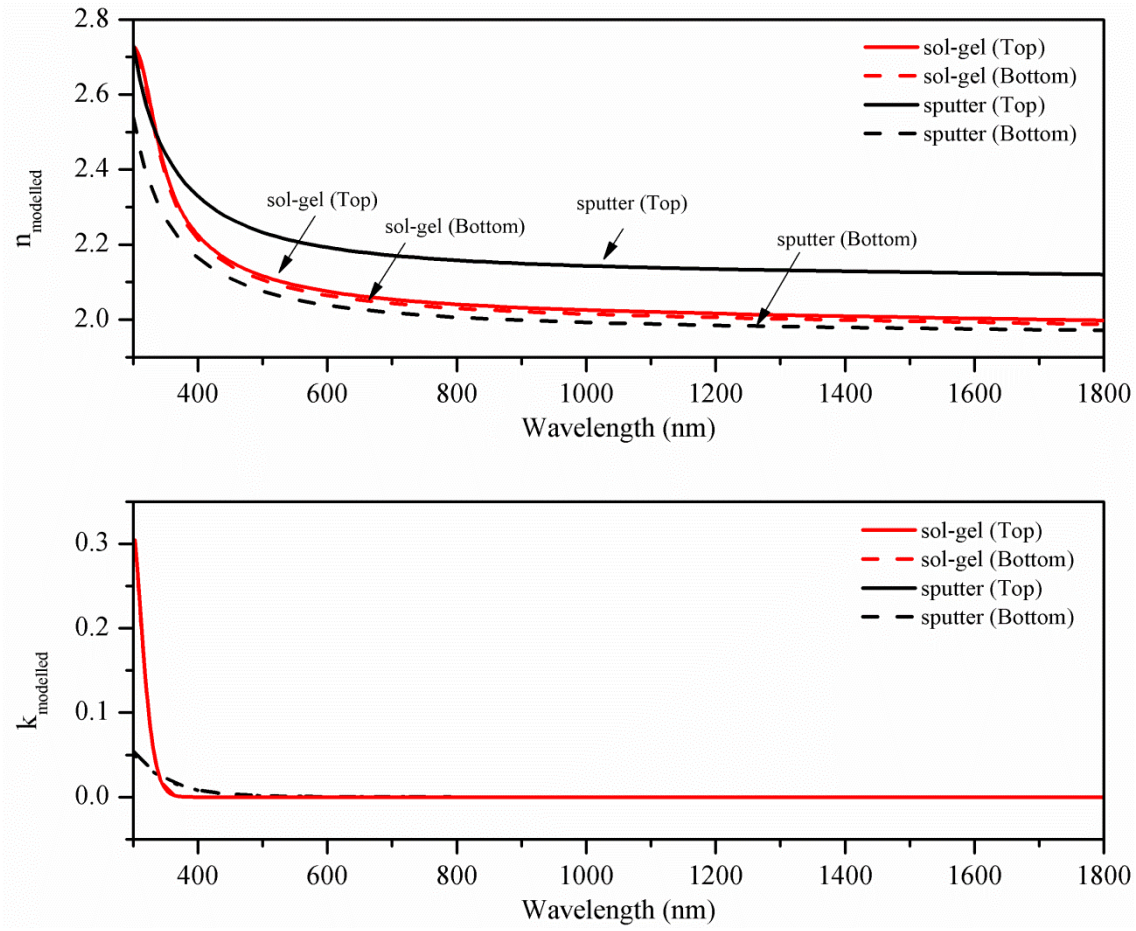

Figure 5-12: Real (*n*) and imaginary (*k*) components of the refractive index for sol-gela dn sputter deposited films. The large separation in the values of the real component of the refractive index for sputter coated films is believed to be due to an initial non-stoichiometric deposition of TiO_2 by sputter coating, followed by a gradient in oxygen uptake with thickness from annealing in air.

Further analysis of the refractive index of the sputter coated films was carried out over a range of annealing temperatures. The refractive index at 980 nm was used for comparison between the different calcination temperatures. A general trend of increasing *n* with calcination temperature was observed for the top of the layer with one exception being the dip at 700°C, as shown in Figure 5-13. The bottom of the layer also reveals an increase in *n* up until 800°C. At 900°C a sharp decrease in *n* is observed, while the ellipsometric data for 1000°C was not possible to model. The imaginary component of the refractive index, *k*, showed the same increasing trend with temperature for the top and bottom of the thin film layer. The repeatability of the measurements was characterised by calculating the mean percentage error between the refractive index calculated using the experimental data from four different locations on the same sample.

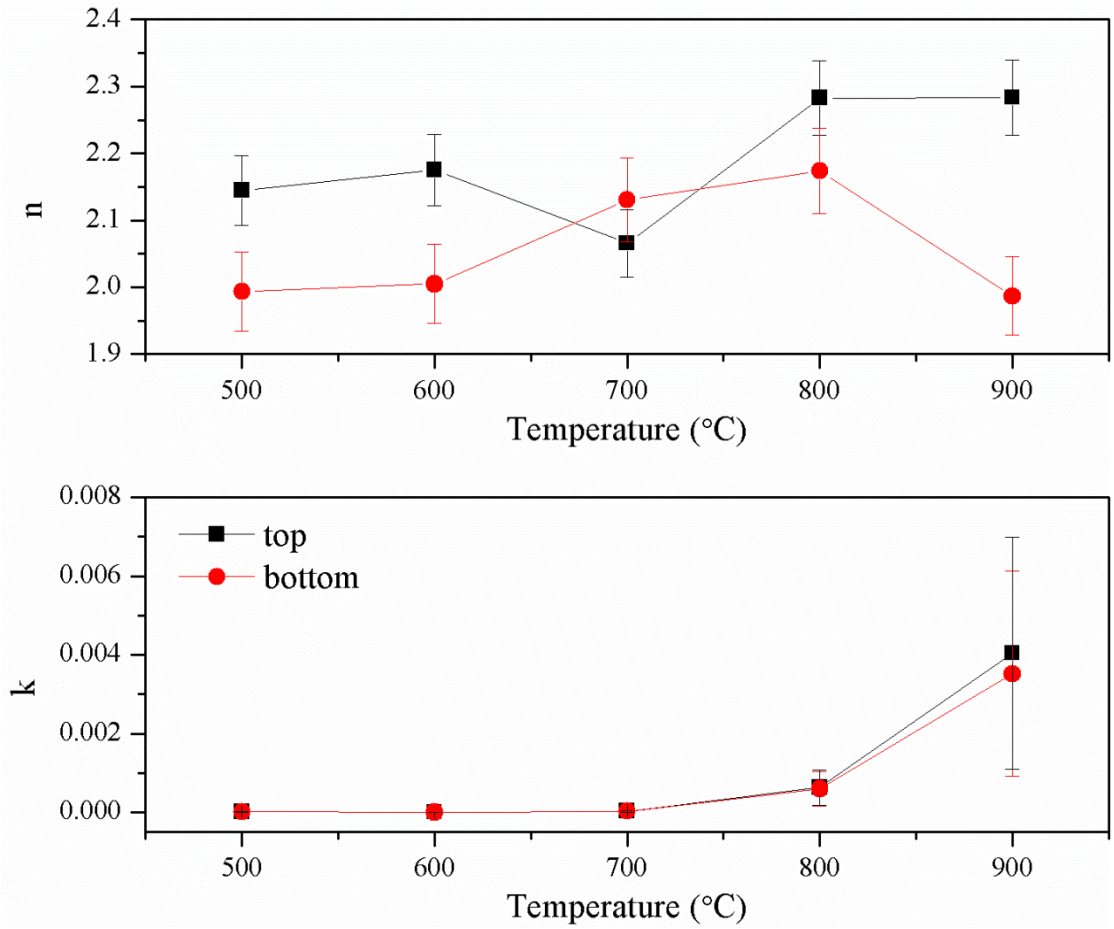

Figure 5-13: Both the real (*n*) and imaginary (*k*) components of the refractive index show a general increase with a rise in annealing temperature.

The increase in refractive index with annealing temperature is expected, due to the gradual change in phase from anatase to rutile. The dip in the refractive index at the top of the thin film annealed at 700°C is unexpected. The overlap of the error bars for n_{Top} and n_{Bottom} at 700°C indicate that it cannot be said for certain whether the refractive index at the bottom of the film is indeed larger than that at the top. However the well separated uncertainties in the measurements for the refractive indices at the other temperatures suggest that a general trend can be concluded. Preparing further samples across the full temperature range would allow for more precise values for the refractive indices to confirm the overall trend.

The change in refractive index with annealing temperature demonstrates how the refractive index of the material can be tuned to the desired optical properties for the photonic crystal. However the variation in refractive index with depth is an unwanted property that would reduce any effect from a photonic crystal created in this film. The wavelength at which a 2D photonic crystal will be resonant is determined by both the geometry and contrast in refractive index between the high and low components. A

variation in refractive index with film depth will result in the resonant wavelength also varying with depth, which will reduce the effect of the photon crystal layer.

5.3.2 Optical Measurements

Photoluminescence measurements of the 4500 nm thick sputter coated TiO_2:Er were carried out using the setup detailed in section 4.3.2. This sample was chosen for carrying out optical measurements as it was the thickest one prepared by sputter deposition. No emission was observed for the thinner samples prepared in this study. The sample was excited at 1523 nm and a 10 nm detection slit width was required to obtain a good signal to noise ratio at peak center. The emission scans were autmatically averaged over 10 repetitions by the software in order to obtain a better representation of the peak profile. The emission profile of the sample calcinated at 500°C is shown in Figure 5-14, in addition to the normalised emission of the sol-gel prepared "highly cracked" film for comparrison. A very small up-conversion emission peak, centered at 981 nm, was observed for the sputter coated sample when normalised against the reference emission spectra.

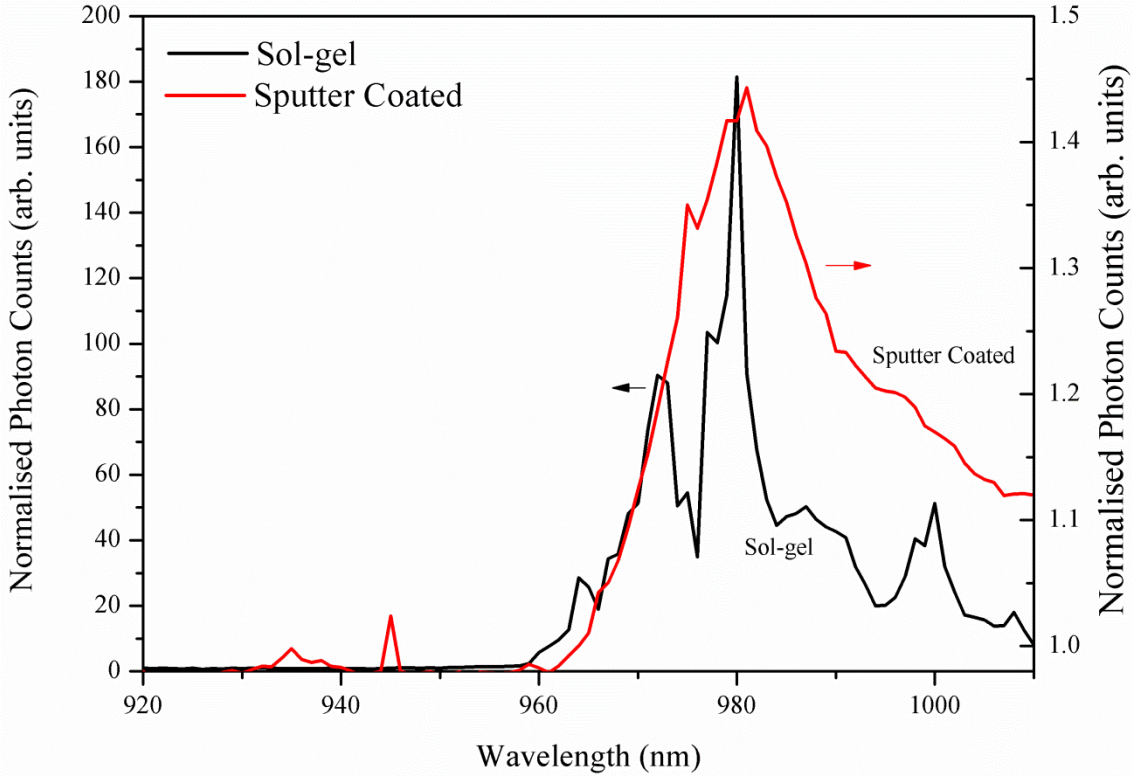

Figure 5-14: Photoluminescence of sputter coated and sol-gel prepared TiO_2:Er films. A very small up-conversion emission at 980 nm was observed for the 4500 nm TiO_2:Er sputter coated film (RED), when excited at 1523 nm. This emission was much less than that observed for the highly cracked sol-gel prepared film (BLACK).

RF sputter deposition allowed for the formation of Er doped TiO_2 films up to a thickness of 4500 nm, without the detrimental cracking that was observed for spin-coated sol-gel films. However, even for these very "thick" thin films, only a very weak up-conversion emission at 980 nm was observed. Furthermore, the exact Er doping concentration could not easily be controlled and was likely to be non-uniform across the area of the film. The facilities to measure the Er doping concentration in the TiO_2 thin film following deposition were not available during this study and so were beyond the scope of this work.

To measure any enhancement in the small up-conversion signal due to a 2D photonic crystal, the desired pattern of holes or pillars would have to be etched through the full depth of the layer. This etch would have to be anisotropic all the way down, to maintain the desired resonance wavelength. In the following section, the development of an anisotropic TiO_2:Er etch will be presented.

5.4 Fabrication of TiO_2:Er 2D Photonic Crystals

RF sputter coating had been shown as a viable technique for the preparation of uniform thin films of TiO_2:Er. Therefore it was important to investigate the fabrication of 2D photonic crystals into these thin film layers, using dry etching techniques. Both reactive ion etching and focused ion beam etching were investigated for the purpose of this study.

5.4.1 Reactive Ion Etching of TiO_2:Er

Reactive ion etching was investigated as a technique for the fabrication of photonic crystals in the TiO_2:Er thin films. Initial etches were carried out to characterise the etch rate of the sol-gel prepared TiO_2:Er under different process conditions. The initial etch chemistry used, detailed in Table 5-4 was based on the work by Setyawati *et al.* and Norasetthekul *et al.* [16, 17]. The sample was kept at 20°C using a carbon carrier wafer and He backside cooling.

RF Power (W)	ICP Power (W)	Pressure (mTorr)	SF_6 (sccm)	Ar (sccm)	Time (min)
100	0	20	10	4	2

Table 5-4: The initial etch chemistry used for the dry etch of TiO_2:Er was based on a fluoride etch using SF_6. (sccm = standard cubic centimetre per minute).

Rectangular Cr masks, 50 nm thick, were prepared on the TiO_2:Er samples using the lift-off technique with a UV photoresist. The deposition of the Cr material was achieved by thermal evaporation using the setup detailed in section 4.2.8. The RF power, ICP power, SF_6 flow rate and Ar flow rate were varied independently to characterise the etch rate. All etches were carried out for 2 minutes. The etch depth was measured using a Dektak profilometer.

The dependence of the etch rate on RF and ICP power is shown in Figure 5-15. An increase in etch rate was observed for an increase in RF power from 50-100 W. A larger RF power provides a higher average ion energy, therefore an increase in etch rate is expected. However at RF powers greater than 100W, the etch rate decreases. The etch rate also decreases for an increase in ICP power. It is believed that these observed decreases in etch rate for both high RF and ICP power are due to the complete removal of the Cr mask during the etching procedure, resulting in a period where both the top and bottom of the feature are etched together. As the etch rate is dependent on the aspect ratio, with the base of features of higher aspect ratio being etched at a faster rate than those with a smaller aspect ratio, the top of the feature will etch faster than the base, resulting in a reduction in the overall etch depth is the mask if removed during the etch [18]. An increase in the mask etch is expected with increasing RF and ICP power due to larger ion bombardment effects, which provide the greatest contribution to metal mask etching.

The remaining Cr mask thickness was calculated for each of the etches by measuring the etch depth before and after the removal of any remaining Cr using a wet etch. The remaining mask thickness following the etch was found to be very small, well within the experimental uncertainty of the etch measurements. This confirmed that most of the Cr masks had indeed been removed during all of the etches, however provided little insight into the selectivity of the etch.

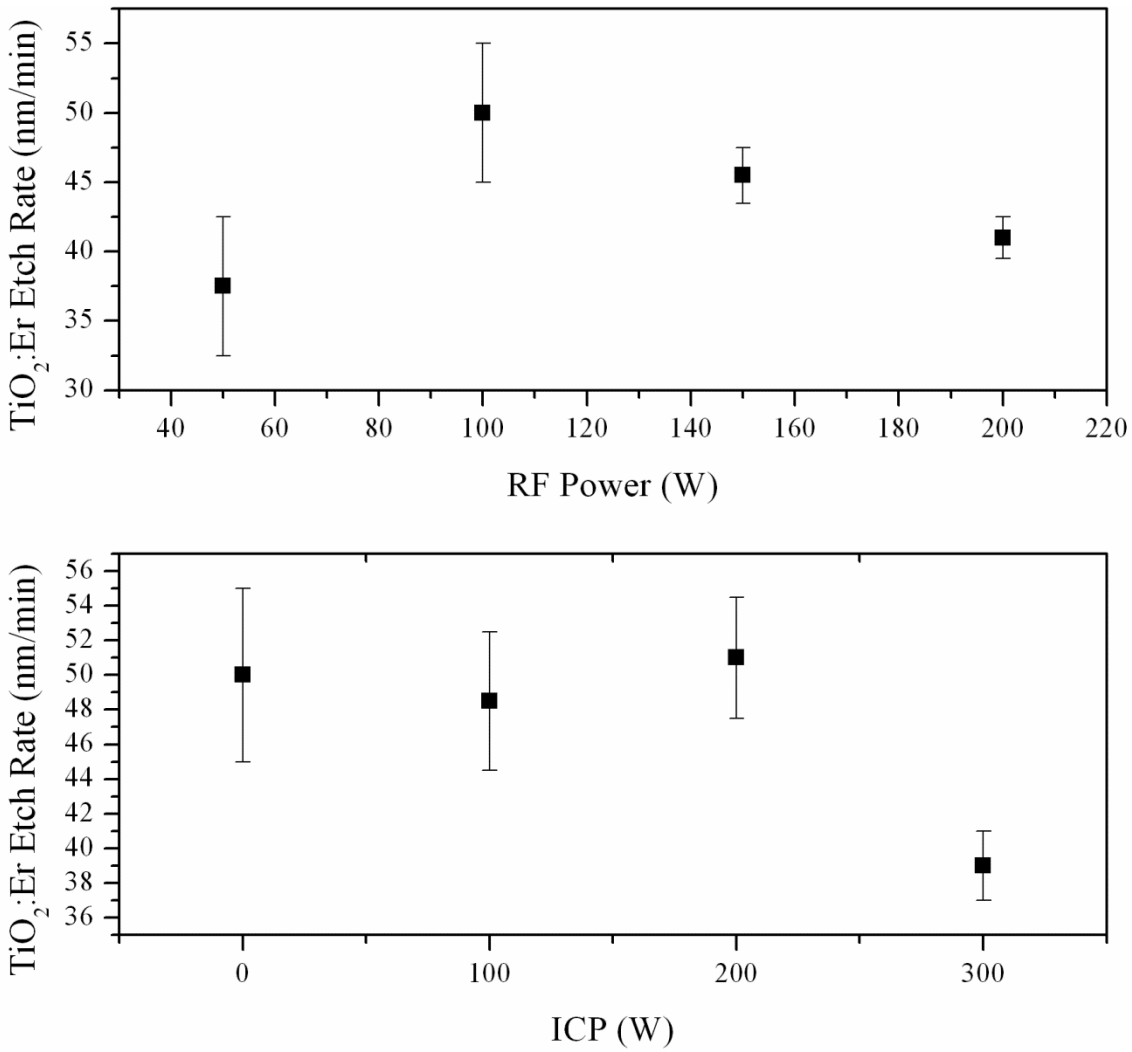

Figure 5-15: TiO_2:Er etch rate as a function of RF and ICP power. The apparent decrease in etch rate observed for both increasing RF and ICP power is believed to be due to the complete removal of the Cr hard mask during the etching process. The increase in etch rate from RF= 50 to 100 W is consistent with that expected for the Cr hard mask remaining for the entirety of the etch.

The complete removal of the Cr mask during these etches was unexpected. The chemical etch rate of Cr to SF_6 is extremely small, <1 nm/min [19]. Therefore the main contributing factor to the Cr etch was from the physical sputtering of the Ar ions. We would therefore expect to see a decrease in the TiO_2:Er etch rate with increasing Ar flow rate above the standard recipe. From Figure 5-16 a decrease in etch rate is indeed observed from 4-6 sccm, however there is an increase in etch rate from 6-8 sccm. The large measurement uncertainties and small sample set means that additional measurements are required to fully ascertain the trend for higher Ar flow rates. The increase in SF_6 flow rate (Figure 5-16) also provides little information due to the large measurement uncertainties.

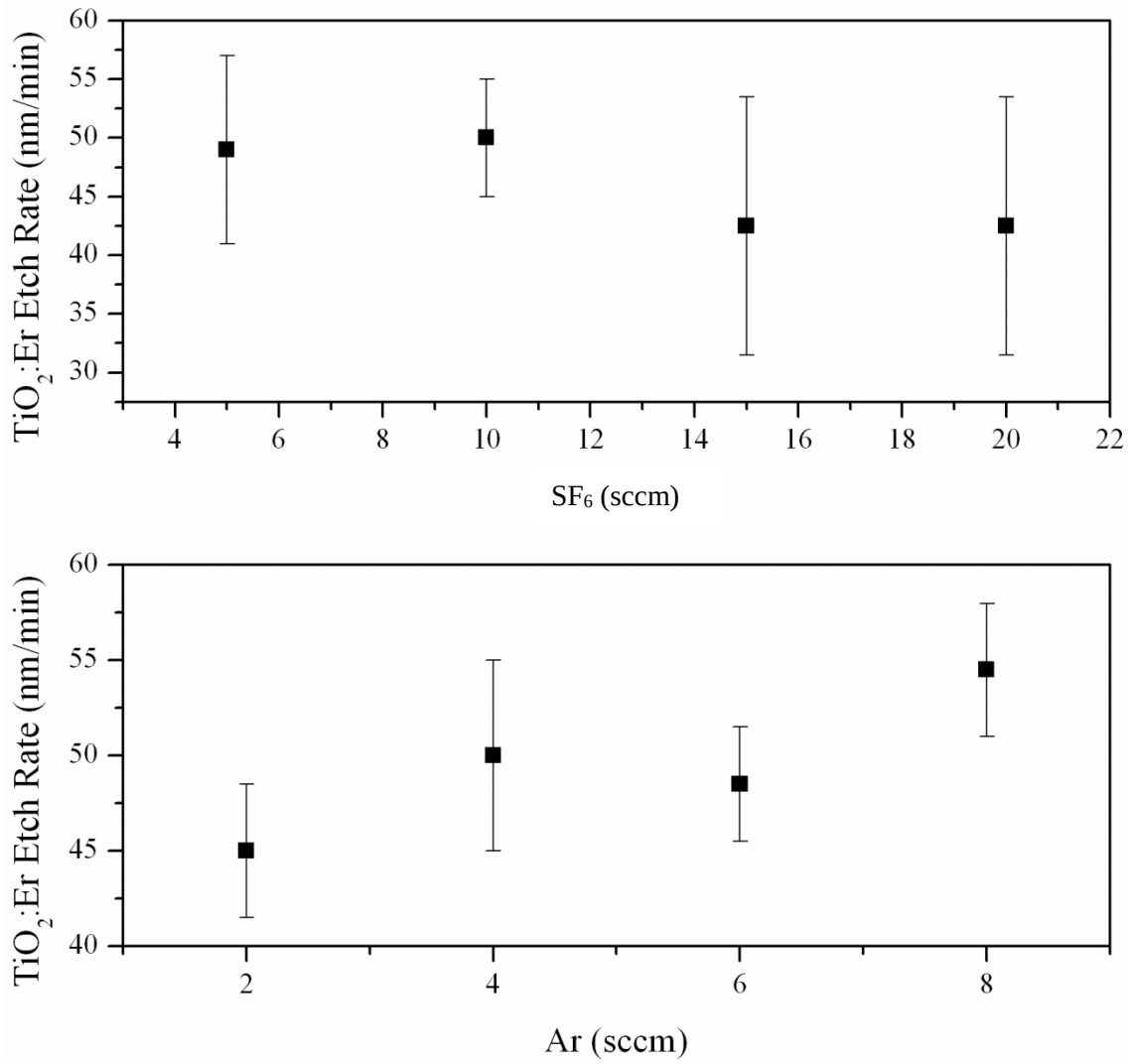

Figure 5-16: TiO_2:Er etch rate as function of SF_6 and Ar flow rate. The large experimental uncertainties in the etch rates mean that it is difficult to draw any firm conclusions about the role that both Ar and SF6 flow rate have on the etch rate.

The removal of Ar from the reaction chemistry should greatly reduce the physical component of the etch. However SF_6 alone results in a very isotropic etch and so would not provide the vertical side walls desired for the 2D photonic crystals. Therefore CHF_3 was chosen to be used as the source of F ions. The advantage of CHF_3 is that it can be used both for etching and side wall passivation through the deposition of perfluoroethylene ($[CF_2]_n$) films on the vertical faces of the feature [20]. The etch conditions of the test are shown in Table 5-5. An increase in pressure was required to start the plasma process. Furthermore a reduction in RF power was required to further increase the selectivity of the mask to the TiO_2:Er.

RF Power (W)	ICP Power (W)	Pressure (mTorr)	CHF_3 (sccm)	Etch rate (nm/min)
50	0	60	13	2.53

Table 5-5: CHF_3 was found to etch TiO_2:Er, however the etch rate was so small that it was unsuitable for use in this study where etch depths of around 4500 nm were required.

It can be seen from

Table 5-5 that the etch rate of TiO_2:Er using a CHF_3 based chemistry is extremely slow, only 2.53 nm/min. Therefore this chemistry is not suitable for achieving the large etch depths of around 4500 nm expected to be required for a TiO_2:Er film thick enough to observe up-conversion.

The Cr masks used in this study were not suitable for fully characterising the etch rate of the TiO_2:Er material due to insufficient resistance to the physical and chemical conditions. This was surprising due to the expected inert nature of the Cr material. Improvements to the hard mask resistance could have been achieved by changing the mask thickness or material.

An increase in the thickness of the metal mask layer would have allowed for deeper TiO_2:Er etches to be carried out. However constraints associated with the lift-off procedure meant that there was a limit to the thickness of metal that could be deposited to allow lift off to be successfully carried out. This maximum thickness of metal is around 1/3 of the thickness of the sacrificial photoresist layer. The PMMA photoresist used for patterning the photonic crystals features was 300 nm thick. This meant that the metal mask layer was limited to a maximum thickness of 100 nm to allow lift-off to be successful. The initial experiments carried out in this study resulted in selectivity of around 1:2 for Cr mask to TiO_2:Er etch. Therefore increasing the Cr mask thickness to the maximum value would only increase the etch depth of TiO_2:Er to around 200 nm; still well below the desired 4500 nm.

The typically very low etch rates of thermal evaporation deposited Cr in a fluoride based chemical etch or an argon sputtering etch [19] meant that the Cr layer was expected to be strong enough to easily withstand the etch chemistry developed in this thesis for etching TiO_2. The reason why the Cr mask was not providing the good etch resistance as expected was unclear. Therefore alternative routes for fabricating photonic crystals of TiO_2 were

explored. One such route was the fabrication of holes in TiO_2 using focused ion beam etching, which will be discussed in the following section.

5.4.2 Focused Ion Beam Etching of TiO_2:Er

Focused ion beam (FIB) etching was investigated as an alternative to ICP-RIE for the etching of holes into TiO_2:Er to form 2D photonic crystals. The advantage of FIB is that no mask is required, therefore selectivity is not an issue. However FIB etching is a purely physical sputtering process, therefore it can be difficult to achieve anisotropic structures with high aspect ratios. For an initial test, holes of around 300 nm diameter were etched into a sample of the RF sputter coated TiO_2:Er.

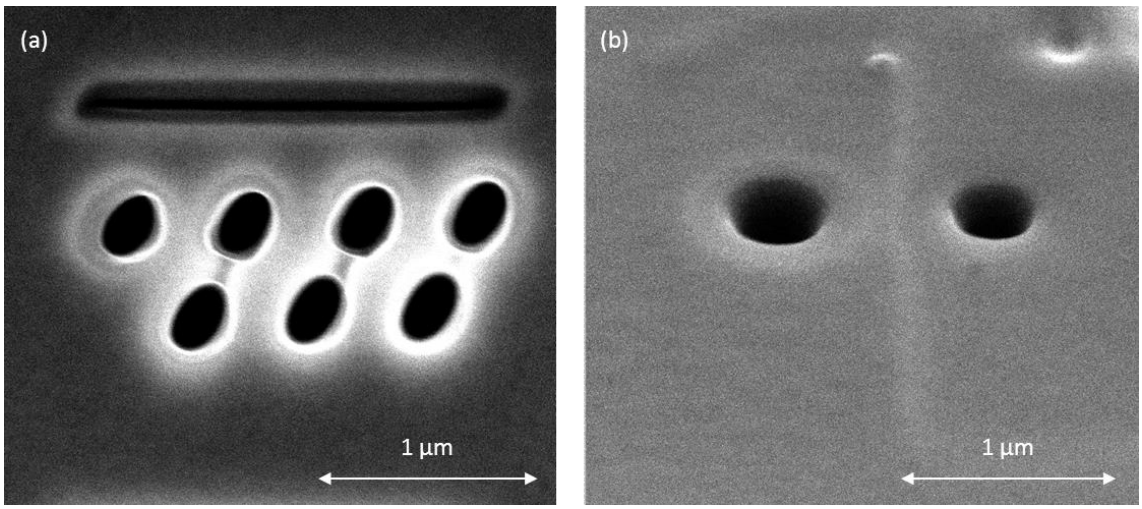

Figure 5-17: SEM micrographs of etched TiO_2:Er films. (a) Directly etching the TiO_2:Er material resulted in loss of geometrical form due to the excessive charging and deflection of the ion beam, forming elliptical holes. (b) The deposition of a thin layer of Pt, on top of the TiO_2:Er surface prior to etching, allowed for the charge to rapidly dissipate and for the desired circular holes to be achieved.

An initial etch was carried out onto the bare TiO_2:Er sample, which resulted in elliptical holes being formed. It can be seen from Figure 5-17 (a) that direct exposure of the TiO_2:Er thin film with the focused ion beam results in significant charging of the dielectric film, leading to localized deflection of the beam and divergence from the desired geometric form of the etch. The deposition of a thin Pt film (~10 nm) onto the region to be etched, prior to etching, provides a thin conductive layer for rapid charge dissipation. From Figure 5-17 (b) it can be seen that the etching of the holes onto regions exposed to a thin Pt film allows for the desired circular holes to be achieved.

The 2D photonic crystals require holes with vertical side walls. Therefore it was important to analyse the anisotropy of the etch. This was achieved by depositing Pt into the holes

and then etching away a trench using FIB at an oblique angle to view the cross section. The Pt fill was required to avoid redeposition of the sputtered material into the hole. The trench and an expanded view of a hole filled with Pt can be seen in Figure 5-18(a) and Figure 5-18(b) respectively. The cross section of the hole shows clearly that the side wall anisotropy is very poor, with the hole diameter decreasing from 258 nm at the top to 63 nm at the bottom of the 1112 nm deep hole.

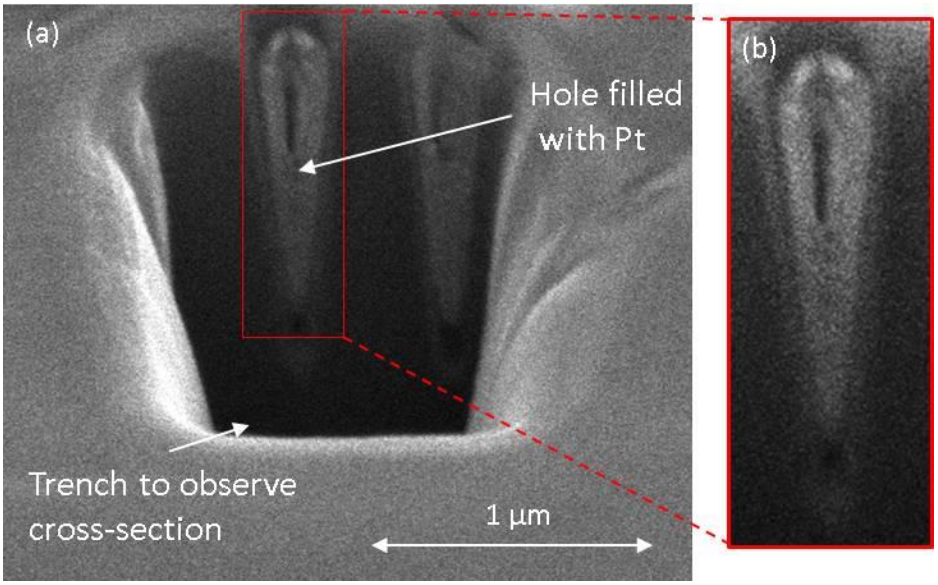

Figure 5-18: (a) The holes fabricated by focused ion beam etching were found to show poor anisotropy, with the hole diameter decreasing from 258 nm at the top, to 63 nm at the bottom of a 1112 nm deep hole. (b) The holes were filled in with Pt prior to exposing the cross section of the holes, to ensure that no redeposition of the sputtered material occurred.

The poor anisotropy means that this method would not be suitable for forming the straight, vertical side walled features that would be required for 2D photonic crystals. The depth achieved was far greater than that for reactive ion etching and no mask was required to prepare these features. However the anisotropy is critical to the effect of the photonic crystal and so focused ion beam etching was not a suitable choice of fabrication method for this study.

5.5 Conclusions of the Fabrication of TiO_2:Er 2D Photonic Crystals

The fabrication of thin films of Er doped TiO_2 was achieved using the sol-gel method. This method allowed for the doping concentration of Er to be accurately controlled, while carrying out the fabrication in ambient conditions. There was found to be a limit to the thickness of a single film that could be deposited due to mechanical failure of the films. This limit was found to be around 130 nm. The cracking was believed to be due to the

evaporation of water, ethanol and the breakdown of other organic compounds during the initial curing of the films. The stacking of multiple films allowed for thicker layers of TiO_2:Er to be achieved, whereby each film was pyrolysed between the application of a subsequent film. However these layers also exhibited a limit to the overall thickness, found to be around 600 nm. Furthermore, the repeatability of obtaining un-cracked stacked films of this thickness was very poor.

The structural and optical properties of the sol-gel prepared films calcified at 500°C and 1000°C were analysed. The films calcinated at 500°C were found to be of a uniform dense structure, with a refractive index at the top of the film consistent with that expected for the anatase phase of TiO_2 (n_{top}=2.03 at 980 nm). The films calcinated at 1000°C were found to be of a granular structure, with a refractive index at the top of the film consistent with that expected for an intermediate anatase-rutile phase of TiO_2 (n_{top}=2.32 at 980 nm). Moreover, the refractive index was found to vary with the depth of the film. The change in the real components of the refractive index was small for the anatase phase (n_{bottom}=2.02, n_{top}=2.03 at 980 nm) and large for the anatase-rutile phase (n_{bottom}=1.38, n_{top}=2.32 at 980 nm). The imaginary component of the refractive index was found to show a small change below 350 nm for the anatase-rutile phase only. It is believed that these changes in refractive index could be due to the varying granular nature of these films. However further investigation beyond the scope of this study is required to fully ascertain the reason.

Diffuse reflectance measurements of the bulk TiO_2:Er material revealed that the electronic transition of the tri-valent Er in the TiO_2 host were in the correct position for the desired application. However up-conversion measurements of emission at 980 nm following excitation at 1523 nm were extremely difficult to observe. The one sample from which an up-conversion signal at 980 nm was observed was shown to be crack damaged, suggesting that the cracking was greatly increasing the path length of the light within the layer, resulting in an increased signal. However this highly cracked film was not suitable for patterning into a 2D photonic crystal.

The deposition of Er doped TiO_2 by sputter deposition was investigated to improve the thickness of un-cracked films. This method allowed for films of up to 4500 nm to be obtained, with the potential to increase the thickness further still. However the doping concentration could not easily be controlled and was subject to non-uniformity. Up-

converted emission at 980 nm following excitation at 1523 nm of this un-cracked film following calcination at 500°C was achieved, however the signal was very weak.

Investigation of the reactive ion etching of the TiO_2:Er films demonstrated that the Cr mask used to calibrate the etch was not strong enough to withstand the etching procedure. This was surprising given the typical properties of a Cr film and the cause of the weak nature of the mask was unclear. The weak nature of the mask material, in addition to the highly anisotropic and high aspect ratio features desired meant that reactive ion etching was not believed to be a suitable method for the fabrication of 2D photonic crystals in a 4500 nm film of TiO_2:Er.

Focused ion beam etching was carried out as a maskless alternative for the fabrication of 2D photonic crystals in TiO_2:Er. Initial investigation revealed that the dielectric nature of the film resulted in significant charging on the surface, resulting in deformation of the desired features. This was overcome by depositing a thin film of Pt prior to the etch, which allowed for the charge to dissipate during the etch. The initial study demonstrated that FIB was suitable for achieving the desired depth, however redeposition of the sputtered material onto the side walls resulted in inverse conical etches: far from the straight vertical side walls desired.

The difficulties highlighted above in the fabrication of Er doped TiO_2 and the subsequent patterning of such a film to achieve anisotropic 2D photonic crystals resulted in alternative materials and fabrication methods being explored to prepare a 2D photonic crystal to enhance up-conversion for silicon photovoltaics. This involved using a well-established technique of using reactive ion etching to fabricate nanostructures in silicon. YF_3, a host material of lower phonon energy than TiO_2, was then doped with erbium and incorporated in the space between the pillars using thermal evaporation. Although the overall fabrication process involves a greater number of steps, it was hoped that the combination of using an etch procedure for silicon that has been very well developed in the microelectronics industry, in combination with a better host material for erbium would improve both the fabrication of the nanostructure 2D photonic crystal and improve the 980 nm emission. The following chapter will detail the fabrication and analysis of this alternative approach.

5.6 References

1. H. Jansen, H. Gardeniers, M. deBoer, M. Elwenspoek, and J. Fluitman, "A survey on the reactive ion etching of silicon in microtechnology," Journal of Micromechanics and Microengineering **6**, 14-28 (1996).
2. R. X. Yan, and Y. D. Li, "Down/Up Conversion in Ln3+-Doped YF3 Nanocrystals," Advanced Functional Materials **15**, 763-770 (2005).
3. D. J. Kim, S. H. Hahn, S. H. Oh, and E. J. Kim, "Influence of calcination temperature on structural and optical properties of TiO2 thin films prepared by sol-gel dip coating," Materials Letters **57**, 355-360 (2002).
4. X. Wang, M. Fujimaki, and K. Awazu, "Photonic crystal structures in titanium dioxide (TiO2) and their optimal design," Optics Express **13**, 1486-1497 (2005).
5. S.-D. Mo, and W. Y. Ching, "Electronic and optical properties of three phases of titanium dioxide: Rutile, anatase, and brookite," Physical Review B **51**, 13023-13032 (1995).
6. T. Nishide, M. Sato, and H. Hara, "Crystal structure and optical property of TiO2 gels and films prepared from Ti-edta complexes as titania precursors," Journal of Materials Science **35**, 465-469 (2000).
7. M.-C. Kao, "Effects of annealing temperature of TiO_2 thin films for application in dye-sensitized solar cells," HSIUPING Journal **22**, 125-134 (2011).
8. T. Hashimoto, T. Yoko, and S. Sakka, "Sol-Gel Preparation and Third-Order NonLinear-Optical Properties of TiO2 Thin-Films," Bulletin of the Chemical Society of Japan **67**, 653-660 (1994).
9. Y. U. Ahn, E. J. Kim, H. T. Kim, and S. H. Hahn, "Variation of structural and optical properties of sol-gel TiO2 thin films with catalyst concentration and calcination temperature," Materials Letters **57**, 4660-4666 (2003).
10. J. A. Woollam, and P. G. Snyder, "Fundamentals and applications of variable angle spectroscopic ellipsometry," Materials Science and Engineering B-Solid State Materials for Advanced Technology **5**, 279-283 (1990).
11. I. J. A. Woollam Co., *Guide to Using WVASE32 Spectroscopic Ellipsometry Data Acquisition and Analysis Software* (Lincoln, NE, 1994).
12. M. Mosaddeq-ur-Rahman, G. Yu, T. Soga, T. Jimbo, H. Ebisu, and M. Umeno, "Refractive index and degree of inhomogeneity of nanocrystalline TiO2 thin films: Effects of substrate and annealing temperature," Journal of Applied Physics **88**, 4634-4641 (2000).

13. H. K. Kim, C. C. Li, G. Nykolak, and P. C. Becker, "Photoluminescence and electrical-properties of erbium-doped indium oxide-films prepared by rf-sputtering," Journal of Applied Physics **76**, 8209-8211 (1994).
14. A. Dakka, J. Lafait, and M. A.-L. a. C. Sella, "Optical studey of titanium dioxide thin films preapred by R.F. sputtering.," M.J.Condensed Matter **2**, 153 (1999).
15. S. H. Jeong, B. S. Kim, B. T. Lee, H. R. Park, and J. K. Kim, "Structural and optical properties of TiO2 films prepared using reactive RF magnetron sputtering," Journal of the Korean Physical Society **41**, 67-71 (2002).
16. O. Setyawati, M. Engenhorst, S. Wittzack, F. Köhler, C. Woidt, T. Woit, V. Daneker, M. Bartels, and H. Hillmer, "Dry etching of TiO2/SiO2 DBR mirrors for tunable optical sensor arrays," (2010), pp. 75910R-75910R-75918.
17. S. Norasetthekul, P. Y. Park, K. H. Baik, K. P. Lee, J. H. Shin, B. S. Jeong, V. Shishodia, E. S. Lambers, D. P. Norton, and S. J. Pearton, "Dry etch chemistries for TiO2 thin films," Applied Surface Science **185**, 27-33 (2001).
18. B. Wu, A. Kumar, and S. Pamarthy, "High aspect ratio silicon etch: A review," Journal of Applied Physics **108** (2010).
19. K. R. Williams, K. Gupta, and M. Wasilik, "Etch rates for micromachining processing-Part II," Microelectromechanical Systems, Journal of **12**, 761-778 (2003).
20. D. L. Flamm, "Mechanisms of silicon etching in fluorine-containing and chlorine-containing plasmas," Pure and Applied Chemistry **62**, 1709-1720 (1990).

Chapter 6 - Silicon 2D Photonic Crystals for Enhancing YF_3:Er Up-Conversion Emission

6.1 Chapter Overview

In this chapter the fabrication and analysis of 2D photonic crystals composed of Si and YF_3:Er is presented. Triangular arrays of Si pillars were prepared using electron beam lithography, lift-off of a metal mask and anisotropic reactive ion etching. Thin films of YF_3:Er were deposited between the Si pillars using thermal evaporation. Structural and optical analysis of the resulting up-conversion thin films and 2D photonic crystals were performed. The key optical parameters for this study were the refractive index of the YF_3:Er layer and the up-conversion photoluminescence, which were analysed using ellipsometry and confocal fluorescence spectroscopy respectively.

2D photonic crystals of Si with vertical side walls were successfully fabricated using ICP-RIE. Thin films of YF_3:Er were prepared, with their crystalline and fluorescence properties found to be directly dependent on the substrate temperature during deposition by thermal evaporation. An increase by a factor of 3.79 to the up-conversion emission at 980 nm (using 1523 nm excitation) was observed, however this could not be directly attributed to band edge enhancement from the photonic crystal. Improvements to the partial filling of the space between the Si pillars with YF_3:Er were explored, however this remained a key limiting factor in the fabrication process.

6.2 Metal Mask Fabrication

In this section the fabrication of metal masks for reactive ion etching is discussed. The use of aluminium and chromium masks prepared by the lift-off technique are compared and evaluated for use in this study.

Initial inspection of mask selectivity was carried out to find the appropriate type of mask material to use to etch silicon. The electron beam lithography system (section 4.2.6) was used to pattern features into the high resolution positive resist PMMA. Direct use of the PMMA resist as a mask was tested using a RIE gas chemistry known to etch silicon. However the PMMA mask was found to be completely removed very quickly and it was evident that it could not provide the desired selectivity to achieve the desired depth of silicon etch required. Therefore investigation of the use of metal masks was carried out to achieve a much higher etch selectivity.

The metal masks were deposited using thermal evaporation (section 4.2.8). Al and Cr were chosen to be investigated as metal mask materials due to their ease of evaporation, inert nature to fluoride based etch chemistries and selective removal in a wet chemical etch.

6.2.1 Metal Mask Fabrication Using Lift Off

Metal masks were prepared using the lift-off method [1, 2]. This method involves the deposition of a metal layer on top of a patterned lower layer, which is selectively removed by a wet chemical etch. This leaves the metal layer in a pattern that is the inverse of that obtained with the lower layer. The method is summarised in Figure 6-1.

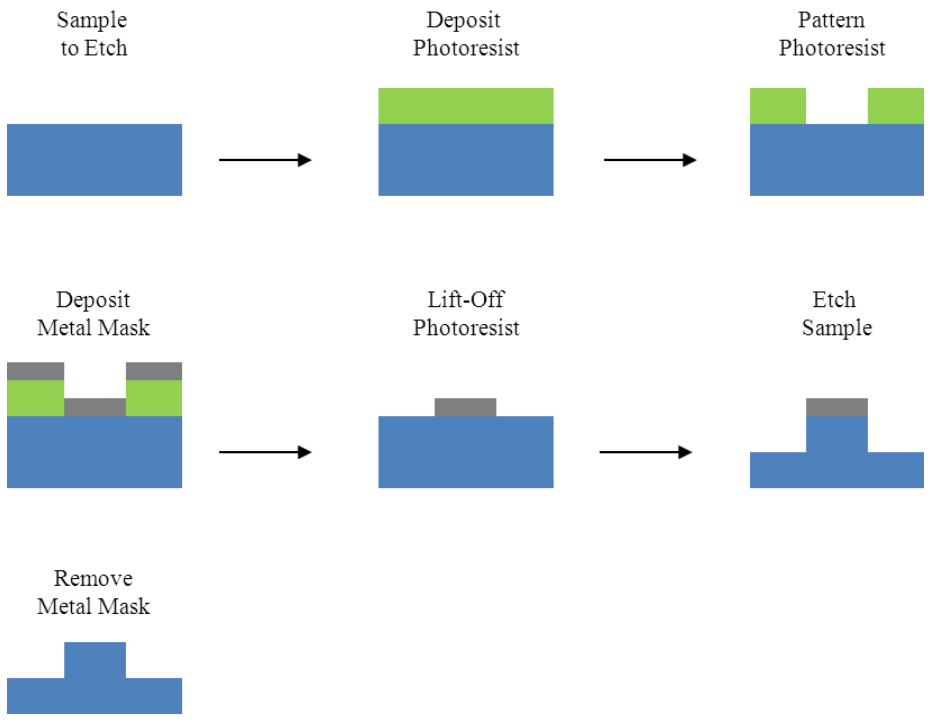

Figure 6-1: Schematic diagram of the lift-off method.

Thermal evaporation was used for the fabrication of metal masks by the lift-off technique. One advantage of thermal evaporation for this technique is that it allows for a highly directed deposition, resulting in lower side wall coverage than would be achieved by sputter deposition [2]. A disadvantage of thermal evaporation is that greater heating of the resist can occur, leading to softening of the edges and hence deposition of material onto the side walls, which inhibits the lift off procedure [2].

The deposition rate and final thickness were carefully controlled to benefit the lift off process. The deposition rate was kept as low as possible (around 5-10 nm/min) to

minimise sample heating [2]. In order to limit side wall coverage, films of no more than around 1/3 of the resist thickness were deposited.

To further minimise side wall coverage, the sample was positioned vertically above the metal source, with as great a distance in between source and substrate as possible. This distance was measured to be 27 cm in the evaporation chamber used.

It is advantageous for the PMMA layer to be as thick as possible; however there is a limit to the thickness available due to the lithography patterning process. A thicker PMMA layer allows for a longer of etch of the material layer below, or provides a greater separation of the top and bottom metal mask layers for lift off. However the thickness is limited by the depth to which the electrons from the electron beam lithography system can penetrate, therefore developing the polymer. For the combination of feature sizes desired and electron beam parameters used, the PMMA layer thickness was limited to around 350 nm.

Following the evaporation of the metal onto a patterned photoresist, the photoresist and upper metal layer were removed using a wet chemical etch. The sample was placed in an acetone solution (>99%) in an ultrasonic bath for 10 minutes. The sample was then blown dry with N_2 before being placed in a fresh solution of acetone in an ultrasonic bath for a further 10 minutes. Finally, the sample was blown dry with N_2. The ultrasonic bath helped to break any metal deposition on the side walls of the patterned photoresist. The second rinse in acetone was carried out to minimise contamination of loose pieces of metal from the surface of the patterned structure.

A comparison was carried out between Al and Cr to compare the adhesion of the metals to the silicon substrate, as well as comparing the overall lift off results. Samples consisting of triangular arrays of holes (~200 nm radius) were patterned in 30 μm x 30 μm squares using e-beam lithography in a PMMA photoresist. The hole radius was decreased between each patterned area. Sets of samples were evaporated with either Al or Cr, with each metal film 50±5 nm thick. Lift off was carried out leaving cylindrical disks of metal masks in place of the PMMA holes. The resulting arrays of cylindrical masks were analysed using optical microscopy, shown in Figure 6-2. The series of optical images show that lift off begins to fail for both Al and Cr as the radius of the masks decrease. At the smallest radius, lift off has failed for both Al and Cr, resulting in the loss of periodic structure and rendering the patterns useless. There is therefore a limit to the minimum radius of metal mask that can be used for further experimental work.

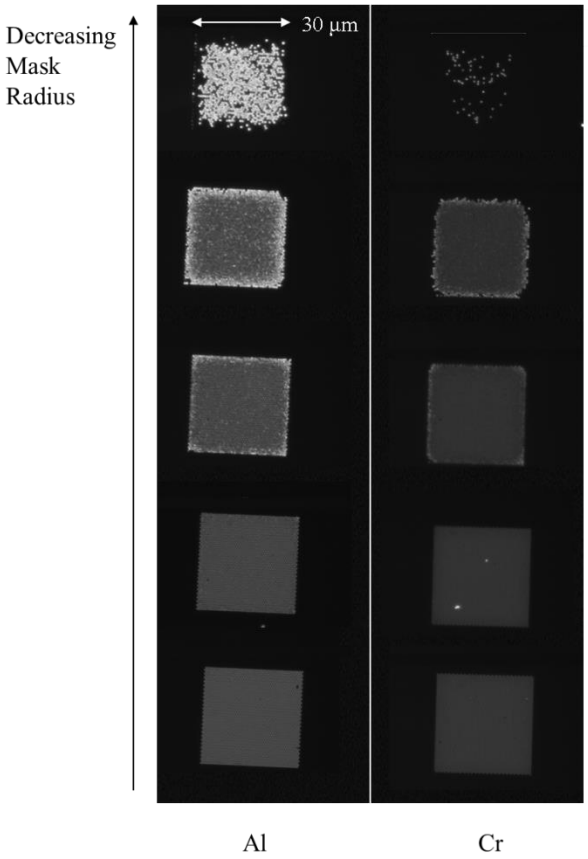

Figure 6-2: Optical microscope image of patterned metal masks. The cylindrical metal masks remaining following lift off for both Al and Cr is shown. As the mask radius decreases, lift off becomes less effective. For the smallest mask radius, successfull lift off is not achieved for either Al or Cr.

For very small mask radii, lift-off fails for both Al and Cr. For larger mask radii, very little difference in the lift off is observed between Al and Cr. Therefore Cr was chosen to use as the metal mask material for future work in this thesis due to its increased etch resistance to physical sputtering [3].

Two methods for metal mask pattern transfer have been successfully developed. Thin films of metal were deposited using thermal evaporation to achieve the desired metal thickness. Pattern transfer from a polymer photoresist was achieved using either dry metal etching of the metal layer below, or lift off of the metal layer above the patterned photoresist. A dry metal etch based on $SiCl_4$ was found to achieve good selectivity with a PMMA mask and good anisotropy. Both Al and Cr were shown to be suitable for lift off for the small geometrical dimensions required. Cr was chosen to be used for future work in this thesis due to its greater etch resistance to physical sputtering.

6.3 Reactive Ion Etching of Silicon

In this section the fabrication of nano-scale holes and pillars in Si by reactive ion etching is discussed. The development of an optimised reaction chemistry for the anisotropic etching of Si will be presented, along with an analysis of the fabrication process.

To achieve the desired Si etch depth, metal masks were prepared as described in the section 6.1. The simulations used to model the effect of the photonic crystal were 2D, therefore deeper Si features (higher aspect ratio) will provide a better representation of the modeled structure. A deeper 2D photonic crystal would also allow for a thicker up-conversion layer to be deposited, increasing the up-conversion signal and hence the signal to noise ratio.

6.3.1 Anisotropic Etching of Silicon

An anisotropic Si etch was required to achieve straight side walls, ensuring that the correct geometric parameters, critical to the device performance, were present throughout the depth of the 2D photonic crystal. Anisotropic etching using RIE is carried out by concurrent downward directed etching in conjunction with side wall passivation. By carefully controlling the etch chemistry and chamber conditions, the side wall angle can be tuned as desired.

Halogen based plasmas are most often used for the RIE of Si [4]. This is because they have high etch rates and the Si-halide etch products are volatile. Anisotropic etches are commonly achieved by using either F or Cl based plasmas.

For F based plasmas, the F atoms have been shown to be directly involved in the etching process [4]. Anisotropic etching can either be achieved by directly using SF_6 and reducing the substrate temperature down to around -120°C to form a passivating Si_xF_y side wall layer [5], or by introducing a polymer forming species to passivate the side walls [6].

For Cl based plasmas, etching is carried out by ion-induced etching only. This is because Cl atoms do not etch Si spontaneously at room temperature [4]. Therefore anisotropic etching is achieved by the inherent directionality of the ion species.

Due the chemicals available in the ICP-RIE system used (section 4.2.7), the etching of Si was limited to the use of F based plasmas. The plasma chemistry chosen, taking into

account the available gases in the system, was based on SF_6 and CHF_3. The main plasma radicals, products and inhibitors of these etch gases are shown in Table 6-1.

Gas	Radicals	Products	Inhibitor
CHF_3	CF_2	HF, (SiF_4)	$Si_xC_yF_z$, ($[CF_2]_n$)
SF_6	F, SF_5	SiF_4	$Si_xS_yF_z$[a]

Table 6-1: Summary of gases used for the RIE of Si, including their main plasma radicals, products and inhibitors. Table adapted from. Table adapted from [4]. [a] Only with cryogenic cooling.

The SF_6 gas provides fast isotropic atomic etching. The atomic F radicals formed in the plasma quickly form a fluorinated crust on the surface of the Si that extends around 5 monolayers into the bulk material [6]. Subsequent F atoms penetrate the top of this layer, attacking Si-Si bonds below the surface. The volatile products released are the stable SiF_4 and the free radical SiF_2. These free radical species combine with F in the surface layer forming further molecules of stable SiF_4 [6].

The CHF_3 gas provides an inhibitor film that induces anisotropy to the etching process. Under suitable plasma conditions the ion flux, which is perpendicular to the sample surface, prevents growth of the inhibitor film on the horizontal surfaces. Therefore selective deposition of the inhibitor layer on the vertical side walls occurs, preventing it from being etched. When using CHF_3 gas, perfluoroethylene ($[CF_2]_n$) films are deposited on the side walls [6]. Varying the ratio of SF_6 to CHF_3 allows for the angle of the side walls during the etch to be controlled. In particular, the ratio F/C is often used as a measure of etching (F^*) over deposition (CF_x^*) [7].

It is important to maintain control of the substrate temperature during the etching process. Temperature is a key parameter in the reaction chamber, controlling every energy step including adsorption and chemical reaction [4]. It was found that the carrier wafer can have a significant effect on the substrate temperature. A silicon etch was performed under the same reaction conditions using both a C (graphite) carrier wafer and a TiO_2 coated Si carrier wafer. The C carrier wafer was 5 mm thick and the sample was placed on the carrier wafer directly, with no intermediate layer. The TiO_2 coated Si wafer was 502 μm thick and a Fomblin oil intermediate layer was used to ensure good thermal contact between the sample and carrier wafer. The Si etch carried out using the TiO_2 coated Si wafer was subject to a 1 minute holding step before the plasma was induced, in order to reach thermal equilibrium with the actively cooled bottom contact of the RIE. All of these

adaptations were carried out to maximize cooling of the substrate during the etching process. The thermal conductivity of Si (12.4 W/m.K) is greater than that of C-graphite (0.18-1.29 W/m.K) [8]. Therefore a greater heat transfer is expected to take place across the thinner Si carrier wafer than the thicker C carrier wafer (assuming the 2 μm TiO_2 layer to be negligible in the heat transfer process).

From Figure 6-3 it can be seen that the temperature of the substrate during the etch plays a critical role in the anisotropy achieved. The base of the carrier wafer was set to 20°C for all etches, using the circulating chiller. The Si etch achieved using the C carrier wafer, shown in Figure 6-3 (a), reveals an isotropic etch with a large undercut of the mask. In comparison the Si etch achieved using the TiO_2 coated Si carrier wafer, shown in Figure 6-3 (b), shows a much smaller undercut with more vertical side walls. This suggests that the sample is cooler during the etch, allowing for increased deposition of the polymer passivation layer on the vertical side walls.

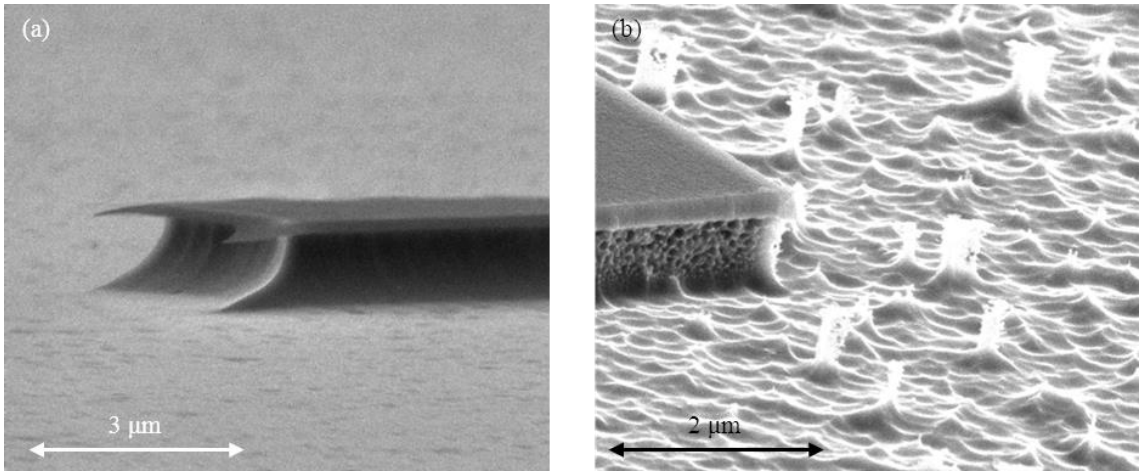

Figure 6-3: SEM micrograph of etched Si features. The carrier wafer has a strong influence on the substrate temperature, which in turn influences the anisotropy of the etch. (a) Si etch with C carrier wafer showing a large undercut from the isotropic etch. (b) Si etch with TiO_2 coated Si carrier wafer showing an anisotropic etch.

It was found that using an uncoated Si carrier wafer resulted in a near identical anisotropy as shown for the TiO_2 coated Si carrier wafer. Therefore a bare Si carrier wafer (with intermediate Fomblin oil contact layer) was used for all subsequent Si etches, with the base of the carrier wafer set to 20°C.

A series of characterisation etches were carried out to determine the F/C ratio to optimise the anisotropy of the Si etch. The etch chemistry was kept constant apart from the SF_6 flow rate, which was decreased stepwise. The parameters for the general etch conditions are detailed in

Table 6-2, where the SF_6 flow rate was decreased in steps of 2 from 10 to 4 sccm. The substrate was maintained at 20°C throughout the etch using water cooling. The results of the characterisation etched are shown in Figure 6-4.

RF Power (W)	ICP Power (W)	Pressure (mTorr)	SF_6 (sccm)	CHF_3 (sccm)
20	200	9.5	x	70

Table 6-2: General etch conditions for anisotropic Si etching. x =4, 6, 8 and 10.

The geometric profiles of the Si etch were analysed to find the optimum parameters for anisotropic etching. Both the side wall angles and vertical etch depths were investigated. The 0 degree angle was chosen to be in the vertical direction, where a negative side wall angle corresponds to an undercut of the mask. The Si etch was measured from the bottom of the mask to the top of the substrate layer below. The results of the characterisation analysis are shown in Figure 6-5.

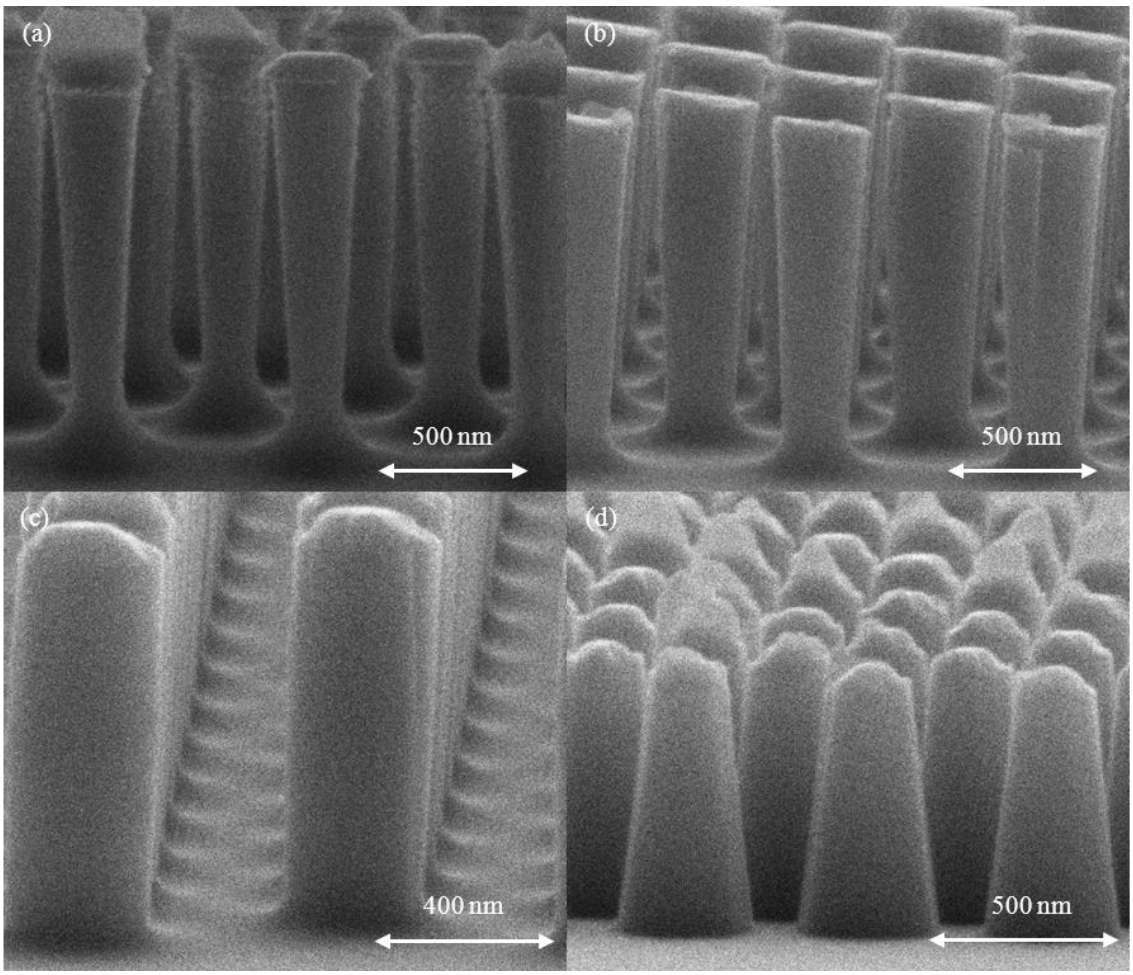

Figure 6-4: SEM micrographs of Si pillars. The SF_6 flow rate, measured in sccm, was decreased from 10 (a), 8 (b), 6 (c) to 4 (d). As the SF_6 flow rate decreased, polymer passivation of the side walls increased and so the anisotropy of the etch could be controlled.

From Figure 6-5 it can be seen that anisotropic etching was found to occur using 6 sccm of SF_6, resulting in a vertical etch rate of 839±19 nm/min. The large uncertainty in the side wall angle measurements are as a result of very shallow angles being measured along a grainy edge boundary from the SEM images.

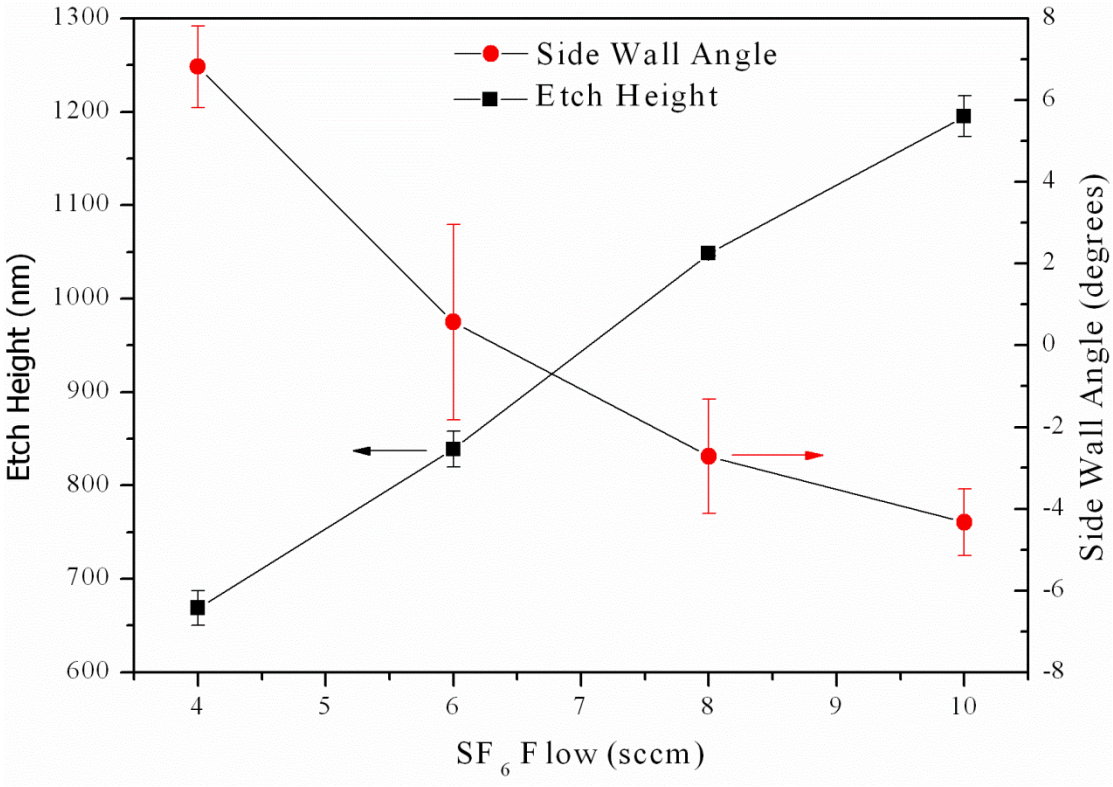

Figure 6-5: Side wall angle and etch height of Si pillars as a function of SF_6 flow. Increasing the SF_6 flow rate increased both the vertical and horizontal etch, resulting in an undercut of the mask (negative side wall angle). Anisotropic etching was found to occur using 6 sccm of SF_6, resulting in a vertical etch rate of 839±19 nm/min.

The condition of the chamber walls can have a significant effect on the etch chemistry. The ICP-RIE system used to carry out the etches was a central research facility and there was no guarantee that the chamber walls would be in the same condition as when the previous etch was carried out, due to other facility users. In a low pressure plasma, the radicals collide just as frequently with the reactor walls as with each other. Recombination reactions, in particular, have a huge effect on the radical densities [9]. During the course of the reaction, the reactor walls will in general be coated with the same material that is forming the passivation layer on the side walls of the etched features. As this layer builds and the temperature and chemical nature of the reactor walls change, process drift can occur whereby the conditions required for anisotropic etching can change slightly from wafer to wafer.

To try to minimise adverse effects from the chamber wall, the chamber was conditioned using a set of etches with a bare Si carrier wafer before the samples were etched. The cleaning and conditioning etches carried out are shown in

Table 6-3.

Etch	RF Power (W)	ICP Power (W)	Pressure (mTorr)	SF_6 (sccm)	CHF_3 (sccm)	O_2 (sccm)	Ar (sccm)	Time (min)
O_2 Clean	0	250	20	0	0	50	10	10
Condition	20	200	9.5	6	70	0	0	10

Table 6-3: The chamber conditioning etches were carried out before each set of samples to minimise adverse effects from the chamber walls. The O_2 cleaning plasma was carried out before the SF_6 conditioning plasma.

The chamber walls required manual cleaning when a thick film of material had built up from successive users running insufficient cleaning etches (see Figure 6-6). If left in this dirty state, the reaction chemistry would not only be altered, there would also be deposition of chamber wall material onto the sample below. Manual cleaning was carried out using a scotch pad and isopropanol. The constantly varying conditions of the chamber walls meant that the SF_6 flow rate was occasionally varied by a very small amount (0.5-1 sccm) in order to fine tune the side wall angle to ensure anisotropic etching.

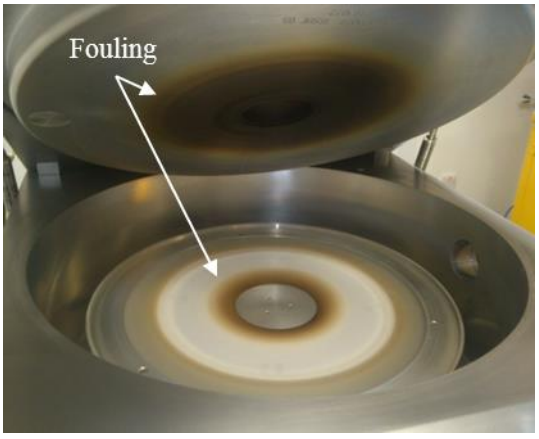

Figure 6-6: ICP-RIE chamber. Insufficient cleaning by multiple users of the ICP-RIE meant that manual cleaning was required. Fouling of the top surface of the reaction chamber and of the quartz ring clamp is apparent as a brown stain in the above image of the reaction chamber.

It has been shown that careful control of the reaction chemistry and understanding of the influencing factors has allowed for characterisation and optimisation of the anisotropic etching of Si to be achieved. The optimised etch chemistry developed was used for the fabrication of 2D Si photonic crystals.

The anisotropic etching of Si using IPC-RIE has been optimised for nanoscale features. An analysis of the factors effecting the anisotropy has been carried out. Investigation of the selectivity of the Cr mask has shown that it can be used to achieve the desired etch depths for fabrication of the 2D photonic crystals.

6.4 YF_3:Er Thin Films by Thermal Evaporation

In this section the fabrication of YF_3:Er thin films by thermal evaporation is discussed. The synthesis of the source material and particular requirements of the deposition procedure are presented, along with an analysis of the optical and structural properties of the thin film.

Thermal evaporation of YF_3:Er was required to achieve a uniform thin film deposition of the up-conversion material between the etched Si features. In this section the synthesis of the YF_3:Er source material is detailed, along with the effects of the substrate temperature on the film crystallinity, and subsequent optical properties, as well as the ellipsometry modelling to determine the refractive index. The refractive index experimental data was vital for the simulation of the 2D photonic crystals. Thermal evaporation was chosen as it provided a convenient way of depositing thin films of material from a powder source.

6.4.1 Chemical Synthesis of YF_3:Er

Powdered YF_3:Er was synthesised for use as the source material for thermal evaporation. Previous laboratory work carried out in the research group by Dr Jose Marques-Hueso had shown that the greatest up-conversion signal from the bulk powder could be obtained with an Er doping concentration of 7.5at%. This doping concentration was therefore chosen as a suitable starting point for the source material for thin film deposition.

A co-precipitation method was used for the fabrication of YF_3:Er. This was based on the work by Pandurangappa *et al.* who used this method to synthesise and characterise CaF_2 [10]. This method was chosen for its repeatable, mature procedure, suitability for Y precursors; and ease of Er doping [11]. The chemical precursors and their respective weights used are detailed in

Table 6-4 with the synthesis procedure below.

Precursor	Atomic Weight (g/mol)	Mol Ratio Required	Weight (g)
$YCl.6H_2O$	303.4	0.925	1.403
NH_4F	37	3	0.555
$ErCl_3.6H_2O$	382	0.075	0.143

Table 6-4: Weight of precursors used for the synthesis of 7.5.at% Er doped YF_3.

The $YCl.6H_2O$ and $ErCl_3.6H_2O$ were dissolved in 10 ml of H_2O in a 20 ml glass vial. NH_4F was then dissolved in 10 ml of H_2O and added very slowly, dropwise, to the chloride solution. This solution was stirred vigorously, using a magnetic stirrer, for 2 hours, transforming the transparent mixture into an opaque pinky white suspension. The mixture was then centrifuged for 10 minutes at 5000 rpm to separate the suspended YF_3:Er powder from the reaming solution, which was decanted from the vial. The powder was washed three times with ethanol (99.99%) plus centrifugation to remove residual chloride and ammonium ions. The final YF_3:Er powder was transferred to a glass dish and allowed to dry in air, before being transferred to a ceramic combustion boat and sintered in a N_2 purged tube furnace. The sintering conditions are detailed in

Table 6-5.

Stage	Procedure
1	Increase temperature by 10°C/min to 300°C and dwell for 1 hour
2	Increase temperature by 20°C/min to 800°C and dwell for 2 hours
3	Allow furnace to cool down to 20°C

Table 6-5: N_2 purged tube furnace conditions for sintering of YF_3:Er.

XRD analysis was used to determine the phase and composition of the YF_3:Er powder formed. The spectra of the powdered sample, along with corresponding peak positions are shown in Figure 6-7 and Table 6-6 respectively. The peak positions were compared against those documented for un-doped orthorhombic YF_3 crystal structure, showing very good correspondence. At the low Er doping concentration of 7.5% there was found to be very little change in the peak positions.

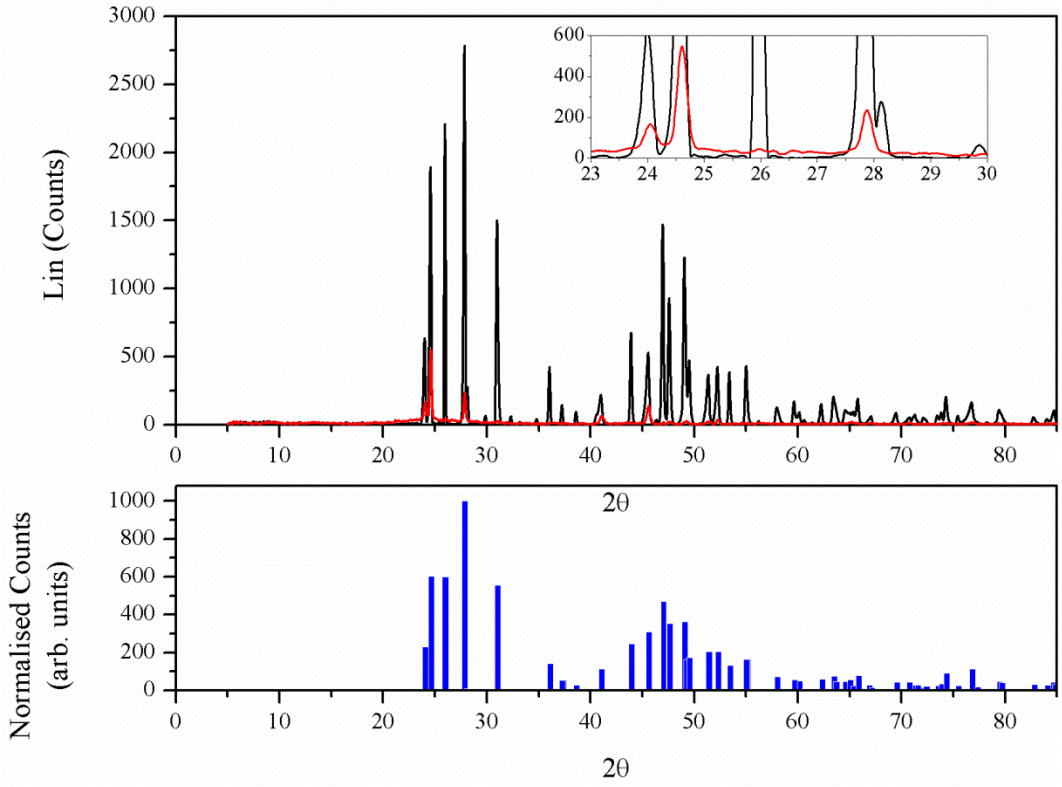

Figure 6-7: XRD results of thin film YF_3:Er deposited onto a 200°C substrate (red) and powdered YF_3:Er bulk material (black). The peak positions found for the thin film layer correspond with peaks observed for the bulk material, indicating that a material of the same crystalline phase has been achieved.

Zalkin *et al.* YF_3		Powdered YF_3:Er		Thin Film YF_3:Er	
d_{hkl}	Intensity	d_{hkl}	Intensity	d_{hkl}	Intensity
3.610	64	3.620	68	3.615	100
3.427	62	3.428	79		
3.194	100	3.201	100	3.188	43
2.882	53	2.883	54		
1.987	39	1.989	19	1.987	25
1.931	46	1.933	53		

Table 6-6: The peak positions for the powder and thin film samples compare well with the literature values for undoped orthorhombic YF_3. The 6 peaks of highest intensity are compared here, with a full comparison available in Appendix B.

The chemical synthesis of Er doped YF_3 has been carried out for a doping concentration of 7.5at.% using the co-precipitation method. XRD analysis showed good correspondence

with the un-doped YF_3 reference, indicating that the YF_3:Er was of an orthorhombic crystal structure.

6.4.2 Thin Film Deposition with Substrate Heating

Thin film deposition was carried out by thermal evaporation (section 4.2.9) and initial evaporation attempts revealed that the temperature of the substrate during evaporation was critical to the final phase of material (see section 6.4.3). This phase was found to have a direct effect on the up-conversion emission of YF_3:Er at 980 nm. Therefore the substrate was heated during the evaporation to maintain a temperature of >200°C.

In order to heat the substrate in a controlled manner within the evaporation chamber, a customised substrate heater was designed and built. The only electrical connection into the chamber was through an 8 pin DIN low voltage connection. The low voltage wires meant that a standard vacuum chamber heater could not be used. Therefore a substrate heater based on coiled resistance wire was constructed, with a thermocouple to provide temperature feedback. A schematic of the low voltage heater is shown in Figure 6-8.

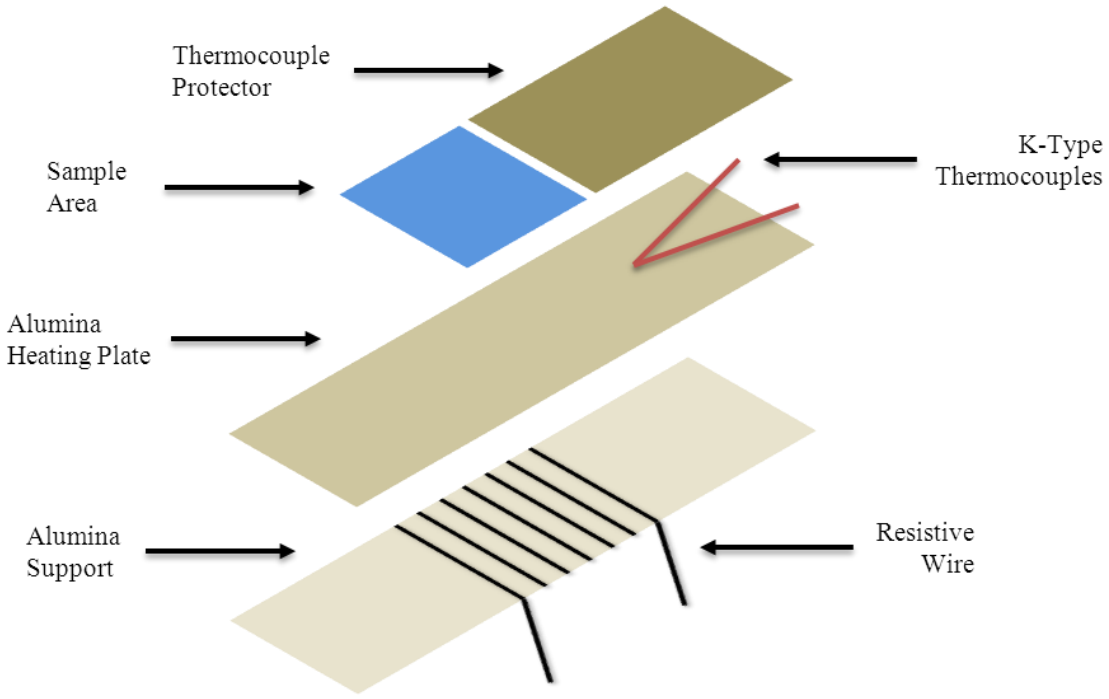

Figure 6-8: Expanded view of low voltage DC sample heater. An increase in temperature was achieved though joule heating of the coiled wire. Temperature feedback was achieved through the K-type thermocouples. Samples were placed directly above the resistive wire coil on the alumina heating plate.

The resistive wire provides heat through joule heating. The 0.318 m length of wire used had a resistance of 78.7 Ω/meter. The current supplied to achieve the desired temperature of 200°C was 624 mA which is a power of 30.66 W. The wire loops were held apart by notches that were ground into the edge of the alumina support sheet to avoid a short circuit. A K-type thermocouple was held against the surface of the alumina heating plate and was protected from the evaporating material by an alumina protecting layer. Samples were clamped in place on the sample area and the whole sample heater was mounted upside down in the vacuum chamber, above the source material. Flexible fiberglass wire jackets were used to protect the loose ends of the resistance and thermocouple wires from the evaporated material.

It was important to increase the temperature of the heater in a slow and controlled manner. Heat dissipation between the resistance wire and the alumina heating plate in the vacuum chamber is limited to conduction and radiation, with no convection. If the current through the resistance wire was increased to fast to too high a current, the low heat dissipation from the wire would result in it melting and breaking the circuit. It was found that a slow increase in the current to 624 mA was sufficient to achieve the required temperature of >200°C, without melting the resistance wire.

Radiant heat from the source filament increased the temperature of the heating plate during evaporation. It was found that the temperature of the alumina heating plate increased to a maximum value of 236°C during evaporation.

Following evaporation, the substrate heater was left on to maintain a temperature of 200°C for 30 minutes. This was to provide additional time for the thin film to anneal and to minimise the risk of cracking during the cooling to room temperature. The chamber was left under vacuum for at least 2 hours following the final annealing stage to ensure that the substrates had reached room temperature before exposing them to air.

The evaporated YF_3:Er formed a homogeneous and dense uniform layer across the sample area. Films were found to deposit well on Si, SiO_2, microscope glass (70% SiO_2) and ITO substrates. The film appeared consistent throughout its cross sectional area when viewed by SEM. An image of the YF_3:Er layer is shown in Figure 6-9. This layer was measured by ellipsometry to be 680±20 nm thick.

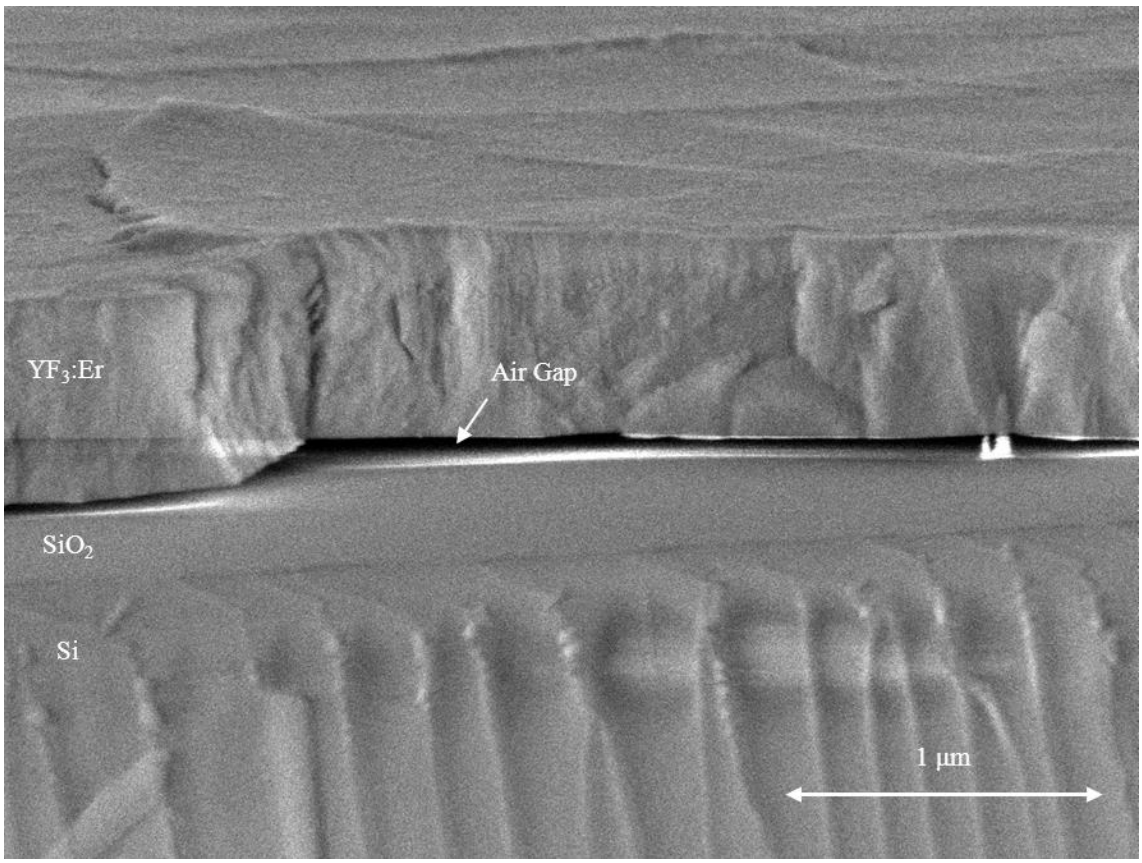

Figure 6-9: The SEM micrograph shows that a homogeneous and dense layer of YF_3:Er was achieved by thermal evaporation. The layer was measured to be 680±20 nm.

6.4.3 Effect of Substrate Temperature on the Crystalline Properties of YF_3:Er

The substrate temperature during evaporation was found to have a direct effect on the crystallinity and optical properties of YF_3:Er. In this section the effects of the substrate temperature on the crystalline properties are investigated. Furthermore the results of post annealing treatment are discussed. XRD analysis was carried out using the system described in section 4.3.4.

The phase of the thin film was found to vary between amorphous and crystalline, according to the temperature of the substrate during deposition. A comparison of the XRD spectra obtained from thin films deposited on substrates at 22°C (room temperature) and 200°C is shown in Figure 6-10. These films were deposited onto an amorphous microscope glass (70% SiO_2) substrate.

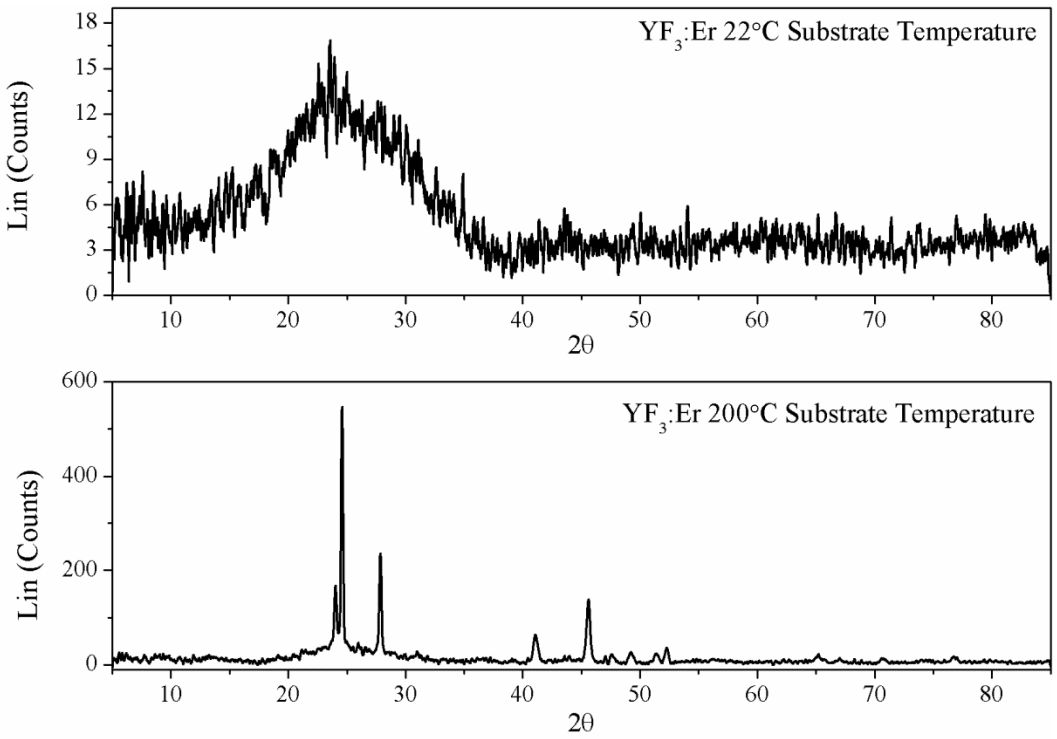

Figure 6-10: The XRD results of the YF_3:Er deposited onto a substrate at 200°C shows clear crystlline peaks in the expected positions for crystalline YF_3, whereas the XRD results of the YF_3:Er deposited onto a substrates at 22°C shows no clear peaks, indicating an amorphous structure. The broad peak at an angle of 25° for the 22°C sample is prodominantly due to the amorphous glass substrate layer.

The XRD result of the YF_3:Er deposited onto a substrate at 22°C shows no distinct peaks and a broad low intensity hump at around 25 degrees. The lack of peaks suggest that the film does not have a crystalline structure and so indicates that the film is amorphous. The broad hump is characteristic of the amorphous substrate on which the film was deposited.

The XRD result of the YF_3:Er deposited onto a substrate at 200°C shows distinctive crystalline peaks. The spectra of the powdered and thin film samples are compared in Figure 6-7. The peaks observed for the thin film sample (red) correspond well with those obtained from the powdered bulk material. This indicates that the thin film layer is of the same crystalline phase as the bulk material. The absence of some of the peaks found in the powder, but not in the thin film sample is believed to be due to alignment of the crystalline thin film within the XRD setup. Powdered samples allow for analysis of every preferential growth of certain crystal planes due to the random orientation of the powdered material. However the thin film layer provides a uniform crystal direction throughout. The increase in crystallinity will reduce the occurrence of defects in the material, which is thought to lead to an increase in the material's luminescent properties [12].

A comparison of the peak positions for the thin film and bulk powder material of YF_3:Er; and literature values for undoped YF_3 was carried out. The six peaks of highest intensity published by Zalkin *et al.* were compared with the peak positons measured experimentally, as detailed in

Table 6-6, and were shown to give a very high correlation. This indicates that the 7.5% Er doped YF_3 in both powder and thin film forms retains the same orthorhombic crystal structure as the undoped material.

Experiments were carried out to establish whether crystalline YF_3:Er could be achieved by post-annealing of a thin film that was deposited onto a substrate at 22°C. The advantage of post-annealing treatment would mean that the substrate area to be deposited would not be limited to the small area of the sample heater (~9 cm^2). Samples were annealed at 250°C, 450°C, 850°C and 1000°C in a N_2 purged tube furnace. The XRD results of the samples annealed at 250°C and 1000°C are shown in Figure 6-11. The spectra of the powdered sample and the sample prepared with a 200°C heated substrate are shown for comparison over the fingerprint region.

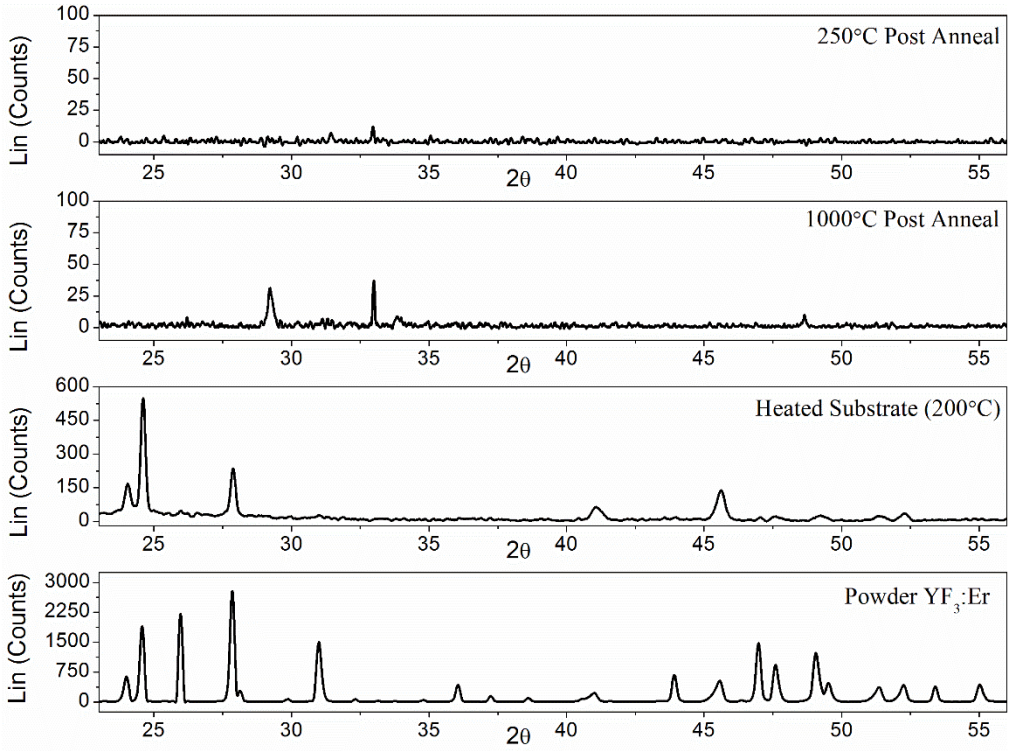

Figure 6-11: XRD results for YF_3:Er thin film (250°C Post Anneal, 1000°C Post Anneal, Heated Substrate) and powder samples across the 2θ range of 20° to 55°. It was found that post-annealing YF_3:Er thin films that were deposited on to substrates at 22°C had little influence on the crystalline phase. Samples were post annealed at 250°C and 1000°C and were compared against the fingerprint regions for both the thin films layers deposited onto a substrate at 200°C, as well as the powder sample.

Post-annealing of the amorphous samples prepared on a substrate at 22°C was shown to have little effect on the crystallinity of the sample. Very small peaks were observed in the XRD spectra, however they were not found to be directly related to the crystal structure observed for the crystallineYF_3:Er observed earlier.

6.4.4 Effect of Substrate Temperature on Optical Properties of YF_3:Er

The temperature of the substrate and subsequent crystallinity were found to have a dramatic effect on the optical properties of the YF_3:Er thin films. The effect on the up-conversion emission at 980 nm was of particular interest for this work.

The up-conversion emission at 980 nm from excitation at 1523 nm of thin films deposited on substrates at 22°C and 227°C are shown in Figure 6-12. These measurements were taken using the confocal set-up and Edinburgh Instruments Fluorescence Spectrometer as detailed in Section 4.3.2**Error! Reference source not found.**. The maximum emission monochromator slit size of 20 nm and maximum excitation power of 1.70±0.05 mW were used for the measurement of both samples in order to detect any very weak emission at 980 nm in the amorphous sample. The samples chosen were of comparable thickness: the amorphous and crystalline thin films were measured using ellipsometry to be 700 nm and 630 nm respectively. Both samples were of 10% Er doping concentration.

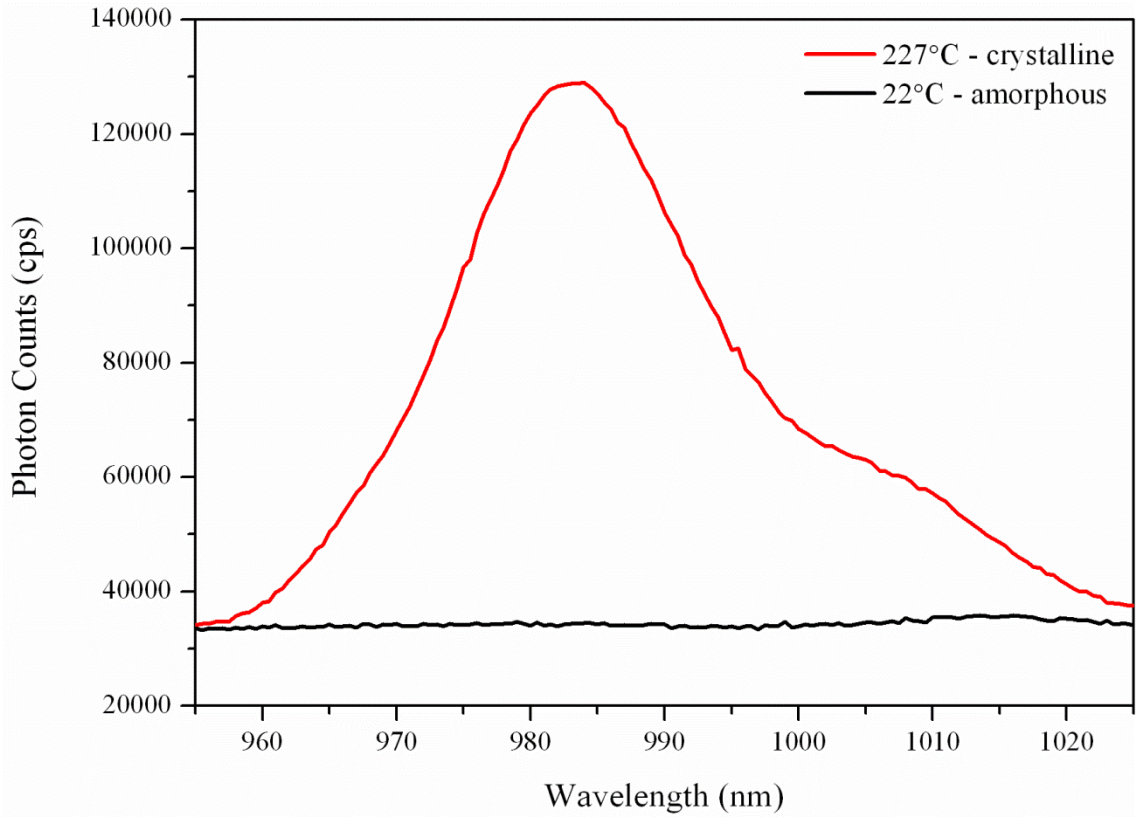

Figure 6-12: A very large up-conversion emission at 980 nm from excitation at 1523 nm was observed for the crystalline YF_3:Er thin film layer deposited on a substrate at 227°C. No emission at 980 nm was observed for the amorphous YF_3:Er thin film layer deposited on a substrate at 22°C.

A strong emission at 980 nm was observed for the crystalline sample, whereas no emission was observed for the amorphous sample. These results agree with those of Yanes *et al.*, who demonstrated that in glassy-amorphous environments luminescent emission can be completely quenched [13]. Furthermore, the effect of the phonon-energy of the host environment on the up-conversion emission of Er^{3+} has been explored in detail by Fischer *et al.*, who demonstrated that the efficiency of up-conversion emission is greatly reduced for host environments with increased phonon energy, which is consistent with a reduction in crystallinity [14].

6.4.5 Ellipsometry Modelling of YF_3:Er

Characterisation of the refractive index of the evaporated YF_3:Er thin films was essential to correctly model the band structure of the 2D photonic crystals. This characterisation was carried out using variable angle surface ellipsometry using the system described in section 4.3.1. The modelling was carried out using the WVASE software. The thin films of YF_3:Er prepared by evaporation have been shown previously in this chapter to be uniform and dense and therefore are ideal for ellipsometry analysis.

The thin films of YF_3:Er investigated using ellipsometry were prepared on bare Si wafers. This provided a high contrast in refractive index between the YF_3:Er layer (expected to be around n=1.5) and the substrate (around n=3.5), ensuring that the signal from the fluoride-silicon interface would be strong and therefore maximising the signal to noise ratio. The YF_3:Er layer in the 2D photonic crystals was expected to be mainly in contact with a Si interface, therefore a bare Si substrate for refractive index analysis was deemed to be the most appropriate.

The general ellipsometry modelling procedure, as detailed in section 4.3.1, was used to model the experimental data. The analysis of the data was carried out over the full spectral range available, from 300-2500 nm, to maximise the accuracy of the model.

A Genosc layer was used to accurately model the real and imaginary components of the refractive index of the YF_3:Er thin film. This Genosc layer models the dielectric function as a linear sum of the real and complex oscillator terms. As detailed in section 4.3.1, every Genosc layer consists of two Pole oscillators and an $e1$ offset. Additional oscillators (e.g. Lorentz, Gaussian) are added to account for absorption where required [15]. The Genosc model optimised for the first thin film deposition of YF_3:Er is detailed in

Table 6-7.

Oscillator	E_n (eV)	A_n (eV)	Br_n (eV)
Pole 1	12.2±0.2	160±11	0
Pole 2	0.001	0.011±0.002	0
Gaussian	3.6±0.1	0.025±0.001	3.1±0.3

Table 6-7: Genosc parameters for the first YF_3:Er film deposited onto a substrate at 200°C. The e1 value for this model was calculated to be 1.29±0.05 eV.

The complete expressions for the oscillators used are detailed in 4.3.1. The additional physical parameters from the modelling were as follows: film thickness = 643±1 nm; thickness non-uniformity = 2.6±0.2%; and the mean square error was calculated to be 14.45. A significant improvement in the MSE was found to occur through the addition of a simple index gradient to the Genosc layer. The minimum MSE value of 14.45 occurred for an effective step in the refractive index at the base of the film. The profile of the refractive index step, measured using ellipsometry, is shown in Figure 6-13.

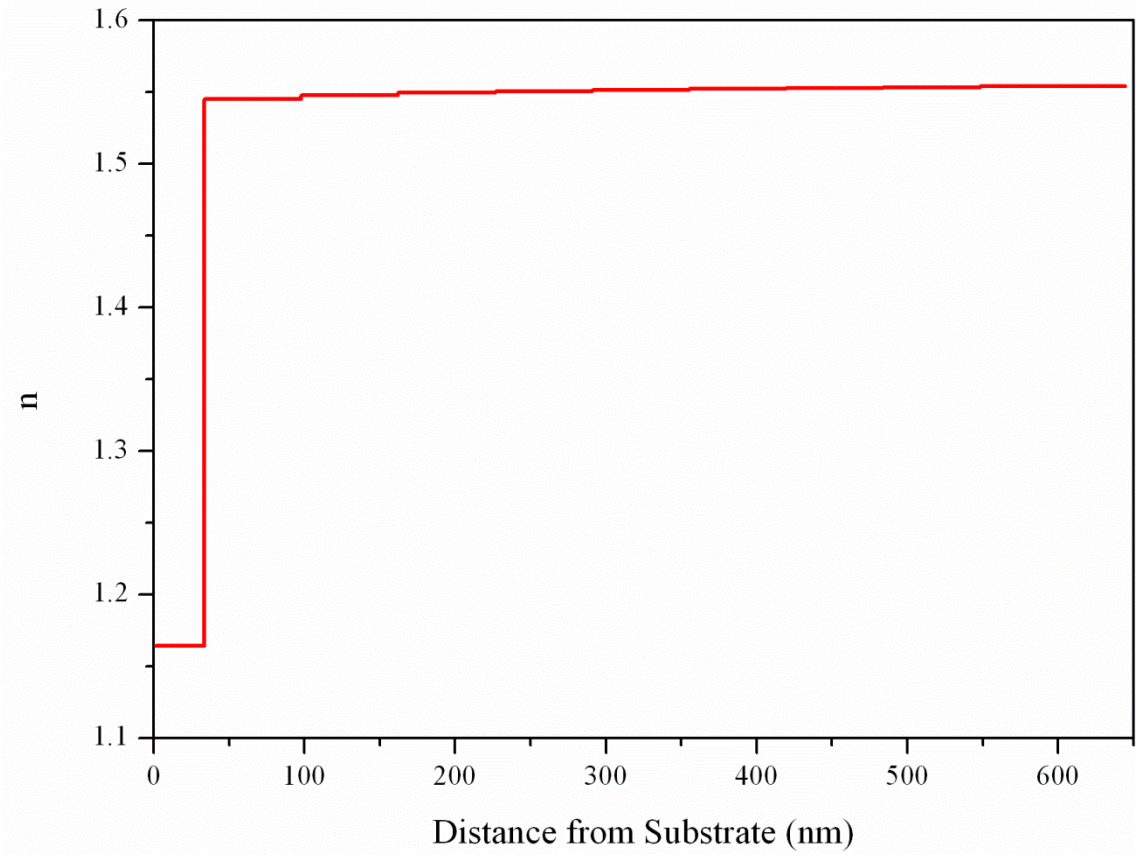

Figure 6-13: The refractive index depth profile modelled for the YF_3:Er layer using ellipsometric data was found to exhibit a step in refractive index at around 34 nm from the substrate surface.

The step in refractive index is most likely attributed to the interface between the top of the thin native layer of SiO_2 formed on the Si surface and the bottom of the YF_3:Er film. The SEM image of the cross-section of the YF_3:Er film in Figure 6-9 shows a thin gap between the YF_3:Er film and the substrate layer below. If this gap existed partially, or completely through the sample area of the ellipsometry analysis, there would be an effective step in refractive index, lower than that of the YF_3:Er film, as observed in the model.

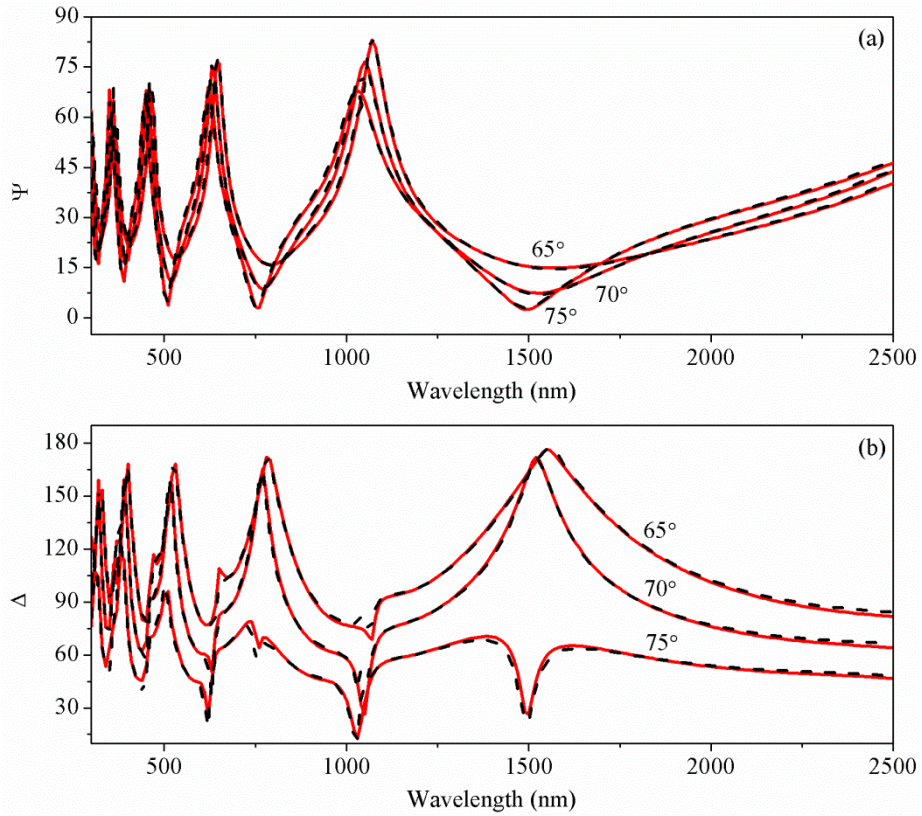

Figure 6-14: The black dotted line shows the experimental data, while the red line shows the model. A very good agreement between the experimental data and the model for both Ψ (top) and Δ (bottom) was achieved, resulting in a low MSE of 14.45. (a) corresponds to the lower wavelength range and (b) to the upper wavelength range, where the elipsometry data was acquired and modelled for the angles of 65°, 70° and 75°.

The same Genosc layer was used to model the subsequent deposited YF_3:Er thin films. The parameters from the original Genosc layer specified above were held constant to optimise the thickness for each of the subsequent layers. This brought the model very close to the experimental data. All parameters were then allowed to vary for a final iterative fitting process to minimise the MSE. The refractive index results for the original (1) and two subsequent films (2,3) are shown in Figure 6-15.

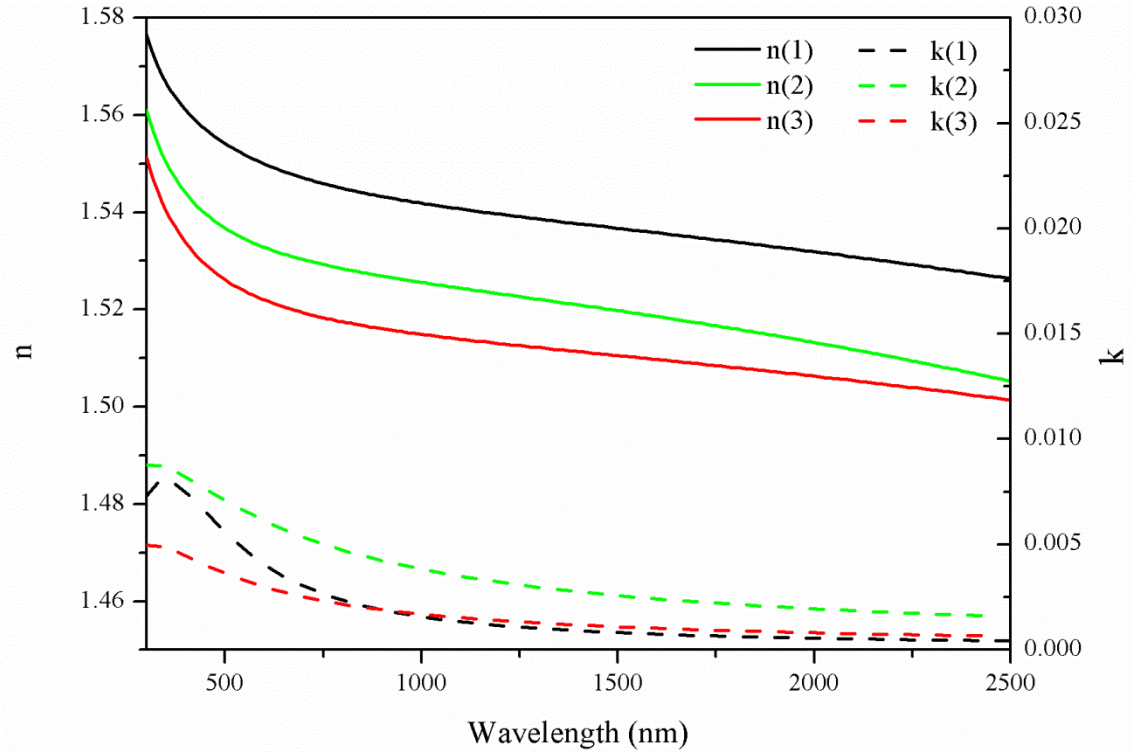

Figure 6-15: The real (n) and imaginary (k) components of the refractive index are shown for three YF_3:Er films (1,2,3). The refractive index was found to vary between the films, which were deposited under near identical process conditions.

Both the real and refractive index parameters were found to vary significantly between films. This was unexpected as the process conditions for all three films were nearly identical. Two changes between the film depositions methods were a slight variation in the final temperature of the substrate during deposition, and the film thickness, which are summarised in

Table 6-8. However no apparent consecutive relationship is observed between the final substrate temperature, or film thickness with the change in refractive index.

The repeatability of the measurement and analysis of a single film was carried out by taking measurements and analysing the data from three different locations on the same film. From this study, the mean percentage uncertainty was found to be ±0.57% for n and ±3.1% for k. In comparison, the mean percentage error between the three films analysed in Figure 6-8 was found to be ±4.62% for n and ±56.9% for k. Therefore the difference between the films is substantially greater than the error in the repeatability of the measurement and analysis.

YF_3:Er Film	Final Substrate Temperature (°C)	Film Thickness (nm)

1	227	643
2	236	1006
3	221	765

Table 6-8: The final substrate temperatures and film thicknesses of the three YF_3:Er films are shown for comparison.

The refractive indices at 600 nm obtained experimentally were compared against those found in literature in

Table 6-9. The comparison showed that the values obtained experimentally lie within the range for rare-earth doped and un-doped YF_3:Er films analysed elsewhere.

Thin Film Composition	Refractive Index at 600 nm
YF_3:Er (1)	1.55
YF_3:Er (2)	1.53
YF_3:Er (3)	1.52
YF_3:Er/Yb [16]	1.51
YF_3 [17]	1.57
YF_3 [18]	1.53

Table 6-9: The refractive indices of the experimentally evaporated YF_3:Er films were found to be within the same range of those detailed for films of YF_3:Er/Yb and YF_3:Er in literature.

The refractive index acquired through ellipsometry was essential for the simulations of the 2D photonic crystals. At the time of carrying out the simulations for the final structures, the refractive index values available were those obtained from the thin films deposited on a substrate at room temperature. The overall refractive index across the spectral range was found to be slightly lower than that obtained for the films evaporated onto the substrate at 200°C. At 600 nm the refractive index of the film evaporated at room temperature was found to be 1.50, which is only 0.02 less than the lowest refractive index measured for the films evaporated at a substrate temperature greater than 200°C. Furthermore, the inhomogeneous filling of the space between the Si pillars, observed in section 6.4.6, will reduce the effective refractive index of the spaces between the pillars. Therefore the small reduction in refractive index used in the simulation of the final structures was not thought to be detrimental to the final optical measurements, given the range of 2D photonic crystals fabricated for the final measurements (section 6.5).

The wavelengths of interest for this work were 1523 and 980 nm, corresponding to the peak of absorption and up-converted emission in Er^{3+}. The refractive indices found experimentally for use in the simulations were $n_{(980)} = 1.53 \pm 0.07$ and $n_{(1523)} = 1.52 \pm 0.07$. These values were incorporated into the 2D photonic crystal simulations, as described in Chapter 3, in order to predict the required geometry for enhancement.

6.4.6 Evaporation of YF_3:Er onto Si 2D Photonic Crystals

The evaporation of YF_3:Er onto the Si 2D photonic crystal was a key step in the fabrication of the final devices. Complete homogenous filling of the space between the Si pillars was essential to achieve the desired refractive index contrast. This would maximise the effect of the 2D photonic crystal as well as provide an analogous structure to the simulated models.

Initial investigation of the filling of the space between the Si pillars revealed non-homogeneous filling. Focused Ion Beam (FIB) etching was carried out, using the system described in section 4.2.10, to investigate the filling of the YF_3:Er material between the Si pillars. The trench fabricated by ion sputtering is shown in Figure 6-16(a), with a cross-sectional view of the filling shown in Figure 6-16(b).

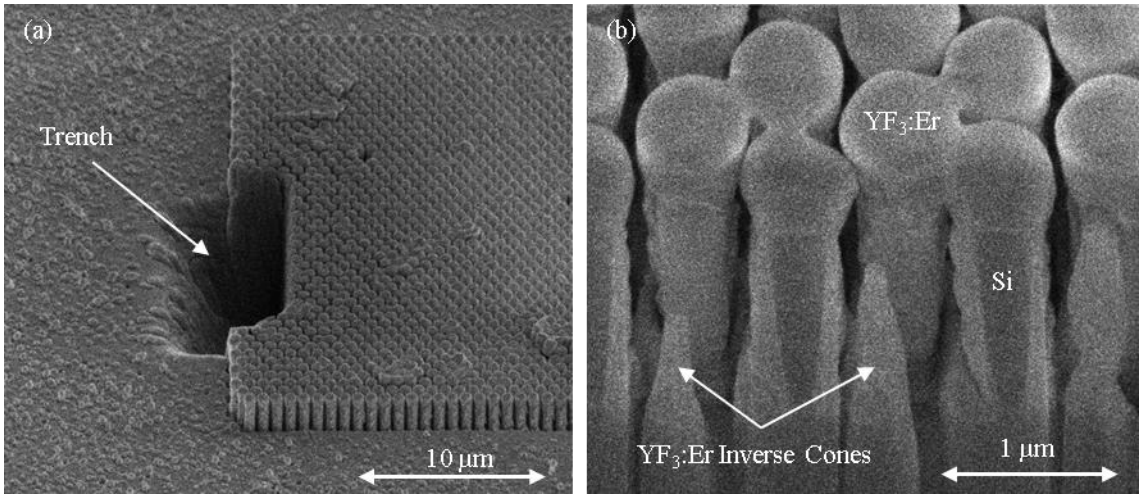

Figure 6-16: (a) A trench was etched into the side of the 2D photonic crystal using FIB to analyse the YF_3:Er filling. (b) The Si pillars (darker shade) are covered in a layer of YF_3:Er. An increased isotropic deposition of the fluoride occurs at the top of the Si pillars, which results in shielding of the fluoride entering the space between the pillars. Therefore large gaps of air appear between the Si pillars, which are inconsistently filled with the fluoride material.

The incomplete filling was found to be caused by an overlapping shielding layer of YF_3:Er forming on top of the Si pillars. In Figure 6-16(b) the cross-sectional view of the

photonic crystal is shown. The lighter shade of grey represents the YF_3:Er layer, with the Si represented by the darker shade of grey. It can be seen that the YF_3:Er deposition between the Si pillars decreases with time as the opening between the pillars narrows, resulting in an inverse cone of YF_3:Er.

A simple calculation of the fill factor was carried out using the SEM images. The YF_3:Er was considered to only occur on the curved surface of the Si pillars and within the inverse cones observed between the pillars, as shown in the plan view schematic of the structure in Figure 6-17. This analysis is likely to underestimate the YF_3:Er fill factor as it assumes that the inverse cones of the up-conversion material are not joined together, which is very unlikely. The fill factor of the structure observed in Figure 6-16 was calculated to be 19±3%, resulting in an effective refractive index of n_{eff} = 1.11±0.18. This represents the minimum average effective refractive index, which will change between the top and bottom of the pillar array due to the conical nature of the deposition between the Si pillars.

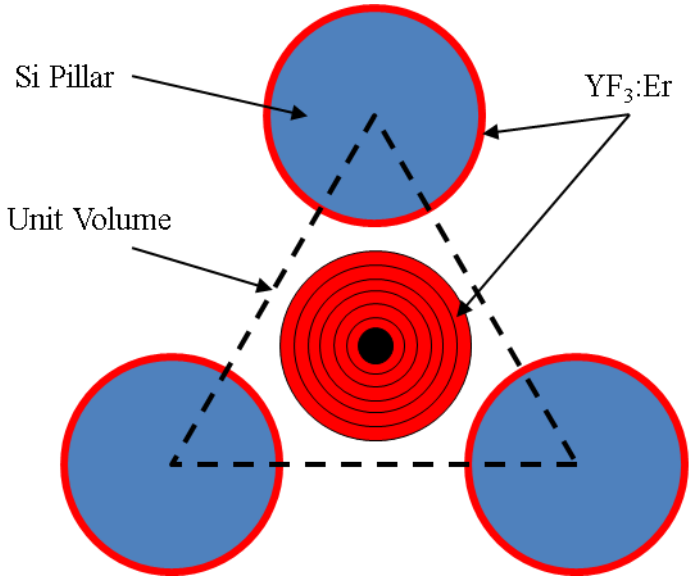

Figure 6-17: The schematic of the top view of the YF_3:Er coated Si 2D photonic crystals shows the simplified geometry that was considered in order to estimate the fill factor. The red disk with concentric black rings represents the conically deposited YF_3:Er between the Si pillars.

To improve the filling of YF_3:Er between the Si pillars, 2D photonic crystals with a smaller aspect ratio (shorter pillar height) were fabricated. A shorter aspect ratio was expected to reduce the adverse effects of the capping layer forming over the top of the Si pillars before the space between the pillars could be filled. The disadvantage of reducing the height of the pillars would be that it would move the system further away from the infinite height 2D photonic crystal structure assumed in the modelling in Chapter 3. A shorter pillar height required a different SOI substrate to ensure that the 2D photonic

crystal sat immediately above the low refractive index SiO_2 layer. Therefore a SOI wafer with a 2 μm SiO_2 intermediate layer and 340 nm Si top layer was used. This SOI wafer was chosen as it is commonly available for industrial use.

The cross sectional analysis shows that there was a small improvement in the filling of YF_3:Er between the Si pillars. Using the same basic estimation for the filling factor, the effective refractive index of this structure was found to be n_{eff} = 1.15±0.07 from a fill factor of 28±2%. In Figure 6-18(a) some of the YF_3:Er capping layer has been removed revealing distinct air gaps between the Si pillars. Furthermore, the cross section observed in Figure 6-18(b) shows the same inverse cone filling is observed with the higher aspect ratio structures. Therefore, even with a greatly reduced Si pillar height, little improvement is observed in the filling of YF_3:Er between the Si pillars.

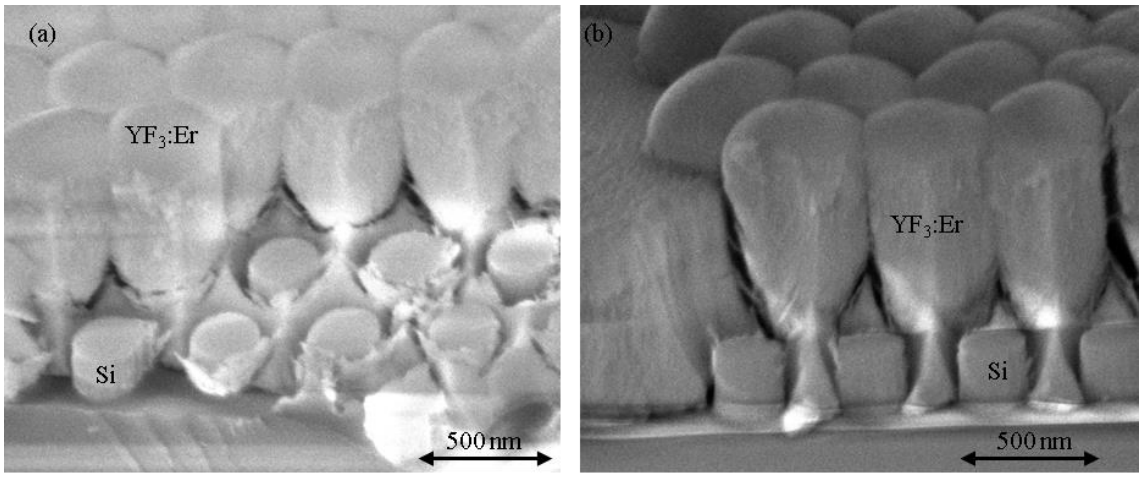

Figure 6-18: (a) When the YF3:Er capping layer is removed, the incomplete filling between the Si pillars is observed. (b) A cross sectional view of the 2D photonic crystal structure reveals incomplete filling between the Si pillars, with inverse cones of YF_3:Er observed as before with the higher aspect ratio structures.

Observation analysis of the evaporation of YF_3:Er onto the Si 2D photonic crystal structures reveals non-homogeneous filling. The crystalline phase that is required for observable up-conversion emission at 980 nm, grows rapidly from the top of the Si pillars in a lateral direction resulting in shielding of the space between the Si pillars and therefore incomplete filling. This incomplete filling reduces the effective refractive index of the volume between the pillars. If the wavelength of interest is large enough, it will observe an effective refractive index that is composed of the average refractive of the volume. In this case, the effective refractive index would be composed of YF_3:Er and air. In order to attempt to compensate for this reduction in effective refractive index, simulations were carried out to optimise the 2D photonic crystal structure for a range of effective refractive

indices from that of YF_3:Er (1.56) to air (1.0). In the following figures, "n=x Tuning" refers to the optimisation of the simulation for a YF_3:Er refractive index of n=x.

The change in wavelength enhancement (band edge position) was analysed as a function of the effective refractive index between the Si pillars. Simulations were carried out to observe the effect of a reduction in the effective refractive index on a 2D photonic crystal tuned for a range of refractive indices at 980 nm. It can be seen from Figure 6-19 that a small change in the effective refractive index of the space between the Si pillars will result in a relatively large change in the enhanced wavelength. A change of 0.1 in the refractive index corresponds to a change in the wavelength of enhancement of around 26 nm.

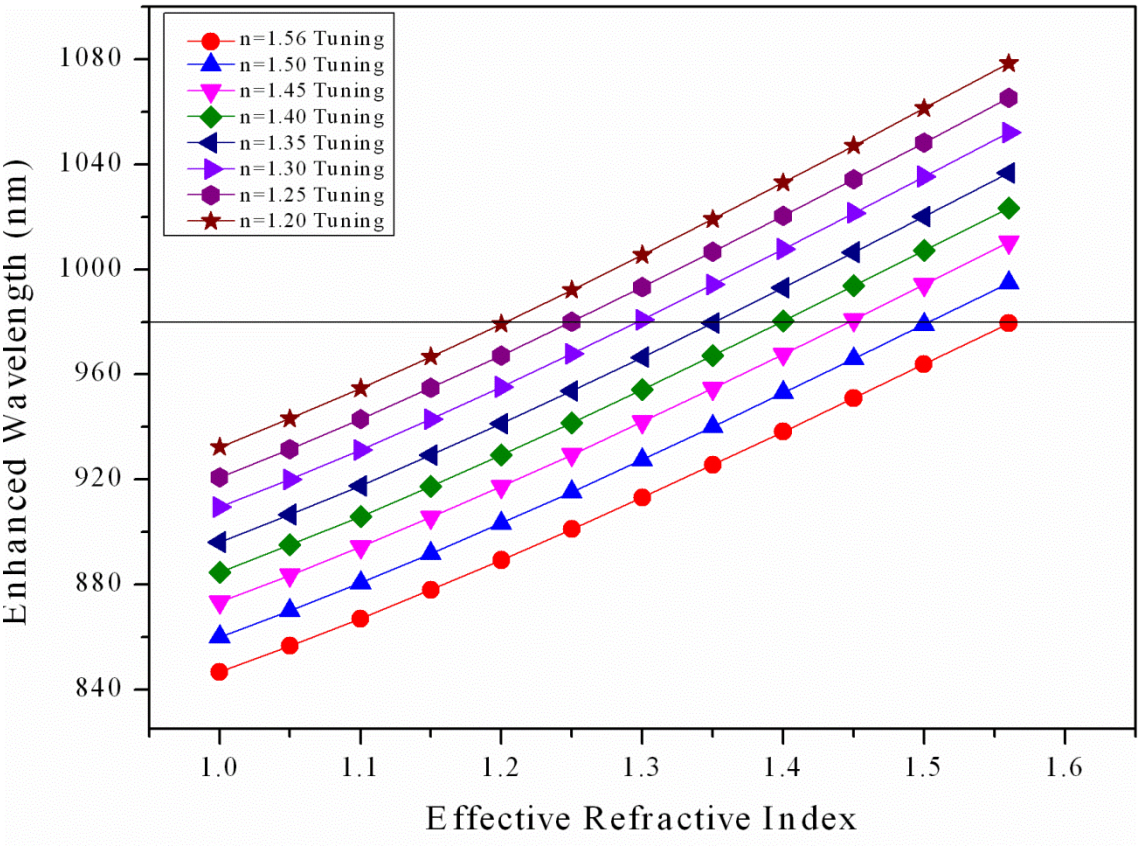

Figure 6-19: The enhanced wavelength is shown as a function of effective refractive index and optimised refractive index. A small change in the effective refractive index of the volume between the Si pillars will result in a relatively large change in the enahnced wavelength.

To compensate for the incomplete filling of the space between the Si pillars, the geometries of the 2D photonic crystals were optimised for a range of effective refractive indices; n=1.56, 1.35 and 1.15. For each refractive index, the change in the enhanced wavelength was analysed as a function of the Si pillar radius. A range of 7 pillar radii

were chosen, based on the pillar radii achieved from the previous photonic crystals fabricated. The pillar radii are expressed as a ratio of the radius (r) to lattice constant (a). The simulated optimised structures were then modelled against a range of effective refractive indices to see the effect on the enhanced wavelength.

An example of the optimised structures for n=1.56, 1.35 and 1.15 when tested with an effective refractive index of 1.25 is shown in Figure 6-20. It can be seen that both the patterns optimised for n=1.15 tuning with radius of r/a=0.27 and n=1.35 tuning with radius of r/a=0.31 lie very close to the 980 nm enhancement line. Taking into account the FWHM of the 980 nm peak, which was shown previously to be around 20 nm, both of these 2D photonic crystal structures would be expected to enhance the up-conversion emission at 980 nm for a 2D photonic crystal with the space between the Si pillars having an actual effective refractive index of 1.25.

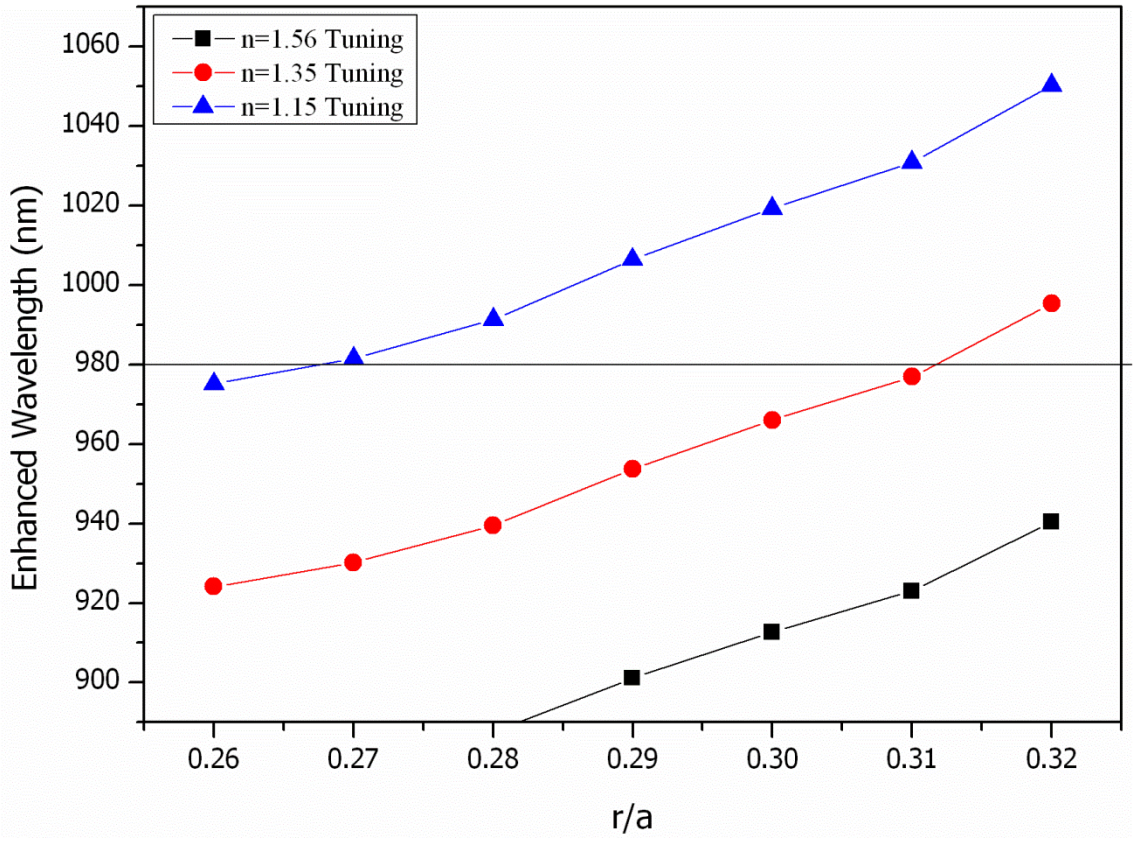

Figure 6-20: The simulated enhanced wavelengths for structures tuned for effective indices of n=1.56, 1.35 and 1.15 with hole radii ranging from r/a=0.26 to 0.32 are shown for the test effective refractive index of 1.25. Therefore if these structures were fabricated and the effective refractive index between the Si pillars of the real devices was actually n=1.25, then there would be two 2D photonic crystal structures that would show enhancement at around 980 nm (n=1/15, r/a=0.26 and n=1.35, r/a=0.31).

A full analysis of the enhanced wavelength with respect to the actual effective refractive index for the three tuned patterns of interest has been carried out. The results shown in Figure 6-21 indicate that 980 nm tuning can be achieved across the range of the actual effective refractive index considered: n(actual)=1.15-1.56. Taking into account the broadening of the 980 nm emission profile, as shown later in Figure 6-25 to be around 50 nm, this indicates further that enhanced emission at 980 nm can be achieved over the effective refractive index range from at least one of the 21 2D photonic crystal structures under consideration.

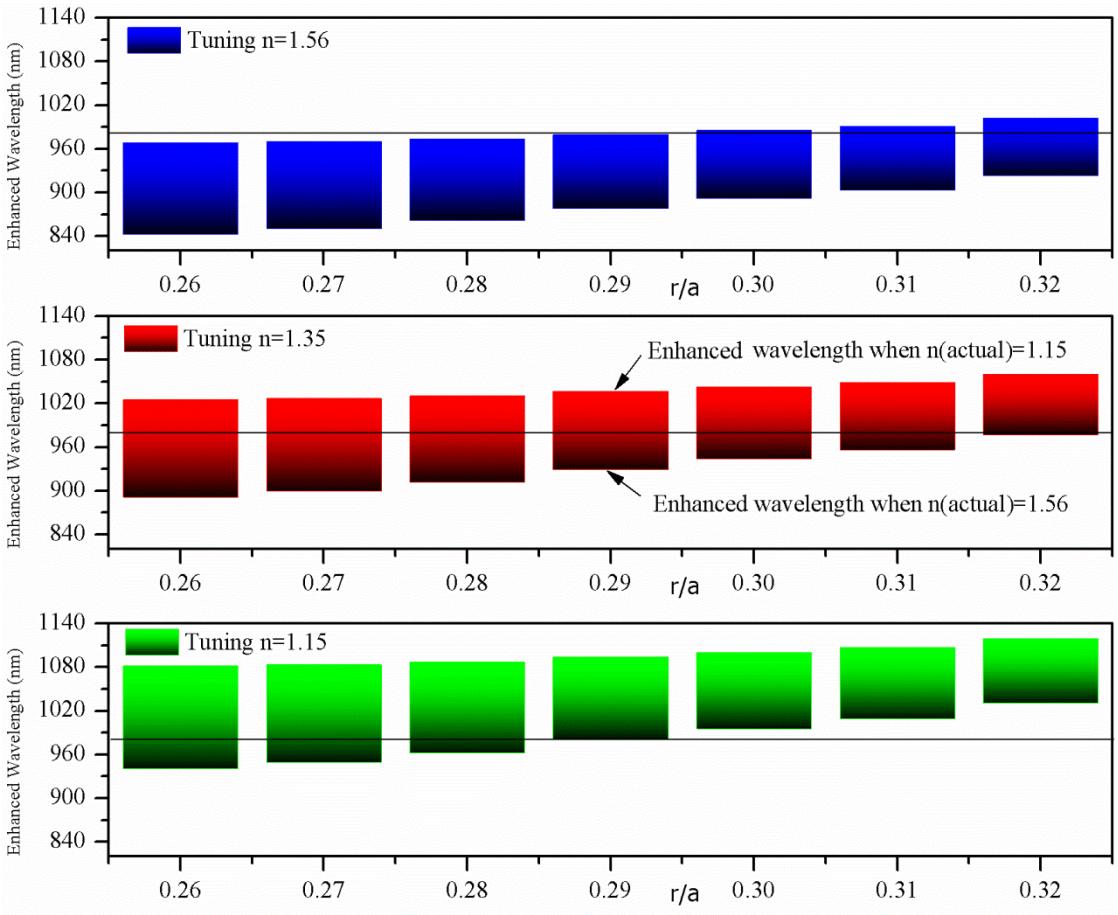

Figure 6-21: A gradual change in the actual effective refractive index is represented by the gradient in colour, from n(actual)=1.15 - 1.56. The line at 980 nm crosses the bars at the effective refractive index at which the pattern with, specified r/a value, would enhance 980 nm emission. It can be seen that the 980 nm line crosses each bar at a different effective refractive index covering the range from 1.15 to 1.56. Therefore there is a high chance that one of the 21 2D photonic crystals shown above will be tuned for the actual effective refractive index. It was not possible to directly calculate the YF_3:Er volume filling factor, however conservative estimates from the SEM micrographs suggest that it lies between 1.15 and 1.56.

The same analysis was carried out for the wavelength enhancement at 1523 nm, indicating that the 21 2D photonic crystals area also tuned over the majority of the range of

n(actual)=1.15-1.56 to provide enhancement of the 1523 nm emission. Therefore these structures were used for the optical characterisation.

6.4.7 Conclusion of YF_3:Er Thin Films by Thermal Evaporation

The thin film deposition of up-converting YF_3:Er by thermal evaporation has been successfully achieved. The chemical synthesis of the initial bulk powder sample allowed for accurate control of the erbium doping concentration to be achieved. The temperature of the substrate during the deposition process was found to play a key role in the crystallinity of the resulting YF_3:Er film. A custom designed low voltage DC substrate heater with temperature feedback was built and successfully incorporated into the existing thermal evaporation chamber to allow for the substrate temperature to be controlled. This allowed for the successful deposition of crystalline YF_3:Er, exhibiting up-conversion emission of 980 nm when excited at 1523 nm. The refractive index of the crystalline YF_3:Er film was measured using ellipsometry. The real components of the refractive indices at the wavelengths of interest were found to be $n_{(980)} = 1.53 \pm 0.07$ and $n_{(1523)} = 1.52 \pm 0.07$, where the predominant uncertainty was from the repeatability between samples.

Incomplete filling of the space between the silicon pillars with YF_3:Er resulted in a lower than expected average refractive index between the pillars. The percentage of volume filled between the pillars was calculated to be only 19±3%, resulting in an effective refractive index of $n_{eff} = 1.11 \pm 0.18$. Silicon pillars with a smaller aspect ratio (shorter in height) were fabricated to try to improve the fill factor. An increase in the fill factor to 28±2% was observed, resulting in an effective refractive index of $n_{eff} = 1.15 \pm 0.07$. To compensate for the incomplete filling, further simulation analysis was carried out to optimise the geometry of 2D photonic crystals tuned to a range of effective refractive indices: from that of the maximum value measured for YF_3:Er at 980 nm (n = 1.56) to that of air (n=1.00). These structures would be used in the following section to optically characterise the resulting 2D photonic crystals.

6.5 Optical Characterisation of YF_3:Er-Si 2D Photonic Crystals

In this section the optical characterisation of YF_3:Er 2D photonic crystals is discussed. The design and fabrication of the optimised structures will be presented, along with photoluminescence up-conversion measurements of the 980 nm excited state.

The final 2D photonic crystals fabricated were designed using the knowledge and understanding developed during the simulation and fabrication development discussed in the previous chapters. The optical characterisation considers the 980 nm up-conversion emission. The final designs fabricated are described in this section, followed by a discussion of the results of the optical characterisation.

6.5.1 Design and Fabrication of 2D Photonic Crystal Structures for Optical Characterisation

Sets of YF3:Er-Si 2D photonic crystals were fabricated using two thicknesses of SOI wafers for optical characterisation. The SOI wafers were used to provide a low refractive index material below the top patterned layer of Si to increase reflection of the up-converted signal to improve the collected signal by the spectrometer. The first set was prepared on a SOI wafer with a 1200 nm top Si layer. The second set was prepared on a SOI wafer with a 340 nm top Si layer. Each contained a range of devices tuned for 1523 nm excitation enhancement, with a second subset tuned for 980 nm emission enhancement. Each subset contained a row of photonic crystals tuned for an effective filling refractive index of n=1.56, 1.35 and 1.15, to compensate for the incomplete filling of YF_3:Er between the Si pillars. Within each row, the pillar lattice constant was kept constant, while the pillar radius increased. The increase in pillar radius was to account for discrepancies between the desired pillar radius constructed in the e-beam writing software and the actual radius achieved following photoresist exposure, metal mask lift-off and the plasma Si etch. The radius was increased over 7 steps. Therefore each SOI wafer initially contained 42 photonic crystal devices. To further extend the spread of devices for optical characterisation, a further 58 devices were patterned onto the 340 nm SOI wafer which offered an extended radius range and effective refractive index parameter.

The effective refractive indices used (n=1.56, 1.35 and 1.15) were chosen in conjunction with the variable radius values to provide a near continuous tuning of the band edge across the whole range of the expected effective refractive index between the Si pillars.

Sample maps were prepared for correct identification of the 2D photonic crystals. A location marker (large rectangle or circle) was patterned at one corner of the set of photonic crystals to provide a reference from which to correctly identify each pattern. Each 2D photonic crystal was patterned over an area of 30 μm x 30 μm, which was deemed to be large enough to accommodate the spot size of the confocal microscope at 1523 nm (spot size = 2.83 μm) and large enough not to lead to significant edge effects from the photonic crystal structure. Each patterned area was separated by 120 μm, which provided sufficient space to ensure that no interaction from neighboring 2D photonic crystals was observed. The sample maps for the 340 nm and 1200 nm SOI wafers are shown in Figure 6-22 and Figure 6-23 respectively.

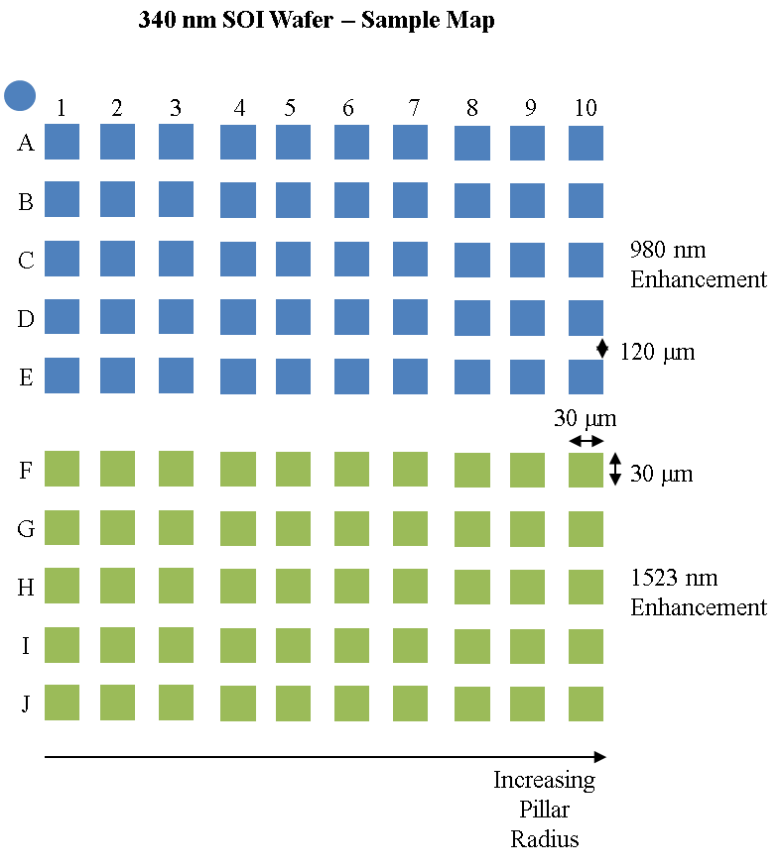

Figure 6-22: Sample map for the SOI wafer with 340 nm top Si layer. Within each set, rows A-E and F-J were tuned for increasing effective refractive index between the Si pillars, while the columns 1-10 were tuned for increasing hole radius of the Si pillars. The large pillar in the top left of the sample map was used for identification of the sample positions.

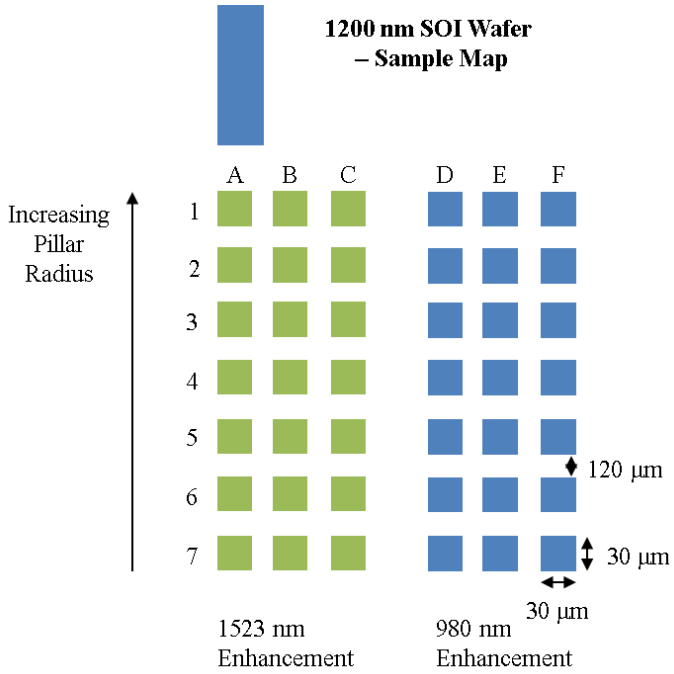

Figure 6-23: Sample map for the SOI wafer with 1200 nm top Si layer. Within each set, columns A-C and D-F were tuned for increasing effective refractive index between the Si pillars. A,D: n=1.56; B,E: n=1.35; C,F: n=1.15. The rows 1-7 were tuned for decreasing Si pillar radius respectively. The rectangle at the top left of the map was used for identification of the sample positions.

The YF_3:Er layer thickness varied between the two SOI wafers, which underwent evaporation in two separate runs. In order to achieve a high signal to noise ratio for the measurement of the 980 nm emission, a thick layer of YF_3:Er was desired. However emission enhancement would only occur from the 2D photonic crystal layer, therefore if there was too much YF_3:Er deposited above the etched Si pillars, there was a risk of not observing the signal enhancement amongst the large overriding signal form the top layer. The total thickness of the YF_3:Er layer was also limited by the amount of powder that could fit inside the filament heater. It was found that a fully packed filament heater with the YF_3:Er powder would produce a film of around 600 nm in thickness. This thickness was found to provide a sufficiently high signal to noise ratio and so was deemed suitable for use. A layer thickness of less than 600 nm was too thin to be able to measure a 980 nm emission signal at the required resolution for detecting the enhancement. There was no internal thickness monitoring device in the evaporation chamber, therefore the final thickness was estimated from the mass of YF_3:Er powder present in the filament. The final YF_3:Er layer thicknesses for the 1200 nm and 340 nm SOI wafers were 1006±3 nm and 680±20 nm respectively.

Analysis of the Cr mask radius was carried out for the 1200 nm SOI wafer sample following Cr evaporation to characterise the hole radii achieved. The results, shown in Figure 6-24, were converted into units of *r/a* for comparison with the simulated data. It was found that the mask radii were all below that of the desired *r/a*=0.29. However they were all sufficiently large to produce a complete photonic band gap, as predicted by the simulation results. Three photonic crystal patterns with increasingly larger radii were added onto the ends of each of the 10 sets prepared on the 340 nm wafer in order to extend the r/a value towards and beyond the desired 0.29 value.

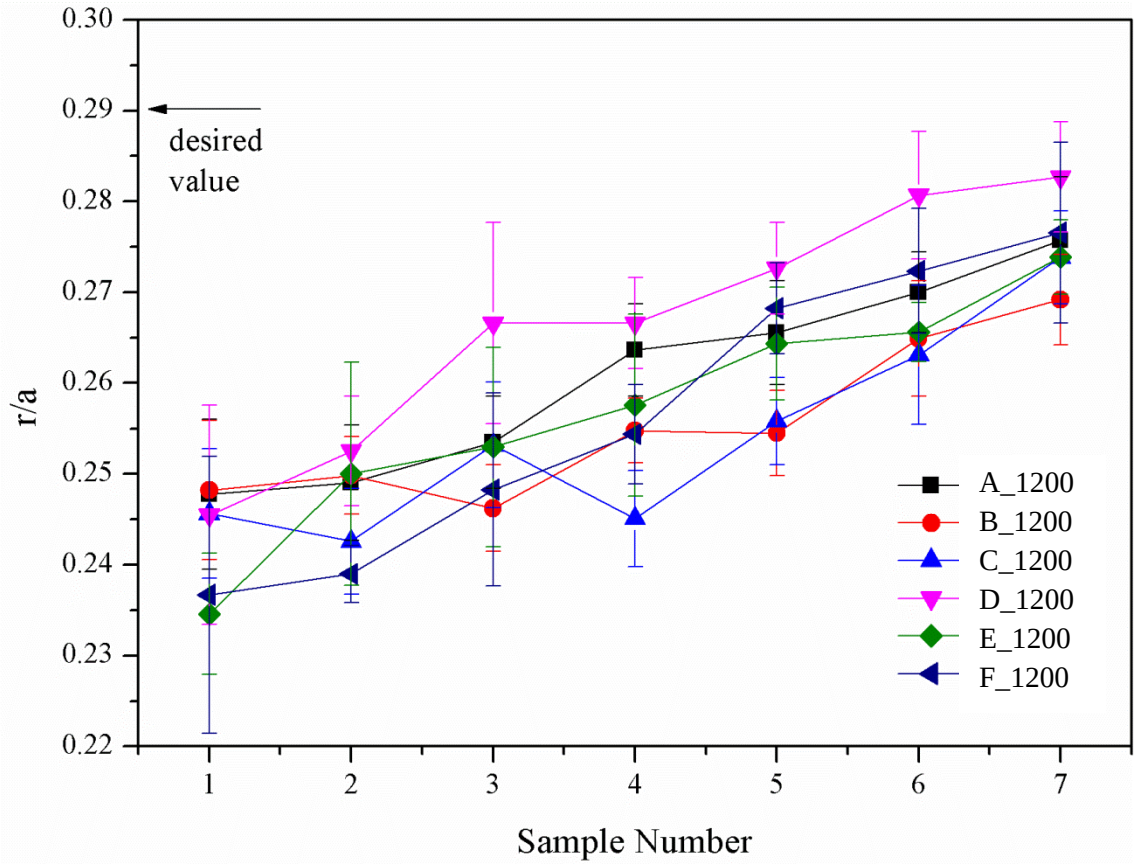

Figure 6-24: Analysis of the hole radii with respect to lattice constant revealed that the holes exposed by electron beam lithography were slightly below the optimum value of r/a=0.29 as predicted by the simulations. However were large enough to exhibit the desired band gap. Each set of values sharing a common line correspond to sequential analysis of the patterned areas down a column as shown in Figure 6-23.

6.5.2 Up-Conversion Measurements of YF_3:Er-Si 2D Photonic Crystals

The up-conversion emission at 980 nm, using 1523 nm excitation, was measured within the YF_3:Er-Si 2D to ascertain whether the photonic crystals enhanced emission. The 2D photonic crystals were measured using the confocal setup and Edinburgh Instruments

Spectrofluorometer as described in section 4.3.2. The emission was acquired at a wavelength resolution of 3 nm to maintain a good signal to noise ratio. The emission was normalised with respect to an unpatterned area of YF_3:Er on Si from the same sample. Measurements were taken for all 142 2D photonic crystal patterns described previously.

The reference emission from an un-patterned area of YF_3:Er reveals the characteristic shape expected from Er in an yttrium fluoride based host. The reference emission used for normalisation of the film on the 1200 nm SOI wafer is shown in Figure 6-25. Peaks in the overall up-conversion emission spectra were observed at 967, 976, 981.5, 991.5 and 1004 nm. These peak positions correspond very well with those observed previously in literature for the 980 nm up-conversion emission from YF_3:Er [19]. The background level was found to be consistent between 86,000-91,000 counts throughout the wavelength range analysed.

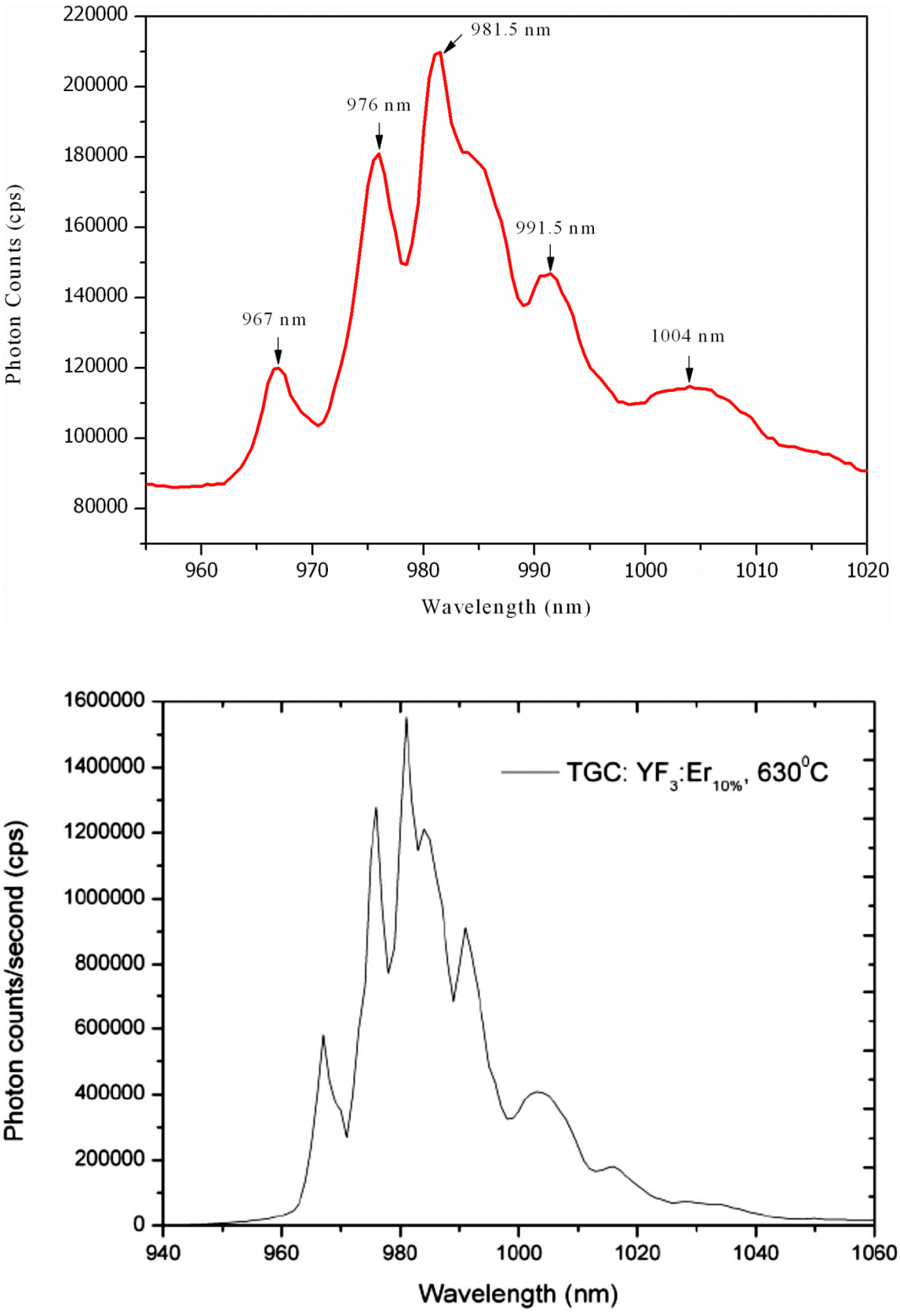

Figure 6-25: The reference up-conversion emission from the un-patterned area YF_3:Er (top graph) shows distinctive peaks at 967, 976, 981.5, 991.5 and 1004 nm, which compare very well with those found in literature (bottom graph) [19].

The 980 nm up-conversion emission acquired for the patterned areas resembled that of the reference data very closely. Due to the imperfections in the 2D photonic crystal structures observed in the fabrication process, it was expected that any enhancement would be of broadband (low quality factor) form. It can be seen from Figure 6-26 that there was no obvious difference between the spectra of the reference and the patterned areas of row F. This lack of difference was observed for all of the spectra from the patterned areas on both SOI wafers.

However in order to gain a better understanding of any enhancement, the spectra from each of the patterned areas were divided by that of the un-patterned reference to provide a normalised signal. The normalised spectra for the 980 nm up-conversion emission from the 1200 nm SOI wafer (Figure 6-27) show very little indication of enhanced 980 nm emission. The spectra are categorised into rows (A-F) and columns (1-7) as described previously, where the rows correspond to a decrease in Si pillar radius from 1-7. The small change in radius along a column was expected to result in a small shift in the enhanced wavelength of the emission. However no such enhancement in the emission profile around 980 nm was observed.

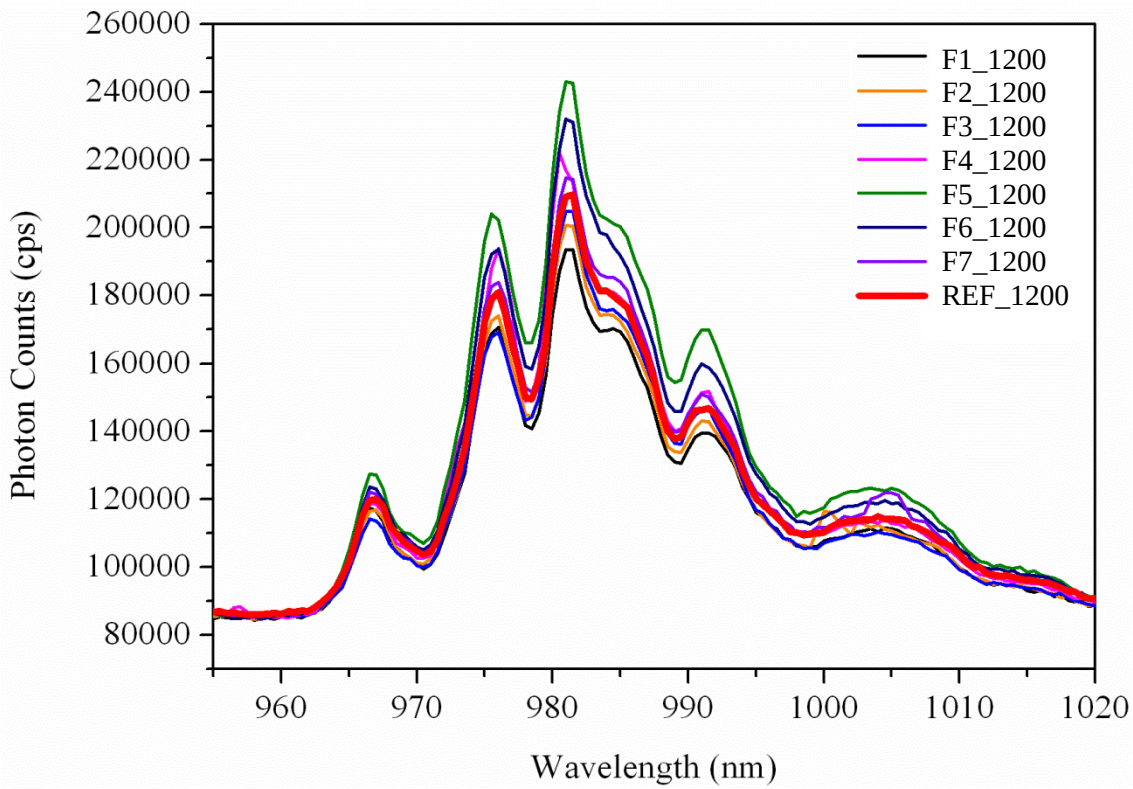

Figure 6-26: Up-conversion emission from samples of Row F with reference signal for comparison. The _1200 in the legend refers to the top Si layer thickness of SOI wafer for reference. The decrease in Si pillar radius with increasing number (F1-7) reveals no corresponding change in photon maximum photon counts. Furthermore, there is very little difference observed between the un-patterned reference and patterned F1- photonic crystal structures.

The standard deviation in the normalised photoluminescence was analysed to provide an estimate of the background noise in the data sets. The standard deviation was carried out for the sample sets for columns A and E as they showed consistent behaviour with no apparent peaks or spikes therefore were assumed to exhibit background noise. The standard deviation analysis was carried out over the range 965 – 1020 nm where the signal was sufficiently greater than the background signal and within each spectrum was found to range from 3.2% to 10.9%.

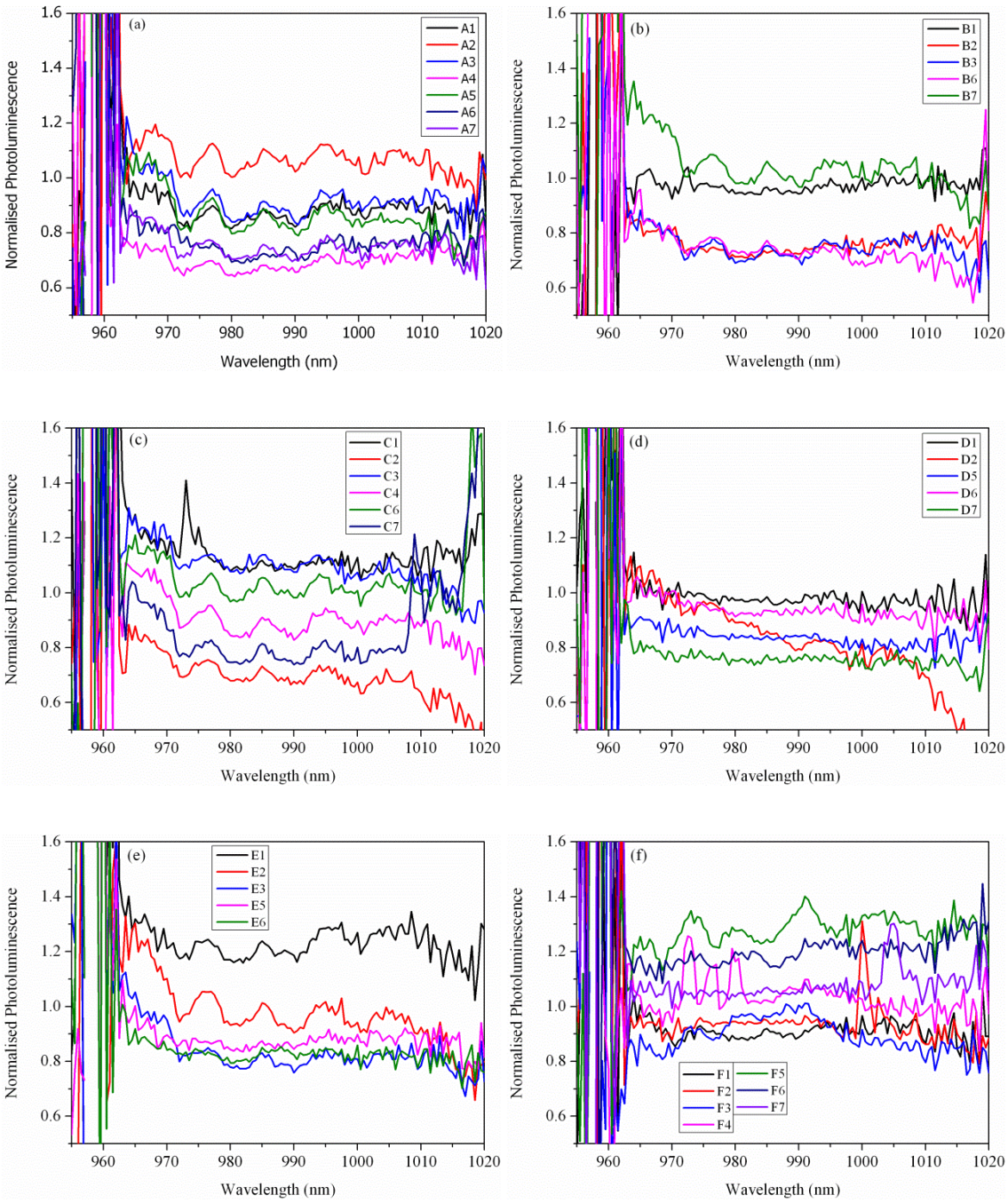

Figure 6-27: Normalised spectra for the 980 nm up-conversion emission. A-J correspond to the columns of photonic crystal patterns, while 1-7 refer to the rows of photonic crystal patterns with their specific geometries referred to in the sample map in Figure 6-23. All of the samples shown here were prepared on a SOI wafer with a top Si layer of thickness 1200 nm Irregular small peals in enhancement are observed, in addition to overall enhancement across the entire spectral range. However these effects cannot be directly attributed to the flat band edge of the 2D photonic crystals.

Small peaks in the normalised up-conversion were observed for several of the data sets. A summary of the peak positions and relative peak heights as a percentage of the base height is shown in Table 6-10. All of the peak heights were found to be above the maximum 10.9% standard deviation calculated previously. However no correlation is

observed between the peak position and change in pillar radius as expected. Furthermore all expect one of the peak heights observed are smaller in normalised photoluminescence than the baseline of other spectra within the set. Therefore it is concluded that these small peaks are not effects of the photonic crystal structure. The maximum normalised photoluminescence intensity enhancement observed from all of the 2D photonic crystals was found to be around 1.4 for both of the patterns C1 and F2.

Pattern	Wavelength (nm)	Relative Peak Height (% increase)
C1	973	25.1
C7	1009	43.2
F2	1000	47.2
F4	972.5	26.0
F4	977	15.6
F4	979.5	21.0
F7	1005	26.2

Table 6-10: The small peaks that were observed for several of the 2D photonic crystal patterns were all found to be above the height of the background noise of up to 10.9% standard deviation calculated previously.

Not all of the patterned areas provided useful spectra. This was due to large deposits of YF_3:Er forming on or near the patterned areas, as shown in Figure 6-28. The deposits were found to be around 10-20 μm in diameter, therefore provided a significant increase in volume of material compared to the thin film below. The increase in up-conversion emission observed was purely dependent on the volume of deposited material and not on the photonic crystals. Therefore the spectra acquired for the areas "enhanced" by the presence of the deposits were ignored.

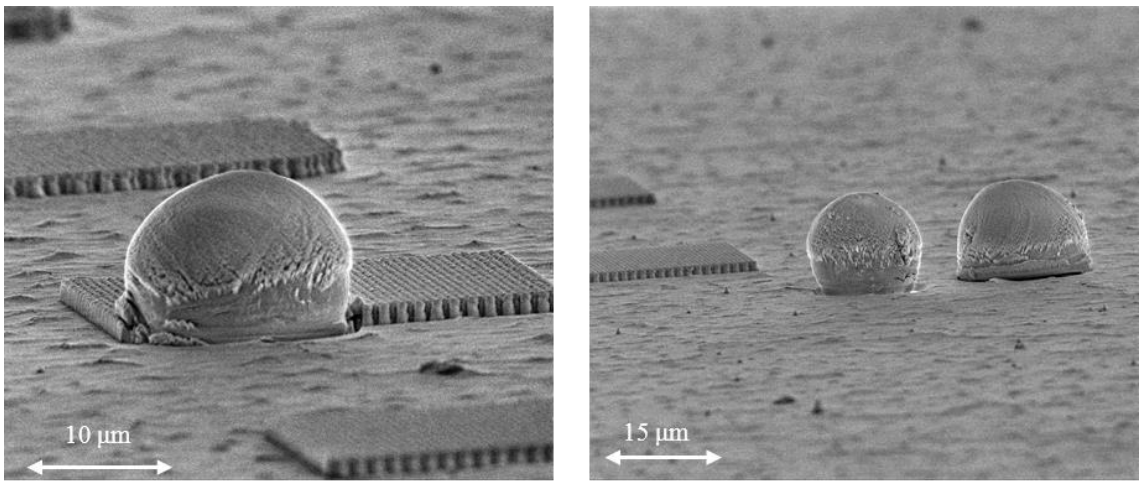

Figure 6-28: Large lumps of YF_3:Er were deposited on the substrate surface. When these deposits were located within the vicinity, or on top of a patterned area, a significant increase in the up-conversion emission was observed.

The normalised photoluminescence for the 980 nm up-conversion emission from the 340 nm SOI wafer (Figure 6-29) shows little indication of an enhanced peak of emission. As mentioned for the 1200 nm SOI wafer samples, the normalised data became very noisy in the regions where the 980 nm signal was negligible compared to the background signal. Therefore the region of interest for further analysis was limited to between 965 and 1015 nm. Although no specific enhanced peaks of enhancement were observed, many of the spectra revealed an overall increase in the emission across the whole of the region of interest.

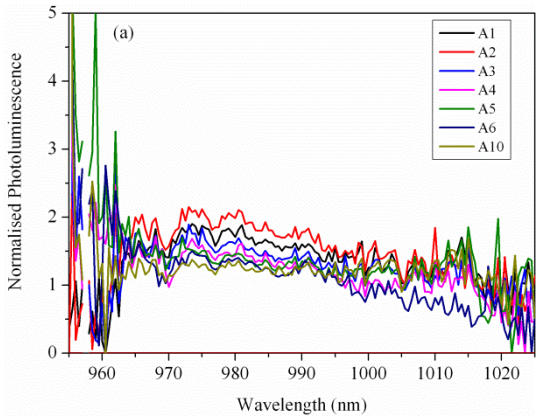
(a)
A1
A2
A3
A4
A5
A6
A10
Normalised Photoluminescence
Wavelength (nm)

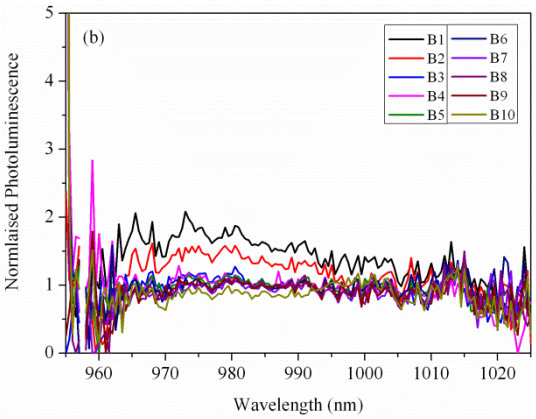
(b)
B1
B2
B3
B4
B5
B6
B7
B8
B9
B10
Normlaised Photoluminescence
Wavelength (nm)

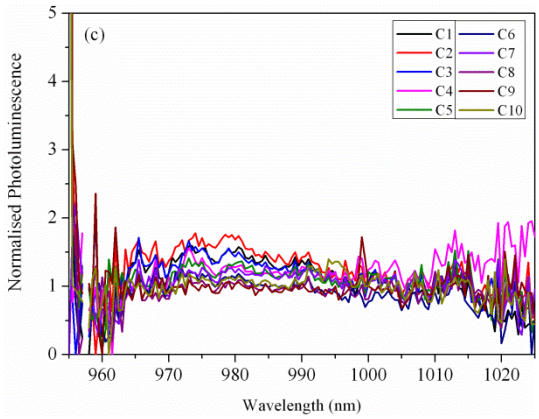
(c)
C1
C2
C3
C4
C5
C6
C7
C8
C9
C10
Normalised Photoluminescence
Wavelength (nm)

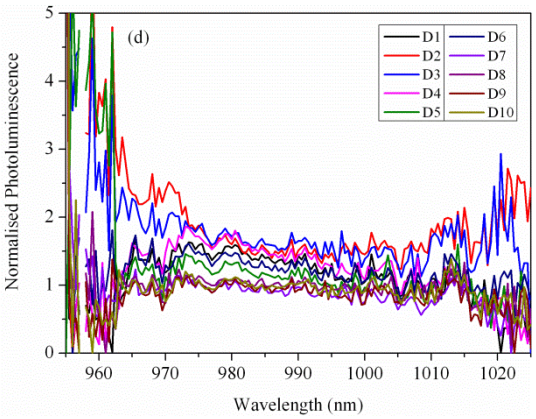
(d)
D1
D2
D3
D4
D5
D6
D7
D8
D9
D10
Normalised Photoluminescence
Wavelength (nm)

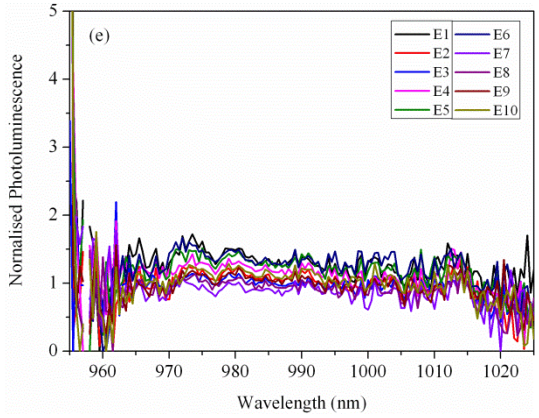
(e)
E1
E2
E3
E4
E5
E6
E7
E8
E9
E10
Normalised Photoluminescence
Wavelength (nm)

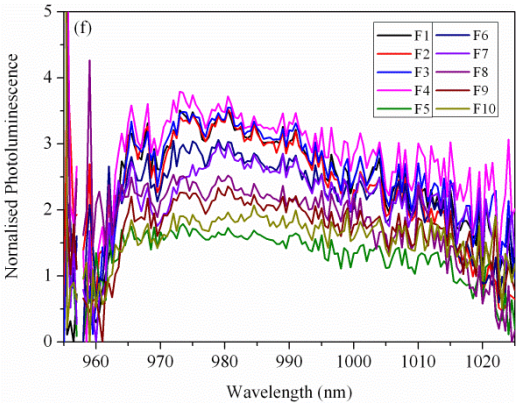
(f)
F1
F2
F3
F4
F5
F6
F7
F8
F9
F10
Normalised Photoluminescence
Wavelength (nm)

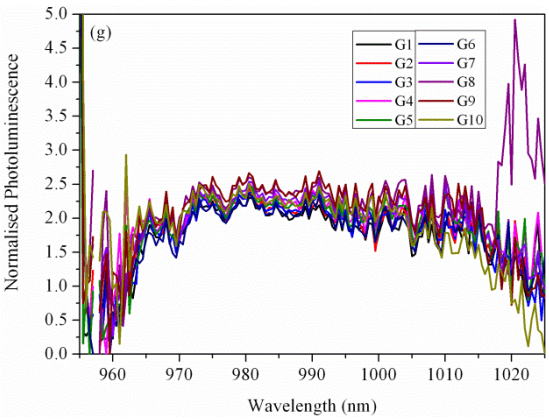
(g)
G1
G2
G3
G4
G5
G6
G7
G8
G9
G10
Normalised Photoluminescence
Wavelength (nm)

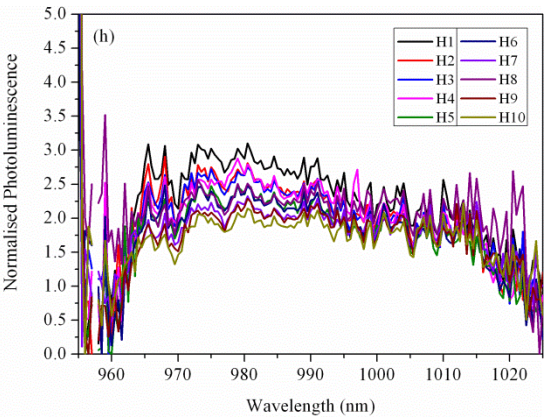
(h)
H1
H2
H3
H4
H5
H6
H7
H8
H9
H10
Normalised Photoluminescence
Wavelength (nm)

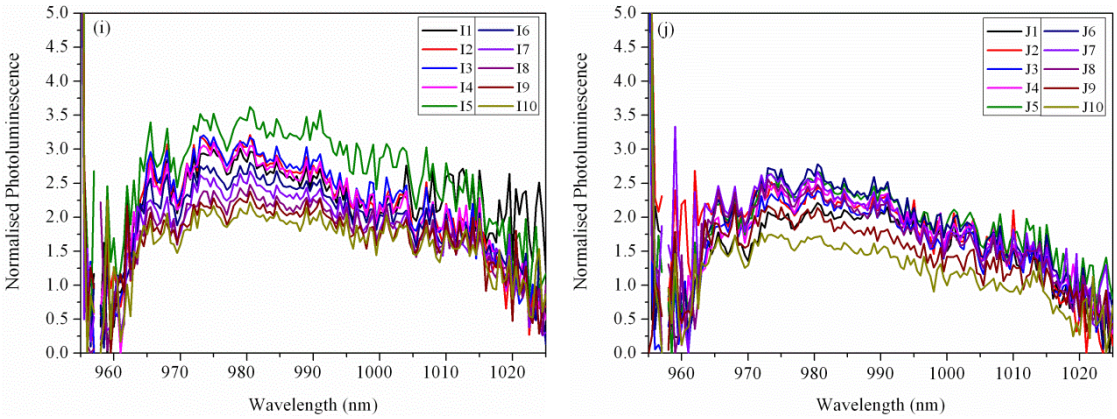

Figure 6-29: Normalised spectra for the 980 nm up-conversion emission. A-J correspond to the columns of photonic crystal patterns, while 1-10 refer to the rows of photonic crystal patterns with their specific geometries referred to in the sample map in Figure 6-22. All of the samples shown here were prepared on a SOI wafer with a top Si layer of thickness 340 nm. Overall enhancements across the entire spectral range is observed for some of the samples; however these effects cannot be directly attributed to the flat band edge of the 2D photonic crystals.

To investigate further the overall enhancement observed, the maximum normalised photoluminescence was acquired for each of the patterns and plotted against the sample number with the results shown in Figure 6-31. Again, the sample number is directly related to the Si pillar radius, with a higher sample number corresponding to a larger pillar radius. A maximum normalised photoluminescence enhancement of 3.79 was observed for the 2D photonic crystal F4. This corresponds to a significant increase in the up-conversion emission, which can be seen in Figure 6-30.

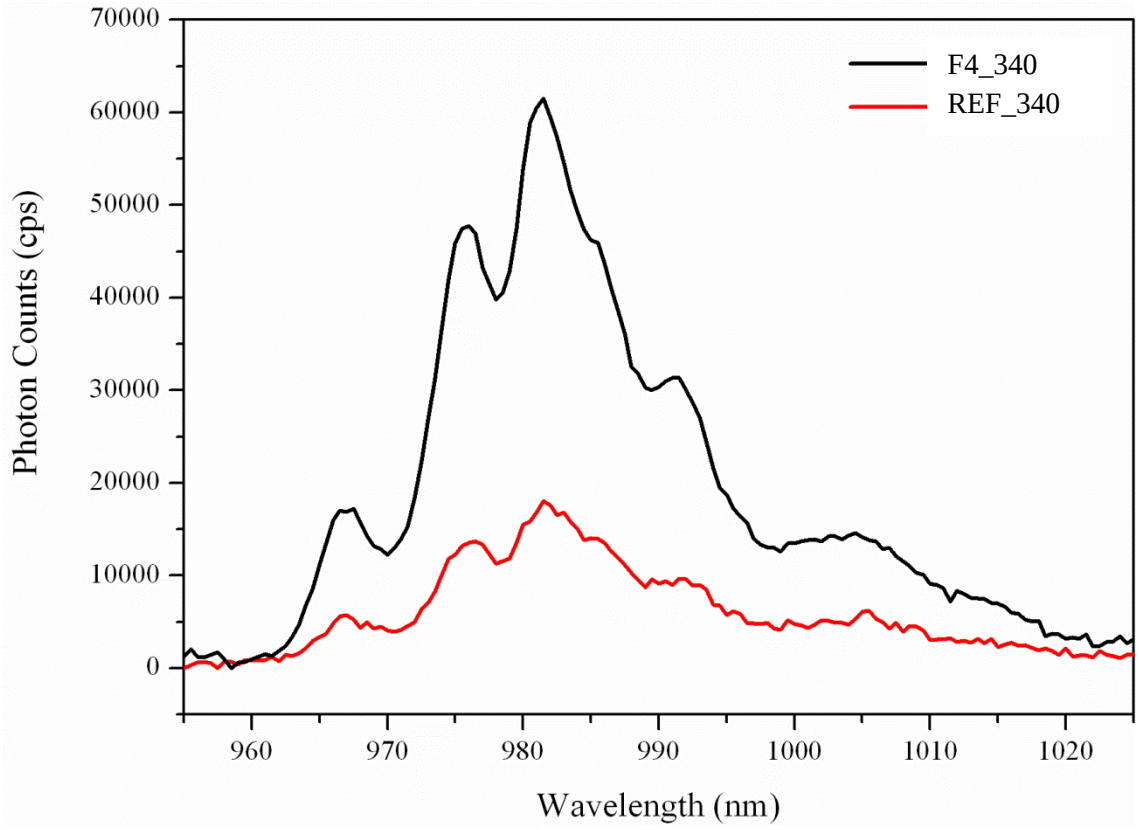

Figure 6-30: The maximum enhancement of the 980 nm up-conversion emission from F4_340 (BLACK) was found to be 3.79. The enhancement was found to occur over the entire wavelength range of the emission. The emission reference emission from the un-patterned layer (RED) is shown for comparison. The _340 refers to the thickness of the top Si layer in the SOI wafer for reference.

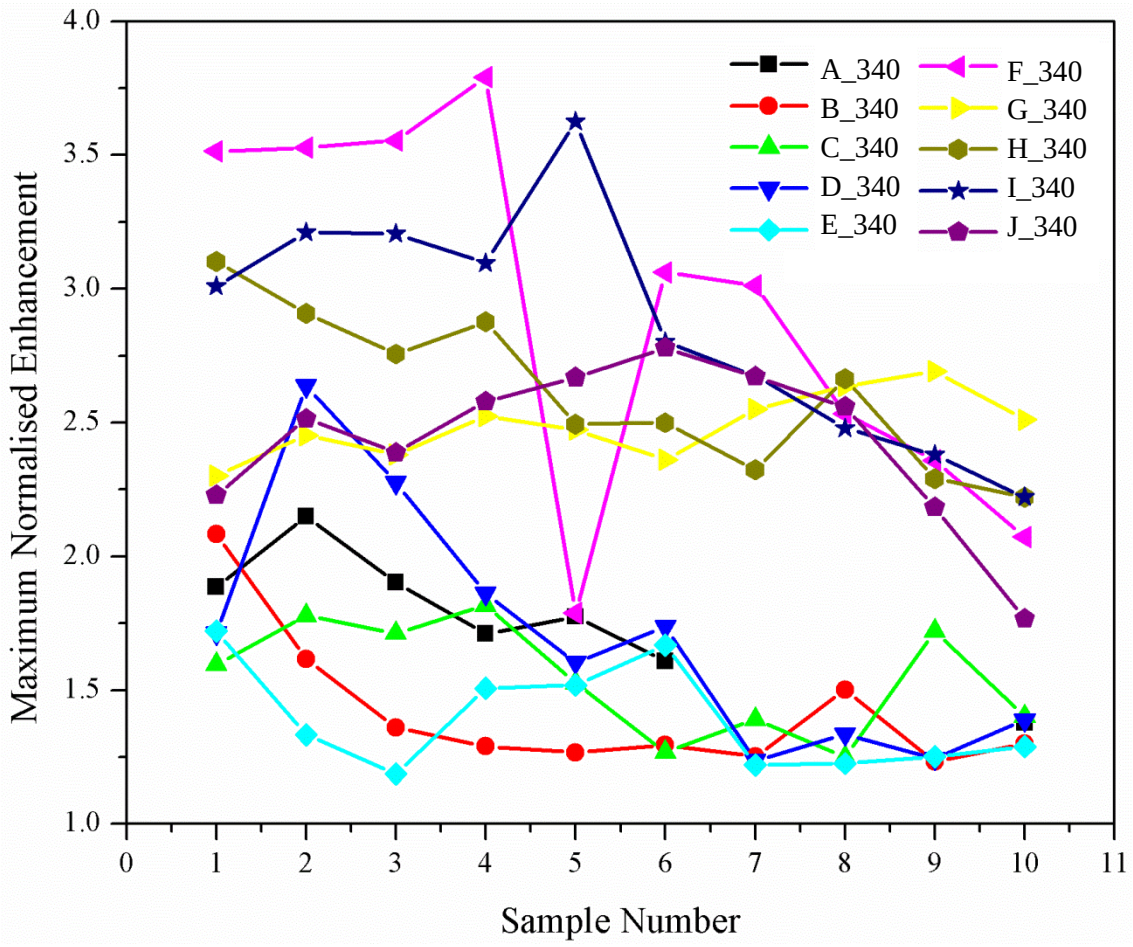

Figure 6-31: The normalised photoluminescence enhancement was found to show an overall decrease with Si pillar radius (increasing sample number). The samples tuned for 1523 nm (F-J) provided a greater overall enhancement than the samples tuned for 980 nm. The _340 in the legend refers to the thickness of the top Si layer in the SOI wafer for reference.

An overall trend of a reduction in the maximum normalised photoluminescence with increasing Si pillar radius is observed for all of the sets of photonic crystals measured. As the pillar radius increases, the space between the Si pillars and hence volume of YF_3:Er deposited between the pillars, decreases. If the pillars were increased in radius, all of the space between them would eventually disappear and therefore the system would become the same as that of the reference photoluminescence signal. Therefore the overall reduction in the maximum normalised enhancement with an increase in Si pillar radius is expected. With the same analysis, we can expect that a decrease in Si pillar radius would eventually result in the maximum normalised enhancement returning to 1 when the pillar radius eventually reduced to zero. This could account for the slight reduction in maximum normalised enhancement observed for the sets C, D, F, G, I and J. This analysis may explain the general trend of the enhancement towards very small or very large Si pillar

radii, however does not explain the cause of the increase observed for the intermediate samples.

The wavelength corresponding to the maximum enhancement was analysed along row F to see whether the change in Si pillar radius corresponded to a shift in the peak position. If the enhanced emission was due to a photonic band edge effect, the center of the peak, corresponding to the maximum enhancement, should move systematically with an increasing hole radius as shown in Chapter 3. This general trend should be apparent even if the enhancement peak is very broad and covers the entire range of interest. The maximum enhancement positions for samples F1-F10 are shown in

Table 6-11. No general trend in the peak position is observed. Furthermore the positions of maximum enhancement were all found to lie within a 13 nm window. This small range could be due to the noise within the normalised photoluminescence data and the peak enhancement position may actually not move at all. The variation of 13 nm is far smaller than was expected for the corresponding change in pillar radius and so it can be concluded that the enhancement is not due to the band edge effect from the 2D photonic crystals.

Sample	Maximum Enhancement Position (nm)
F1	980.5
F2	980.5
F3	980.5
F4	973
F5	973.5
F6	979
F7	979
F8	972
F9	980.5
F10	984.5

Table 6-11: The wavelength corresponding to the maximum enhancement position does not show a general trend with increasing sample radius as would be expected for an enhancement from a 2D photonic crystal.

A second trend observed within Figure 6-31 is that overall enhancements for the structures tuned for 1523 nm (F,G,H,I and J) are consistently greater than those tuned for 980 nm (A,B,C,D and E). The main difference between the two sets of structures is the absolute dimensions of the pillar radii. The reason for this difference in overall enhancement is unclear. It may be a result of a scattering effect, however the simulation work required to theoretically test this hypothesis is beyond the scope of this thesis.

6.5.3 Conclusion of Optical Characterisation of YF3:Er-Si 2D Photonic Crystals

Sets of 30 μm × 30 μm photonic crystal structures were fabricated to be tuned for a range of effective refractive indices for the space between the silicon pillars. Two of these sets were fabricated, one where the band edge had been tuned to the excitation wavelength of 1523 nm and the second tuned to 980 nm. These resulting patterns were fabricated firstly using a SOI wafer with a 340 nm top silicon layer and secondly using a SOI wafer with a 1200 nm top silicon layer. The top silicon layer of the SOI wafer corresponded to the final pillar height of the silicon pillars. Post analysis of the resulting hole radii exposed by the e-beam lithography system indicated that the radii were slightly smaller than expected, however were still large enough to exhibit a complete photonic band adjacent to the flat band edge as desired.

Reference up-conversion emission measurements were successfully acquired and compared well with measurements reported elsewhere in literature for the expected emission of YF_3:Er up-conversion. The resulting analysis of the up-conversion emission at 980 nm from all of the patterned areas revealed that a maximum enhancement of 3.79 was observed for a 2D photonic crystal of a triangular array of 340 nm high silicon pillars and YF_3:Er. This enhancement was apparent for nearly the full wavelength range of the 50 nm broad emission signal. To test whether the enhancement observed was due to the photonic band edge effect, the wavelength of the maximum peak position was analysed as a function of silicon pillar radius. A change in the silicon pillar radius should result in a shift of the resonant wavelength of the photonic band edge and therefore wavelength of peak enhancement. However the peak wavelength was found to be relatively stable and did show the general trend envisaged.

6.6 Conclusions of Silicon 2D Photonic Crystals for Enhancing YF_3:Er Up-Conversion Emission

A combination of silicon and YF_3:Er was investigated for use as a 2D photonic crystal enhanced up-conversion layer. The advantage of using silicon is that there is a well-documented procedure developed for the microelectronics industry for etching this material. Furthermore, YF_3 has been shown in literature to be a good host material for up-converting rare earth ions.

A procedure for the anisotropic etching of silicon was developed using a chromium hard mask, which allowed for the angle of the side walls to be accurately controlled. Thermal

evaporation was used to deposit thin films of YF_3:Er into the gaps between the silicon pillars. Initial investigation revealed that the temperature of the silicon substrate during deposition was critical to the resulting crystallinity and up-conversion properties of the YF_3:Er layer. Crystalline YF_3:Er layers were achieved by maintaining the temperature of the substrate to be greater than 200°C during deposition. The resulting crystalline thin film materials were found to show good 980 nm emission following excitation at 1523 nm for films of around 630 nm or greater. Amorphous films achieved by deposition onto silicon substrates at room temperature (22°C) of comparable thickness (700 nm) were found to exhibit no observable up-conversion emission at 980 nm.

Ellipsometry analysis was carried out to model the refractive index of the crystalline YF_3:Er films. The real component of the refractive index at a wavelength of 600 nm (n=1.54) was found to be comparable to other reported results for un-doped YF_3 in literature. Analysis of the repeatability of the measurements between samples found that there was a variation of ±4.62% for the real component of the refractive index for films produced under the same process conditions.

The YF_3:Er up-conversion material was deposited by thermal evaporation onto the arrays of silicon pillars fabricated using reactive ion etching. However the YF_3:Er did not fill the space between the pillars as expected, resulting in a low volume fill factor. This significantly changed the effective refractive index of the volume between the silicon pillars, and as a result the associated band structure of the photonic crystal. Further modelling of 2D photonic crystals consisting of an effective refractive index of YF_3:Er and air in varying combinations was carried out to account for the incomplete filling. These structures were experimentally fabricated and optically characterised. A maximum photoluminescence enhancement of 3.79 times was observed (compared to a flat un-structured film of identical thickness). However this enhancement could not be directly attributed to the effect of the flat band edge of the photonic crystal and was more likely due to an increase in scattering from the structured silicon substrate. Further simulation work of the effects of scattering would be required to confirm this hypothesis, however this was beyond the time frame of this thesis.

6.7 References

1. W. Chen, and H. Ahmed, "Fabrication of sub-10 nm structures by lift-off and by etching after electron-beam exposure of poly(methylmethacrylate) resist on solid substrates," Journal of Vacuum Science & Technology B **11**, 2519-2523 (1993).
2. "Lift-off Processes with Photoresists," (MicroChemicals, micro resist technology GmbH, Koepenicker Str. 325, 12555 Berlin, Germany, www.microchemicals.com/downloads/application_notes.html, 2013).
3. K. R. Williams, K. Gupta, and M. Wasilik, "Etch rates for micromachining processing-Part II," Microelectromechanical Systems, Journal of **12**, 761-778 (2003).
4. H. Jansen, H. Gardeniers, M. deBoer, M. Elwenspoek, and J. Fluitman, "A survey on the reactive ion etching of silicon in microtechnology," Journal of Micromechanics and Microengineering **6**, 14-28 (1996).
5. S. Tachi, K. Tsujimoto, and S. Okudaira, "Low-temperature reactive ion etching and microwave plasma-etching of silicon," Applied Physics Letters **52**, 616-618 (1988).
6. D. L. Flamm, "Mechanisms of silicon etching in fluorine-containing and chlorine-containing plasmas," Pure and Applied Chemistry **62**, 1709-1720 (1990).
7. J. W. Coburn, and H. F. Winters, "Plasma-etching - discussion of mechanisms," Journal of Vacuum Science & Technology **16**, 391-403 (1979).
8. *CRC Handbook of Chemistry and Physics* (CRC Press, 2004-2005).
9. G. Cunge, *Plasma etching and reactive ion etching: the fundamentals and applications* (CEI-Europe AB, 2013).
10. C. Pandurangappa, B. N. Lakshminarasappa, and B. M. Nagabhushana, "Synthesis and characterization of CaF2 nanocrystals," Journal of Alloys and Compounds **489**, 592-595 (2010).
11. G. Chai, G. Dong, J. Qiu, Q. Zhang, and Z. Yang, "Phase Transformation and Intense 2.7 mu m Emission from Er3+ Doped YF3/YOF Submicron-crystals," Scientific Reports **3** (2013).
12. R. X. Yan, and Y. D. Li, "Down/Up Conversion in Ln3+-Doped YF3 Nanocrystals," Advanced Functional Materials **15**, 763-770 (2005).
13. A. C. Yanes, A. Santana-Alonso, J. Méndez-Ramos, J. del-Castillo, and V. D. Rodríguez, "Novel Sol–Gel Nano-Glass–Ceramics Comprising Ln3+-Doped YF3

Nanocrystals: Structure and High Efficient UV Up-Conversion," Advanced Functional Materials **21**, 3136-3142 (2011).

14. S. Fischer, H. Steinkemper, K. W. Krämer, and J. C. Goldschmidt, "Concepts to enhance the efficiency of upconversion for solar applications," (2012), pp. 843806-843806-843808.
15. I. J. A. Woollam Co., *Guide to Using WVASE32 Spectroscopic Ellipsometry Data Acquisition and Analysis Software* (Lincoln, NE, 1994).
16. E. L. Payrer, R. M. Almeida, C. Jimenez, P. D. Szkutnik, and J. L. Deschanvres, "Growth of lanthanide-doped YF3 thin films by pulsed liquid injection MOCVD: Influence of deposition parameters on film microstructure," Surface & Coatings Technology **230**, 22-27 (2013).
17. P. Chindaudom, and K. Vedam, "Characterization of inhomogeneous transparent thin-films on transparent substrates by spectroscopic ellipsometry - refractive-indexes n(lambda) of some fluoride coating materials," Applied Optics **33**, 2664-2671 (1994).
18. D. F. Bezuidenhout, K. D. Clarke, and R. Pretorius, "The optical-properties of YF_3 films," Thin Solid Films **155**, 17-30 (1987).
19. S. K. W. MacDougall, I. Aruna, J. Marques-Hueso, D. Chen, Y. Wang, and B. S. Richards, "Broadband excitation of upconversion in lanthanide doped fluorides for enhancement of Si solar cells," in *Photonics for Solar Energy Systems Iv*, R. Wehrspohn, and A. Gombert, eds. (2012).

Chapter 7 - PEDOT:PSS for Use as the Back Contact of a Bifacial Silicon Solar Cell and for Silicon Wafer Bonding

In this chapter the optical, electrical and structural analysis of thin films of PEDOT:PSS is presented. Uniform thin films of the conductive polymer were fabricated by spin coating. The refractive index of the films were measured as a function of thickness and annealing temperature. Optical absorbance measurements were performed to corroborate the results. The electrical measurements were carried out using a 4-point-probe and were investigated as a function of film thickness and annealing temperature. Finally, the shear stress of thin films of PEDOT:PSS used as an adhesive for the binding of Si wafers is investigated.

Thin films of PEDOT:PSS were prepared over a thickness range of 56-133 nm and annealed over a temperature range of 50-195°C. A novel anisotropic ellipsometry model was developed that showed that the index of refraction in the plane of the thin film shows metallic like behaviour. The annealing temperature was found to be critical to both the electrical conductivity of the PEDOT:PSS films and shear stress of silicon wafers bonded together using a thin film of PEDOT:PSS. A critical annealing temperature of 100°C was identified, corresponding to the complete removal of water from the thin film.

7.1 Deposition of PEDOT:PSS by Spin Coating

PEDOT:PSS can be used as a back contact for nano-structured bifacial solar cells. This would be of particular importance for the surface of a 2D photonic crystal patterned bifacial solar cell, where traditional metallic contacts would destroy the photonic crystal structure beneath and partially shadow the active area of the photovoltaic layer. The use of a polymer back contact would allow for the nano-structured area of the cell to remain intact, maximising any increase in efficiency from the photonic crystal structure.

The successful spin coating of PEDOT:PSS onto nano-arrays of pillars has been previously reported by Pudasaini *et al* [1]. They demonstrated that a 40 nm layer of PEDOT:PSS could be coated onto the surface of pillars of height 200-1200 nm, spacing of 650 nm and radius of 200-250 nm. The pillar dimensions used by Pudasaini *et al*. are comparable to those used in this work and so it can be concluded that spin coating could also be used to effectively coat a thin film of PEDOT:PSS onto the surface of Si based pillars of the dimensions considered in this thesis.

The work carried out for this thesis provides a broad characterisation of the deposition parameters and optical, electrical and mechanical properties of thin films of PEDOT:PSS on a flat uniform surface. The second stage of this investigation would be to investigate the properties of these films on a textured photonic crystal array of pillars to fully address the fabrication and performance constraints. However this work was beyond the scope of this thesis.

Thin films of PEDOT:PSS (Clevios^{TM} P VP AL 4083) were prepared by spin coating (section 4.2.3) for characterisation for the use as a back contact for a bifacial Si solar cell and for Si wafer bonding. Spin coating is commonly used deposition technique for polymer thin films. During the spin coating process the solvent dries relatively fast, not allowing much time for the molecules to become ordered [2]. Therefore a post annealing treatment is often required to achieve high molecular ordering, which is critical to the charge transport properties of a conductive polymer like PEDOT:PSS [3, 4]. Spin coating can be carried out at atmospheric pressure, achieving good uniformity, which makes it a fast and inexpensive method for preparing thin films of nanoscale thickness.

7.1.1 Fabrication of PEDOT:PSS Thin Films

The PEDOT:PSS thin films were prepared by spin coating in air and annealed in a vacuum oven to enhance the electrical conductivity. The films were prepared on both Si(111) (10 mm × 10 mm) and glass microscope slides (70% SiO_2) (25 mm x 25 mm) square substrates to allow for a full range of optical and electrical characterisation techniques. The samples for Si wafer bonding were prepared by spin coating a thin film of PEDOT:PSS onto the base Si wafer substrate, before placing the top Si wafer onto the thin film layer by hand. The two wafers were aligned using metal blocks before being annealed. The Si and glass substrates were cleaned prior to spin coating using the procedures detailed in sections 4.2.1 and 4.2.2 respectively.

Initial characterisation of the film thicknesses achievable by spin coating of the PEDOT:PSS was carried out in order to maximise the set of thicknesses to be used in this study. The spin coating was carried out using the system described in section 4.2.3 and the film thickness was varied by changing the spin speed. The film thickness determined experimentally as a function of spin speed is shown in in Figure 7-1. It can be seen that the film thickness reduces by ever smaller amounts with increasing spin speed. The expected dependence of the film thickness (d) with rotational speed (w) is $d \propto 1/\sqrt{w}$ [2, 5]. Due to the slight deviation of the thickness from that expected at 6000 rpm, the upper

spin speed limit for further analysis was chosen to be 5500 rpm. At a low spin speed of 1500 rpm, a large film thickness of 133 nm was achieved, however this film was not uniformly distributed across the surface of the substrate. It was found that the centre of the wafer acquired a uniform distribution, however a thick buildup of the polymer at the corners of the substrate was observed. Therefore optical and electrical measurements were taken from the uniform central section of the film.

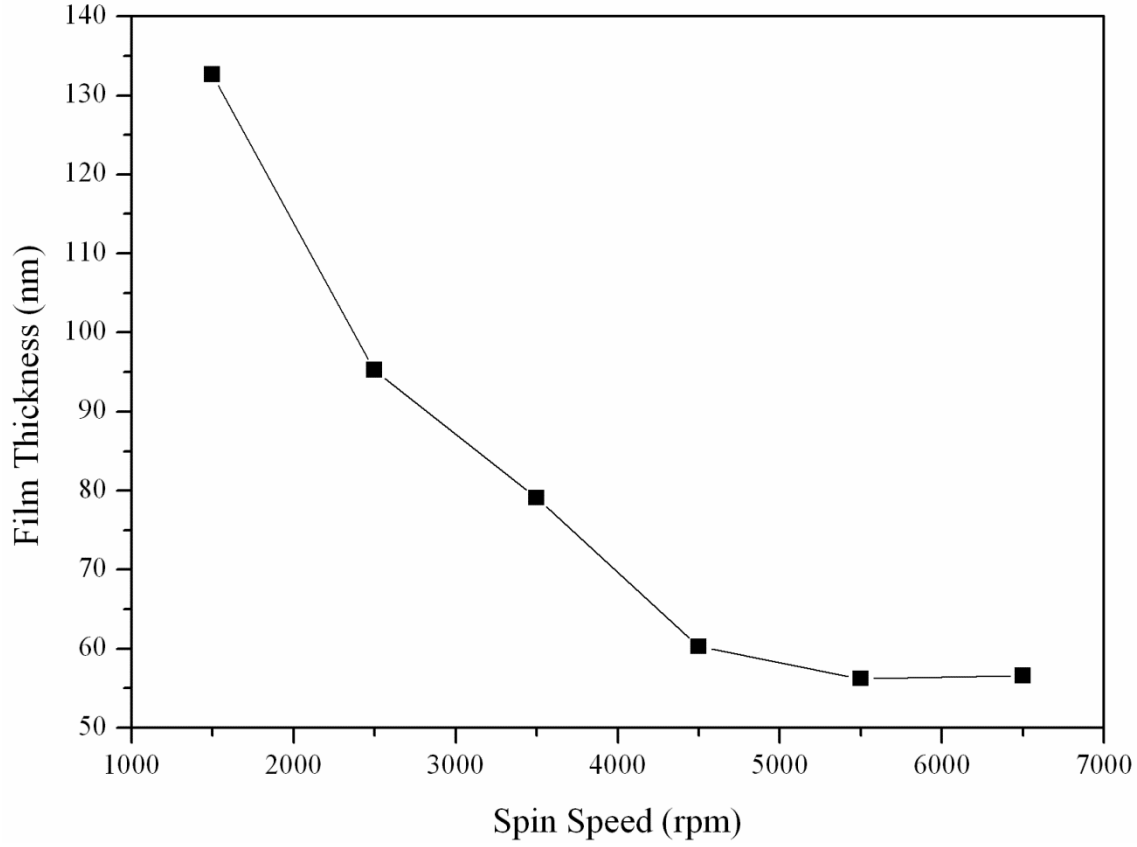

Figure 7-1: The film thickness of PEDOT:PSS is shown to plateau at a minimum value of around 56 nm with increasing spin speed.

Once the thin films had been spin coated, they were annealed in a vacuum oven (Gallenkamp). The oven was evacuated and then purged with N_2 three times prior to heating in order to minimise any O_2 or H_2O uptake [6]. The samples were annealed at the desired temperature for 1 hour.

7.2 Optical Properties of PEDOT:PSS

The optical properties of the PEDOT:PSS films are essential for its effective use as a back contact for a bifacial solar cell. A back contact must exhibit high transmission in the wavelength range over which the solar cell is most efficiently absorbing. Furthermore knowing the refractive index of the polymer layer can allow for the thickness of the back contact to be tuned in order to use the layer as an anti-reflective coating [7] thereby improving the transmission of light of a specific wavelength range.

Spectroscopic ellipsometry is a very powerful technique, providing both optical and structural information. The weak inter-chain coupling of conducting polymers means that they can be considered to be quasi-one-dimensional, showing preferential orientation of the polymer chains depending on the processing conditions [8]. Therefore polymer thin films can be anisotropic in both their structural and optical properties. The optical uniaxial anisotropy in PEDOT is thought to occur from the main polymer chains lying flat and parallel to the surface of the film, randomly ordered azimuthally [8]. This orientation may occur from the high angular velocity of the spin coating process.

7.2.1 Ellipsometry Modelling of PEDOT:PSS

Ellipsometry analysis was carried out on the PEDOT:PSS deposited onto the Si substrates. The general ellipsometry modelling procedure, as detailed in section 4.3.1, was used to model the experimental data. The analysis of the data was carried out over the full spectral range available, from 300-2500 nm, to maximise the accuracy of the model.

PEDOT:PSS film are uniaxial anisotropic, showing distinctly different refractive indices parallel and perpendicular to the plane of the thin film [9]. This provided additional complexity to the modelling procedure. The modelling was carried out using two separate generalised oscillator layers to model the refractive index of the parallel in-plane (x-y) and out-of-plane (z) components separately (Figure 7-2). These two proxy layers became the inputs to the overall uniaxial layer that also incorporated the layer thickness (Figure 7-2). This initial model was developed with the help of Dr Thomas Wagner of LOT-QuantumDesign [10]. The test sample (2500 rpm spin coat and 80°C anneal) on which this model was developed provided the optimised oscillator parameters for the in-plane and out-of-plane layers detailed respectively in

Table 7-1 and

Table 7-2.

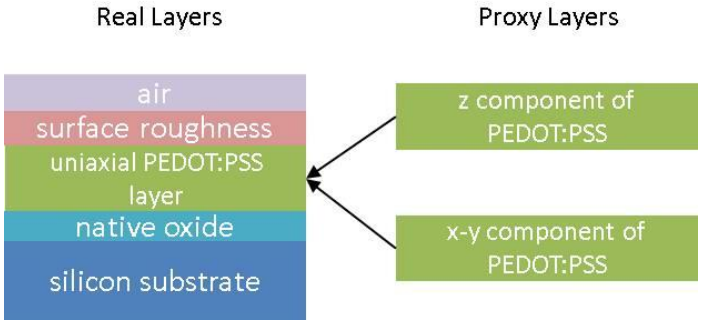

Figure 7-2: This schematic details the model used to calculate the refractive index for the PEDOT:PSS films. Separate generalised oscillator models were optimised as proxy layers in the z and x-y directions. These layers were inputs for the overall uniaxial layer, which incorporated the layer thickness.

Oscillator	E_n(eV)	A_n [Pole]	Br_n(eV)	e1 offset (eV)	ρ_n (Ω-cm)	$\tau_n(10^{-15}$ s)
Pole 1	7	13	0	-	-	-
e1 offset	-	-	-	1.99	-	-
Gaussian	6.72	0.49	3.38	-	-	-
Drude	-	-	-	-	0.00048	6.37

Table 7-1: The optimised Oscillator fit parameters for the in-plane (x-y) layer are shown. These values were calculated for the test sample spin coated at 2500 rpm and annealed at 80°C.

Oscillator	E_n/Eo_n (eV)	A_n (eV)	Br_n (eV)	e1 offset (eV)	C_n (ev)	Eg_n (eV)	ρ_n (Ω-cm)	$\tau_n(10^{-15}$ s)
Pole 1	7	0.019	0	-	-	-	-	-
e1 offset	-	-	-	1.29±0.05	-	-	-	-
Tauc-Lorentz	5.42	11.33	-	-	$1.0\cdot10^{-6}$	2.67	-	-
Drude	-	-	-	-	-	-	$1.1\cdot10^{-5}$	230.62

Table 7-2: The optimised Oscillator fit parameters for the out-of-plane (z) layer are shown. These values were calculated for the test sample spin coated at 2500 rpm and annealed at 80°C.

The experimental and simulated data (Ψ and Δ) for the test sample are shown in Figure 7-3 for comparison. The model is shown to provide a very good fit to the experimental data, with a very low MSE value of 2.45.

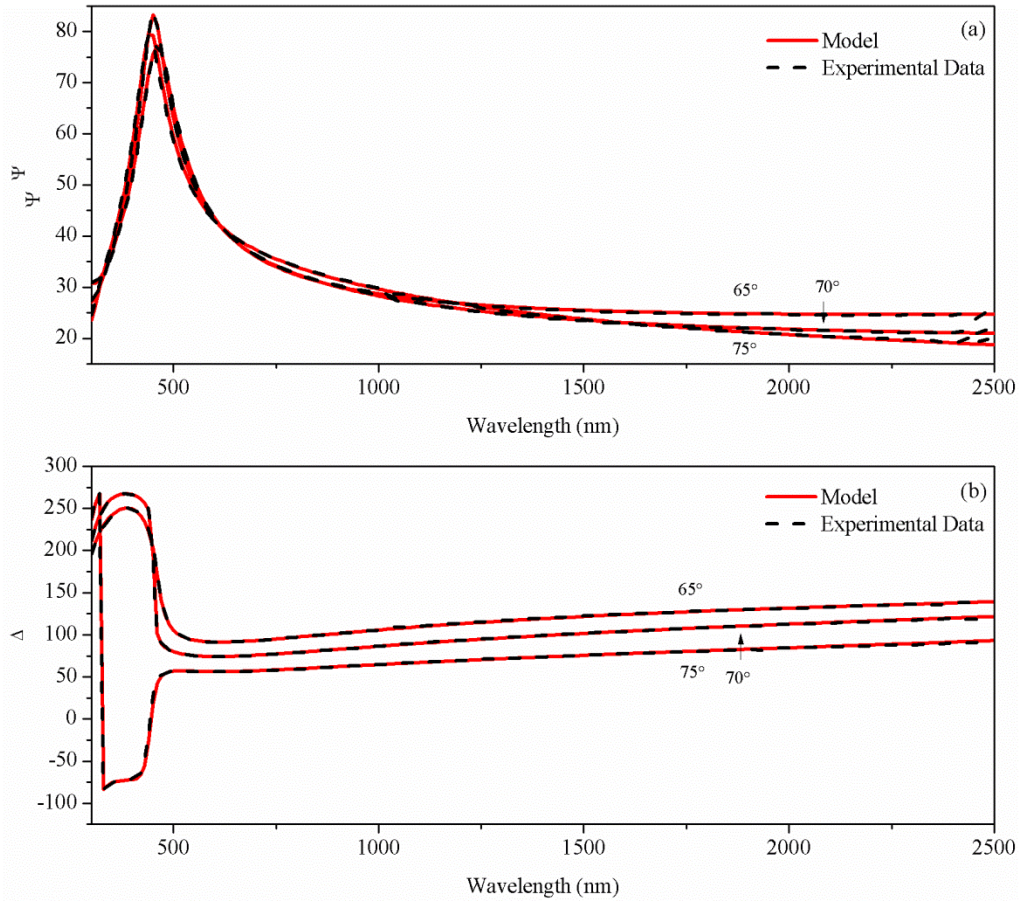

Figure 7-3: The experimental (black dotted) and modelled (red) data is shown as a function of wavelength from 300-2500 nm. The model developed for the PEDOT:PSS sample spin coated at 2500 rpm and annealed at 80°C was shown to give a very good fit to the experimental data. The resulting MSE value was 2.45.

The real and imaginary parts of the refractive index corresponding to the modelled test sample are shown in Figure 7-4. The real and imaginary components of the index of refraction within the plane of the film (n_{xy} and k_{xy}) show metallic like behaviour, whereas the corresponding components perpendicular to the film (n_z and k_z) shows dielectric like behaviour. The metallic like behaviour corresponds to the high conductivity of the material [8]. The expansion of k_z in the inset reveals that the absorption follows the same overall trend as that of k_{xy}, only scaled, which indicates that the absorption is of the same nature. The overall refractive index results are in good agreement with those published elsewhere for the lower wavelength range of 300-1700 nm [9].

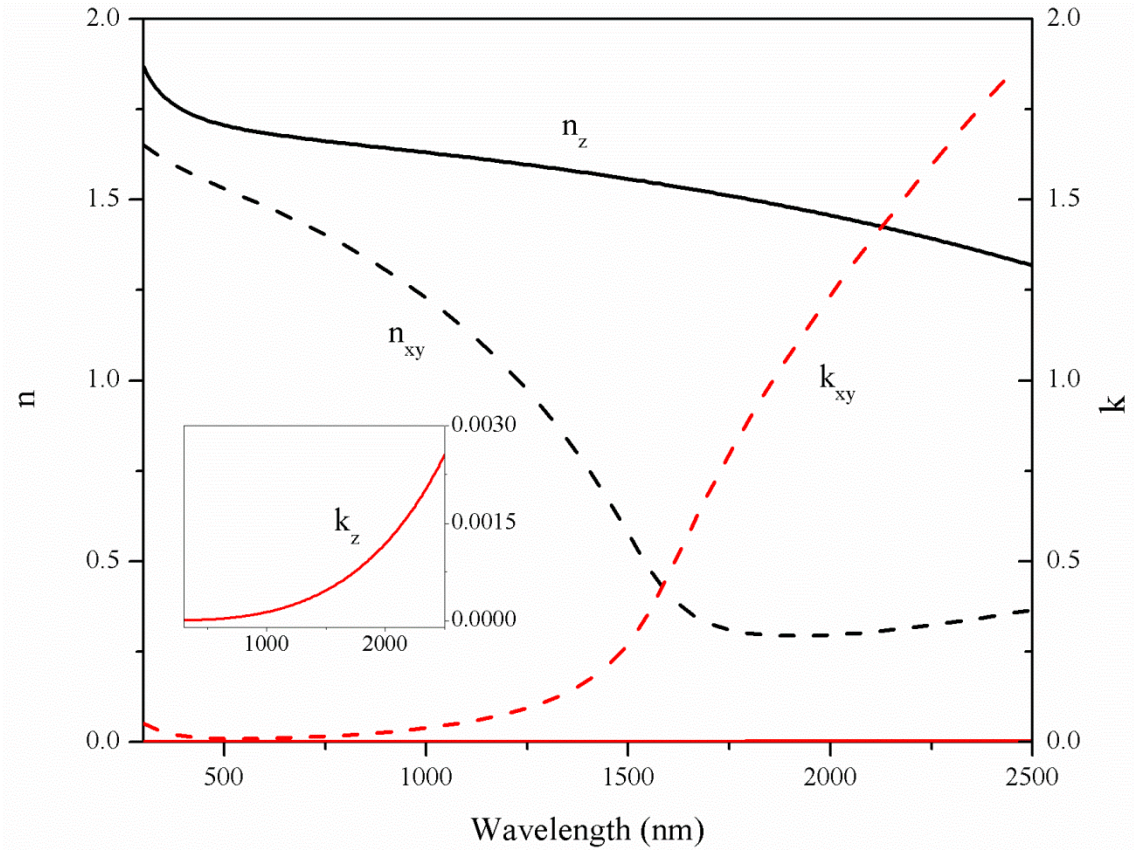

Figure 7-4: The real and imaginary components of the index of refraction within the plane of the film (n_{xy} and k_{xy}) shows metallic like behaviour, whereas the corresponding components perpendicular to the film (n_z and k_z) shows dielectric like behaviour.

Measurements of the refractive index were carried out on three different areas of the same PEDOT:PSS sample to provide an estimate of the repeatability of the results. The sample chosen for the repeatability study had been spin coated at 2500 rpm, resulting in a thickness of 95 nm. The repeatability measurements were taken 3 months after the sample was prepared. The sample was stored in a nitrogen purged cabinet, however the effects of aging of the sample over this time are unknown and may have affected its composition. The MPE between the optimised refractive indices obtained from three locations on the same sample was compared against the MPE obtained from the refractive indices of the samples of varying thickness measured at the start of this study.

The mean percentage error (MPE) was used to quantify the error in the repeatability of the measurements across the sample area. The MPE computes the average percentage error by which the forecasts of a model differ from the actual values of the quantity being forecast [11]:

$$MPE = \frac{100\%}{n}\sum_{t=1}^{n}\frac{a_t - f_t}{a_t}$$

where n is the number of times the variable is forecast, a_t is the actual value of the quantity being forecast, and f_t is the forecast.

The MPE of the measurements at three locations on the same sample (95 nm thick) was found to be 5.7 for n and 15.9 for k. The MPE between successive thicknesses of PEDOT:PSS layers annealed at 50°C are shown in

Table 7-3. While the MPE between the thickest sample (133 nm) and those of subsequent reduced thicknesses are shown in

Table 7-4. The results of the MPE between areas on the same sample (bold) are included for comparison.

Samples compared according to their thickness (nm)	MPE_n	MPE_k
REF 95, 95, 95	**5.7**	**15.9**
133, 95	5.6	19.8
95, 79	3.8	12.2
79, 60	4.0	38.6
60, 56	1.9	29.0

Table 7-3: The mean percentage error between successive samples of reducing thickness are compared against the mean percentage error of different areas on the same sample.

Samples compared according to their thickness (nm)	MPE_n	MPE_k
REF 95, 95, 95	**5.7**	**15.9**
133, 95	5.6	19.8
133, 79	9.3	20.8
133, 60	5.5	51.0
133, 56	5.7	34.4

Table 7-4: The mean percentage error between the thickest and subsequent samples of reducing thickness are compared against the mean percentage error of different areas on the same sample..

It can be seen from both

Table 7-3 and

Table 7-4 that the MPE of the k component of the refractive index is in general smaller between different areas of the same sample, than between samples. However the MPE for the n component of the refractive index is larger between different areas of the same sample, than between samples of successive thickness and roughly the same as between

samples compared against the thickest sample. The latter suggests that there is as much variability between different areas on the same sample as there is between the thinnest sample compared to the thickest sample.

The fact that the MPE for the *n* component of the refractive index between different areas on the same sample is larger than the MPE between all other samples of successive thickness (

Table 7-3) is a strong indication that aging effects detrimental to the *n* component of the refractive index have occurred, as the measurements used to compare samples of successive thickness were taken at the time of sample fabrication. It is therefore difficult to confirm the reliability of the refractive index measurements across the sample areas used for this study. The long term effects of aging of the PEDOT:PSS were beyond the scope of this study, however would be essential to know for the practical application in a solar cell.

The MPE was also analysed between samples of the same thickness (95 nm), but different annealing temperatures. The MPE between successive annealing temperatures of PEDOT:PSS are shown in Table 7-5. While the MPE between the sample annealed at the lowest temperature (50°C) and those of subsequent increasing annealing temperature are shown in Table 7-6.

Samples of annealing temperature (°C)	MPE(n)	MPE(k)
REF 95, 95, 95 (nm)	**5.7**	**15.9**
50, 80	1.2	10.6
80, 120	1.1	19.4
120, 160	2.9	16.9
160, 195	5.4	17.6

Table 7-5: The mean percentage error between successive samples of increasing annealing temperature are compared against the mean percentage error of different areas on the same sample annealed at 50°C.

Samples (nm)	MPE(n)	MPE(k)
REF 95, 95, 95 (nm)	**5.7**	**15.9**
50, 80	1.2	10.6
50, 120	2.2	20.8
50, 160	2.3	9.9
50, 195	5.1	15.3

Table 7-6: The mean percentage error between the thickest and subsequent samples of reducing thickness are compared against the mean percentage error of different areas on the same sample annealed at 50°C.

It can be seen from both Table 7-5 and Table 7-6 that once again the MPE for the *n* component of the refractive index is larger between different areas on the same sample, than between different samples, which in this case differing in their annealing temperature. Therefore again it is difficult to draw conclusions as to the repeatability of the measurements across a sample area.

7.2.2 Effect of Thickness on Absorbance and Refractive Index

The refractive indices of thin films of polymers can have a strong dependence on the thickness of the film. This dependence was shown by Kim *et al*. to be related to the microsctructure, density and morphology of a polymer film [12]. Furthermore they showed that a reduction in the effective density normal to the surface occurred for thinner films, which resulted in a corresponding reduction in the real component of the refractive index. Therefore a reduction in the effective density of the out-of-plane direction may be the cause of the reduction in the real component of the refractive index observed in Figure 7-5 for the PEDOT:PSS films. The purpose of the investigation carried out for this thesis was to characterise the optical properties of the PEDOT:PSS film over a wide spectral range as a function of the processing conditions, temperature and film thickness. Further experimental investigation of the effective density of the film was beyond the scope of this work.

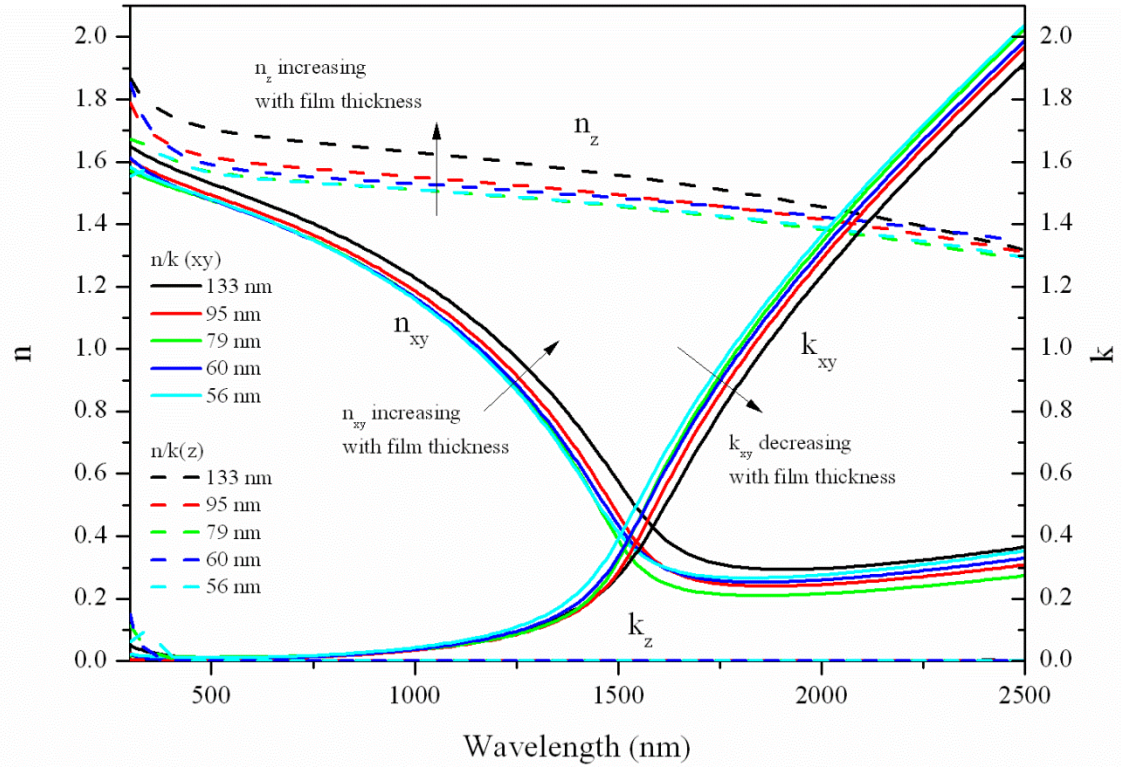

Figure 7-5: The real component of the refractive index (*n*) and the imaginary part of the refractive index (*k*) in both the *xy* and *z* planes are shown as a function of wavelength for a sample annealed at 50°C for samples of varying thickness.

The absorbance of the PEDOT:PSS films on glass was analysed over the same wavelength range as that of the refractive index, from 300 – 2500 nm, as a function of film thickness and annealing temperature (section 7.2.3). The absorption of the films was measured using an integrating sphere in a Perkin Elmer Lambda 950, as detailed in section 4.3.3. The absorption measurements shown in Figure 7-6 and Figure 7-7 are for the PEDOT:PSS layer on the glass substrate, with the absorption of the bare glass substrate included for comparison.

There was found to be a large uncertainty in the repeatability of the absorption measurements. This was of particular significance to the measurements of the bare glass substrate, which showed very low absorbance, often resulting in unphysical negative absorbance being introduced for part of the spectral range. To quantify the stability of the measurement system, four repeated scans were taken sequentially with a bare glass substrate remaining in place throughout. An overall shift in the absorbance was observed across the whole spectral range. The average absorbance at 1100 nm was found to be 0.027±0.004, which corresponds to ±15% of the average value. A second set of

measurements were carried out to quantify the uncertainty introduced from placing a sample into the sample holder within the integrating sphere. Four repeated scans were carried out with the same bare glass substrate removed and inserted back into the sample holder before each scan. Again, an overall shift in the absorbance was observed across the whole spectra range. The average absorbance at 1100 nm was found to be 0.012±0.007, which corresponds to ±58% of the average value. However the most significant observation is that the average values obtained for each set of measurements do not lie within the bounds of uncertainty for their counterpart sets of data. This indicates that a more significant error in the system is present, which could be a result of an overall drift of the system due to the excitation lamp nearing the end of its life. Combining all eight sets of data to provide a more accurate estimate of the error provides an average value of 0.018±0.013. The absolute uncertainty in the absorbance provides an indication of the confidence in the absorbance data shown below. Due to the large uncertainty found in the absorbance of the substrate, the PEDOT:PSS absorbance spectra was not normalised to remove the influence of the substrate. Instead, the substrate absorbance is plotted on the same graph for comparison.

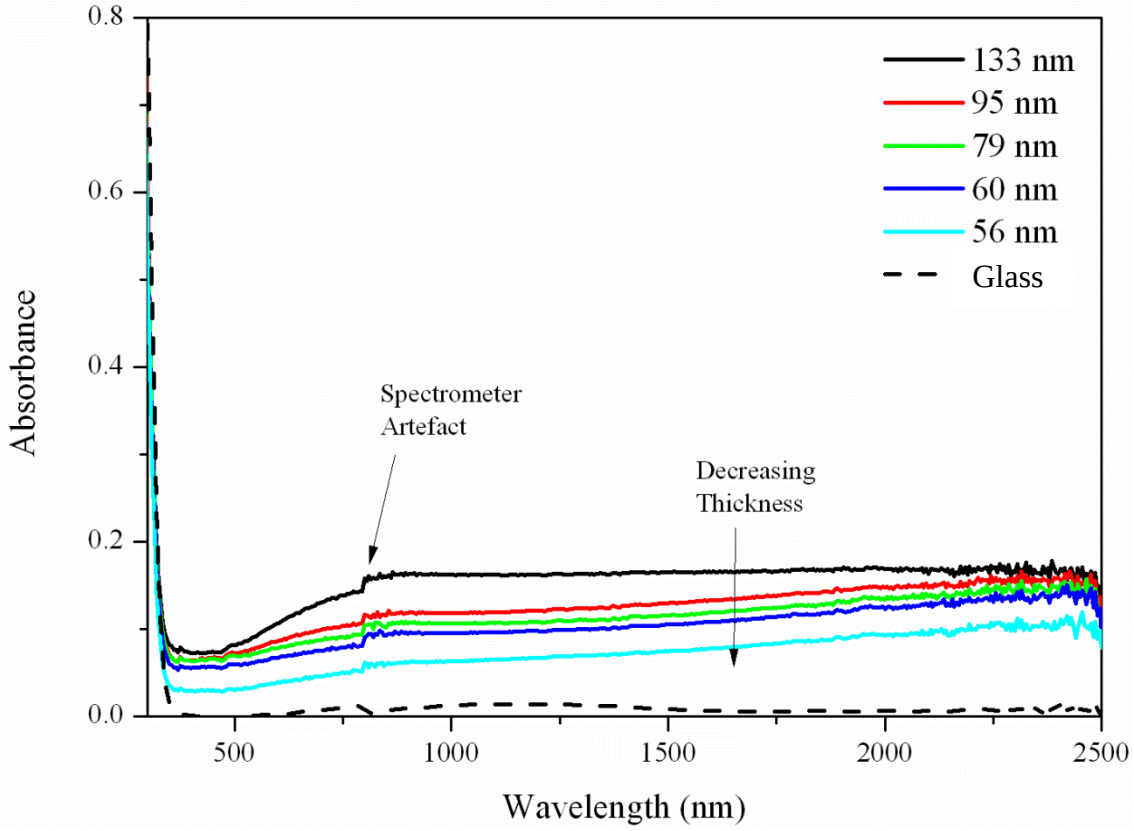

Figure 7-6: The absorbance of the PEDOT:PSS films for a range of thicknesses is shown as a function of wavelength. The broad absorption band from 500-2500 nm can either be attributed as a free charge contribution to the absorption, or mid-gap states (polaron or bi-polaron).

A broad absorbance in the PEDOT:PSS layer is observed in Figure 7-6 from around 500 nm all the way up to 2500 nm. This feature can either be attributed as a free charge contribution to the absorption, or mid-gap states (polaron or bi-polaron states) [9]. A broad absorption spanning the wavelength range of the solar spectrum will have an associated loss to the conversion efficiency of the photovoltaic layer due to a small absorption of part of the solar spectrum. This should be accounted for when choosing an appropriate transparent conductive layer for use in photovoltaics. The broad absorbance peak below 350 nm is dominated by the glass substrate.

7.2.3 Effect of Annealing Temperature on Transmission and Refractive Index

An overall decrease in the absorbance is observed with increasing annealing temperature in Figure 7-7. In section 7.3.1 it is shown that a rise on conductivity also occurs for increasing annealing temperature. Therefore increasing conductivity is accompanied by a decrease in absorbance for PEDOT:PSS. This effect has been reported elsewhere and is believed to be due to a red shift in the absorbance maximum of mid-band gap states, resulting from the increased conductivity [9].

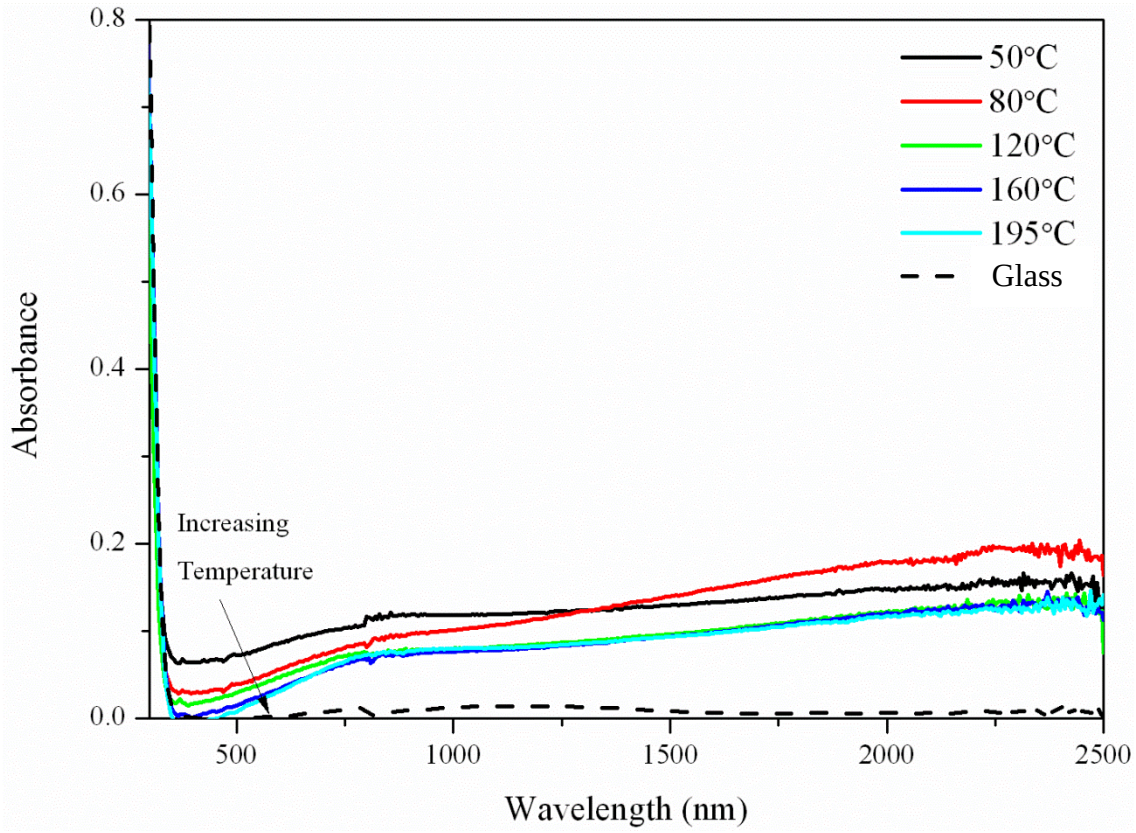

Figure 7-7: The absorbance of the PEDOT:PSS films for a range of annealing temperatures is shown as a function of wavelength. The overall decrease in the absorbance with increasing annealing corresponds to a rise in conductivity of the thin film. The decrease in absorbance is believed to be

due to a red shift in the absorbance maximum of mid-band gap states, resulting from the increased conductivity.

The overall decrease in absorbance with increasing annealing temperature is also suggested in the extinction coefficient k_{xy} results. It can be seen from the expanded section in Figure 7-8 that the minimum and maximum extinction coefficients correspond to the minimum and maximum conductivities observed in Figure 7-9 for annealing temperatures of 80°C and 194°C respectively.

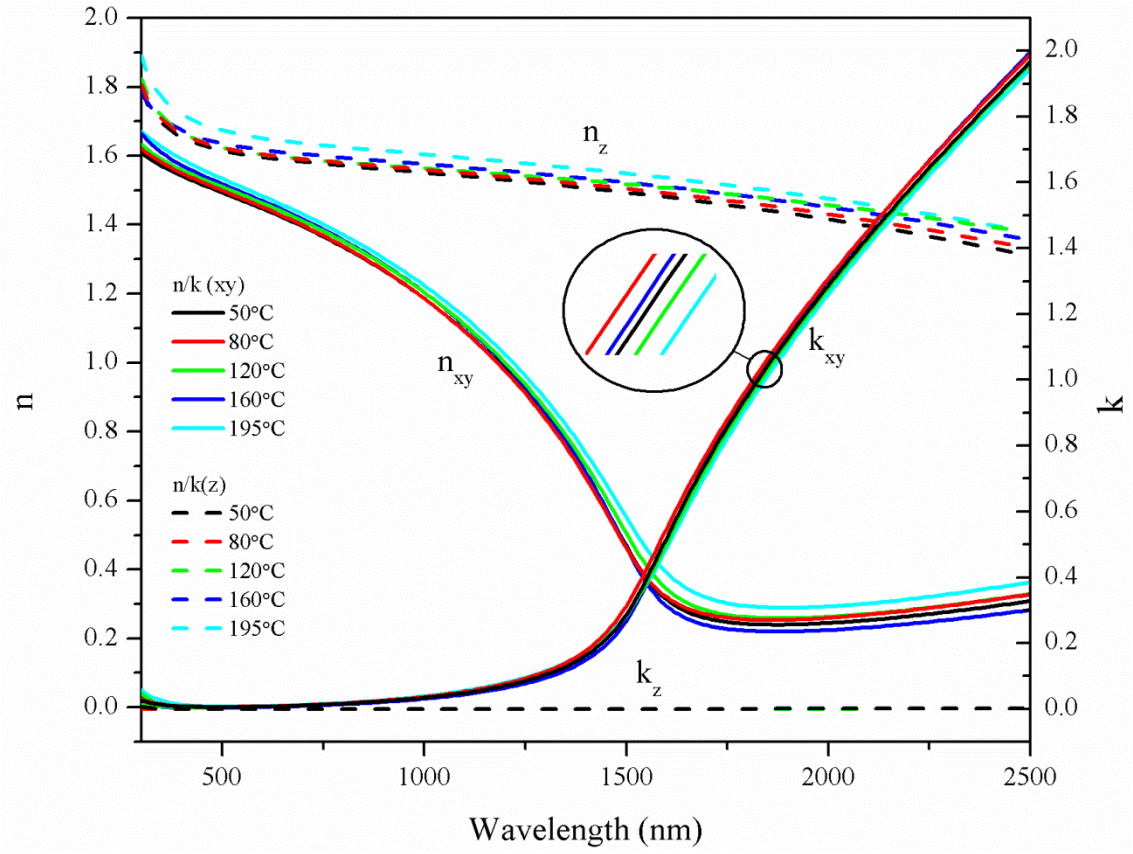

Figure 7-8: The real component of the refractive index (*n*) and the imaginary part of the refractive index (*k*) in both the *xy* and *z* planes are shown as a function of wavelength for samples of 133 nm thick and varying annealing temperature.

The refractive index was compared to that of the well-used inorganic transparent conductive electrode indium tin oxide (ITO). The real component of the refractive index of ITO decreases from around 2.2 at 350 nm, to around 1.5 at 1000 nm [13]. Therefore the refractive index of PEDOT:PSS is substantially lower in general across the range of comparison. This is likely to lead to a reduction in the antireflection properties of PEDOT:PSS compared to ITO on silicon. Minimum reflection occurs for an antireflection

coating that has a refractive index which is the average of the materials below and above it [14]. The average refractive index at 600 nm for an antireflection coating between silicon and air is around 1.87 and between silicon and glass is around 2.3. Therefore the refractive index of ITO at 600 nm (~1.8) is closer to the desired value than that of PEDOT:PSS in the *z* direction (1.6).

7.3 Electrical Properties of PEDOT:PSS

The processing conditions of PEDOT:PSS have been reported to play a significant role in the conductivity of the film [15]. In particular, the annealing temperature can significantly alter the material's conductivity. In the usual aqueous PEDOT:PSS solution, the polymer chains form compact coils that pack randomly when dried. Therefore conductivity measurements reported cover a wide range of values [6].

In this work the electrical characterisation was carried out using a 4-point probe, as detailed in section 4.3.7. The PEDOT:PSS films on the insulating glass substrates were used for the characterisation. These substrates (15 mm × 15 mm) were large enough to ensure that the distance from any probe to the edge of the film was greater than five times the spacing between the probes (300 μm) and is negligible and so no correction for a boundary configuration is required [16].

7.3.1 Effect of Thickness and Annealing Temperature on Conductivity

An overall increase in conductivity is observed in Figure 7-9 for an increase in the annealing temperature. The increase in conductivity over the annealing range of 80-120°C is likely to be caused by shrinking of the insulating PSS shell that surrounds the conducting PEDOT rich grains due to the evaporation of water [6]. Beyond 160°C the increase is predominantly due to PSS segregation effects [6, 17]. At these relatively low temperatures, it is most likely that the increases in conductivity observed are due to loss of water and structural changes, rather than chemical alterations. The conductivity would be expected to increase still further with increasing temperature, until degradation of the PSS at around 300°C [6].

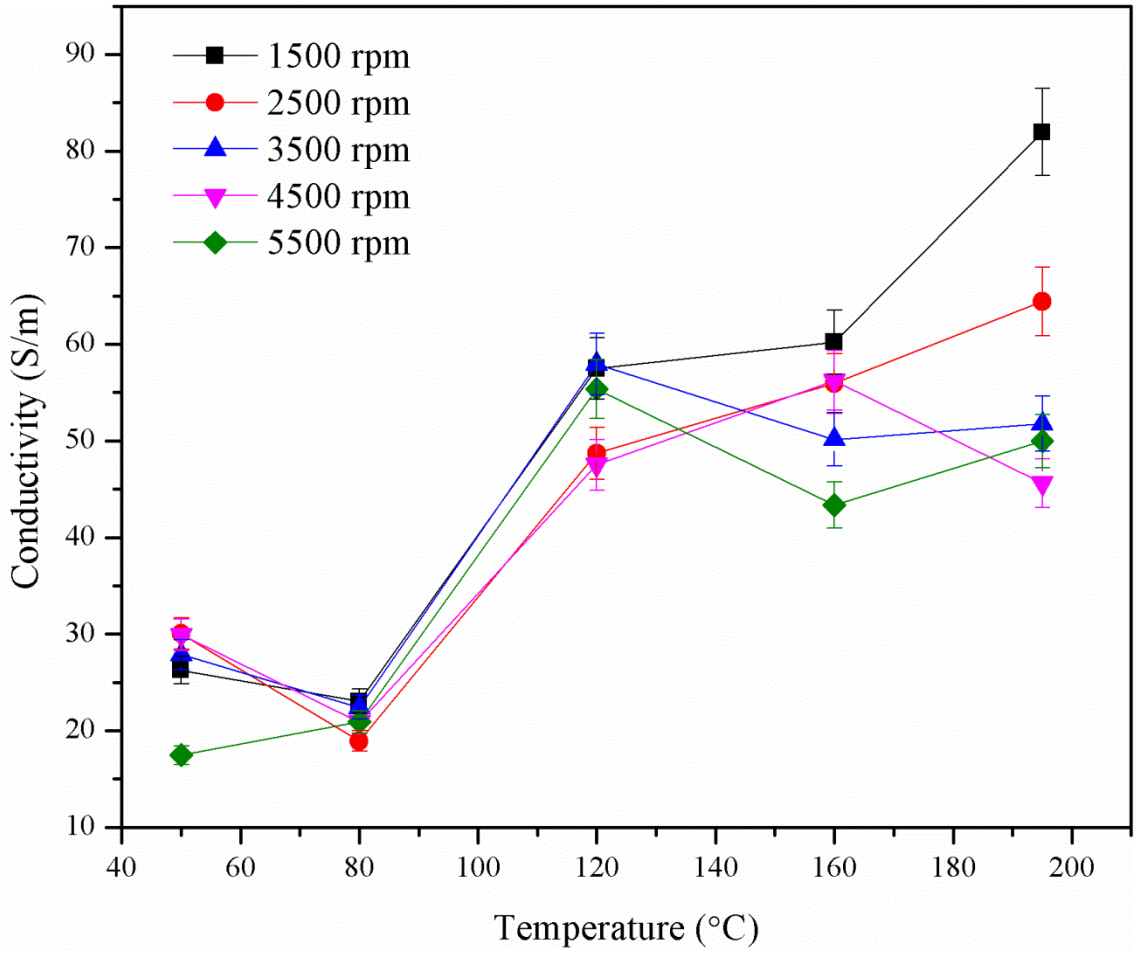

Figure 7-9: The conductivity of PEDOT:PSS films is shown for a range of spin speeds as a function of annealing temperature. An overall increase in conductivity is observed between 50°C and 195°C. The increase in conductivity from 80°C to 120°C is most likely due to water loss, whereas further increase at higher temperatures is due to the reduction of the insulating PSS shell.

No well-defined trend is evident for the change in conductivity with thickness at any given temperature. However it is evident that the thickest film is associated with the highest conductivity. A general trend of increasing conductivity with increased sample thickness of PEDOT:PSS has previously been presented by Yoo *et al* [18]. The authors measure the carrier mobility using the Hall effect and found a systematic increase in mobility with thickness, for thicker samples over the range of 89-357 nm [18]. It is unclear why the experimental results measured in this thesis do not show the same clear trend. One possible cause could be the uptake of atmospheric water vapour within the samples between preparation and measurement. Repeating the measurements using multiple samples for each thickness and temperature, with a standard time between fabrication and measurement would help to reduce the scatter observed and may result in the trend being shown.

The main source of variation in the conductivity measurements was found to come from the probe positioning on the sample. A set of four measurements were carried out within the central region of the film at different locations that all satisfied the condition for negligible boundary effects. A 5.5% variation in the final conductivity measurements was observed, which was an order of magnitude greater than the error associated with IV gradients from which the conductivity was extracted (section 4.3.7). It is believed that this variation is due to non-uniformity in the film thickness across the sample. The ellipsometry analysis indicated typical 8-9% thickness non-uniformity across the 3 mm spot diameter.

A general requirement for the electrical properties of a transparent conductive oxide for use in a solar cell is that the sheet resistance should be <10 Ω/□ [19]. For a 100 nm film, this corresponds to a conductivity $>10^6$ S/m. The sheet resistance for common inorganic transparent conductive electrodes are ITO 3-5 Ω/□, SnO_2F 6-15 Ω/□ and ZnO:Al 4-15 Ω/□. The conductivity measurements achieved for the work in this thesis are very much lower than those desired for use in a solar cell. However they are suitable for an electrically conductive adhesive layer for bonding silicon wafers, as discussed in section 7.4.

Electrically conductive adhesives (ECAs) have had growing interest recently, particularly in the semiconductor industry. These conductive adhesive materials are split into two categories: Isotropic Conductive Adhesives (ICAs) and Anisotropic Conductive Adhesives (ACAs), depending on their electrical characteristics. They typically consist of an epoxy resin to provide the physical and mechanical properties, with a conductive filler for the electrical conduction. The filler is typically a metal such Ag/Au/Ni/Cu or more recently a carbon derivative (e.g. carbon nanotubes). Typical electrical properties of ECAs vary from 10^{-2} to 10^5 S/m, depending on the application [20]. However there has been no evidence found of ECAs used in Si wafer bonding. Furthermore, the microscopic nature of the filler metal particles would be far too large for direct use with a nanostructured layer such as the 2D photonic crystals in this thesis.

The PEDOT:PSS conductivity measured in this work is at the lower end of typical ECA electrical properties. However the introduction of an organic co-solvent has been shown by Xia *et al.* to increase the conductivity of the PEDOT:PSS layer beyond 10^5 S/m [21]. It is therefore expected that a PEDOT:PSS adhesive layer could achieve comparable

electrical properties of current ECAs, without the need for additional highly conducting carbon derivative or metallic fillers.

7.4 Mechanical Properties of PEDOT:PSS for Si Wafer Bonding

The mechanical properties of thin films of PEDOT:PSS for Si wafer bonding were investigated by analysing the shear stress of the films. The shear stress is the component of stress in the plain of the material cross section.

7.4.1 Fabrication of PEDOT:PSS Bonded Si Wafers for Shear Stress Measurements

Si(111) wafer substrates (10 mm × 10 mm) were bonded together using a PEDOT:PSS adhesive layer as described in section 7.1.1. The samples were annealed in a vacuum oven, which removed any trapped bubbles of gas from the adhesive layer. The bottom Si substrates of the annealed samples were then fixed to a mounting block using a thin layer of araldite adhesive. The mounted samples were positioned under the load cell (Instron 3367) and the load tool was applied down onto the top Si substrate at a rate of 5 μm/s until the sample was broken, as shown in Figure 7-10. The maximum force applied at failure of the PEDOT:PSS adhesion layer was recorded.

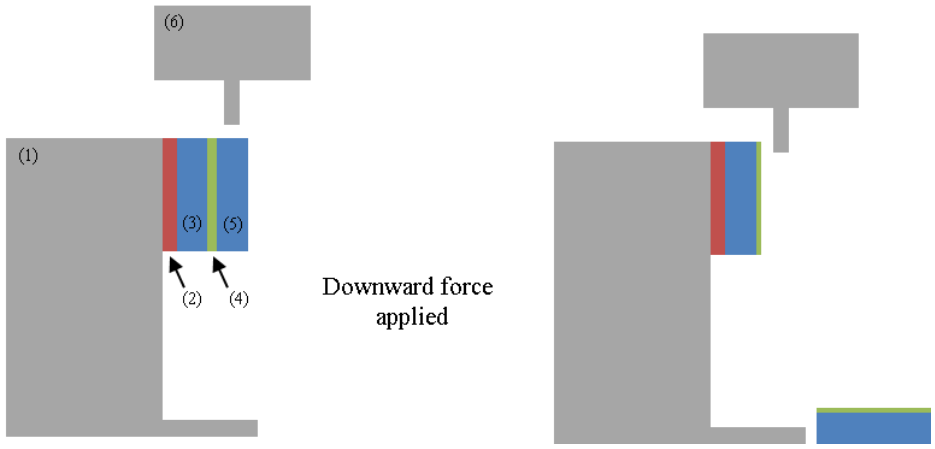

Figure 7-10: Schematic drawing of the apparatus used to measure the shear stress of the PEDOT:PSS adhesive bond: (1) sample mount; (2) mounting adhesive layer; (3) rear Si substrate; (4) PEDOT:PSS bond; (5) top Si substrate; and (6) load cell.

7.4.2 Effect of Annealing Temperature on Shear Force

The shear force was measured for bonded Si wafers annealed at 50°C, 80°C, 120°C, 160°C and 195°C. Ten samples were measured for each annealing temperature to assess the reliability. The PEDOT:PSS adhesion layer was spin coated at 2500 rpm for each sample. At faster spin speeds, the solvent present in the thin film evaporated too quickly to allow for the top Si substrate to be wetted upon contact, resulting in very poor adhesion between the PEDOT:PSS layer and the top Si wafer. At speeds lower than 2500 rpm, the film was found to show significant non-uniformity at the edges of the Si wafers, therefore was not suitable for uniform wafer bonding.

The shear stress measurements upon failure of the PEDOT:PSS adhesion bond is shown in Figure 7-11(a). There was a relatively large spread of measurements within the 10 samples for each annealing temperature, however a general trend in the average shear stress is observed. To minimise the effect of anomalous measurements, the results were re-evaluated in Figure 7-11(b) excluding the maximum and minimum result from each set of measurements. The same overall trend is observed, with a significant decrease in the associated errors. These anomalous results will most likely have occurred from alignment of the load tool above the top Si substrate. On preliminary testing, it was noticed that incorrect alignment of the load tool could result in the tool catching on part of the bottom Si substrate, resulting in a much larger than expected shear stress. Incorrect alignment could also result in the leading edge of the loading tool not being perpendicular with the edge of the top Si substrate.

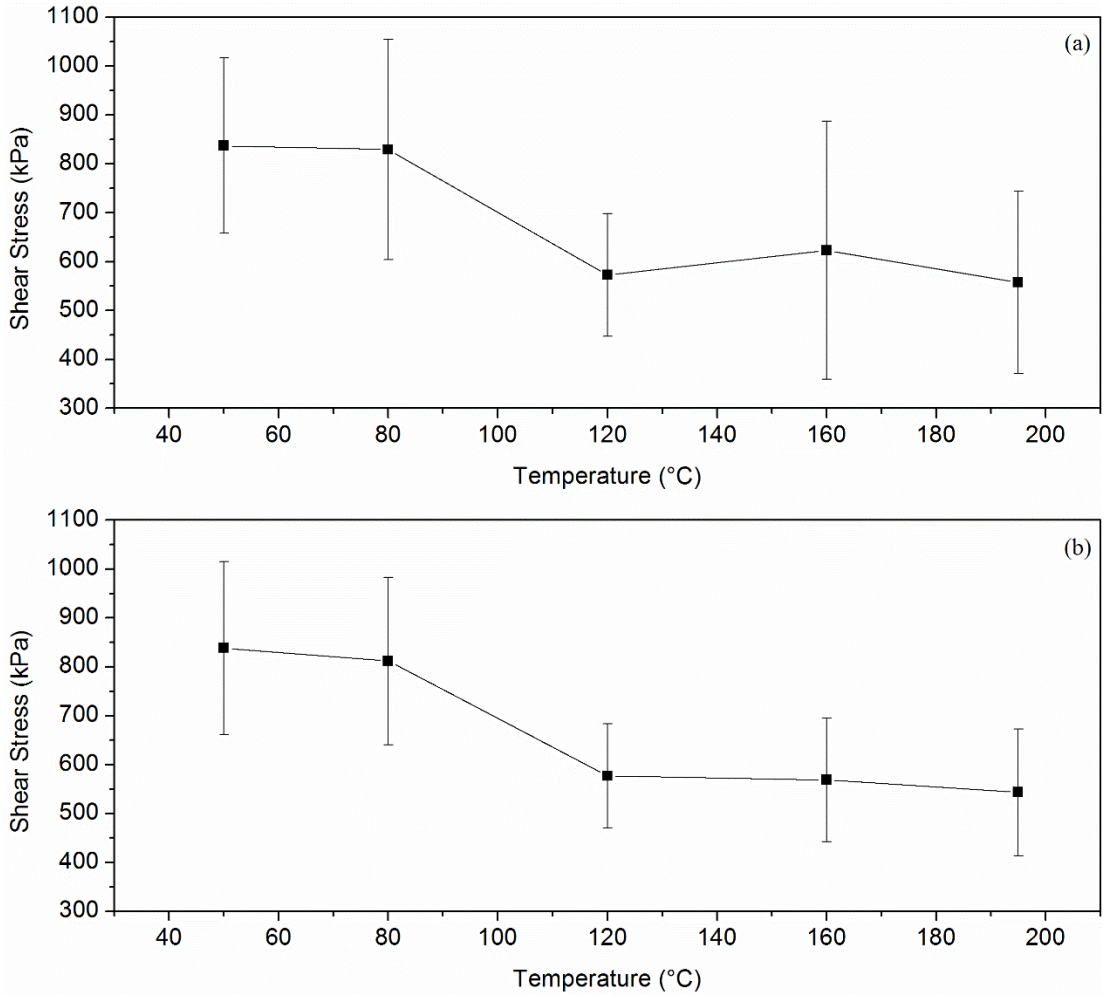

Figure 7-11: (a) The results of the shear stress for the 10 samples measured at each annealing temperature shows a general trend of a stepwise reduction between 80°C and 120°C. (b) The results of the shear stress after removing the maximum and minimum result from each set of data shows the same general trend, with a much improved random uncertainty.

A significant reduction in shear stress is observed between the annealing temperatures of 80°C and 120°C, from 812 kPa to 577 kPa respectively. This reduction is believed to be due to the evaporation of H_2O from the PEDOT:PSS adhesion layer during annealing. The expansion of the H_2O from liquid to gas above 100°C is likely to modify the maro-structure of the PEDOT:PSS layer and weaken its structural integrity as the gas tries to escape form the film. As discussed previously, a wet PEDOT:PSS film is required to achieve the initial adhesion of the top Si substrate to the thin film layer. Therefore it would not be possible to remove the water prior to the application of the top Si substrate.

A final test was carried out where by both the top and bottom Si substrates were spin coated with a PEDOT:PSS film before being brought together. However following annealing, the two Si substrates fell apart, indicating that the adjacent PEDOT:PSS films had not bound together.

The shear stress measured for the PEDOT:PSS layer is only slightly lower compared to results for various other conductive wafer bonding techniques. Abouie *et al.* measured the shear strength of both solid state and eutectic bonding of Si using an Au intermediate layer, which they found to be 15.2 MPa and 13.2 MPa respectively [22]. However both of the bonding procedures required sputtering of the Au layer and annealing temperatures >250°C. Although providing high shear strength and conductivity, this type of Si wafer bonding is unsuitable when low temperatures are required and involves expensive bonding materials and deposition techniques.

Adhesive bonding using polymers provides a low temperature and cheap alternative for Si wafer bonding. Lo *et al.* demonstrated the use of a silicone polymer for Si wafer bonding, achieving a shear strength average of 8.09 MPa [23]. The samples were prepared in a vacuum at a temperature of 150°C with 0.1 MPa of bonding pressure. However, silicone is electrically insulating, unless doped with a conducting material, therefore does not offer the desired electrical properties.

The principle of using derivatives of PEDOT:PSS as an adhesive has previously been proposed by Tung *et al.*, who demonstrated the application of bonding of poly(ethylene terephthalate) (PET) strips using a PEDOT:PSS film of unspecified thickness [24]. This film was found to have a shear strength of 0.2 MPa. They further showed that through the addition of graphene oxide, the conductivity and shear strength could be greatly increased. All of the films in Tung *et al.*'s study were annealed at 60°C and the thicknesses of the films used to measure the shear stress were not presented.

The work carried out here demonstrates the importance of the annealing temperature to the bonding strength and electrical conductivity of the film. The sharp reduction in bond strength between 80°C and 100°C means that a trade off in bonding strength occurs for increased electrical conductivity of the film. This trade off must be taken into account when optimising the annealing temperature for the desired conductive adhesive characteristics.

7.5 Conclusions of PEDOT:PSS for Use as the Back Contact of a Bifacial Silicon Solar Cell and for Silicon Wafer Bonding

The optical, electrical and mechanical properties of thin films of PEDOT:PSS were analysed for use as the back contact of a bifacial silicon solar cell. The thin films were prepared by spin coating to cover the thickness range of 56 nm to 133 nm, with samples from each thickness annealed for 2 hours over the range of 50°C to 195°C.

The optical properties of thin films of PEDOT:PSS were measured using ellipsometry and absorption spectroscopy. The refractive indices were found to be anisotropic, differing between the in-plane and out-of-plane directions. The real component of the refractive index was found to decrease with reducing thickness, which could be due to a reduction in the effective density of the film in the out-of-plane direction. However, due to the very small changes in refractive index observed between the samples, further investigation is required to fully quantify the repeatability of the ellipsometry modelling process for these films to confirm the qualitative changes observed.

The absorption measurements indicated that a broad absorption band exists from 500 nm to 2500 nm, which is believed to be due to a free charge contribution to the absorption, or mid-gap states (polaron or bi-polaron states). An overall decrease in absorbance is observed for increasing annealing temperature. This was also seen to be accompanied with an increase in electrical conductivity. The observed change in absorbance is believed to be due to a red shift in the absorbance maximum of mid-band gap states, resulting from the increased conductivity.

The conductivity of the PEDOT:PSS films was found to increase with annealing temperature, resulting in a maximum conductivity of 82 S/m. This corresponds to a much lower conductivity than that desired by a transparent conductive electrode for use in a solar cell of $>10^6$ S/m. However the conductivity of PEDOT:PSS has been shown elsewhere to be increased to beyond 10^5 S/m [21], through the addition of an organic co-solvent. Therefore there is substantial potential for the use of a PEDOT:PSS based layer as a transparent conductive electrode.

The shear stress of PEDOT:PSS thin films with annealing temperature was measured for use as a conductive adhesive for Si wafer bonding. The shear stress was found to exhibit two distinct regions, above and below an annealing temperature of 100°C. The maximum shear stress of 820 kPa is only slightly lower than that observed for many other electrical

conductive adhesives, however this is the first study to report the application of Si wafer bonding using an ECA.

One application of the PEDOT:PSS as an ECA would be to provide an intermediate film to bond the up-conversion layer to the rear surface of a bifacial solar cell. This bonding layer would also act as the rear electrode of the solar cell and reduce the detrimental scattering of the up-conversion emission that would occur if an air gap existed between the up-conversion layer and the rear photovoltaic surface. The work by Fischer *et al*. demonstrated that a non-structured (flat) rear surface of a bifacial silicon solar cell is optimal for maximising the potential of the up-conversion emission [25, 26], therefore the results carried out in this study for measuring the shear stress between two PEDOT:PSS bonded planar silicon wafers is of greater relevance.

7.6 References

1. P. R. Pudasaini, A. A. Ayon, and Iop, "Low-cost, high-efficiency organic/inorganic hetero-junction hybrid solar cells for next generation photovoltaic device," 13th International Conference on Micro and Nanotechnology for Power Generation and Energy Conversion Applications (Powermems 2013) **476** (2013).
2. M. M. Ling, and Z. N. Bao, "Thin film deposition, patterning, and printing in organic thin film transistors," Chemistry of Materials **16**, 4824-4840 (2004).
3. W. Chen, M. P. Nikiforov, and S. B. Darling, "Morphology characterization in organic and hybrid solar cells," Energy & Environmental Science **5**, 8045-8074 (2012).
4. M. A. Ruderer, and P. Muller-Buschbaum, "Morphology of polymer-based bulk heterojunction films for organic photovoltaics," Soft Matter **7**, 5482-5493 (2011).
5. M. C. Petty, *Molecular Electronics: From Principles to Practice* (Wiley, 2008).
6. B. Friedel, P. E. Keivanidis, T. J. K. Brenner, A. Abrusci, C. R. McNeill, R. H. Friend, and N. C. Greenham, "Effects of Layer Thickness and Annealing of PEDOT:PSS Layers in Organic Photodetectors," Macromolecules **42**, 6741-6747 (2009).
7. R. C. Neville, *Solar Energy Conversion: The Solar Cell* (Elsevier Science, 1995).
8. L. A. A. Pettersson, F. Carlsson, O. Inganäs, and H. Arwin, "Spectroscopic ellipsometry studies of the optical properties of doped poly(3,4-ethylenedioxythiophene): an anisotropic metal," Thin Solid Films **313–314**, 356-361 (1998).
9. L. A. A. Pettersson, S. Ghosh, and O. Inganas, "Optical anisotropy in thin films of poly(3,4-ethylenedioxythiophene)-poly(4-styrenesulfonate)," Organic Electronics **3**, 143-148 (2002).
10. T. Wagner, "E-mail correspondance," (2014).
11. C. L. J. J. Malehorn, *Practical Guide to Business Forecasting* (Graceway, 2005).
12. H. K. Kim, and F. G. Shi, "Refractive index of polycrystalline submicrometer polymer thin films: Thickness dependence," Journal of Materials Science: Materials in Electronics **12**, 361-364 (2001).
13. H. Kim, C. M. Gilmore, A. Pique, J. S. Horwitz, H. Mattoussi, H. Murata, Z. H. Kafafi, and D. B. Chrisey, "Electrical, optical, and structural properties of indium-

tin-oxide thin films for organic light-emitting devices," Journal of Applied Physics **86**, 6451-6461 (1999).

14. L. Castaner, and S. Silvestre, *Modelling Photovoltaic Systems Using PSpice* (Wiley, 2003).
15. J. Gasiorowski, R. Menon, K. Hingerl, M. Dachev, and N. S. Sariciftci, "Surface morphology, optical properties and conductivity changes of poly(3,4-ethylenedioxythiophene): poly(styrenesulfonate) by using additives," Thin Solid Films **536**, 211-215 (2013).
16. L. B. Valdes, "Resistivity measurements on germanium for transistors," Proceedings of the Institute of Radio Engineers **42**, 420-427 (1954).
17. L. S. C. Pingree, B. A. MacLeod, and D. S. Ginger, "The changing face of PEDOT : PSS films: Substrate, bias, and processing effects on vertical charge transport," Journal of Physical Chemistry C **112**, 7922-7927 (2008).
18. D. Yoo, W. Son, S. Kim, J. J. Lee, S. H. Lee, H. H. Choi, and J. H. Kim, "Gradual thickness-dependent enhancement of the thermoelectric properties of PEDOT:PSS nanofilms," RSC Advances **4**, 58924-58929 (2014).
19. J. Poortmans, and V. Arkhipov, *Thin Film Solar Cells: Fabrication, Characterization and Applications* (Wiley, 2006).
20. A. Santamaria, M. Eugenia Munoz, M. Fernandez, and M. Landa, "Electrically conductive adhesives with a focus on adhesives that contain carbon nanotubes," Journal of Applied Polymer Science **129**, 1643-1652 (2013).
21. Y. Xia, and J. Ouyang, "PEDOT:PSS films with significantly enhanced conductivities induced by preferential solvation with cosolvents and their application in polymer photovoltaic cells," Journal of Materials Chemistry **21**, 4927-4936 (2011).
22. M. Abouie, Q. Liu, and D. G. Ivey, "Eutectic and solid-state wafer bonding of silicon with gold," Materials Science and Engineering B-Advanced Functional Solid-State Materials **177**, 1748-1758 (2012).
23. J. C. C. Lo, Z. Rong, S. W. R. Lee, and W. Zelin, "Evaluation of polymer wafer bonding with silicone adhesive and patterned trenches," in *12th International Conference on Thermal, Mechanical and Multi-Physics Simulation and Experiments in Microelectronics and Microsystems (EuroSimE)*(2011), pp. 1/5-5/5.

24. V. C. Tung, J. Kim, L. J. Cote, and J. Huang, "Sticky Interconnect for Solution-Processed Tandem Solar Cells," Journal of the American Chemical Society **133**, 9262-9265 (2011).
25. S. Fischer, B. Fröhlich, H. Steinkemper, K. W. Krämer, and J. C. Goldschmidt, "Absolute upconversion quantum yield of β-NaYF4 doped with Er3+ and external quantum efficiency of upconverter solar cell devices under broad-band excitation considering spectral mismatch corrections," Solar Energy Materials and Solar Cells **122**, 197-207 (2014).
26. S. Fischer, A. Ivaturi, B. Frohlich, M. Rudiger, A. Richter, K. W. Kramer, B. S. Richards, and J. C. Goldschmidt, "Upconverter Silicon Solar Cell Devices for Efficient Utilization of Sub-Band-Gap Photons Under Concentrated Solar Radiation," Photovoltaics, IEEE Journal of **4**, 183-189 (2014).

Chapter 8 - Conclusions of the Thesis and Future Work

In this chapter the conclusions of the work carried out in this study are brought together to provide an overall perspective of the progress made. The suggested direction of future work in this area of research is presented.

8.1 Conclusions of 2D Photonic Crystals for Enhanced Up-Conversion Emission in Photovoltaics

Up-conversion offers significant potential to increase the efficiency of silicon solar cells, without affecting the electronic properties of the photovoltaic material. A passive optical layer can be applied at the rear of a bifacial silicon solar cell, absorbing low energy photons that would otherwise be transmitted through the solar cell, and emitting photons of energy greater than the band gap of the silicon semiconductor; thereby improving the spectral range over which the solar cell can utilise. Theoretical calculations performed elsewhere have shown that the efficiency of a single junction silicon solar cell can be increased from the Shockley-Quieser limit of around 30% to 47.6% for non-concentrated sunlight. However the efficiency of current up-conversion materials published in literature is very low. The highest reported increase in current density for a silicon photovoltaic cell by the application of an up-conversion layer is of 4.03 mA/cm^2 for concentrated solar radiation of 77 suns. Therefore there remains great potential to improve the efficiency of up-conversion layers and significant commercial potential for the resulting highly efficient solar cells.

2D photonic crystals offer an effective way of controlling the interaction of light with matter in 3 dimensions. Tuning the geometry of a 2D photonic crystal to align a flat band edge in the Γ-direction has been shown elsewhere to significantly improve the emission of luminescent materials, in some cases resulting in lasing of emission [2-5]. It is this property of 2D photonic crystals, the enhancement of emission through the high density of states and low group velocity at a flat photonic band edge, which has been the motivation behind the work of this thesis to enhance the emission of up-converting material tuned for use with crystalline silicon photovoltaics.

The integration of a nanostructured optical up-conversion layer to the rear of a bifacial silicon solar cell requires careful consideration of the rear conducting electrode used to maximise the effect of the up-conversion layer. Present electrode configurations are based on either metal strips that result in a high degree of shadowing, or inorganic transparent

conductive electrodes which require complex deposition procedures. The highly conductive polymer PEDOT:PSS can be deposited in air at room temperature by a simple spin coating procedure. It can also act as an adhesive layer to bind the up-conversion layer to the rear surface of a bifacial photovoltaic layer. However no wide ranging analysis of the electrical, mechanical and optical properties had previously been found in literature to fully compare and understand the potential of this material for such an application.

Two simulation methods were chosen for use in this thesis to theoretically explore and optimise the properties of 2D photonic crystals: plane wave expansion and finite-difference time-domain. The simulation code developed for use in this work was shown to provide consistent results with work published elsewhere, providing confidence in the approach. Furthermore, the two methods were shown during this study to provide consistent descriptions of the electromagnetic field distribution, providing additional confidence. Triangular, hexagonal and square arrays of holes and pillars were compared for use with the experimentally determined refractive indices of the materials to be used for the practical fabrication work in this study. For a 2D photonic crystal consisting of TiO_2:Er and air, the optimised structure for a discrete flat band edge in the Γ-direction was found to be a triangular array of holes of radius 203 nm and lattice constant 633 nm for tuning the band edge to 980 nm (and a radius of 315 nm and lattice constant of 984 nm for 1523 nm tuning). For a 2D photonic crystal consisting of silicon and YF_3:Er, the optimised structure for a discrete flat band edge in the Γ-direction was found to be a triangular array of silicon pillars of radius 127 nm and lattice constant 439 nm for tuning the band edge to 980 nm (and a radius of 198 nm and lattice constant of 682 nm for 1523 nm tuning).

A wide range of fabrication and characterisation procedures were developed for this study. In particular, a customised confocal microscope was integrated into a spectrofluorometer to locate and record the luminescent properties of the very small (30 μm × 30 μm) 2D photonic crystal sample areas. Furthermore, novel ellipsometry analysis of thin films of TiO_2:Er and YF_3:Er was carried out providing detailed refractive index data required for accurate simulation of the proposed 2D photonic crystals.

The first 2D photonic crystal to be experimentally explored in this work consisted of holes of air in a TiO_2:Er thin film. The initial deposition method of spin coating a sol-gel of TiO_2:Er allowed for very accurate control of the erbium doping concentration, however resulted in layers with a high degree of cracking that increased with sample thickness.

This limited the sample thickness achievable from a single spin coated layer. Further analysis of the microstructure of the films revealed that the anatase/rutile multiphase of the TiO_2:Er material was composed of adjoined grains, making this phase unsuitable for use as a 2D photonic crystal due to the inhomogeneity. In contrast, the amorphous phase of the film was found to be dense and homogeneous, therefore would be suitable for patterning. For both phases, ellipsometry was used to successfully model the associated refractive indices. The real component of the refractive index was found to vary throughout the thickness of the thin films; in particular for the anatase/rutile mixed phase, which varied from 1.38 at the bottom of the film to 2.32 at the top (at a wavelength of 550 nm). This variation in refractive index was consistent with results published elsewhere for TiO_2 on a SiO_2 substrate. The variation in refractive index was expected to be the reverse direction for a silicon substrate, therefore the work in this thesis indicates the important effect of the native oxide on the silicon surface for the resulting refractive index of the deposited TiO_2 based film. A procedure for producing a stack of TiO_2:Er layers (overall 600 nm thick) was developed to achieve the overall thickness required for detecting an up-converted emission of 980 nm, following excitation at 1523 nm. However the multi-stacked films had significant issues with cracking that made them unsuitable due to the microscopic variations in refractive index.

The limitations in the sol-gel prepared TiO_2:Er films led to investigation of the deposition of this material using an alternative method of RF sputter deposition. A crude method of erbium doping was carried out for proof of concept using erbium metal placed on a TiO_2 sputter target. This resulted in the ability to achieve much thicker films that were believed to be required to observe a strong up-conversion emission signal, however the exact doping concentration of erbium was not known. Films of 4500 nm were achieved using this method. Ellipsometry analysis was used to show that the gradient in refractive index of TiO_2:Er observed for the sol-gel prepared films was also present for the sputter coated films. Up-conversion emission of 980 nm following 1523 nm excitation was observed for the sputter coated film of 4500 nm thickness, however this signal was much weaker than that obtained by the highly cracked sol-gel prepared film of 600 nm. The cause of this difference is believed to be due to either the different erbium concentrations, or an increased optical path length in the cracked film due to internal scattering from the cracks. As the exact erbium concentration of the RF sputtered film was not known, further work beyond the scope of this thesis is required to determine the cause of this effect.

Reactive ion etching of the TiO_2:Er layers was investigated using a hard mask of chromium to fabricate the 2D photonic crystal structure of holes in the thin film. During the characterisation of the etch chemistry, it became apparent that the chromium mask was not strong enough to resist the etch to achieve the deep 4500 nm anisotropic etches required to pattern the RF sputtered TiO_2:Er homogeneous film. Therefore an alternative fabrication method of focused ion beam etching was explored. This method was found to be suitable for achieving much deeper etches, without the need of a mask, however could not produce the anisotropic etch features required for the 2D photonic crystal.

A second material combination was investigated for use as an 2D photonic crystal enhanced up-conversion layer: silicon and erbium doped YF_3. The advantage of these materials was that the anisotropic etching of silicon is a well-documented procedure, developed for the microelectronics industry, while YF_3 had been shown in literature to be a good host for up-converting rare earth ions. A procedure for the anisotropic etching of silicon was developed using a chromium hard mask, which allowed for the angle of the side walls to be controlled accurately. A method for depositing thin films of YF_3:Er was explored to fill in the gaps between the silicon pillars with the up-converting material. Initial investigation revealed that the temperature of the silicon substrate during deposition was critical to the resulting crystallinity of the YF_3:Er layer, which in turn had a significant effect on the up-conversion properties of the material. A customised substrate heater was integrated into the evaporation chamber to allow for crystalline YF_3:Er layers to be achieved (at a substrate temperature of 227°C), which were found to show good 980 nm emission following excitation at 1523 nm for films of around 630 nm or greater. Amorphous films achieved by deposition onto silicon substrates at room temperature (22°C) of comparable thickness (700 nm) were found to exhibit no observable up-conversion emission at 980 nm.

Ellipsometry analysis was carried out to model the refractive index of the experimentally produced films. The real component of the refractive index of the YF_3:Er films at a wavelength of 600 nm (~1.54) was found to be comparable to other reported results for un-doped YF_3 in literature. A variation of ±4.62% was found for the real component of the refractive index for films produced under the same process conditions.

The YF_3:Er up-conversion material was successfully deposited onto the arrays of silicon pillars fabricated using reactive ion etching. However the YF_3:Er did not fill the space between the pillars very well, resulting in a low volume fill factor. This greatly altered

the effective refractive index of the volume between the silicon pillars, and hence the resulting band structure of the photonic crystal. Further modelling of 2D photonic crystals consisting of an effective refractive index of YF_3:Er and air in varying combinations was carried out to try to account for the incomplete filling. These structures were experimentally fabricated and optically characterised. A maximum photoluminescence enhancement of 3.79 times was observed for the 980 nm emission profile, however this could not be successfully attributed to a photonic crystal effect. This enhancement was more likely due to an increase in scattering from the structured silicon substrate, however the further work required to confirm this hypothesis was beyond the time frame of this thesis.

Thin films of PEDOT:PSS were prepared over a thickness range of 56-133 nm and annealed over a temperature range of 50-195°C to characterise their electrical, mechanical and optical properties. A novel anisotropic ellipsometry model covering the wavelength range of 300-2500 nm was developed to fully characterise the real and imaginary components of the refractive index of the PEDOT:PSS thin films. The model confirmed results presented elsewhere in literature that the index of refraction in the plane of the thin film shows metallic like behaviour. General trends of decreasing absorbance were observed for decreasing thickness and increasing annealing temperature as expected.

The annealing temperature was found to be critical to both the resulting electrical conductivity and shear stress of silicon wafers bonded together using a thin film of PEDOT:PSS. A critical annealing temperature of 100°C was identified, corresponding to the complete removal of water from the thin film. Electrical conductivity was found to increase beyond 100°C, while the shear stress was found to decrease. Therefore this tradeoff must be taken into account when optimising the process conditions for using PEDOT:PSS as an electrically conductive adhesive.

This novel extensive analysis of the electrical, mechanical and optical characteristics of thin films of PEDOT:PSS over the wavelength range of 300-2500 nm and annealing temperature of 50-195°C provides a catalogue of properties from which PEDOT:PSS can be accurately compared with other transparent conductive oxides to allow an informed choice of contact for a potential solar cell application. The additional characterisation of the shear stress of the PEDOT:PSS allows for the optimum process conditions to be found for its potential use as an adhesive transparent electrical contact to bond an up-conversion layer the rear of a bifacial silicon solar cell.

The work carried out in this thesis has provided extensive analysis of two particular routes of using 2D photonic crystals to enhance up-conversion emission from thin films. Up-conversion emission at 980 nm from excitation at 1523 nm was measured for both thin films of TiO_2:Er and YF_3:Er, however difficulties remain in fabricating the defect free, ideal 2D photonic crystal structures required to accurately characterise an enhancement in emission. Enhancement of the 980 nm emission was observed for photonic crystal structures of silicon pillars and YF_3:Er, however the exact cause of the enhancement could not be identified, however is likely to be as a result of an increased optical path length of the excitation light of 1523 nm due to scattering.

In the process of exploring these two routes, novel ellipsometry analysis has been carried out on TiO_2:Er, YF_3:Er and PEDOT:PSS. The refractive indices determined using ellipsometry were used in the customised simulation code to determine the optimum geometrical properties of 2D photonic crystals of TiO_2:Er/air and silicon/YF_3:Er for band edge enhancement in the Γ-direction, perpendicular to the plane of the photonic crystal slab. A spectrofluorometer was adapted with a custom built confocal microscope allowing for the emission from both continuous wave and pulsed laser excitation of thin films of up-conversion material to be measured. This work has presented the first characterisation of thin films of YF_3:Er >85 nm thick. Only one previous study has investigate the up-conversion properties of YF_3:Er, which was deposited using atomic layer deposition to achieve films of up to 85 nm in thickness [6]. The current work also represents the first characterisation of the refractive index of YF_3:Er. The work carried out in this thesis on the ellipsometry analysis of TiO_2:Er is believed to be the first for this material and covers a wider wavelength range and depth of analysis of the variation in refractive index with thickness than any other previous study. Finally, the work carried out on PEDOT:PSS is the first to characterise its use as an electrical adhesive layer for silicon wafer bonding.

8.2 Future Work to Enhance Up-Conversion for Silicon Photovoltaics using 2D Photonic Crystals

In this section a broad overview of the key aspects of future work to be carried out to enhance up-conversion using 2D photonic crystals for silicon photovoltaics will be presented. This includes an analysis of methods to improve the simulation and fabrication of 2D photonic crystals of Si and YF_3:Er, which formed the main focus of the work carried out in this thesis. Suggested improvements to the fabrication of nanostructured thin films of TiO_2:Er are also presented, along with an up to date review of the most recent developments in enhancing up-conversion emission.

8.2.1 Improving Si/YF_3:Er 2D Photonic Crystal Structures for Enhanced Up-Conversion Emission

Simulating the 2D photonic crystal structures in three dimensions would allow for an improvement in the accuracy of the band structure. Taking into account the height of the 'photonic crystal slab' and the refractive index of the material layers above and below by using three dimensional simulations would allow for the thickness of the slab and nature of the surrounding medium to be optimised for the particular situation. Initial three dimensional simulations were carried out using the PWE method and a 'supercell' approach. However the additional computational time required to complete these simulations using the available computational hardware did not allow for this analysis to be a sensible route to explore during the limited time of the PhD. An example of a band structure simulated using the 3D PWE method is shown in Figure 3-1, along with a comparison of results published elsewhere in literature for the same structure [7]. Improved computational facilities would allow for more accurate 3D simulations to be carried out to find the optimum geometries for the 2D photonic crystals.

An enhancement of the 980 nm up-converted emission from Si/YF_3:Er photonic crystal structures was observed during the work of this thesis, however the cause for the broad wavelength range enhancement is not known. Therefore, investigation into the cause of this enhancement would be useful for directing further research into improving the efficiency of up-conversion layers. In particular, a computer model simulating the scattering of light for use as a 2D photonic crystal enhanced up-conversion layer as a result of the nanostructured substrate would provide much needed characterisation of the scattering effects in the non-linear material.

Improvements to both the volume fill factor and starting up-conversion efficiency could be achieved by embedding nanocrystals of the best performing up-conversion material into a PMMA host. The PMMA solution could then be spin coated onto a substrate of pillars of silicon, to fill in the gaps between the pillars with PMMA and nanocrystals. The concept of embedding the high performing β-$NaYF_4$:Er nanocrystals into PMMA for use with silicon photovoltaics has been detailed recently by Fischer *et al* [8]. The successful in-fill of the space between nanostructures with a polymer using spin-coating has also been reported elsewhere [9].

8.2.2 Improved Fabrication Techniques for Nano-Structured Thin Film Up-Converting TiO_2:Er

Initial investigation carried out in this thesis have shown that sputter deposited TiO_2:Er produces dense homogeneous films showing the desired up-conversion properties. However the current method used of placing metal erbium strips on top of a TiO_2 sputter target does not allow for the doping concentration of erbium to be accurately controlled. Therefore future work should investigate preparing pre-doped TiO_2:Er targets of varying erbium concentration to allow for a complete controlled analysis to be carried out.

During the etch of TiO_2:Er carried out in this work, the resistance of the Cr mask to the etch chemistry was found to be very poor. Characterisation of the resistance of the Cr mask to similar etch chemistries detailed elsewhere [10] suggests that the resistance should have been adequate to achieve good selectivity and deep etches of the TiO_2:Er sample. Additional mask fabrication techniques, including sputter deposition of a NiCr composite, could allow for more resistant masks to be fabricated and therefore a thorough characterisation of the etch chemistry for TiO_2:Er to be carried out.

8.2.3 Recent Developments in the Field of Enhancing Up-Conversion Emission for Silicon Photovoltaics

Spectral concentration of the un-used near infrared radiation into near infrared wavelengths that are suitable for up-conversion has become an emerging area of interest [11]. A very recent study by Marques-Hueso *et al.* has demonstrated a proof of concept to show that the combined use of InP 2D photonic crystals and PbSe quantum dots can be used to red-shift the wavelengths of the solar spectrum of energy less than that of the silicon band-gap, but greater than that of the absorption of the up-conversion absorber: 1100 nm – 1470 nm [12]. The quantum dot provided the luminescent red-shifting, while

the photonic crystal was used to narrow the quantum dot emission, increasing the emission overlap with the up-converter absorber by up to 158%. Furthermore, the quantum dot emission in the vertical direction (perpendicular to the plane of the photonic crystal was found to increase by a factor of 7.8× due to the band edge effect [12]. Theoretical analysis accompanying these measurements showed that a maximum enhancement of the up-conversion emission using could be increased by a factor of 13×.

Recent developments in the field of up-conversion for enhancing silicon photovoltaics have provided further evidence for the potential benefits of nano-structured materials to enhance the up-conversion emission. This is an exciting time for this field of research that offers great potential for significant gains to be made. Continued work in the area of up-conversion enhancement has potential not just for fundamental scientific research, but for the continued uptake of sustainable energy power generation devices over the coming years.

8.3 References

1. S. Fischer, B. Fröhlich, H. Steinkemper, K. W. Krämer, and J. C. Goldschmidt, "Absolute upconversion quantum yield of β-NaYF4 doped with Er3+ and external quantum efficiency of upconverter solar cell devices under broad-band excitation considering spectral mismatch corrections," Solar Energy Materials and Solar Cells **122**, 197-207 (2014).
2. H.-Y. Ryu, S.-H. Kwon, Y.-J. Lee, Y.-H. Lee, and J.-S. Kim, "Very-low-threshold photonic band-edge lasers from free-standing triangular photonic crystal slabs," Applied Physics Letters **80**, 3476-3478 (2002).
3. S. H. Kwon, H. Y. Ryu, G. H. Kim, Y. H. Lee, and S. B. Kim, "Photonic bandedge lasers in two-dimensional square-lattice photonic crystal slabs," Applied Physics Letters **83**, 3870-3872 (2003).
4. S. Kim, S. Ahn, J. Lee, H. Jeon, P. Regreny, C. Seassal, E. Augendre, and L. Di Cioccio, "Milliwatt-level fiber-coupled laser power from photonic crystal band-edge laser," Optics Express **19**, 2105-2110 (2011).
5. K. Sunghwan, L. Jeongkug, J. Heonsu, and K. Hyo Jin, "Fiber-coupled surface-emitting photonic crystal band edge laser for biochemical sensor applications," Applied Physics Letters **94**, 133503-133503-133503 (2009).
6. C. Andriamiadamanana, A. Ferrier, L. Lombez, A. L. Joudrier, N. Naghavi, P. Ghenuche, N. Bardou, J. L. Pelouard, S. Collin, F. Pelle, and J. F. Guillemoles, "Plasmonic enhancement of up-conversion in ultrathin layers," Physics, Simulation, and Photonic Engineering of Photovoltaic Devices **8256**, 8 (2012).
7. S. G. Johnson, S. Fan, P. R. Villeneuve, J. D. Joannopoulos, and L. A. Kolodziejski, "Guided modes in photonic crystal slabs," Physical Review B **60**, 5751-5758 (1999).
8. S. FIscher, "Upconversion of sub-band-gap photons for silicon solar cells," in *Fraunhofer-Institut für Solare Energiesysteme ISE*(2014).
9. P. R. Pudasaini, A. A. Ayon, and Iop, "Low-cost, high-efficiency organic/inorganic hetero-junction hybrid solar cells for next generation photovoltaic device," 13th International Conference on Micro and Nanotechnology for Power Generation and Energy Conversion Applications (Powermems 2013) **476** (2013).

10. K. R. Williams, K. Gupta, and M. Wasilik, "Etch rates for micromachining processing-Part II," Microelectromechanical Systems, Journal of **12**, 761-778 (2003).
11. J. C. Goldschmidt, P. Loper, S. Fischer, S. Janz, M. Peters, S. W. Glunz, G. Willeke, E. Lifshitz, K. Kramer, and D. Biner, "Advanced upconverter systems with spectral and geometric concentration for high upconversion efficiencies," in *Optoelectronic and Microelectronic Materials and Devices, 2008. COMMAD 2008*(2008), pp. 307-311.
12. J. Marques-Hueso, R. Peretti, R. Abargues, B. S. Richards, C. Seassal, and J. P. Martínez-Pastor, "Photovoltaics: Photonic Crystal-Driven Spectral Concentration for Upconversion Photovoltaics (Advanced Optical Materials 4/2015)," Advanced Optical Materials **3**, 594-594 (2015).

Appendix A – Simulation Code

An example of a MEEP control file used to define the geometry, symmetry, optical properties, boundary conditions and simulation output.

```
; Some parameters to describe the geometry:

(define-param eps 12.11) ; dielectric constant of surrounding

(define-param epshole 2.4336) ; dielectric constant of hole

(define-param r 0.29) ; radius of holes


; The cell dimensions

(set! geometry-lattice (make lattice (size 1 (sqrt 3) no-size)))

(set! geometry

      (list (make block (center 0 0) (size infinity infinity infinity)

                  (material (make dielectric (epsilon eps))))

            (make cylinder (center 0 0) (radius r) (height infinity) (epsilon epshole))

                  (make cylinder (center (/ -1 2) (/ (sqrt 3) 2)) (radius r) (height infinity) (epsilon epshole))

                  (make cylinder (center (/ 1 2) (/ (sqrt 3) 2)) (radius r) (height infinity) (epsilon epshole))

                  (make cylinder (center (/ -1 2) (* (/ (sqrt 3) 2) -1)) (radius r) (height infinity) (epsilon epshole))

                  (make cylinder (center (/ 1 2) (* (/ (sqrt 3) 2) -1)) (radius r) (height infinity) (epsilon epshole))))


(set-param! resolution 20)


(define-param fcen 0.3) ; pulse center frequency

(define-param df 0.6) ; pulse freq. width: large df = short impulse


;***************
```

```
(define-param k-interp 9)
(define Gamma (vector3 0 0 0))
(define M     (vector3 0.288675134594813 -0.5 0))
(define K     (vector3 0.0 -0.666666666666667 0))
(define dtime 0)
(define gauss (make gaussian-src (frequency fcen) (fwidth df)))

(define a1 (vector3 0.5 (/ (sqrt 3) 2)  0))

(define k-points (list Gamma M K Gamma))
(set! k-points (interpolate k-interp k-points))
(define R (vector3* (* 2 pi) a1 ))

(define s1 (vector3 -0.1234 -0.2468 0))
(define s2 (vector3+ s1 a1))

(define n 0)
(define rfreqs (list ))
(map (lambda (kvec)
       (restart-fields)
       (change-k-point! kvec)
       (set! dtime (vector3-dot kvec R))
       (change-sources! (list
          (make source (src gauss) (component Ez) (center s1))
          (make source (src gauss) (component Ez) (center s2)
                    (amplitude (exp (* 0+1i dtime))))))
       (run-sources+ 300
          (after-sources (harminv Ez s1 fcen df)
```

```
                (harminv Ez s2 fcen df)))
  (set! rfreqs (map  harminv-freq-re  harminv-results))
  (print "freqs:, " (+ n 1) ", " (vector3-x kvec) ", " (vector3-y kvec)
       ", " (vector3-z kvec))
  (map  (lambda (f) (print ", " f))  rfreqs)
  (print "\n")
  (set! n (+ n 1)))
k-points)
```